

The stellate microcircuit of the cochlear nucleus: design and optimisation of a biophysically-realistic neural network model

Michael Allan Eager

Submitted in total fulfilment of the requirements of the degree of
Doctor of Philosophy

Department of Otolaryngology
THE UNIVERSITY OF MELBOURNE

August 2013

Produced on archival quality paper.

Copyright © 2013 Michael Allan Eager

All rights reserved. No part of the publication may be reproduced in any form by print, photoprint, microfilm or any other means without written permission from the author.

Abstract

Biophysically-realistic neural network (BNN) models provide an important means to improve understanding of neural processing of sound. The quality of BNN models is dependent upon the experimental data and optimisation methods used in their development. The cochlear nucleus stellate microcircuit (CNSM) provides a robust spectral representation of sound and plays an essential part in speech communication. Existing BNN models of the CNSM have not been sufficiently considerate of the most current physiological data. Additionally, optimisation methods used in these models have not been adequately documented.

This thesis presents a novel BNN model of the CNSM. The model was optimised using rigorous sequential methods and simultaneous genetic algorithms (GAs).

The first investigation developed the neural models and synaptic connections of the CNSM model in a sequential optimisation procedure. Auditory nerve fibre (ANF) input to the CNSM model used phenomenologically-accurate output of the Carney AN model. Each CNSM cell type model was designed using appropriately detailed neural models. Their synaptic parameters were optimised based on established physiological data.

The second investigation analysed the output responses of the optimised CNSM model to amplitude modulation (AM) tones. Encoding of AM tones undergoes important transformations in the cochlear nucleus (CN) from purely spike-timing temporal encoding in ANFs to feature-based rate encoding in higher auditory centres. Rate and temporal information was analysed in each CNSM cell type in response to changes in sound level and modulation frequencies. The CNSM model adequately reproduced experimental responses.

The third investigation used GAs to simultaneously fit all network parameters to a

simplified CNSM model. Pre-defined target parameters were used to generate surrogate data for the optimisation to fit. The ability of novel BNN cost functions to constrain the model was also investigated, including (1) dynamic spike-time programming (finding minimum distance between two spike trains), (2) instantaneous firing rate comparisons, and (3) average intracellular voltage comparisons.

Through the design and optimisation of the CNSM model, the thesis demonstrates the utility of evidence-based sequential methods and whole-network simultaneous optimisation methods using GAs for BNN development.

Declaration

This is to certify that

1. The thesis comprises only my original work towards the PhD.
2. Due acknowledgement has been made in the text to all other material used.
3. The thesis is less than 100,000 words in length, exclusive of tables, maps, bibliographies and appendices.

Michael Allan Eager, August 2013

This page intentionally left blank.

To Genevieve

This page intentionally left blank.

Contents

1	Introduction and Literature Review	1
1.1	Introduction	1
1.2	Literature Review	2
1.2.1	Auditory System	2
1.2.2	Auditory Nerve Fibres	3
1.2.3	Cochlear Nucleus	4
1.2.4	T Stellate Cells	6
1.2.5	Function of the Stellate Microcircuit	12
1.2.6	Computational Models of the Cochlear Nucleus	15
1.2.7	Optimisation in Neural Modeling	20
1.3	Overview of Thesis	21
2	Methods	23
2.1	Auditory Input Model	23
2.1.1	Frequency Channels	24
2.1.2	Inner and Outer Hair Cell Compression	26
2.1.3	High and Low Spontaneous Rate Fibres	26
2.2	Neural Cell Models	27
2.2.1	Neural Sub-types in the Cochlear Nucleus	30
2.3	Connectivity and Topology	31
2.3.1	Connectivity Parameters	32
2.3.2	Synapse Models	34
2.3.3	Delay and Latency Variables	36
2.4	Implementation of the Cochlear Nucleus Stellate Microcircuit Model	37
2.4.1	Simulation Environment	37
2.4.2	Stimulus Generation and Analysis	37
2.5	Optimisation Techniques	38
2.5.1	Sequential Methods	40
2.5.2	Simultaneous Methods	40
3	Sequential Optimisation	41
3.1	Introduction	41
3.1.1	Cochlear Nucleus Stellate Microcircuit Model	42
3.2	Methods	45
3.2.1	Auditory Nerve Fibre Model	45
3.2.2	Neural Models	45
3.2.3	Connectivity and Network Parameters	45

3.2.4	Synapse Models	46
3.2.5	Synaptic Jitter	46
3.2.6	Synaptic Delay Additional Parameter	48
3.2.7	Simulation Specifications	49
3.2.8	Optimisation Routine	49
3.2.9	Verification of Cell Model Responses to Simple Tones and Noise .	50
3.3	Golgi Cell Model	52
3.3.1	Background	52
3.3.2	Implementation	55
3.3.3	Optimisation Results	59
3.3.4	Verification of the Golgi Cell Model	60
3.3.5	Discussion of the Golgi Cell Model	62
3.4	D Stellate Cell Model	64
3.4.1	Background	64
3.4.2	Implementation	66
3.4.3	Results of Click Recovery Optimisation	71
3.4.4	Results of Rate Level Optimisation	74
3.4.5	Verification of the DS Cell Model	77
3.4.6	Discussion of the DS Cell Model	78
3.5	Tuberculoventral Cell Model	82
3.5.1	Background	82
3.5.2	Implementation	85
3.5.3	Results of Tone and Noise Rate Level Optimisation	88
3.5.4	Results of Notch Noise Optimisation	91
3.5.5	Verification of the TV Cell Model	93
3.5.6	Discussion of the TV Cell Model	96
3.6	T Stellate Cell Model	97
3.6.1	Background	98
3.6.2	Implementation	101
3.6.3	Optimisation Results	107
3.6.4	Verification of the TS Cell Models	113
3.6.5	Overview of TS Cell Model Results	116
3.7	Discussion	118
3.7.1	Optimised Parameters of the CNSM Model	118
3.7.2	Limitations of the CNSM Model	119
3.7.3	Implications for BNN Optimisation	121
3.8	Conclusion	122
4	AM Coding in the CNSM Model	123
4.1	Introduction	123
4.1.1	Definition of Amplitude Modulation	124
4.1.2	Temporal Measures of Amplitude Modulation	125
4.1.3	Amplitude Modulation Coding in the Auditory Pathway	126
4.2	Methods	131
4.2.1	Stimulus	131
4.2.2	Simulations and Analysis	131
4.2.3	CNSM model	131

4.3	Results	134
4.3.1	Responses to Changes in Stimulus Intensity	134
4.3.2	Responses to Changes in Modulation Frequency	139
4.4	Discussion	157
4.4.1	Golgi Cells	157
4.4.2	D Stellate Cells	158
4.4.3	Tuberculoventral Cells	159
4.4.4	T Stellate Cells	159
4.4.5	Limitations of the CNSM Model in Modelling AM Encoding . . .	161
4.4.6	Implications for Temporal Processing in BNN Models	161
4.5	Conclusion	162
5	GA Optimisation	163
5.1	Introduction	163
5.1.1	Stellate Microcircuit of the Cochlear Nucleus	165
5.2	Methods	168
5.2.1	Genetic Algorithm Implementation	168
5.2.2	Cost Functions	171
5.2.3	Stimulus Generation	177
5.2.4	Auditory Nerve Model	178
5.2.5	Neural Models	179
5.2.6	Connectivity	179
5.2.7	Simulation Environment	180
5.2.8	Analysis of Genetic Algorithms and Cost Functions	181
5.3	Results	182
5.3.1	Genetic Algorithm Performance	182
5.3.2	Parameter Sensitivity	185
5.3.3	Effects of Noise	188
5.4	Discussion	191
5.4.1	Matching a BNN to a Known Target Network: Performance of GA and Cost Functions	191
5.4.2	Benefits of Reducing Noise	193
5.4.3	Comparison with Other Studies	194
5.4.4	Other Considerations for Constraining BNNs	195
5.5	Conclusion	197
6	Discussion and Conclusion	199
6.1	Introduction	199
6.2	Overview of Research Findings	200
6.3	Synthesis and Contributions	203
6.3.1	The CNSM Model Advances BNN Models of the Stellate Microcircuit	203
6.3.2	Optimisation Methods Must be Shared to Facilitate Model Reproducibility	204
6.4	Limitation of the Research	204
6.5	Recommendations for Future Work	205
6.6	Concluding Remarks	206

A Appendix: Rothman and Manis neural model	207
A.1 Activation and Deactivation Current Equations	207

List of Figures

1.1	Tonotopic ANF innervation in the CN in cats and humans	3
1.2	Schematic of the cochlear nucleus stellate network	5
1.3	Characteristic PSTH, ISI and CV responses in TS cells	10
1.4	Vowel representation in AN and CN	15
2.1	Auditory periphery schematic of the Zilany AN model	25
2.2	Cat and Rat audiograms and compression curves for the AN model . .	26
2.3	Voltage-dependency of potassium channel dynamics in existing CN models	29
2.4	Stellate microcircuit of the ventral cochlear nucleus	32
2.5	Distribution of synaptic connections	33
3.1	Cochlear nucleus stellate microcircuit model	44
3.2	Gaussian connection between cell types in the CNSM model.	46
3.3	Response of TS cells to isolated synaptic inputs with variable delays . .	47
3.4	Whole network response of ANFs to tones and noise	51
3.5	Rate level response of marginal shell units	53
3.6	GLG cell model diagram	56
3.7	GLG cell model optimisation results	59
3.8	Optimised GLG cell model responses to tones and noise	61
3.9	Rate level response of marginal shell units	62
3.10	Whole network response of GLG cell model	63
3.11	DS cell retrogradely labeled from the DCN	65
3.12	Intracellular membrane current clamp response of DS cells to depolarising and hyperpolarising current	67
3.13	Click recovery stimulus and recording procedure	72
3.14	Experimental data showing click recovery in onset choppers.	73
3.15	Click recovery optimisation results in DS cell model	73
3.16	Tone and noise rate level response of OnC units (DS cell)	74
3.17	Rate level optimisation results in the DS cell model	76
3.18	Optimised DS cell model responses to tones and noise	77
3.19	DS cell PSTHs to CF and off-CF tones	78
3.20	Whole network response of DS cell model	79
3.21	Typical responses of a Type II DCN unit	83
3.22	Experimental data of Type II DCN unit	87
3.23	Rate level optimisation results in the TV cell model with and without inhibition	89

3.24	Experimental notch-noise data of a single Type II DCN unit	91
3.25	TV model optimisation configuration	92
3.26	Best-fit result of TV cell model notch optimisation	93
3.27	Optimised TV cell model PSTH responses	94
3.28	Whole network response of TV cell model	95
3.29	Response of optimised TV cell to notch noise and band-pass noise sweeps	96
3.30	Regularity categorisation in chopper units	99
3.31	Average intracellular response to BF tones in TS cells	99
3.32	Intracellular membrane voltage response of a TS cell model to isolated synaptic inputs	103
3.33	IV categorisation in chopper units	106
3.34	Sustained chopper optimisation results	108
3.35	Transient chopper type 1 optimisation results	110
3.36	Transient chopper type 2 optimisation results	112
3.37	Whole network response of ChS TS cell model	114
3.38	Whole network response of ChT ₁ TS cell model	115
3.39	Whole network response of ChT ₂ TS cell model	117
4.1	Amplitude modulation and its response in the auditory nerve	124
4.2	Temporal modulation transfer function	127
4.3	Rate and temporal response in ANF unit to AM	128
4.4	Temporal response in choppers on-CF	129
4.5	Schematic temporal responses of ANFs and TS cells	130
4.6	The temporal f ₀ response in the CNSM model	135
4.7	The rate level response in the CNSM model to AM tones	136
4.8	Rate and temporal MTF maps of HSR ANFs	140
4.9	Modulation transfer functions of LSR ANFs	142
4.10	On-CF rate and temporal responses in ANFs	144
4.11	GLG cell rate and temporal MTF responses	145
4.12	DS cell rate and temporal MTF responses	147
4.13	On CF rate and temporal MTFs of DS cells	148
4.14	TV cell rate and temporal MTF responses	149
4.15	On CF rate and temporal MTFs of TV cells	150
4.16	Rate and temporal MTF responses for the ChS model	151
4.17	Rate and temporal MTF responses in ChS and ChT ₁ units on-CF	153
4.18	Rate and temporal MTF responses for the ChT ₁ TS cell model	154
4.19	Rate and temporal MTF responses for the ChT ₂ TS cell model	156
5.1	Synaptic connections in the mammalian CNSM	166
5.2	CN stellate microcircuit	167
5.3	Network projections	167
5.4	Cost functions	172
5.5	Dynamic spike time algorithm	173
5.6	Notch stimulus and HSR ANF filterbank output	178
5.7	Performance of the GA (25 repetitions)	183
5.8	Cross comparison of best genomes (25 repetitions)	184
5.9	Best genome parameter errors	186

5.10	Histograms of parameter perturbations	187
5.11	Performance of the GA (100 repetitions)	189
5.12	Cost function histograms of parameter perturbations (100 repetitions) . .	190
5.13	Cross comparison of best genomes (100 repetitions)	191

This page intentionally left blank.

List of Tables

1.1	BNN model studies of the VCN	18
2.1	Basilar membrane frequency-distance function parameters	26
2.2	Cell-type membrane current parameters	31
2.3	Nordlie Model Summary Table Framework	39
3.1	Additional delay component of ANF to CN cell types	48
3.2	Golgi cell model summary	58
3.3	Best-fit parameters of the Golgi cell model optimisation	59
3.4	D stellate cell model summary	69
3.5	Best-fit parameters for the DS cell model in the click recovery optimisation	74
3.6	Best-fit parameters for DS cell model using the rate-level optimisation .	75
3.7	Tuberculoventral cell model summary	86
3.8	Best-fit parameters of the TV cell model using the rate-level optimisation	90
3.9	TV cell model notch noise optimisation	91
3.10	Best fit parameters of DS to TV cell connections using the notch optimisation.	93
3.11	T stellate cell model summary	102
3.12	Optimised synaptic weight and number of connections in the CNSM model	119
4.1	CNSM model summary for AM tone study	132
5.1	Network parameter-to-genome encoding scheme	170
5.2	CNSM model and simulation parameters	176
5.3	Cell-type membrane current parameters	180
5.4	Best genome parameter errors (100 repetitions)	191

This page intentionally left blank.

Acronyms

f_0 fundamental frequency.

f_c carrier frequency.

f_m modulation frequency.

AIV average intracellular voltage.

AM amplitude modulation.

AMPA α -amino-3-hydroxy-5-methyl-4-isoxazolepropioic acid.

AN auditory nerve.

ANF auditory nerve fibre.

AP action potential.

AVCN anteroventral cochlear nucleus.

BF best frequency.

BMF best modulation frequency.

BNN biophysically-realistic neural network.

CF characteristic frequency.

ChS sustained chopper.

ChT transient chopper.

CN cochlear nucleus.

CNSM cochlear nucleus stellate microcircuit.

CV coefficient of variation.

DCN dorsal cochlear nucleus.

DR dynamic range.

DS D stellate.

DSAM Development system for auditory modelling.

EIRA excitatory-inhibitory response area.

EPSC excitatory post-synaptic current.

EPSP excitatory post-synaptic potential.

FFT fast Fourier transform.

FSL first spike latency.

GA genetic algorithm.

GABA gamma-aminobutyric acid.

GABA_A GABAergic subtype A.

GAD glutamic acid decarboxylase.

GCD granule cell domain.

GLG Golgi.

GlyR glycine receptor.

HH Hodgkin-Huxley.

HSR high spontaneous rate.

IC inferior colliculus.

IFR instantaneous firing rate.

IHC inner hair cell.

IPSC inhibitory post-synaptic current.

IPSP inhibitory post-synaptic potential.

KLT low-threshold potassium channel.

LSR low spontaneous rate.

MAR mean absolute relative.

MNTB medial nucleus of the trapezoidal body.

MOC medial olivocochlear.

MTF modulation transfer function.

NMDA N-Methyl-D-aspartic acid.

On_C onset chopper.

On_L onset with latent response.

PL primary-like.

PLn primary-like with notch.

PSP post-synaptic potential.

PSTH peri-stimulus time histogram.

PVCN posteroverentral cochlear nucleus.

RM Rothman and Manis.

RMP resting membrane potential.

RMS root mean squared.

SI synchronisation index.

SNR signal-to-noise ratio.

SPL sound pressure level.

SR spontaneous rate.

ST spike timing.

TS T stellate.

TV Tuberculoventral.

VCN ventral cochlear nucleus.

This page intentionally left blank.

Chapter 1

Introduction and Literature Review

1.1 Introduction

The development of biophysically-realistic neural network (BNN) models is a major objective of computational neuroscience. Recent advances in the field have made this goal more achievable than it has ever been before. The auditory system is characterised by the high fidelity of acoustic information it processes. Consequently, modelling of neural processing in the auditory system should be conducted on a fine-grained scale to enhance the representation of the stimulus spectrum and temporal periodicities. Given this complexity, BNNs are a promising avenue by which we can expand our understanding of neural processing of sound.

In the cochlear nucleus (CN), the first processing stage in the auditory brainstem, histological and pharmacological labelling techniques have produced a flood of information about the anatomy, physiology, immunohistochemistry, pharmacology and intrinsic membrane properties of the different cell types. There is scope for more extensive exploitation of this experimental data in the design and optimisation of computational models. Success in this endeavour will enable us to improve the accuracy and value of BNNs for use in the investigation of brain networks.

This thesis presents a novel BNN model of the CN stellate cell microcircuit (hereafter, the CNSM model). This microcircuit provides a robust spectral representation of sound and plays an essential part in speech communication. The model was optimised using rigorous sequential methods and simultaneous genetic algorithms. The analyses of the results demonstrate the utility of this approach for using BNN models to help us better understand complex neural processing.

This chapter critically reviews the major bodies of literature relevant to the design and optimisation of the CNSM model, and provides an overview of the thesis. The next section introduces the auditory system, the CN, existing computational models of the CN and optimisation methods in neural modelling. This evidence is drawn upon in the development, analysis and verification of the CNSM model in the remainder of the thesis.

1.2 Literature Review

1.2.1 Auditory System

Speech is a unique and fundamental tool for communication between humans. We continually deal with various distortions of the acoustic environment, such as background noise and reverberation, as we extract information from signals entering the ear. Vowels are a salient feature of speech and are spectrally and temporally distinct from other natural sounds. The spectrum of each vowel is distinguished by the location of high-energy spectral peaks, known as formants. Robust representation of spectra at different intensities is important for speech and other auditory communication (for review see Bregman 1990). The main tasks of the auditory system are to (1) separate out individual frequency components of sound, (2) enhance spectral and temporal contrasts to improve meaningful signal-to-noise ratio (SNR), and (3) extract behavioural frequency cues (Evans 1992).

Advanced auditory fidelity and localisation are exceptional features of hearing perception in animals. These specialities work to a high degree despite the input at the round window of the cochlea being one-dimensional. Rough frequency decomposition is performed by the basilar membrane and organ of Corti in the mammalian cochlea, which transforms mechanical signals to neural signals in the auditory nerve (AN). The next stage of the auditory process occurs in the CN, the first processing stage of the central auditory pathway in which all auditory nerve fibres (ANFs) end. Enhancing spectral and temporal contrasts requires sophisticated parallel processing strategies involving networks of neurons with feed-forward and feedback connections.

The auditory system is topographically ordered from the basilar membrane to

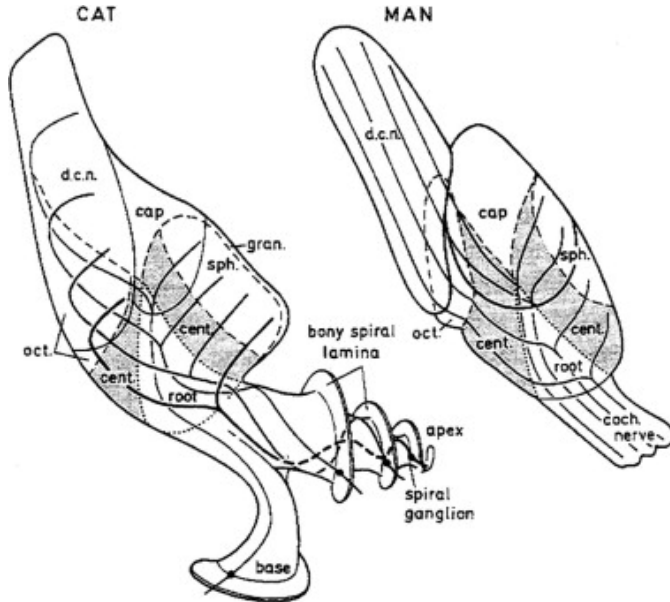


Figure 1.1: Cochlear nucleus innervation by ANFs follows the same tonotopic organisation in cats and humans (Ryugo 1992; Ryugo and Parks 2003; Spoendlin 1973). Image reprinted from Moore and Osen (1979).

the cortex in terms of frequency selectivity, also known as tonotopicity (for a review of cochlear nucleus synapto-physiology and topology see Young and Oertel 2004). The population of ANFs (Figure 1.1) bifurcate after entering the CN to innervate the ventral cochlear nucleus (VCN) and dorsal cochlear nucleus (DCN), retaining their tonotopic order (Liberman 1982, 1993; Lorente de Nó 1981). The different cell types of the CN, each with unique cell properties and synapto-physiology, produce six major outputs from the CN (Cant and Benson 2003). Binaural pathways converge in the inferior colliculus (IC) before projecting to the medial geniculate nucleus in the thalamus and then to the auditory cortex.

1.2.2 Auditory Nerve Fibres

ANFs are narrowly tuned to their characteristic frequency (CF), the frequency at the minimal point of its acoustic threshold curve. Acoustic threshold is defined as the sound pressure level (SPL) where the neuron's firing rate is significantly above its spontaneous rate (SR). The average bandwidth of ANFs is $Q_{10} = 6.3$ octaves (Jiang et al. 1996), where Q_{10} is the width of the tuning curve at 10 dB above acoustic

threshold at CF divided by the CF. The acoustic physiology of ANFs form a bi-modal distribution where 30–40% of the fibres have SR less than 2 spikes/s and 60–70% have SR above 30 spikes/s (Ryugo and Parks 2003). Type 1 ANFs are categorised into high spontaneous rate (HSR) and low spontaneous rate (LSR) fibres (Liberman 1978). LSR fibres have relatively higher thresholds, whereas HSR fibres have thresholds close to 0 dB SPL. Fibres of similar CF can vary in SR from near 0 to 100 spikes/s. The bi-modal SR distribution is present across the entire audible frequency range for the animal, and implies a general organisational principle for the mammalian AN (Arnesen and Osen 1978; Liberman 1991, 1993). ANFs of the different SR groupings exhibit distinct physiological features, especially in terms of their contribution to the dynamic range of hearing and representation of speech sounds (Ryugo and Parks 2003). The collective evidence suggests that different SR groupings of ANFs play distinct roles in acoustic information processing. It might be that the HSR fibres with their low thresholds function in quiet settings, whereas LSR fibres with their high thresholds operate better in loud and noisy environments.

The morphology of LSR and HSR ANFs is essentially similar. Characterised as bipolar neurons, their cell bodies lie in the retinal ganglion region (Rosenthal's canal) of the cochlea and their peripheral process contacts one inner hair cell (IHC). The myelinated AN axonal processes form the vestibulocochlear nerve (the eighth cranial nerve) and enter the brainstem at the CN root. The AN fibres bifurcate into the ascending and descending branches. The ascending branch has a relatively straight trajectory into the anteroventral cochlear nucleus (AVCN) (many small collaterals with terminal boutons contacting cell bodies and dendrites) and terminate as a large, axosomatic ending called the endbulb of Held. The descending branch passes through the posteroventral cochlear nucleus (PVCN) and octopus cell region before entering the DCN. Fibres of similar CFs disperse to form a three-dimensional sheet running through the nucleus, and stacks of these sheets represent the isofrequency contours of the nucleus (Figure 1.2). These projections underlie the tonotopic organisation of the resident neurons of the CN (Ryugo and Parks 2003). LSR fibres also project to the granule cell domain (GCD) (Ryugo and Parks 2003; Ryugo et al. 2003) along with the smaller, unmyelinated type 2 ANFs, which suggests that they play a different role in sound pro-

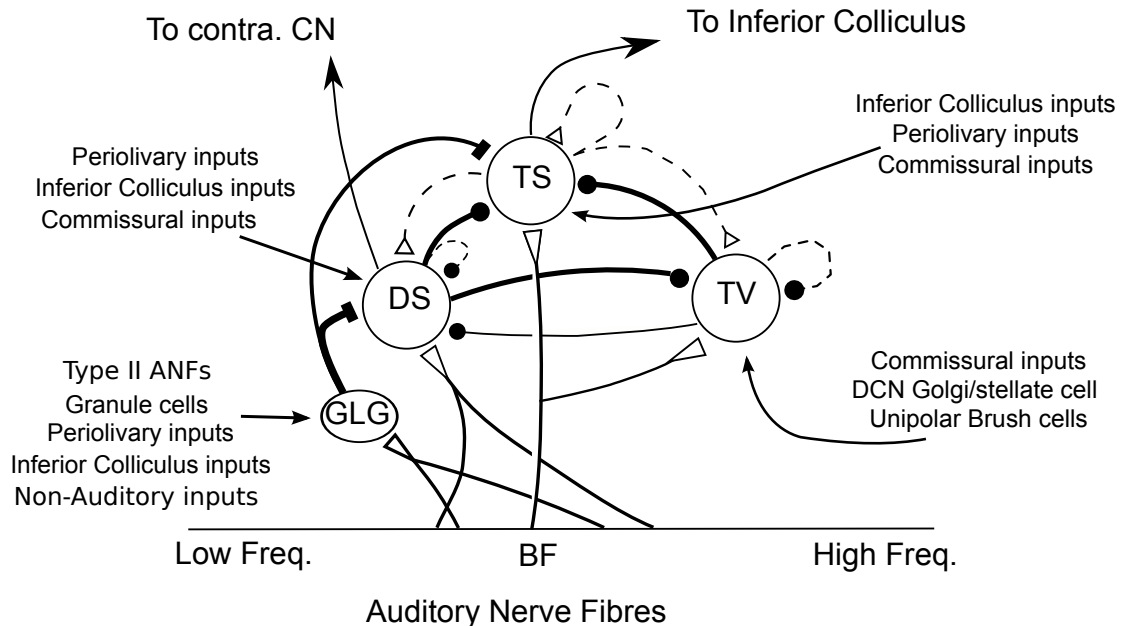


Figure 1.2: Schematic of the cochlear nucleus stellate network showing connections between T stellate (TS), D stellate (DS), Tuberculoventral (TV) and Golgi (GLG) cells. Triangles indicate glutamatergic excitation from ANFs, solid circles indicate glycinergic inhibition, and solid rectangles indicate GABAergic inhibition. Dotted lines are likely connections; solid lines are experimentally confirmed connections. TS cells excite DS and TV cells (and possibly recurrently excite other TS cells) as well as projecting to nuclei in the superior olive and the IC. DS cells are wide-band inhibitory cells that inhibit TS and TV cells. TV cells are narrow-band inhibitory cells from the DCN that inhibit TS and DS cells. GLG cells are GABAergic inhibitory cells that are thought to strongly inhibit DS cells and moderately inhibit TS cells.

cessing to HSR fibres.

1.2.3 Cochlear Nucleus

There is a rich tradition of experimental investigation of the CN, dating back more than eighty years (Lorente de Nò 1933). The synaptic organisation of cells in the CN has been examined in detail in various species including cats (Cant 1981; Saint Marie et al. 1989; Tolbert and Morest 1982a); mice (Wickesberg and Oertel 1988, 1990; Wickesberg et al. 1991); guinea pigs (Juiz et al. 1996; Ostapoff et al. 1997); and rats (Friedland et al. 2003; Rubio and Juiz 2004). Physiological studies combined with labelling have given greater certainty to correlations between physiological response types and morphological cell types (Arnott et al. 2004; Ostapoff et al. 1994; Palmer et al. 2003; Smith and Rhode

1989). Intracellular recordings have ascertained the electrical properties and different synaptic inputs of TS, D stellate (DS) and Tuberculoventral (TV) cells (Ferragamo et al. 1998b; Zhang and Oertel 1993). Descriptions of current dynamics for synaptic receptors (Gardner et al. 1999; Harty and Manis 1998) and membrane channels (Rothman and Manis 2003a,b) specific to the VCN have enabled accurate mathematical models to be developed at the cell and synaptic level.

The CN receives the primary ascending input from ANFs and contains a heterogeneous population of cell types. Cell types have been classified using criteria including morphology, immunohistochemistry, synaptic organisation, response to acoustic stimuli and frequency tuning (Cant and Benson 2003; Ryugo and Parks 2003; Young and Oertel 2004). The two major divisions are the VCN and DCN. The different projections out of the nucleus reflect the highly specialised parallel processing that is performed to extract particular acoustic information contained in the AN. The DCN in mammals generally has a cerebellar-like laminar structure with many interneurons, whereas the VCN consists of a magnocellular core and a marginal shell (otherwise called the GCD in rodents). The marginal shell is thought to be involved in regulating the gain in the magnocellular core from inputs outside the CN (Evans and Zhao 1993a; Ghoshal and Kim 1997).

Recent reviews of characterised cells in the CN have examined the association between the projection characteristics and the corresponding physiological acoustic characteristics (Cant and Benson 2003; Oertel et al. 2011; Ryugo and Parks 2003; Smith et al. 2005; Young and Oertel 2004). Doucet and Ryugo (2006) showed that a limited number of VCN multipolar neuron studies have performed physiological unit assessments as well as classification of morphology via labelling. The peri-stimulus time histogram (PSTH) response to short tone bursts has been used to classify CN neurons into primary-like, chopper, or onset chopper (Blackburn and Sachs 1989; Bourk 1976; Pfeiffer 1963; Shofner and Young 1985; Smith et al. 1993; Young et al. 1988).

The afferent and intrinsic synaptic connectivity in the CN have also been the subject of sustained attention in the literature (Oertel et al. 2011; Young and Oertel 2004). The network in Figure 1.2 shows the connections within the CN that are involved in modulating TS cells' activity. The TS cells and their synaptic interactions are the focus of the

CNSM model and are discussed in detail in the next section.

1.2.4 T Stellate Cells

This section provides an overview of TS cells, including their cell morphology, immuno-histochemistry, intrinsic membrane properties, synaptic contacts and physiological properties. The respective contribution of these elements to the heterogeneous acoustic behaviour of different TS cell subtypes is yet to be thoroughly determined.

TS cells are located in the core region of the VCN, primarily in the PVCN with some in the posterior part of the AVCN (Brawer et al. 1974; Doucet and Ryugo 1997, 2006; Lorente de N o 1981; Oertel et al. 1990; Osen 1969). TS cells encode complex features of the stimulus that are important for the recognition of natural sounds and are a major source of excitatory input to the IC (Oertel et al. 2011). TS cells of the VCN encode a robust representation of the stimulus spectra in their average rate and a temporal representation essential for speech (Keilson et al. 1997). They project directly to the IC, and are therefore important in conveying information to higher auditory centres. TS cells are known to form a local microcircuit network with neurons within their isofrequency lamina and across the frequency range of the nucleus. The microcircuit includes DS cells (a wide-band inhibitory cell in the VCN), TV cells (a narrow-band inhibitory cell in the DCN) and Golgi cells (a GABAergic neuron in the GCD, an outer shell of the CN) (Ferragamo et al. 1998b; Zhang and Oertel 1993). Inhibition is known to play a key role in shaping the average rate response, synchronisation to modulation and onset delay of cells in the CN (Backoff et al. 1999; Caspary et al. 1994; Evans and Zhao 1998; Paolini et al. 2004).

Intracellular current-clamp recordings of TS cells have categorised them as type 1 (Ferragamo et al. 1998b; Oertel 1983; Oertel et al. 1988). This integrative intrinsic cell membrane behaviour allows phasic input from ANFs to be converted to a tonic or chopping output. The tonic behaviour enables encoding of spectrum across populations since encoding the peaks and valleys is relatively independent of time after onset of sound. It also suits encoding of envelopes of sounds, which is important for speech (Oertel et al. 2011). The presence of active membrane channels at rest means that TS cells are sensitive to neuromodulatory currents (Ferragamo et al. 1998b; Fujino and

Oertel 2001; Rothman and Manis 2003a) and increases their response time to temporally important features like vowel transitions and glottal pulses (Clarey et al. 2004; Paolini et al. 2004). The average discharge rate of the two chopper populations provides either a low-contrast representation independent of level (sustained chopper (ChS)) or a high-contrast representation of stimulus spectrum (transient chopper (ChT)) (Blackburn and Sachs 1990; May 2003). The temporal coding of cells in the CN has also been studied extensively with amplitude modulation (AM) tones (Frisina et al. 1990a,b; Rhode and Greenberg 1994a) and ripple noise (Winter et al. 1993). Keilson et al. (1997) went further, showing that chopper cells provide a periodicity-tagged spectral representation that can be used to separate simultaneously presented vowels.

1.2.4.1 Morphology of T Stellate Cells

The practice of classifying and naming distinct cell types in the CN began in the first half of the twentieth century (Lorente de Nó 1933). Star-like cell bodies observed with Golgi impregnation were called *stellate* cells (Osen 1969). Nissl staining showed the multiple dendritic morphology of TS and DS cells, hence the name *multipolar* was adopted (Brawer et al. 1974; Lorente de Nó 1981). Multipolar cells were also divided into two groups, disperse or clumped Nissl, according to their cytoplasmic appearance in thionin-stained sections (Liberman 1991, 1993). Further nomenclature based on dendritic differences involving distinguishing between planar (TS cells) and radial (DS cells) has also been suggested in rats (Doucet and Ryugo 1997, 2006).

Distinctions based on somatic innervation in multipolar neurons separated them into two types: type I (few somatic) and type II (many somatic and dendritic) (Cant 1981). DS cells' axons project dorsally toward the DCN via the dorsal acoustic stria (hence D in D stellate), while TS cells leave the CN ventrally through the ventral acoustic stria or trapezoid body (hence T) (Oertel et al. 1990). Some DS cells are also commissural, exiting the CN via the dorsal acoustic stria and crossing the midline to terminate in the contralateral CN (Needham and Paolini 2007; Oertel et al. 1990; Smith et al. 2005).

For consistency, the TS cell modelled in this thesis represents each of the various names given to neurons with similar characteristics (TS, type I multipolar, planar, and chopper PSTH units) in different animals, with closest association with rodents and

cats. The DS cell type includes all those previously named as DS, type II multipolar, radial, and units classified as onset chopper (On_C) PSTH units.

1.2.4.2 Intrinsic Mechanisms of T Stellate Cells

The intrinsic cell-based properties of VCN neurons have typically been investigated using *in vitro* current clamp experiments (Manis and Marx 1991; Oertel 1983; Oertel et al. 1988; Wu and Oertel 1984). TS cells are classified as type I due to the regularly spaced firing of action potentials (APs) to steady depolarising current, and can be classified as simple integrators. They have a linear current-voltage response (Feng et al. 1994; Manis and Marx 1991; Oertel 1983; Oertel et al. 1988; Rhode et al. 1983a; Smith and Rhode 1989). The response to strong negative current in TS and DS cells is double-exponential, which shows the presence of hyperpolarisation-activated mixed cation current I_h (Ferragamo et al. 1998b; Fujino and Oertel 2001; Rothman and Manis 2003a,b). I_h is higher in TS and activated more at lower potentials than in bushy and octopus cells, so that it is less active at rest and produces a higher membrane resistance. This high resistance induces greater voltage changes in small modulating current, which enhances I_h , making TS more sensitive to neuromodulatory currents (Fujino and Oertel 2001; Rodrigues and Oertel 2006).

The TS cell AP has a single exponential undershoot that shows the absence of I_{KLT} , which is strongly present in bushy cells, and to a moderate degree in DS cells (Feng et al. 1994; Manis and Marx 1991; Rothman and Manis 2003a; Wu and Oertel 1984). Low threshold potassium current (I_{KLT}) in bushy cells is responsible for their phasic response (i.e. PSTH classified primary-like units) and its moderate effect in DS cells is to enhance coincidence detection at stimulus onset (Manis and Marx 1991; Rothman and Manis 2003c).

In recent experiments with mice, a fast, transient-deactivating potassium current (I_{KA}) has been found only in TS cells (Rothman and Manis 2003a,b,c). I_h and I_{KA} are active at rest and play a role in modulating the rate of repetitive firing of TS cells (Rothman and Manis 2003c). The effect of inhibition on TS cells could be to reset I_{KA} (Rothman and Manis 2003c), thus priming cells for oncoming activation (Kanold and Manis 2001, 2005). Fast onset inhibition has been shown to enhance place-coding across

TS cells by enhancing the first-responder activation (Paolini et al. 2004).

1.2.4.3 Acoustic Responses of T Stellate Cells

TS cells receive a narrow frequency band of ANF inputs and have a chopping response to CF tone bursts (Blackburn and Sachs 1989; Smith and Rhode 1989). Few synaptic terminals contact on their soma; the majority of inputs contact the proximal dendrites (Cant 1981). TS cells are the primary excitatory output to the IC (Oertel et al. 1990; Smith and Rhode 1989). The response to acoustic stimulation is measured from a PSTH to short tone bursts (Blackburn and Sachs 1989; Pfeiffer 1966a). The level of tuning and suppression of neurons receptive field is examined using the excitatory-inhibitory response area (EIRA) method (Arle and Kim 1991b; Evans and Nelson 1973; Spirou and Young 1991; Spirou et al. 1999; Young et al. 1992, 1993). ANFs have a Type I EIRA with narrow tuning and no inhibitory areas. TV cells are narrowly tuned but have strong wide-band inhibition, creating a Type II EIRA (Spirou et al. 1999). TS cells are not as strongly inhibited and fall into the Type III EIRA category, with lateral inhibitory regions at the sides of their response areas.

The regular-firing chopping pattern shown in Figure 1.3 is characteristic of TS cells (Blackburn and Sachs 1989). ChS and ChT subtypes are differentiated by the regularity of discharge throughout the stimulus using the coefficient of variation (CV) statistic (Young et al. 1988). These classification techniques expanded the level of physiological understanding in the complex neural processes in the CN and their relationships with intracellular behaviour (Blackburn and Sachs 1989; Ostapoff et al. 1994; Smith and Rhode 1989). Recurrent excitation among TS cells of similar CFs was first suggested by Ferragamo et al. (1998b). The small numbers of axonal collaterals in the VCN are confined to the same frequency band as their dendrites, indicating possible recurrent connections between cells encoding a similar frequency (Ferragamo et al. 1998b; Palmer et al. 2003). This feature may compensate for rapid transient adaptation in AN excitation, allowing a robust representation of the spectral energy in the cell's response area to be transmitted to higher centres.

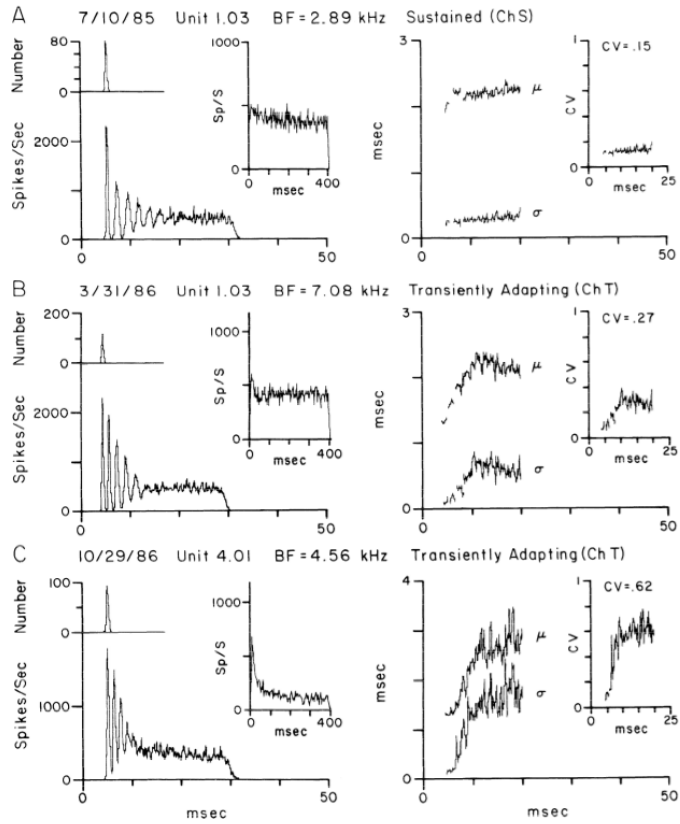


Figure 1.3: TS cell characteristic PSTH, ISI and CV responses to a short 25 msec CF tone. PSTH (left) with first spike (inset axis above PSTH) and long tone PSTH (inset showing 400 msec tone response). Mean and standard deviation of ISI (right) with CV (inset). Sound level was 30 dB above threshold for each unit. Figure reproduced from Blackburn and Sachs (1989).

1.2.4.4 Synaptic Inputs to T Stellate Cells

The driving excitatory inputs of TS cells come from afferent ANFs. ANFs provide glutamatergic excitation using AMPA receptors (Alibardi 1998; Cant 1981; Ferragamo et al. 1998b). AMPA excitatory post-synaptic currents (EPSCs) have a time constant of 0.36 msec in TS and DS cells, with a slight deviation in TV neurons (0.4 msec) (Gardner 2000; Gardner et al. 1999). ANF synapses are commonly located on TS cells' proximal dendrites and are rarely on the soma, which distinguishes them from DS cells (cat (Smith and Rhode 1989); mice (Cao and Oertel 2010; Ferragamo et al. 1998b); chinchilla (Josephson and Morest 1998)). Variability in the number and location of ANF inputs to TS cells and the type of ANFs (HSR or LSR) results in a heterogeneous classification of TS cells based on their chopper-like physiological responses (Paolini et al. 2005; Smith

and Rhode 1989; Young et al. 1988).

Fast, glycinergic synapses arrive on TS cells from DS and TV cells (Ferragamo et al. 1998b; Smith and Rhode 1989; Wickesberg and Oertel 1990; Zhang and Oertel 1993). The glycine receptor (GlyR) in VCN and other auditory brainstem units has a faster rise time (0.4 msec) and decay time (2.5 msec) compared with other glycinergic synapses in the brain, which is critical for fast encoding of sounds (Awatramani et al. 2005; Harty and Manis 1998; Leao et al. 2004; Lim et al. 2003). The function of DS cell inputs has been suggested to include: wide-band lateral suppression (especially in noise) (Recio and Rhode 2000b; Rhode and Greenberg 1994b); enhancement of modulated inputs by providing phase-locked inhibition (Rhode 1994; Rhode and Greenberg 1994a); enhancement of the volley by suppressing the first spike in lateral side-bands of a spectrum (Joris and Smith 2008; Needham and Paolini 2003); and enhancement of voice onset encoding (Clarey et al. 2004). The function of TV cells in the CN stellate microcircuit has been hypothesised to include: narrow-band inhibition around low level tones and band-pass noise (Spirou et al. 1999); delayed echo-suppression (Burck and van Hemmen 2007; Parham et al. 1998; Wickesberg and Oertel 1990); and spectrum modification around notch noise gaps (Reiss and Young 2005). In mice, TS cells have been found to excite TV cells in several intracellular studies (Wickesberg and Oertel 1990; Zhang and Oertel 1993) but TS cell terminals are absent on TV cells in rats (Rubio and Juiz 2004). If this connection is present, it creates a complicated recurrent loop in the CN stellate microcircuit and would contribute to non-linear activity in the main output of the network, TS cells.

GABAergic inputs to TS cells have been verified by optical microscopy immunohistochemistry (Awatramani et al. 2005; Babalian et al. 2003; Smith and Rhode 1989) and electrophysiological studies through the use of iontopopheretic application of the GABAergic subtype A (GABA_A) antagonist, bicuculline (Backoff et al. 1999; Caspary et al. 1994; Evans and Zhao 1998; Ferragamo et al. 1998b). The source of GABAergic inputs to cells in the mammalian CN is somewhat contentious. Studies show that GABAergic inputs to the CN generally arise in the peri-olivary regions of the medulla in cats (Ostapoff et al. 1997). Slice preparations of the isolated murine VCN show strong and immediate sensitivity to bicuculline in TS and DS cells from a source within the CN

complex (Ferragamo et al. 1998b). The only known source of gamma-aminobutyric acid (GABA) intrinsic to the VCN is the Golgi (GLG) cells of the GCD overlying the VCN (Ferragamo et al. 1998a; Mugnaini 1985). Only one electrophysiological study of the GCD (or marginal shell of the VCN in cats) has been done and found monotonic responses in units assumed to be GLG cells (Ghoshal and Kim 1997). The assumed functional role of GLG cells is to regulate granule cells but they may also regulate the level of excitability in DS and TS cells (Ferragamo et al. 1998b; Ghoshal and Kim 1997).

Sources of polysynaptic excitation, observed with late excitatory post-synaptic potentials (EPSPs) in TS cells, indicate that TS cells receive excitatory input from excitatory interneurons within the VCN (Ferragamo et al. 1998b). When separated from their natural synaptic inputs, isolated axons cannot contribute to polysynaptic responses. Monosynaptic responses have latencies between 0.5 (synaptic delay) and 3 msec (2.5 msec conduction delay for an unmyelinated fibre of 0.5 mm plus 0.5 msec synaptic delay). Therefore EPSPs with latencies of 3 msec are polysynaptic and must be generated by excitatory interneurons (Ferragamo et al. 1998b). The ultrastructure of TS cell terminals and functional studies of the inputs to the inferior colliculi is consistent with TS cells being excitatory and the source of poly-synaptic excitation in the VCN (Cant and Benson 2003, 2006; Smith and Rhode 1989).

1.2.5 Function of the Stellate Microcircuit

Glycinergic and GABAergic inhibition are thought to play different spectro-temporal processing roles in the CN. Glycinergic inputs from DS and TV cells are predominantly active at the onset of stimuli; accordingly, they provide enhanced temporal acuity and dynamic range at onset. Post-onset and tonic inhibition is provided by GABA inputs. GABAergic inhibition acting on slow and fast receptors (GABA_A and subtype B (GABA_B) respectively) is likely to mediate the strong post-onset inhibition in DS cells (Evans and Zhao 1998; Ferragamo et al. 1998a). TS cells are weakly inhibited by GABA (Ferragamo et al. 1998a), reflecting the smaller number of GABAergic synapses on their dendrites (Friedland et al. 2003; Smith and Rhode 1989). GABAergic inhibition in the VCN derives from a number of possible sources, intrinsically from Golgi cells in the granule cell layer of the VCN or extrinsically from olivocochlear efferents (Ostapoff

et al. 1997).

Axo-somatic inhibition from flat and pleomorphic terminals has been observed adjoining prominently on DS cells and could possibly explain the On_C response to tones and noise. Evidence of axo-dendritic inhibition on TS cells (Cant 1981; Smith and Rhode 1989) led Winslow and Sachs and colleagues to suggest that TS cells overcome saturation of high spontaneous rate AN fibres by proximal inhibitory inputs that shunt excitation from more distal inputs (Winslow et al. 1987). This mechanism was explored using steady-state continuous inputs (Lai et al. 1994a; Wang and Sachs 1994) and there is strong potential to explore this using more realistic inhibitory circuits.

GABAergic inhibition regulates the level of activity in the VCN (Palombi and Caspary 1992). The application of bicuculine abolishes the onset response of On_C and onset with latent response (On_L) units (Evans and Zhao 1998; Palombi and Caspary 1992). Bicuculine, a GABA_A antagonist, raises the threshold and significantly increases the On_C receptive field to high and low frequencies, to up to 10 times the receptive field width of ANFs (Evans and Zhao 1998). Facilitation of response by spectral inputs outside the conventional receptive field (Jiang et al. 1996; Winter and Palmer 1995) indicates the presence of tonic inhibition in On_C units. Inhibition acting post-onset is likely to be a dominant factor in the cells' onset response properties rather than membrane-based mechanisms (Evans and Zhao 1998). On_C units showed little difference in response to cosine or random phase harmonics, which improves temporal encoding in reverberant environments (Evans and Zhao 1998). The post-onset inhibition can last for up to 400 msec, as observed by hyperpolarisation of the soma potential (Paolini et al. 2004) and a reduction in spontaneous firing rate (Rhode and Greenberg 1994b). Mahendrasingam et al. (2004) demonstrated the co-localisation of glycine and GABA transporters by immunofluorescence labelling of endings contacting spherical bushy cells. The functional significance of co-localisation of these two inhibitory neurotransmitters is uncertain, but it is possible that glycinergic transmission may be modulated by the activation of pre- and post-synaptic GABA_A receptors (Lim et al. 2000).

Mixed glycine and GABA terminals, with pleomorphic vesicles, have been observed in the VCN (Altschuler et al. 1993), but these are most likely from GABA and glutamic acid decarboxylase (GAD) immunoreactive periolivary neurons whose axons termi-

nate in the VCN (cats (Adams 1983; Spangler et al. 1987); guinea pig (Helfert et al. 1989; Ostapoff et al. 1990; Qiu et al. 1995; Schofield 1991); rat (Campos et al. 2001)). Periolivary neurons receive afferent inputs from monotonic units in the VCN (Schofield 1995, 2002) and are thought to play a role in sound duration (Dehmel et al. 2002; Kadner et al. 2006; Kulesza et al. 2007).

1.2.5.1 Synchronisation to Amplitude Modulated Tones

The temporal modulation transfer function (MTF) measures the precision of phase-locking to envelope modulations of a CF tone by different modulation frequencies (f_m). Frisina and colleagues first showed that phase-locking to AM in the CN is enhanced relative to the AN (Frisina 1983; Frisina et al. 1990a). A number of studies have shown that the fundamental frequency is represented as an interval code in most CN units (Cariani and Delgutte 1996; Rhode 1995, 1998). Modulated signals have been used extensively to analyse temporal coding in the CN (Frisina et al. 1990a,b; Kim et al. 1990; Møller 1976; Rhode 1994; Rhode and Greenberg 1994a). Some response types in the CN preserve envelope information over a wide range of stimulus levels, even above 100 dB SPL, where ANFs have reduced synchronisation (Frisina et al. 1990a, 1994; Rhode 1994).

Studies of modulation in the AVCN show a hierarchy of temporal enhancement: On_C → ChS/ ChT → primary-like (PL)/ primary-like with notch (PLn) (Recio and Rhode 2000a; Rhode 1998; Wang and Sachs 1994). This enhancement is relative; since choppers only phase-lock to modulations below 500Hz, PL and PLn units perform better at higher modulation frequencies (Rhode and Greenberg 1994a).

The dynamic range of chopper neurons to AM tones (up to 90 dB) (Frisina et al. 1990b) is significantly greater than individual ANFs (30–40 dB) (Frisina et al. 1985). The change in AM dynamic range may be due to a number of mechanisms in the stellate microcircuit. Selective processing of HSR and LSR fibres (Lai et al. 1994a; Winslow et al. 1987) is one proposed mechanism; however, this is unlikely due to the degradation of temporal information in ANFs at high SPL (Joris et al. 2004). Inhibition from DS cells is a more likely mechanism. DS cells integrate ANFs over a wide frequency range (Golding et al. 1999; Oertel et al. 2000; Palmer et al. 1996), enhance temporal information

(Rhode and Greenberg 1994a), and have a large dynamic range to tones (Rhode and Greenberg 1994b). GABAergic GLG cells have a large dynamic range to tones and noise (Ghoshal and Kim 1996a), and are proposed as a regulator of gain in the activity of TS cells (Ferragamo et al. 1998a). These mechanisms have not been fully explored in the literature and will be discussed further in Chapter 4.

Chopper units generally have band-pass tMTF at high SPL, with the f_m inducing the highest synchronisation called the best modulation frequency (BMF) (Frisina et al. 1990a). Chopper units are important in the transition of a temporal-place code in the AN to a rate-based coding of BMF in the IC (Joris et al. 2004). Rhode and colleagues confirmed the presence of band-pass tMTFs as well as some band-pass rate-based MTFs in chopper units in the cat (Rhode 1994; Rhode and Greenberg 1994a). The BMFs of chopper units lie between 50 and 500Hz (Frisina et al. 1990a; Rhode and Greenberg 1994a), which is critical in speech modulation and segregation of sounds (Bregman 1990). On_C units are well suited to encode a wide range of f_m with strong synchronisation due their precise onset (Joris and Smith 1998; Kim et al. 1986; Rhode 1998; Rhode and Greenberg 1994a).

1.2.5.2 Vowel Representation in TS cells

The representation of vowels in the auditory periphery has been studied using recordings from a large population of ANFs (Delgutte and Kiang 1984a,b,c,d; Sachs and Young 1979; Young and Sachs 1979) and CN cells (Blackburn and Sachs 1990; Keilson et al. 1997; Recio and Rhode 2000a). Reviews of vowel encoding in the VCN (May 2003; Palmer and Shamma 2003) highlight the spectral enhancement of formant peaks and suppression of formant troughs by chopper units. Figure 1.4 shows the estimated rate-place representation of ANF and VCN units. HSR ANFs and primary-like VCN units show saturation of trough frequencies at moderate sound levels. LSR units in the AN and primary-like VCN units are able to encode spectrum at high SPL. The rate-place representation in chopper units (ChS and ChT) shows considerable robustness, maintaining spectral peak information across a wide range of intensity levels (right panels in Figure 1.4). Suppression of spectral troughs in the rate-place representation of ChT and ChS units is greater than the suppression in LSR ANFs at high SPL. Spectral enhance-

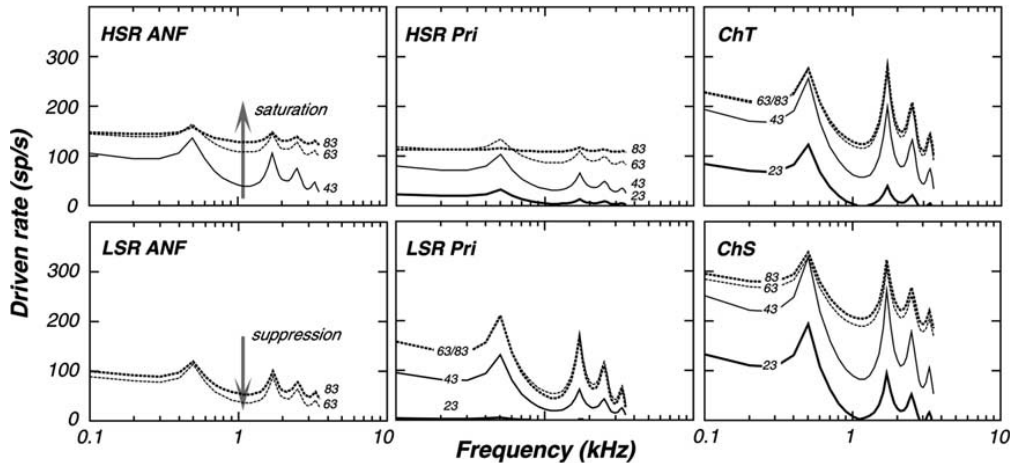


Figure 1.4: Rate-place representation in AN and CN neurons. May and colleagues used a spectral manipulation procedure to change the location of the first and second formant and the first trough frequencies to coincide with the CF of a recorded cell. HSR high spontaneous rate, LSR low spontaneous rate, ANF auditory nerve fibre, PL primary-like VCN unit. Figure reproduced from May 2003.

ment in TS cells cannot be attributed to lateral suppression in the AN alone; it requires some form of lateral inhibitory mechanism that can perform spectral enhancement by suppression of noise between peaks (Shamma 1985).

Lateral inhibition of varying strengths is found in the responses of most cell types in all divisions of the CN (Evans and Nelson 1973; Rhode and Greenberg 1994b; Young 1984). ChT TS cells exhibit strong side-band inhibition and respond to vowels with a clear and stable representation of acoustic spectrum in their average firing rate at all stimulus levels (Blackburn and Sachs 1990; May et al. 1998; Recio and Rhode 2000a). Selective listening to LSR and HSR ANFs could be one possible mechanism for TS cell sensitivity over a wide sound level range to vowels (Winslow et al. 1987). TS cells are candidates for a range of spectro-temporal operations including lateral inhibition (Smith and Rhode 1989), automatic gain control (Ferragamo et al. 1998a,b) and echo-suppression (Fitzpatrick et al. 1999; Parham et al. 1998; Wickesberg and Oertel 1990). Recurrent excitation by TS cells within the same frequency band could also introduce non-linear effects (Ferragamo et al. 1998b).

Taken together, the experimental evidence demonstrates that there is much that remains unknown about the functioning of neural processing in the CN stellate cell microcircuit.

1.2.6 Computational Models of the Cochlear Nucleus

Advances in understanding membrane kinetics and synaptic organisation in the CN have increased the feasibility of investigations of synaptic influences (cf Meddis and Hewitt 1993). Combined with massively increased computational power available to researchers, highly detailed models can provide great insight into the function of regulatory mechanisms within and outside the CN. This knowledge can also drive methods for constraining such detailed models based on the known physiological responses in other neural networks of the brain.

1.2.6.1 Modelling of the Auditory Periphery

Accurate computational models of CN neurons require adequate representation of their inputs, ANFs. Models of the auditory periphery over the last 30 years have expanded our understanding of the mechanical processes in the middle ear and cochlea, and the specialised synapse between the IHC and the AN (Carney 1993; Davis and Voigt 1991; Meddis et al. 1990). Modelling in the auditory periphery has benefited extensively from the work of Liberman, Greenwood, Patterson, Young, Sachs and others, in acoustic *in vivo* experiments.

A review by Lopez-Poveda (2005) shows the two model groups with the strongest correlation between known phenomenological behaviour and model outputs are the DSAM model (Meddis (2006); Meddis et al. (1990); Sumner et al. (2002))¹ and the Carney model (Carney (1993); Heinz et al. (2001); Jackson and Carney (2005); Tan and Carney (2001, 2003); Zhang et al. (2001); Zilany and Bruce (2006); Zilany and Carney (2010); Zilany et al. (2009))². These models both show good representation of rate behaviour in LSR and HSR models, as well as temporal phenomena in ANFs. This thesis uses the Carney model for all AN simulations.

¹DSAM <http://www.essex.ac.uk/psychology/department/HearingLab/modelling.html>

²Carney model <http://www.urmc.rochester.edu/labs/Carney-Lab/publications/auditory-models.cfm>

1.2.6.2 Single neuron models of the chopper unit

A number of neural models of CN neurons have been developed. The basic approaches include point neuron models (Arle and Kim 1991a; Hewitt et al. 1992) and conductance based, Hodgkin-Huxley (HH)-like compartmental models (Original: Hodgkin and Huxley (1952a), HH models of CN neurons: Banks and Sachs (1991); Lai et al. (1994a); Wang and Sachs (1995); White et al. (1994)). Point neuron models based on MacGregor (1993) were able to replicate intrinsic chopping behaviour (Arle and Kim 1991a; Hewitt et al. 1992) and synchronisation to stimulus envelope (Ghoshal et al. 1992) with simple mathematical models. *In vitro* recordings in the VCN of potassium and sodium currents found unique specialisations that enabled faster acoustic processing (Manis and Marx 1991; White et al. 1990). Banks and Sachs (1991) used modified HH equations (Hodgkin and Huxley 1952a) to develop a fast sodium (I_{Na}) current and a high-threshold (I_{KHT}) potassium current. Further modifications of the Banks and Sachs (1991) conductance model improved the adaptive chopping behaviour due to inhibition (Lai et al. 1994a; Wang and Sachs 1995) and the model's synchronisation to envelope (Wang and Sachs 1995).

Rothman and Manis (2003c) developed a single compartment model with accurate membrane conductances was developed based on whole cell recordings in VCN neurons Rothman and Manis (2003a,b). The voltage-gated ionic currents that give the cell its chopping behaviour are the major mechanism contributing to the electrical activity of stellate cells (Rothman and Manis 2003a,b). Rothman and Manis (2003c) presented three new current models from whole cell recordings in the VCN (hereafter called the 'RM' neural model). These included the low-threshold potassium current (I_{KLT}), the transient potassium current (I_{KA}) and the hyperpolarisation-activated mixed cation current (I_h). I_{KA} and I_h have a role in modulating the response of TS cells, enhancing their sensitivity to small input changes.

1.2.6.3 Microcircuit Models in the Cochlear Nucleus

Table 1.1 summarises neural network studies of the VCN with emphasis on the output of TS cells. Studies investigating TS cells with local interneurons have not utilised

the important membrane cell properties of TS cells, are limited by outdated input AN models, and generally have insufficiently complex neural models or contain errors in their network connectivity.

The first network models of the CN were in the DCN (Arle 1992; Arle and Kim 1990, 1991b; Davis and Voigt 1991). The cerebellar-like circuitry of the DCN and its complex EIRA cell type behaviours were modelled by Blum and colleagues (Blum and Reed 1998, 2000; Blum et al. 1995; Reed and Blum 1995, 1997) and in greater detail by Davis and colleagues (Davis and Voigt 1996; Hancock et al. 1997, 2001; Spirou et al. 1999). The role of DS cell inhibition in the DCN circuitry, particularly on TV cells (Spirou et al. 1999), is critically important to the VCN stellate microcircuit. Strong, fast, wide-band inhibition of TV cells induces non-linear rate-level response to tones and minimal response to noise. The topological properties of DS to TV connectivity have been explored even further, with suggestions of an offset of the DS connections from high CF to low CF frequency bands (Lomakin and Davis 2008; Reiss and Young 2005; Young and Davis 2002).

Table 1.1: BNN model studies of the VCN. These studies were selected for their attempts to replicate the T stellate cell microcircuit, which excludes DCN neural network models. The studies in the left column were analysed for the types of neural model, AN input model, the connectivity between cells types, and methods for parameter selection used. Parameter selection methods: UD (undisclosed), VI (visual inspection), HD (hand-tuned), FV (fixed values), V (variable).

Study	Input Model	Neural Model	Connections	Parameter Selection
Wang and Sachs 1995	Real ANF spikes (Wang and Sachs 1993)	HH-like conductance model with passive dendrite, current models updated from Banks and Sachs (1991)	ANF → TS Inhibitory (Poisson model) → TS	UD UD
Lai, Winslow, and Sachs 1994a,b	In-paper (Lai et al. 1994a), simple rate responses	HH-like conductance model with passive dendrite based on Banks and Sachs (1991). Additional potassium current (Wang 1991).	ANF → TS Inhibitory (Poisson model) → TS	Hand-tuned Hand-tuned
Eriksson and Robert 1999	In co-paper Robert and Eriksson (1999), simple rate responses with onset adaptation	Point neuron	ANF → TS, ANF → DS, ANF → TV DS → TV, DS → TS, TV → TS, TV → DS	Hand-tuned, fixed Hand-tuned, variable
Hand-tuned				
Wiegrefe and Meddis 2004	DSAM (Meddis et al. 2001), phenomenologically realistic model	Hewitt et al. (1992) point neuron model	ANF → TS TS → TS	Hand-tuned, fixed Hand-tuned, fixed
Pressnitzer et al. 2001	In-paper based on (Meddis et al. 1990), precursor to DSAM (Meddis et al. 2001), co-modulation masking of pure and AM tones	Hewitt et al. (1992) point model plus filtered PSPs	ANF → TS TS → TS	Hand-tuned, fixed Hand-tuned, fixed
Bahner and Langner 2006b	In-paper (Bahner and Langner 2006b), sinusoidal AM responses	Onset neuron: Rothman and Manis (2003c) conductance model, chopper neuron: leaky integrate and fire with PSP filter	ANF → TS, TS → TS, Octopus → TS	Hand-tuned
Burck and van Hemmen 2007	In-paper, Poisson process, simple rate responses	Integrate and fire neural model	ANF → TS, ANF → TV, TV → TS	
Xu, Zhou, and Xiao 2011	In-paper, Poisson process, simple rate and temporal responses		ANF → TS, ANF → TV, TV → TS	

Selective processing of different ANF inputs using some form of inhibition was the first step toward including interneurons in a TS cell model (Lai et al. 1994a,b; Wang and Sachs 1995). Lai et al. (1994b) used the ball-and-stick (i.e. soma and dendrite) HH conductance neural model based on Banks and Sachs (1991). The mechanism of selective processing removes the saturation of HSR fibres by shunting inhibition at synapses proximal to the soma. This group of models enhanced the dynamic range of the TS cell model to tones and highlighted the need for inclusion of inhibitory interneurons in VCN models.

Lateral inhibition has been a strong feature in most VCN network models. Shamma (1985) first proposed lateral inhibition in the auditory pathway as a means of enhancing rate-place processing, and led to biologically-inspired automatic speech recognition models (Shamma 1998; Xu et al. 2011). The VCN stellate network model developed by Eriksson and Robert (1999) was the first to include topographically connected TV and DS cells. This model included a simplistic AN model (Robert and Eriksson 1999) but was still able to reproduce chopper-like PSTH and rate-level responses to tones.

Recurrent excitation between TS cells has been observed in mice (Ferragamo et al. 1998b) and has been investigated in two modelling studies (Bahmer and Langner 2006a; Wiegrebé and Meddis 2004). However, neither study provides a realistic implementation of the stellate microcircuit. In a speculative model, Wiegrebé and Meddis (2004) included a range of TS cells in each frequency band, each with a different intrinsic firing rate. The goal of their model was decoding AM properties in the IC. Unfortunately, the intrinsic firing rate of the TS cell model exceeded physiologically observed rates. Additionally, the AN model, developed in-paper, used was limited by the dated nature of the experimental data (Meddis et al. 2001).

The network model by Bahmer and Langner (2006a) proposed a new VCN network design, with an excitatory onset unit contacting recurrently connected TS cells. The purpose of this model was to show that recurrently connected TS cells, with synaptic delay of 0.4 msec, form the best basis for modulation frequency peaks in the IC. Bahmer and Langner (2006a) assert that octopus cells form excitatory synapses with TS cells. Octopus cells do not have axonal collaterals in the VCN (Adams 1997; Cant and Benson 2003); consequently, the inclusion of octopus cells in a network of the VCN is specula-

tive. Despite using the most up-to-date currents in the onset neural model (Rothman and Manis 2003c), Bahmer and Langner (2006b) did not include the I_h current, a unique characteristic of octopus cells (Cai et al. 2000). Recurrent networks in the cortex prefer inhibition for synchronisation (Bush and Sejnowski 1996; Lytton and Sejnowski 1991). In theoretical terms, inhibitory phasic input is significantly better than excitatory phasic inputs at improving synchronisation in recurrent neural networks (van Vreeswijk et al. 1995). The lack of inclusion of contemporary AN models as input to the Bahmer and Langner (2006b) CN model means that there is much scope for improvement in computational modelling in the CN stellate microcircuit.

1.2.7 Optimisation in Neural Modeling

Neuronal modelling demands of a series of design choices, guesses and assumptions that try to balance the level of detail in the model with the accuracy and realism of the output (Segev et al. 1998). Reviews of spiking networks and BNNs show there are many problems with optimisation of parameters in these models (Brette 2007; Eggert and van Hemmen 2001). Increasing the complexity of neural models and networks of synaptic connections creates large parameter spaces. Large networks may use randomisation for synaptic connectivity between cell populations which introduces indeterminate noise. Noise is present at multiple stages in BNNs that create additional problems for optimisation. These sources of noise include stimulus noise, Poisson noise in neural AP signals, background noise from extrinsic inputs, and stochastic noise in vesicle release probabilities. Without limitations and constraints on parameters and an efficient optimisation technique, these problems can become computationally prohibitive.

Current methods used in constraining spiking networks can be categorised as follows:

- **Self-organising maps (SOM)** are used in artificial neural networks for finding topographic relationships between feature detectors (input layers) and some sensory or abstract feature output (Kohonen 2001). There are two major difficulties in applying SOMs to realistic neural networks: the SOM does not transfer signal patterns due the singular response of the ‘winner-take-all’ function (Kohonen

2006) and HH models are not analytical (in terms of its input/output relationship), rendering SOMs unsuitable for error back-propagation.

- **Reverse correlation and principal component analysis** make up into a class of statistical methods that use covariance in network activity to infer underlying connectivity (Chichilnisky 2001; Dahlhaus et al. 1997; Eichler et al. 2003).
- **Information Theoretic Analysis** includes coherence-based causality chains and directed transfer functions that can be used to identify feedback relationships between neurons (Kaminski et al. 2001; Korzeniewska et al. 2003).
- **Single Neuron Dynamics** determine the effects of the activity of a network on BNNs (Pillow et al. 2005). Makarov et al. (2005) extended this method to include observation of neural architecture derived from extracellular recordings. Further advances using analytical methods enable ensembles of integrate and fire neurons to be precisely fit to spiking data (Brette 2006, 2007; Brette and Guigon 2003) and experimental data (Rossant et al. 2010).
- **Evolutionary algorithms** have been shown to be suitable for noisy, large parameter spaces of spiking neural networks (Takahama and Sakai 2005; Yao 1999). Genetic algorithms (GAs) have been used to constrain parameters in single cell models (Keren et al. 2005; Van Geit et al. 2008; Vanier and Bower 1999) or small BNNs (Taylor and Enoka 2004).

1.3 Overview of Thesis

As the foregoing literature review has demonstrated, current TS cell microcircuit models make insufficient use of experimental data and optimisation techniques. This thesis seeks to address these deficiencies through the design and optimisation of the CNSM model. The remainder of this chapter introduces the work undertaken in this thesis to develop and test the CNSM model.

Chapter 2 establishes the general methods for use in the design of the CNSM model. It introduces the basic building blocks of individual cells (membrane currents, different cell types and characteristics), and their neural connectivity (including synapse types

and kinetics), and cell type to cell type connections within and across frequency channels. The chapter describes the the AN input model and the stimuli used to generate acoustic input to the AN model. Finally, it foreshadows the optimisation techniques deployed in Chapters 3 and 5.

Chapter 3 presents the detailed design of the CNSM model using a sequential method of optimisation. The cells of the CNSM model (Golgi, DS, TV and three categories of TS cells) and the cost function used to fit the model to experimental data are each laid out in turn. The CNSM model was tested using a series of tone and noise stimuli for validation with experimental data not utilised in the optimisation procedure.

Chapter 4 presents a case study involving the validation of the CNSM model using complex stimuli, AM, which is a key component of animal communication. Through this application of the CNSM, Chapter 4 demonstrates that connectivity within the microcircuit enhances temporal coding from the AN to higher centres through the TS cells.

Chapter 5 uses a simplified version of the CNSM model to explore simultaneous optimisation, a faster means of establishing network parameters in BNNs. Through this analysis, Chapter 5 demonstrates that GAs may have utility as an expedient optimisation method for large BNNs, even where experimental data are limited.

Chapter 6 draws together the findings of the design, optimisation and analysis of the CNSM model. It describes the usefulness of the model as well as the optimisation methods used throughout the thesis. It canvases the limitations of the research and makes recommendations for future work arising out of the thesis.

This page intentionally left blank.

Chapter 2

Methods

This chapter introduces the general methods used in the development and testing of the CNSM model. More specific descriptions of the methods and procedures used are provided in the relevant chapters.

2.1 Auditory Input Model

To understand the auditory system, one must first understand the transformations preceding neural signals in the auditory nerve. Mechanical vibrations at the eardrum (tympanic membrane) are conducted by the middle ear bones to vibrations of fluid in the inner ear (cochlea). They are then transferred to chemical signals in the inner hair cells and then to electrical potentials of the ANFs.

ANFs project to the CN in a tonotopic fashion (Fekete 1984; Feldman 1969; Leake et al. 1993; Liberman 1991). They bifurcate after passing the central nervous system barrier to innervate the VCN and DCN (Liberman 1991; Lorente de Nó 1981). Based on their cell bodies, myelination and prevalence, ANFs are categorised as type I (large, myelinated and highly prevalent) and type II (small, unmyelinated and less prevalent). The dominant type I ANFs are further categorised as HSR and LSR fibres. HSR fibres have a low threshold to tones and have limited dynamic range (saturating to tones of moderate sound levels) (Sachs and Young 1979). LSR fibres have a higher threshold to stimulus sound level, and have a monotonic response to increasing sound levels. LSR fibres also project to the GCD (Liberman 1993; Ryugo and Parks 2003; Ryugo et al. 2003) along with the smaller, unmyelinated type II ANFs (Hurd et al. 1999), which suggests they play a different role in sound processing to HSR fibres.

The above-mentioned characteristics of ANFs are essential as input to models of the CN. To examine the properties of a detailed neural model of the CN, a phenomenologically-realistic auditory model is required to represent sounds and transformations that occur in the central auditory system. Simple attempts to recreate rate-level behaviour in ANFs (e.g. Sachs et al. 1989) are not sufficient to reproduce complex non-linear behaviours when dealing with arbitrary stimuli (Arnesen and Osen 1978; Clopton et al. 1974; Leake et al. 1993). Since those early efforts, there has been great advancement in auditory periphery models; for an extensive review see Lopez-Poveda (2005).

The AN input model in the CNSM model is called the Carney AN model, where each version is derived from the original model of low CF fibres (Carney 1993). Carney and colleagues have made a series of improvements to the original model over the last 20 years (Bruce et al. 2003; Heinz et al. 2001; Zhang et al. 2001; Zilany and Bruce 2006, 2007; Zilany and Carney 2010; Zilany et al. 2009). Heinz et al. (2001) incorporated cochlear filters based on the critical bandwidths obtained from psychophysical experiments, improving the non-linear compression and two-tone suppression behaviour in the model. Chapter 5 uses this model exclusively. Zilany and Bruce (2007), version 5, added a parallel signal control path and its predictions have matched a wide range of physiological data in normal and impaired cat studies. Version 6 was developed by Zilany et al. (2009) and includes an additional power-law synapse model, which enhances the temporal recovery behaviour in ANFs. Versions 5 (Zilany and Bruce 2007) and 6 (Zilany et al. 2009) of the Carney AN model are used in Chapters 3 and 4.

Figure 2.1 shows the schematics of the Zilany version of the Carney AN model (Zilany and Carney 2010; Zilany et al. 2009). The Carney AN model consists of an outer/middle ear pre-processing filter, a cochlear filterbank, IHC to AN synapse model and dead-time modified Poisson spike generator (Zhang et al. 2001). Zilany et al. (2009) improved the classic Westerman and Smith (1988) three-store diffusion model of the IHC-AN synapse with dual power-law adaptation models and the inclusion of fractional Gaussian noise.

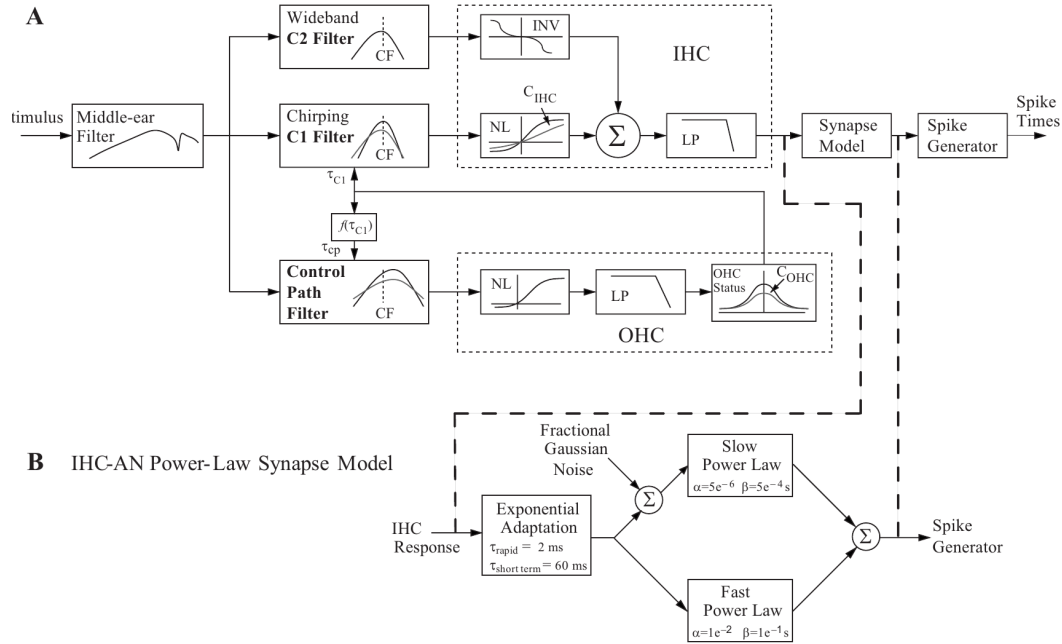


Figure 2.1: Auditory periphery schematic of the Zilany version of the Carney AN model (Zilany et al. (2009), reproduced from their Fig. 2). (A) The Carney AN model is comprised of a middle and inner ear filter model, and a synapse between inner hair cells (IHC) and type I ANFs. (B) The Zilany AN model has added a dual power-law synapse model.

2.1.1 Frequency Channels

The organisation of the auditory system is described as “tonotopic” after the continuous logarithmic frequency tuning along the basilar membrane (Greenwood 1990). The CF of ANFs is typical of the resonant frequency of the adjacent basilar membrane and forms a topographical receptive field, according to place along the central auditory nervous system.

The input auditory models used in this thesis mimic the major phenomenological qualities of experimentally recorded ANFs. The centre frequencies across N_{channels} is determined by the logarithmic Greenwood function (Greenwood 1990) of the basilar membrane in cats. Centre frequencies of the channels were spaced logarithmically according to the basilar membrane frequency-place map function, Equation 2.1 (Greenwood 1990):

$$f(x) = A \left(10^{ax/L} - k \right) \quad (\text{Hz}) \quad (2.1)$$

Table 2.1: Frequency to basilar membrane distance function parameters.
Data obtained from <http://earlab.bu.edu>.

	A	a	k	L
Human ¹	165.4	2.1	1.0	35
Cat ²	456	2.1	0.8	25
Rat ³	7613.3	0.928	1.0	8.03

¹Greenwood (1990), ²Liberman (1982), ³Mller (1991).

where x is the distance along the basilar membrane from the stapes, and variables A , a , L and k are dependent on the species. The data in Table 2.1 show the currently accepted parameters for humans, cat and rat.

The range and number of frequency channels used in the auditory filterbank is defined in each of the following chapters. These parameters set the level of spatial resolution required in the network model. An increase in the number of frequency channels greatly increases the computational load and simulation time in the AN input generation and CNSM model. The model reproduces responses for 50 high and 30 low SR ANFs in each frequency channel, across the frequency range 200 Hz to 64 kHz.

2.1.2 Inner and Outer Hair Cell Compression

The most recent AN model incorporates species-specific compression functions of outer and IHC to facilitate accurate audiograms in the ANFs (Zilany and Carney 2010; Zilany et al. 2009). Figure 2.2 shows the implementation of the compression functions of the inner and outer ear for the cat and rat. The acoustic thresholds of the cat and rat (Heffner et al. 2001) were obtained from <http://earlab.bu.edu>.

2.1.3 High and Low Spontaneous Rate Fibres

The level of spontaneous activity and minimum thresholds in ANFs are separated into two distinct groups, HSR and LSR fibres (Liberman 1978, 1993; Schmiedt 1989; Wang et al. 1997). The spontaneous rate of HSR and LSR fibers were set to 50 Hz and 0.5 Hz, respectively. HSR and LSR ANFs were simulated for each frequency channel. The stimulus was passed through the AN model for each frequency channel for both

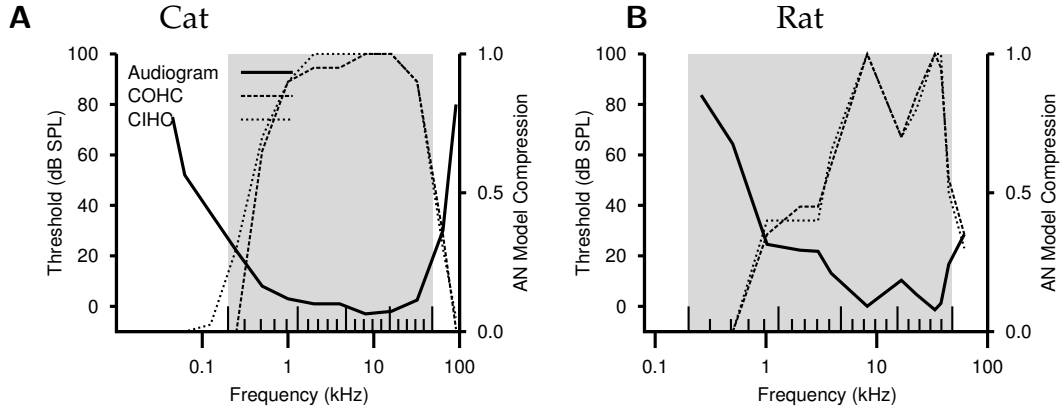


Figure 2.2: Animal auditory thresholds (audiograms) were used to calculate the inner and outer hair cell (IHC and OHC) compression values in the AN models (Zilany and Carney 2010; Zilany et al. 2009). Audiograms and compression values are shown for (A) cat and (B) rat.

LSR and HSR fibres, producing an instantaneous firing rate response that was down-sampled to 20 kHz.

The spiking neural model used in the ANFs (and the Golgi cell model in Chapters 3-4) are inhomogeneous Poisson processes with refractory effects. These properties are typical of ANFs (Heil et al. 2007; Jackson and Carney 2005). Spike times were generated independently for each HSR and LSR fibre from the instantaneous firing rate using a pseudo-random Poisson spike generator (Jackson and Carney 2005), with refractory effects similar to those present in ANFs. The double exponential relative refractory functions, specific to ANFs, were

$$y_0(t) = c_0 \exp(-(t' - t_a)/s_0) \quad (2.2)$$

$$y_1(t) = c_1 \exp(-(t' - t_a)/s_1), \quad (2.3)$$

where t' is the time relative to the last spike, $c_0 = 0.5$, $c_1 = 0.5$, $s_0 = 0.001$ msec and $s_1 = 0.0125$ msec. The absolute refractory period, t_a , was 0.75 msec. Spike trains for each Poisson-based neural model in the CNSM model were created at the start of each repetition of the stimulus.

2.2 Neural Cell Models

Single compartment conductance models, similar to those presented by Hodgkin and Huxley (1952b), were used to model the CN neurons. The dynamics of the membrane voltage, $V(t)$, is described by

$$C_m \frac{dV}{dt} = -\bar{g}_{\text{leak}}(V - E_{\text{leak}}) - I_{\text{Na}} - I_{\text{KHT}} - I_{\text{KLT}} - I_{\text{KA}} - I_{\text{h}} - \sum I_{\text{SYN}}, \quad (2.4)$$

where C_m is the specific membrane capacitance; \bar{g}_{leak} is the specific leak conductance with associated leak reversal potential E_{leak} ; I_{Na} is the sodium current density; I_{KHT} , I_{KLT} , and I_{KA} are three types of potassium current densities; I_{h} is a hyperpolarization-activated current density; and I_{SYN} are synaptic input current densities. The compartmental nature of the neural model and the voltage measured in millivolts means that conductance is measured in Siemens per centimetre squared (S cm^{-2}) and the membrane capacitance in micro Farads per centimetre squared.

The voltage-dependent relationship in each current model has a peak conductance parameter and gating variables for activation and de-activation. The formula for the sodium current, I_{Na} , was based on the studies of Costa (1996) and Belluzzi et al. (1985) and given by

$$I_{\text{Na}}(t, V) = \bar{g}_{\text{Na}} m^3 h(V - E_{\text{Na}}), \quad (2.5)$$

where m is the activation function, h is the de-activation function, \bar{g}_{Na} is the maximum sodium conductance, and $(V - E_{\text{Na}})$ is the relative potential between the membrane voltage and the sodium reversal potential. The sodium current in VCN neurons has not been measured, but measurements in other mammalian neurons were deemed sufficient for use in the model.

The potassium and mixed-cation current models used here were drawn from an investigation of isolated VCN neurons *in vitro* (Rothman and Manis 2003a,b,c), which yielded accurate mathematical descriptions of:

- the high-threshold rectifying potassium current density,

$$I_{\text{KHT}}(t, V) = \bar{g}_{\text{KHT}}(\varphi n^2 + (1 - \varphi)p)(V - E_K) \quad (2.6)$$

- the fast-activating transient potassium current density,

$$I_{KA}(t, V) = \bar{g}_{KA} a^4 b c (V - E_K) \quad (2.7)$$

- the low-threshold, fast-activating, slowly-deactivating potassium current density,

$$I_{KLT}(t, V) = \bar{g}_{KLT} w^3 z (V - E_K) \quad (2.8)$$

- the mixed-cation hyperpolarization-activated current density,

$$I_h(t, V) = \bar{g}_h r (V - E_h). \quad (2.9)$$

The formal equations of the activation and deactivation functions are shown in the Appendix (Section A).

Figure 2.3 shows the voltage-dependent relationship of the activation function and time constants in potassium currents (I_{KLT} and I_{KHT}) from each of the previous VCN neural models. The threshold for the activation variable of I_{KLT} , w^λ , is below the resting membrane potential (RMP) around -65 mV. Only I_{KHT} is present in regular firing (current-clamp type I) units, and behaves as a rectifier by activating when the membrane voltage rises above -20 mV during an AP. The active voltage-dependent activation and deactivation functions (a , b , c , h , m , n , p , r , w and z) are described in detail by Rothman and Manis (2003a,b,c) and the NEURON source code is available online at neural model database ModelDB (Hines et al. 2004).

Membrane and synapse channels are temperature dependent and most CN *in vitro* experiments are performed at room temperature, 22°C. All simulations in this thesis were performed at body temperature, 37°C. Accordingly, modification of the appropriate variables had to be performed. This included activation and deactivation time constants, and maximum conductance of the currents. For any variable, x , the temperature scaling is performed by

$$x = x / Q_{10}^{\Delta T}, \quad (2.10)$$

where ΔT is the temperature difference in degrees Celsius and Q_{10} is the temperature coefficient calculated at a temperature difference of 10 °C. Temperature scaling of each membrane current's activation and deactivation time constant parameters was calcu-

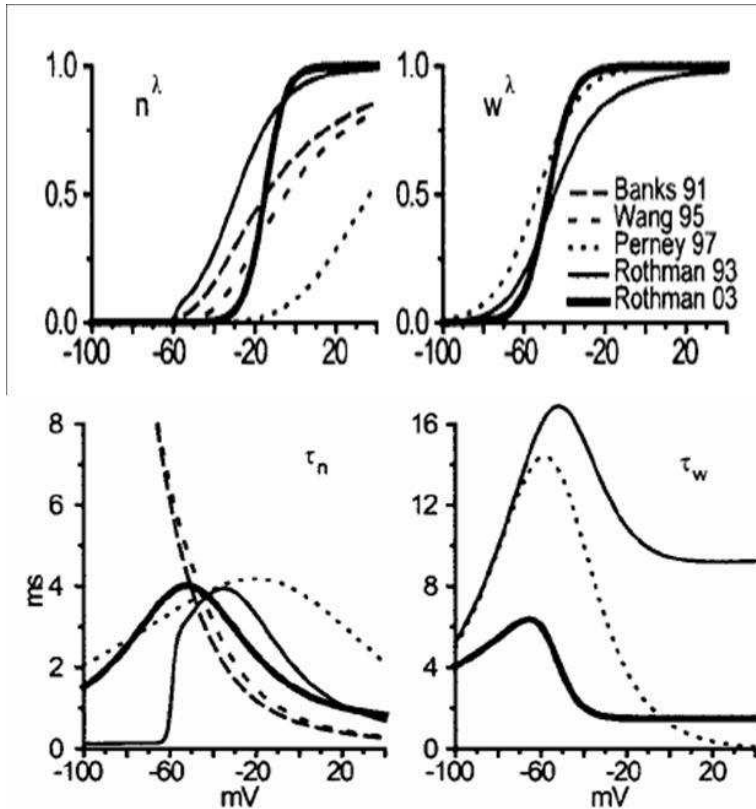


Figure 2.3: Rothman and Manis (2003c) compared their kinematic model of activation gating variables of I_{KLT} and I_{KHT} with equivalent rectifying potassium channel models used by existing CN neural models. Top figures show normalised voltage dependency of activation gating variables in I_{KHT} (n^λ) and I_{KLT} (w^λ) currents. Corresponding time constant voltage dependencies (τ_n , τ_w) in bottom figures. Figure reproduced from Fig. 2 in Rothman and Manis (2003c).

lated with $Q_{10} = 3.0$. Maximum conductance parameters, \bar{g} , were adjusted with temperature coefficient $Q_{10} = 2.0$, except for I_h which had a temperature coefficient $Q_{10} = 1.3$.

2.2.1 Neural Sub-types in the Cochlear Nucleus

Table 2.2 shows the maximum conductances, \bar{g} , for each cell type in the network. The neurons in the ventral CN differ in their composition of these currents on the basis of their current-clamp type. They are classified as either type I or type II based on their response to intracellular current injection (Oertel et al. 1988). The response of type I neurons to current injection is regularly spaced APs. TV (Zhang and Oertel 1993) and

Table 2.2: Cell-type membrane current parameters

Cells RM Type		TS I-t	DS I-II	TV I-c	GLG * I-c
$\bar{g}_{Na'}$	S cm ⁻²	0.2367	0.3062	0.249	0.235
$\bar{g}_{KHT'}$	S cm ⁻²	0.0189	0.0306	0.0374	0.019
$\bar{g}_{KLT'}$	S cm ⁻²	0	0.0164	0	0
$\bar{g}_{KA'}$	S cm ⁻²	0.0154	0	0	0
\bar{g}_h'	mS cm ⁻²	0.062	0.214	0.0653	0.6178
$\bar{g}_{leak'}$	mS cm ⁻²	0.4735	0.247	0.249	0.249
E_{Rev}	mV	-65	-65	-72	-65
Soma Diameter, μm		21	25	19.5	15
Input Resistance, M Ω		163	77	320	130

Conductance-based GLG cell model only in Chapter 5.

Golgi cells (Ferragamo et al. 1998b) are classic type I, and have I_{Na} , I_{KHT} and I_h currents. TS cells are type I, and they have additional A-type transient potassium channels, I_{KA} (Ferragamo et al. 1998a; Rothman and Manis 2003c).

Type II responses have only one phasic AP at the start of the stimulus, characteristic of ventral CN bushy cells, which enables them to rapidly follow ANF input events (Oertel et al. 1988; Smith and Rhode 1989). I_{KLT} is present in type II units and is active at resting membrane potential, which allows for rapid changes depending on the input. DS cells respond with a single AP for injected current levels near threshold, and then discharge regularly for higher current levels (Oertel et al. 1988; Paolini and Clark 1999), corresponding to an intermediate type I-II response. DS cells have a small amount of I_{KLT} current to reduce the cells' input resistance and enhance coincidence detection.

In the CNSM model, the membrane parameters were developed and refined after we established the *in vitro* characteristics of each cell type from the literature (Ferragamo et al. 1998a,b; Oertel et al. 1988; Zhang and Oertel 1993).

2.3 Connectivity and Topology: Network Organisation in the Cochlear Nucleus Stellate Microcircuit Model

Like many neural networks in the brain, the likelihood of connectivity between two cells in the CN is a function of distance, cell type, and spatial spread of dendrites. Connectivity between cells in a post-synaptic group onto individual cells is described by a

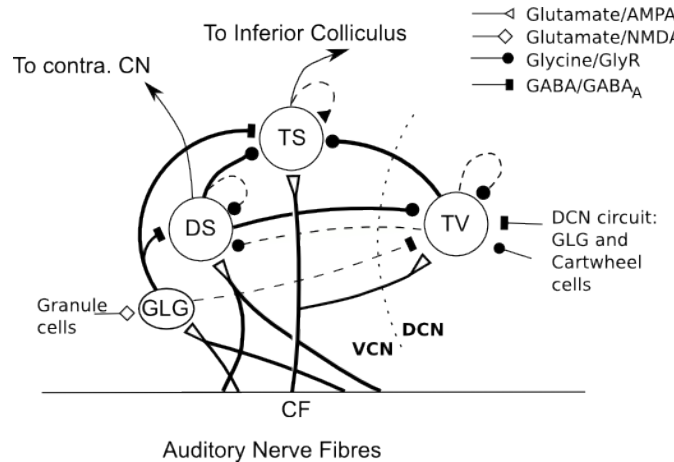


Figure 2.4: Microcircuit showing proposed synaptic interaction between cell types in the CN stellate microcircuit in one isofrequency lamina. Strong evidence for connection is shown with a solid line. Weak evidence for connection is shown with a dashed line, for example recurrent connections between TS cells.

synaptic strength or weight, w , the number of synapses, n , and the spatial spreading parameter, s , which were taken to be uniform across the network for each connection type. The allocation of pre-synaptic cells to post-synaptic cells was random based upon a Gaussian function, with mean equal to the post-synaptic cell's CF channel and standard deviation $\sigma^2 = s$ (in channel units).

The basic unit of sensory networks is the place-channel or feature-channel of the microcircuit, which separates the receptive field into independent adjacent groups. The creation of neural microcircuits based on “place” is easily amenable to different sensory neural network models; however, attention to a given network’s unique features is necessary to ensure realistic representation of the system. In the CNSM model, one isofrequency channel receives afferent input from the narrowest receptive field possible in the AN model. Figure 2.4 shows the intra-nuclei microcircuit connections and connectivity type (neurotransmitter and receptor type) in the CNSM model based on existing experimental evidence in mammals. Chapter 3 provides more detail regarding the evidence for each of the connections in the microcircuit.

Connection variables between cell types are generally uniform across the network but may be adjusted to suit the model. Model parameters may be different between species or within species; therefore, in the absence of adequate evidence regarding exact neuron to neuron connections, average population data were used. Issues also

arise at the ends of large-scale topographic BNNs with overlapping (place) channel connections. Boundaries are considered closed bookends, where post-synaptic neurons select only from those within their connection range.

2.3.1 Connectivity Parameters

The probability of pre-synaptic to post-synaptic connection is defined as a Gaussian probability distribution. The distribution is centred on the post-synaptic cell's position, i , with an optional offset parameter, o , in this case frequency channels. Figure 2.5 shows the method used in the CNSM model for establishing Gaussian spread of connections between cell types.

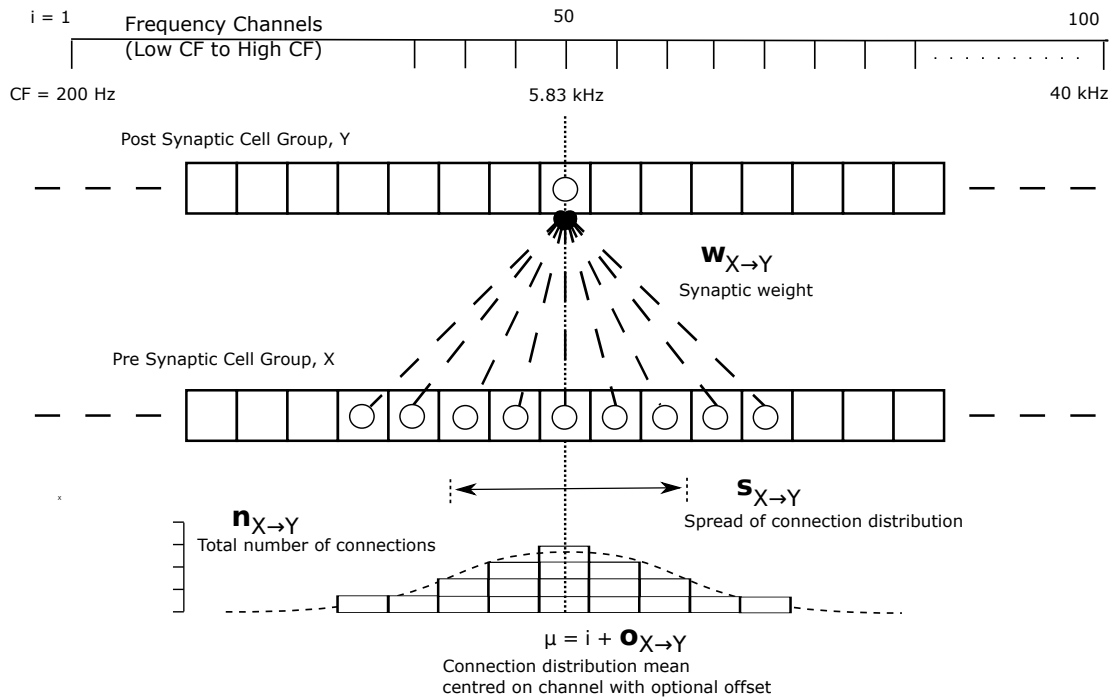


Figure 2.5: Distribution of synaptic connections between cell types in the CN stellate microcircuit. A post-synaptic neuron receives n synapses from pre-synaptic neurons (from one cell type group) with equal weight, w . The post-synaptic cell is selected using a Gaussian random process, centred on the same frequency channel (with optional offset, o) and spread equal to twice the variance.

Network parameters that control the connectivity between two cell type groups are defined as follows:

$w_{X \rightarrow Y}$ The synaptic weight of the post-synaptic current influx caused by the

pre-synaptic cells neurotransmitter activating the receptor channels of the post-synaptic cell. This value may be either uniform for all synapses across the connection type or defined by a function of the receptive field.

$n_{x \rightarrow y}$ The total number of synaptic connections on post-synaptic cells from pre-synaptic cells.

$s_{x \rightarrow y}$ The spatial or feature-specific spread of connections from pre-synaptic cells onto post-synaptic cells. The spread parameter, s , is half the variance of the Gaussian function, thus has standard deviation $\sigma^2 = 2s$. The distributions are uniform across the CNSM network, which ignores channels outside the network's range. A spread of zero means all connections come from the same frequency channel.

$o_{x \rightarrow y}$ The offset in distribution of connections between pre-synaptic cell types and post-synaptic cells. The offset variable adjusts the centre point of the probability distribution, $\mathcal{N}(i + o, \sqrt{s}/2)$, away from the post-synaptic cell's position, i .

$d_{x \rightarrow y}$ The temporal delay between a pre-synaptic cell's AP trigger and the onset of the post-synaptic current. This delay incorporates the axonal conduction delay and diffusion time across the synaptic cleft. In a single-compartment model, additional delay can also be used to represent dendritic delay.

ANFs with similar CFs were spatially organised into N_{Channel} isofrequency lamina or channels, which translated to frequency channels in the CN. The dendrites of TS and TV cells are located within the isofrequency lamina of the VCN and DCN, respectively. The receptive field and bandwidth of TS and TV cells are also similar to ANFs of similar CF. In the CNSM model, synapse inputs to these cells were chosen from ANFs within the same frequency channel (i.e. spread of zero, $s = 0$). DS cells have many arborisations extending perpendicular to ANF axons and have a typical physiological responses to frequencies 2 octaves below and 1 octave above their CF (Palmer et al. 1996; Paolini and Clark 1999).

Fast, glycinergic inhibition from TV cells and DS cells (Figure 2.4) is involved in modulating the firing rate and spike interval variability in TS cells (Ferragamo et al. 1998a; Wickesberg and Oertel 1993). TV cells in the deep layer of the dorsal CN provide

a delayed narrowband inhibition to TS and DS cells in the VCN. The dendrites of DS cells cover one third of the CN, contributing to this cell's wide frequency response. In turn this cell is responsible for altering the frequency responses in TS and TV cells (Spirou et al. 1999). DS cells are coincidence detectors and have a precisely timed onset response that affects the temporal properties of TS cells (Paolini et al. 2005; Rhode and Greenberg 1994b) and completely inhibits TV cell responses to loud clicks (Spirou et al. 1999).

GABAergic synapses are present in each of the cells in the CNSM model. Inhibition from GABA cells modulates the level of excitation necessary to reach threshold for all CN cells (Caspary et al. 1994; Ferragamo et al. 1998a). Feedback circuits from the olfactory complex to the ventral CN are also known to use GABA as a neurotransmitter (Saint Marie et al. 1989), however only the Golgi cell was included the CNSM model.

2.3.2 Synapse Models

Synapses were modeled with either a single or a double exponential time-dependent conductance change. The current density equation used was

$$I_{\text{SYN}}(t) = g_{\text{SYN}}(t)(V - E_{\text{rev}}), \quad (2.11)$$

where E_{rev} is the associated reversal potential. NEURON's conductance synapse model classes `ExpSyn` and `Exp2Syn` (Hines and Carnevale 2000) were used in the CNSM model. The strength of the synapses was determined by a normalised conductance kernel with decay time-constants and a multiplicative weight parameter, w , as follows:

$$g_{\text{Exc}}(t) = w_{\text{Exc}} \exp(-t/\tau_{\text{Exc}}) \quad (\mu\text{S}) \quad (2.12)$$

$$g_{\text{Inh}}(t) = w_{\text{Inh}} \eta (\exp(-t/\tau_{\text{Inh2}}) - \exp(-t/\tau_{\text{Inh1}})) \quad (\mu\text{S}) \quad (2.13)$$

where η normalises the peak of the double-exponential function to 1. Normalisation factor, η , for double exponential synapse model (Hines and Carnevale 2000) is given by

$$\eta = \frac{1}{-\exp(t'/\tau_{Inh1}) + \exp(t'/\tau_{Inh2})} \quad (2.14)$$

where

$$t' = \frac{\tau_{Inh1}\tau_{Inh2}}{\tau_{Inh2} - \tau_{Inh1}} \ln(\tau_{Inh2}/\tau_{Inh1}). \quad (2.15)$$

Excitatory inputs to CN cells from type I ANF terminals were mediated by fast glutamatergic-AMPA receptors (Gardner 2000; Gardner et al. 1999). Spontaneous EP-SPs in VCN DS and TS neurons had a decay time constant of $\tau_{AMPA} = 0.36$ msec (Gardner et al. 1999). TV cells the DCN had a decay time constant of $\tau_{AMPA} = 0.40$ msec (Gardner et al. 1999). The reversal potential of the excitatory synapse was 0 mV.

Double exponential inhibitory synapses used in the network were derived from inhibitory post-synaptic potentials (IPSPs) in glycinergic and GABAergic synapses. The glycine receptor (GlyR) is the fastest inhibitory synapse in the mammalian brain and is blocked by the neurotoxin strychnine. The GlyR synapse model was based on miniature glycinergic IPSPs recorded in mature AVCN in rats and mice (Lim et al. 2003) and in rat MNTB neurons (Awatramani et al. 2004, 2005). Room temperature whole cell patch recordings of spontaneous inhibitory post-synaptic currents (IPSCs) in mature AVCN in rats and mice neurons showed these synapses have a fast rise time (10% to 90%), $\tau_{Gly1} = 0.4$ msec, and a decay time constant $\tau_{Gly2} = 2.5$ msec (Lim et al. 2003). In MNTB rat neurons at body temperature, GlyR decay constants of miniature and evoked IPSCs were 0.8 ± 0.2 msec and 1.1 ± 0.2 msec (37°C), respectively (Awatramani et al. 2004). GABA_A synapses were modeled from MNTB recordings in mature guinea pigs (Awatramani et al. 2005). GABA_A receptor currents have a fast (9 msec) and a slow (150 msec) decay component (Awatramani et al. 2005; Davis and Young 2000), but for short stimuli only the fast component was modeled ($\tau_{GABA1} = 0.7$ msec, $\tau_{GABA2} = 9.0$ msec). Chlorine reversal potential in GlyR and GABA_A receptors was set to -75 mV.

2.3.3 Delay and Latency Variables

For the CNSM model, delay was defined as the time between activation of the pre-synaptic neuron and the activation of the post-synaptic potential, which includes axonal conduction and synaptic diffusion. Synaptic transmission and axonal conductance delay between adjacent neurons is typically measured in experiments to be 0.4 – 0.5 msec. Delays between neurons in the ventral and DCN were measured using electric shocks and found to be approximately 1.0 msec, but ranged from 0.15 to 2 msec (Wickesberg and Oertel 1993).

Latency was defined in the CNSM model as the time difference between a stimulus of reference event and the mean activation of the post-synaptic neuron. The formula for the latency of acoustic stimulation to the mean first spike latency (FSL) in ANFs was first derived by Carney and Yin (1988). Carney and Yin (1988) fitted the ANF first spike latency against the CF of the fibres in cats from click responses in the cat to obtain the formula:

$$d = A_0 \exp(-x/A_1) \times 10^{-3} - 1/\text{CF}_x, \quad (2.16)$$

where x is the distance along the basilar membrane from the apex, CF_x is the CF (Hz) at this location, and constants A_0 and A_1 are 8.3 msec and 6.49 cm for cats, respectively.

The latency of CN neurons is not only affected by the properties of the basilar membrane, but also by the twisting of axons by the spiral ganglion neurons and the organised innervation of the CN by the same fibres. Consequently, an additional delay parameter is required that combines the intrinsic ANF delay and the effective axonal conductance to the CN neurons. Mean first spike latency to click stimuli was used in Section 3.2.6 to set the delay times between ANFs and CN cells.

2.4 Implementation of the Cochlear Nucleus Stellate Microcircuit Model

2.4.1 Simulation Environment

Neural models and network connections were generated using the neural simulation package NEURON (Carnevale and Hines 2006). NMODL, an extension of NEURON (Hines and Carnevale 2000), was used to implement membrane current models and interface with the AN model. The AN model and the neural cell models were combined into the CNSM software code called *cnstellate* (in preparation for open-source online access). This code is implemented in NEURON, NMODL and C source code, and plotting scripts in gnuplot and MATLAB. Numerical integration was performed using the Crank-Nicholson method with second order accuracy (in NEURON, *secondorder* = 2) and fixed time step of either 0.1 or 0.05 msec.

The computations of the NEURON model were distributed on a single personal computers (PC); a cluster of nine PCs (3.0 GHz Intel Pentium4)¹; an SGI Altix system (*soma*: 64 32-bit Itanium CPUs)²; and an iDataPlex IBM system (*merri*: 1024 64-bit Intel x86 CPUs)³.

The parallel capabilities of the network model presented in Chapter 3 were based on the NEURON network model *netmod* (see other neural models that also use *netmod* at ModelDB, particularly models 52034, 2730, and 51781 (Migliore, Cannia, Markram, and Hines 2006)). The genetic algorithms and sensitivity analyses in Chapter 5 were implemented in C++ using GAlib (Wall 2006) and the parallel virtual machine libraries (Geist et al. 1994).

2.4.2 Stimulus Generation and Analysis

In order to emulate sound entering the ear, acoustic sounds were generated and passed into the auditory model. The acoustic stimuli were generated in NEURON, with the

¹Systems provided by the Department of Otolaryngology, the University of Melbourne.

²System *soma* provided by the Neuroimaging Group and Department of Electrical and Electronic Engineering, the University of Melbourne.

³System *merri* provided by the Victorian Life Sciences Computing Initiative (VLSCI) an initiative of the Victorian Government.

exception of notch noise, which was generated in MATLAB/GNU Octave. The stimulus types included pure tones, white noise, sinusoidal amplitude modulated sounds and clicks. Sound levels are given in decibel SPL (i.e., root mean square of pressure levels in dB re 20 μPa).

Temporal resolution in the CNSM model is variable at each stage: the stimulus, the ANF spiking model, and the NEURON simulation. The stimulus sampling rate of version 4 of the Carney auditory model was 50 kHz (Heinz et al. 2001). The middle ear filter in the Bruce model (Bruce et al. 2003; Zilany and Bruce 2006, 2007) required a sampling rate of 500 kHz in the stimulus. The Zilany model (Zilany et al. 2009) improved the processing to allow for a stimulus sampling rate of 200 kHz for CFs above 20 kHz; 100 kHz sampling was used for other CFs.

In the CNSM model, the instantaneous rate output profiles of all AN models was down-sampled to a lesser sampling rate for the ANF spike generator and saved for further use. The resolution of the spike generator was either 20 or 50 kHz. The integration time-step of the NEURON simulations was 0.05 msec.

Notch noise was used as the stimulus for Chapter 5 and the optimisation of DS cell connections to TV cells (see Section 3.5.4 in Chapter 3). Notch noise was generated from Gaussian white noise filtered using a stop-band filter in MATLAB/GNU Octave. The notch noise sample was stored in a file so that it could be retrieved by NEURON in the simulation.

2.5 Optimisation Techniques

To develop and optimise detailed neural models and their synaptic connections, reproducible research methods are required. Hand-tuning and gradient-decent optimisation are commonly used in realistic neural and network models (Segev et al. 1998), but may have poor replicability. Parameter estimation and fitting routines in BNN models are also becoming more advanced, for example SSNS (Sichtig et al. 2008), NeuroFitter (Van Geit et al. 2007) and MultiRunFitter (a feature in NEURON). In this thesis, a table method introduced by Nordlie et al. (2009) is used to summarise the neural models used in each optimisation step to improve reproduction. The Nordlie tables shown

Table 2.3: Nordlie Model Summary Table Framework

i		Model Summary	
Populations			
Topology			
Connectivity			
Input model			
Neural models			
Synapse model			
Input			
Measurements			
ii		Populations	
Name	Elements	Size	
iii		Connectivity	
Name	Source	Target	Pattern
iv		Neuron and Synapse Models	
Name			
Type			
Subthreshold dynamics			
Spiking			
v		Optimisation	
Input Stimulus			
Parameters			
Fitness Function			
Measurements			

in Table 2.3 consist of (i) the model summary; (ii) cell type populations; (iii) connectivity between two cell types; (iv) neuron and synapse models; and (v) optimisation parameters. This method provides a consistent and recognisable format for presenting various neural network models and their constituents.

The standard methods for optimisation can be simply described with the following steps:

1. Specify the function or model to be optimised.
2. Specify the fitting function to be satisfied.
3. Specify the parameters that will be adjusted, and any constraints on those para-

meters.

4. Perform the optimisation.

The fitting function includes specifying the stimulation routine, analysis of neural outputs and the formula with which to compare simulated results with experimental data. The large number of parameters in the CNSM model created challenges for realistic optimisation. The model implementation, the choice of experimental data and evaluation of the fitness function are important factors in determining the speed and efficiency of the algorithm. The following sections introduce the two optimisation methods used in this thesis to generate a realistic model of the stellate microcircuit of the CN.

2.5.1 Sequential Methods

To create a realistic microcircuit from a wide range of experimental data, Chapter 3 develops a parameter optimisation routine in sequential stages. The network parameters were chosen in the sequential optimisation stages to encompass synaptic inputs to each individual cell type in the CN stellate microcircuit. Chapter 3 uses the praxis method, an algorithm for finding the minimum of a function of several variables without needing the derivative (Brent 1976).

2.5.2 Simultaneous Methods

Chapter 5 presents a method to optimise the network parameters in the CNSM model simultaneously. New techniques in multi-unit electrophysiological recording are being developed that are able to record from multiple neurons simultaneously. A simultaneous optimisation method requires complete data from the majority of neurons in the network, and is therefore not possible given existing experimental methods. The method in Chapter 5 used surrogate target data by simulating the network with user selected or randomised parameter values.

The optimisation method used in Chapter 5 is a derivation of the genetic algorithm method (Holland 1975; Koza and Rice 1991). The genetic algorithm optimisation procedure uses operations analogous to natural selection to search for the optimal solu-

tion (Mitchell 1996). This procedure is used when the standard analytical and gradient search methods are ineffective or computationally expensive. The basic response properties of the neurons are used to set the fitness criteria of the genetic algorithm. The design and implementation of the genetic algorithm search method is discussed in Chapter 5.

Chapter 3

Optimisation of the Cochlear Nucleus Stellate Network Model: Sequential Parameter Fitting of Synaptic Variables Using Simple Acoustic Responses

3.1 Introduction

This chapter draws on the wealth of experimental data accumulated in auditory neuroscience to create a detailed biophysically-realistic neural network (BNN) model of the T stellate (TS) microcircuit in the cochlear nucleus (CN) (the cochlear nucleus stellate microcircuit (CNSM) model, as described in Chapter 2). The design and methods used for the construction of the model provide insights relevant to other neural network models of the brain, especially those that use sensory pathways.

Despite advances in computational neuroscience, it remains a challenging task to develop an accurate representation of the complex behaviour of real neural networks. Choices, guesses and assumptions continue to be required in neuronal modelling (Segev et al. 1998). With the acceleration of computational power and enhanced experimental techniques in multi-unit recordings, it is possible to develop more detailed neural models. There is much to be gained from biophysically-realistic modelling approaches, especially in the thoroughly investigated CN of mammals, bats and birds.

To develop and optimise detailed neural models and neural network models, reproducible research methods are required. In this chapter, the table method in-

troduced by Nordlie et al. (2009) is adopted to summarise the neural models used in each optimisation step (as described in Chapter 2). In order to create a realistic microcircuit, the connections within the CNSM model (Figure 3.1) were developed using a sequential method of optimisation steps. Parameters in the microcircuit can be separated into two classes: cell-based and connectivity-based. The cell-based parameters for each cell model in the CNSM model, discussed in Section 2.2, remain relatively fixed. The connectivity-based parameters, introduced in Section 2.3.1, are the main focus of this chapter. The parameters in the sequential optimisation stages were chosen so that they did not influence the properties of previously fitted parameters. The parameters of each cell type were based on experimental data or optimised on the basis of responses to simple stimuli. Each cell type was typified with its characteristic peri-stimulus time histogram (PSTH) in response to short tone bursts (Blackburn and Sachs 1989; Pfeiffer 1966a; Young et al. 1988), and the excitatory-inhibitory response area (EIRA) to tones across the frequency spectrum (Evans 1992).

3.1.1 Cochlear Nucleus Stellate Microcircuit Model

The CNSM model shown in Figure 3.1 comprises the following cells:

1. High spontaneous rate (HSR) and low spontaneous rate (LSR) auditory nerve fibres (ANFs): A phenomenological auditory model provides spiking input to CN neurons across frequencies and spontaneous rate types of the ANFs from an arbitrary input stimulus (Zilany et al. 2009). The baseline in Figure 3.1 is a representation of ANFs from low characteristic frequency (CF) to high CF (left to right). The model reproduces responses for high and LSR ANFs at 100 channels across the frequency range 200 Hz to 48 kHz.
2. Golgi (GLG) cell: A GABA-ergic ventral cochlear nucleus (VCN) marginal shell unit that is presumed to regulate excitability in the granule cell domain (GCD) and core VCN units (Ferragamo et al. 1998a). Only one *in vivo* study has recorded extracellular data in the marginal shell area of the CN (Ghoshal and Kim 1997). The presumed characteristics of GLG cells are taken from that study and are defined by a monotonic response to tones and noise, a Type I/ III EIRA, and an

unusual or chopper PSTH.

3. D stellate (DS) cell: A large, glycinergic, multipolar neuron with onset chopper (On_C) PSTH response that acts as a coincidence detector. Its large dendritic area increases its response to noise, allowing it to behave as a wide-band lateral inhibitor in the VCN, dorsal cochlear nucleus (DCN), and contralateral CN (Arnott et al. 2004; Needham and Paolini 2007; Smith et al. 2005).
4. Tuberculoventral (TV) cell: A glycinergic neuron in the deep layer of the DCN categorised typically as Type II EIRA units due to their greatly reduced response to noise (Spirou et al. 1999). This cell acts as a delayed echo-suppressor and narrow-band inhibitor, with connections to DS and TS cells in the VCN (Alibardi 2006; Oertel and Wickesberg 1993; Wickesberg et al. 1991).
5. TS cell: One of the major output projection cells of the CN to the inferior colliculus (IC) and the primary output of the CNSM model. This multipolar neuron has been shown to have robust spectral representation and enhanced synchronisation to modulation in speech sounds (Blackburn and Sachs 1990; Keilson et al. 1997).

Optimisation of a detailed BNN model requires a realistic input model with which to mimic the behaviour observed in live neural networks. For a detailed neural model of the CN, a realistic and phenomenologically robust auditory periphery model is needed to represent sounds and transformations that occur in the central auditory system. The input to the CNSM model, the ANFs, is discussed in the next section. To further fit the parameters of the CNSM model, a simple and sequential method was applied to each of the cell types using experimental data.

The order of the optimisation routines is important because of the dependencies within the isofrequency microcircuit and across the whole nucleus. In the CNSM model, Golgi cells only receive inputs from the ANFs and are the first model and network parameters to be optimised. DS cells are modeled next because they receive inputs from ANFs and GABA-ergic Golgi cells. The TV cells' input network parameters are optimised next as they are strongly inhibited by DS cells and receive excitation from ANFs. In the CNSM model, GLG cells connect to TV cells as a replacement to GABAergic Golgi-stellate and cartwheel cells, with similar Type I/III EIRA properties.

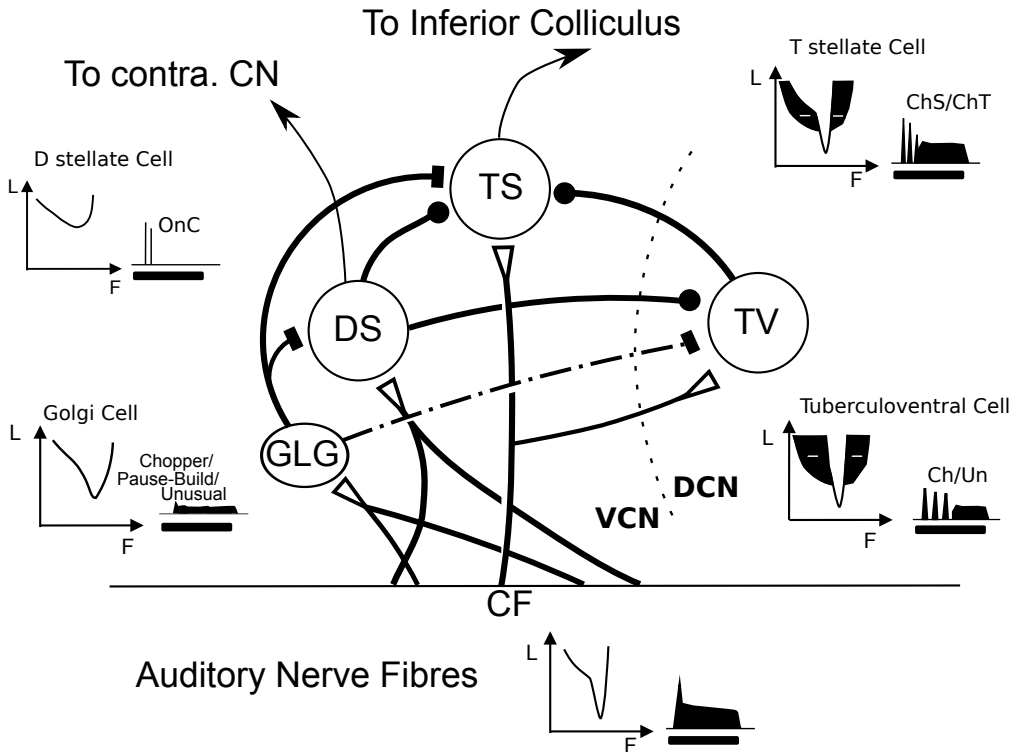


Figure 3.1: Cochlear nucleus stellate microcircuit (CNSM) model showing synaptic connections between cell-types in one iso-frequency channel. LSR and HSR ANFs are represented by the one line to TS and TV cells and as a fan of connections (from fibres in adjacent channels) for connections to GLG and DS cells. GLG cell connections to TV cells replicate GABA inputs to TV cells from local Type I/III DCN units. Synaptic types: unfilled triangle = excitatory glutamatergic synapse with AMPA receptors; filled circle = inhibitory glycinergic synapse with GlyR receptors; filled rectangle = inhibitory GABAergic synapse with GABA_A receptors.

Input parameters to TS cells, which receive inputs from all other cell types in the CNSM model, are optimised last.

Due to the variety of possible inputs to TS cells (and the observed physiological classification sub-types in chopper units), three TS cell model sub-types were optimised. Glycinergic input to DS cells from TV cells and other DS cells was not included due to its weak effects *in vitro* (Ferragamo et al. 1998b) and the added complexity of a negative feedback loop in the microcircuit. Recurrent synaptic connections between TS cells have been the focus of other CN models (Bahmer and Langner 2006a,b; Wiegrefe and Meddis 2004). They were not included in the CNSM model because of the rarity of small round vesicles on sustained chopper (ChS) units (Smith and Rhode 1989). Additionally, Ferragamo et al. (1998b) reported that excitatory post-synaptic potentials (EP-

SPs) in one TS cell were likely to come from only one input. Given the weak influence of TS cell recurrent connections, they were also not included in the CNSM model.

3.2 Methods

This section describes the specific methods used in this chapter.

3.2.1 Auditory Nerve Fibre Model

As discussed in Section 2.1.3, the ANF inputs to the CNSM model neurons were drawn from the Carney auditory nerve (AN) model (Carney 1993), a phenomenological auditory periphery model. This chapter uses more recent derivations of the Carney model: the Bruce model (Bruce et al. 2003; Zilany and Bruce 2006, 2007) and the Zilany model (Zilany et al. 2009).

The neural models used in the ANFs and Golgi cell model were inhomogeneous Poisson processes. The instantaneous rate produced the input AN model (chosen from the Bruce or Zilany model) and was passed through the Jackson spiking model (Jackson 2003; Jackson and Carney 2005), which includes refractory effects typical of ANFs. The fractional Gaussian noise component in the IHC synapse (Zilany et al. 2009) was removed to obtain fixed spontaneous rates for HSR and LSR ANFs. Spike trains for each neuron in the AN model were created at the start of each repetition of the stimulus.

3.2.2 Neural Models

Single-compartment Hodgkin-Huxley (HH)-like neural models were used for the DS, TV and TS cells in the CNSM model. The Rothman and Manis (RM) neural model is a conductance-based neural model with membrane current models developed by Rothman and Manis (2003c). The CNSM model makes extensive use of the RM neural model, which was discussed in detail in Section 2.2.

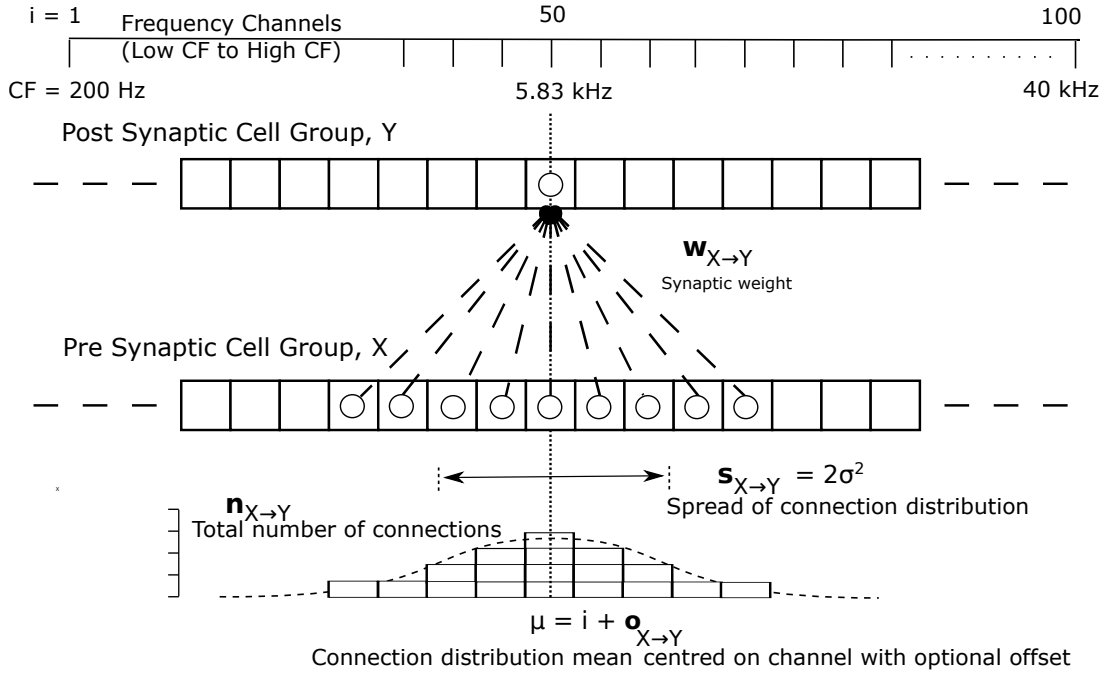


Figure 3.2: Gaussian connection between cell types in the CNSM model.

3.2.3 Connectivity and Network Parameters

Tonotopic connectivity in the CNSM model was defined by the regular organisation of afferent ANFs into distinct isofrequency channels. The channels were separated using even spatial distance (based on the basilar membrane frequency sensitivity) with centre frequency calculated by the Greenwood function for the cat (see Chapter 2, Greenwood 1990). The HSR ANF terminals of individual fibres generally cover 70 μm and LSR fibres cover 100 μm in mice (Oertel and Wu 1989; Oertel et al. 1988).

Figure 3.2 shows the Gaussian distribution of connections between cell types in the CN. The CFs of the CN channels were separated using the same Greenwood function used for the filterbank of AN frequency channels.

3.2.4 Synapse Models

The synaptic models for AMPA, GlyR and GABA_A receptors were described in Section 2.3.2. The synapses act by changing the conductivity at a single point in the neural compartment with either single or double exponential dynamics. All weight variables

(in microsiemens) and delay parameters (in milliseconds) are the same for each synapse in a connectivity group.

3.2.5 Synaptic Jitter

Precise onset cues are a critical feature of the auditory pathway, especially for the localisation of sounds. In modeling the CN, onset precision is essential for enhancing periodic stimuli in TS cells (Keilson et al. 1997) and echo-suppression in TV cells (Burck and van Hemmen 2007; Wickesberg and Oertel 1990). Stochastic behaviour at the inner hair cell (IHC)-AN synapse limits the onset encoding performance in the AN. Jitter of the first spike latency (FSL) is commonly measured by the standard deviation; jitter in ANFs is 0.73 msec (Rhode et al. 1983a). Most units in the VCN exhibit reduced onset jitter through sampling multiple ANFs, but onset units like DS cells have additional morphological and intrinsic specialisations for greater onset precision.

A random jitter was introduced to the AN synaptic delay to account for ANF variation and synapses placed at various distances along the dendrites of TS, DS and TV cells. Figure 3.3 shows the effects of jitter on the intracellular responses of a Type I-t RM neural model (Rothman and Manis 2003c), averaged over 25 repetitions. Jitter was added separately to each ANF synapse using an absolute Gaussian distribution random number with standard deviation of 0.1 msec and mean dependent on the cell type (e.g. $d_{\text{ANF} \rightarrow \text{TS}}$). The effect of adding jitter to individual ANF synapses in the CNSM model was to increase the mean and standard deviation of FSL in CN neurons. These effects replicated dendritic delays without the added computational cost of a passive neural compartment in the model. The models did not account for dendritic attenuation of the EPSP.

3.2.6 Synaptic Delay Additional Parameter

The effective delay of the AN model does not take into account the conduction and synaptic transmission delay in reaching post-synaptic neurons in the CNSM model. Accordingly, an additional delay component was required in each of the synaptic connections in the CNSM model involving ANFs. Mean FSL to short CF tones and click

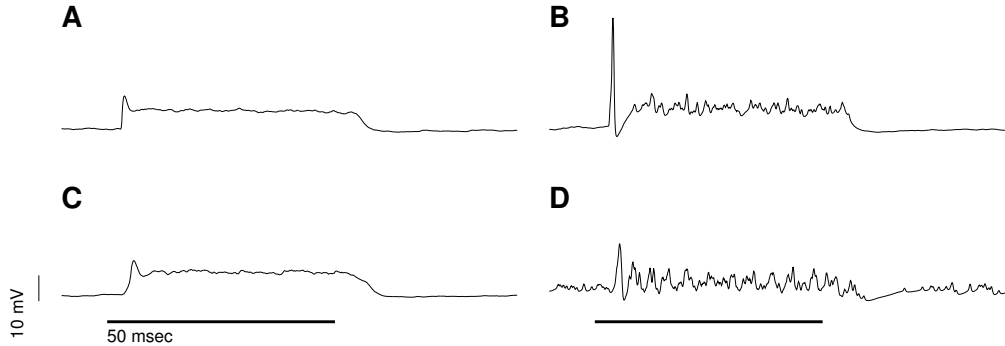


Figure 3.3: Intracellular membrane voltage response of a TS cell model (Type I-t RM model) to isolated synaptic inputs with variable delays. A jitter around a minimum delay $d_{\text{ANF} \rightarrow \text{TS}}$ was calculated as an absolute Gaussian distribution with zero mean and standard deviation of 0.1 msec. A pure tone stimulus of 8.2 kHz at 85 dB SPL was presented to the CNSM model. Jitter responses were averaged over 25 repetitions. All weights were set to 0.5 nS. Twenty HSR and 30 LSR ANFs connected with the recorded TS cell model. A. No jitter in ANF synapses on TS cell without the sodium channel. B. No ANF jitter on TS cell with sodium channel active. C. TS cell with jitter and without the sodium channel. D. TS cell with jitter and with the sodium channel.

stimuli was used to set delay times between ANFs and CN cells (Ferragamo et al. 1998b; Rhode and Smith 1986; Rhode et al. 1983a; Spirou et al. 1999). The additional delay was defined using the FSL of high frequency units as the sum of the ANFs' FSL, ANF conduction delay and the synaptic transmission delay. The first spike latency measured in high CF units in the ARLO AN model (Heinz et al. 2001) for HSR fibres was 1.5 msec.

Table 3.1 shows the additional delay component for each cell type, calculated from population statistics, to ensure the first spike latency in the models matched the experimental data. The models were derived from the basic RM neural models (Rothman and Manis 2003c). The relative difference between the DS cell model's mean FSL and the other Type I cell types can be attributed to the additional I_{KLT} channels in the Type I-II RM neural model. I_{KLT} is active at resting membrane potential (RMP) and decreases the overall input resistance and membrane time constant, reducing the time to fire an action potential. TS cells were designed with the Type I-t RM model, which contains an additional I_{KA} channel current over the Type I-c RM model, but were not significantly different from the classic Type I RM models in the TV cell model.

Table 3.1: Additional delay component of ANF to CN cell types

	ANF	TS	DS	TV	Golgi
RM cell type		I-t	I-II	I-c	I-c
Experimental FSL (msec)	2.4 0.73 ¹	± 0.36 ¹	3.6 0.09 ^{1,2}	2.8 4.0 ³	4.3 ⁴
Default model FSL (msec)	1.5	2.0	1.6	2.0	2.0
Additional delay (msec)	-	1.6	1.2	2.0	2.3

¹Rhode and Smith (1986), ²Rhode et al. (1983a), ³Spirou et al. (1999), ⁴Ghoshal and Kim (1997)

3.2.7 Simulation Specifications

All simulations were performed in the neural simulation package NEURON. The time step of the numerical integration performed in each of the simulations in this chapter was 0.05 msec. Input spikes for Poisson neural models (HSR and LSR ANFs, and GLG cell models) were calculated at the start of repetitions.

3.2.8 Optimisation Routine

The optimisation routine used in this chapter was NEURON's fit_praxis function, which uses the principal axis algorithm (PRAXIS, Brent 1976). The PRAXIS method returns the minimum of the fitness function of n variables using the principal axis method without using the function's gradient. The fitness function converts the parameters to a single measure by simulating the CNSM model using the parameters, then comparing selected neural outputs to experimental data. Root mean squared (RMS) error was used as the comparison measure of similar data points, e.g.

space mean firing rate at different sound levels in a rate-level simulation. The equation for RMS error in a rate level response is

$$\sqrt{\frac{1}{N} \sum_{n=1}^N (r(n) - r^*(n))^2}, \quad (3.1)$$

where N is the number of data points, $r(n)$ is the rate response of the model unit at a particular level, and $r^*(n)$ is the rate response of the target unit. The units for RMS error are dependant on the data points; for rate level cost functions, the RMS the unit is spikes per second. Mean absolute relative (MAR) error was also used to ensure there

was no bias between data points with large variation in magnitude. The equation for MAR error using rate level responses is

$$\frac{1}{N} \sum_{n=1}^N \left(\frac{|r(n) - r^*(n)|}{r^*(n)} \right). \quad (3.2)$$

3.2.9 Verification of Cell Model Responses to Simple Tones and Noise

To verify the optimisation processes, a suite of tests was run across the whole CNSM model. The purpose of these simulations was to ensure the optimised parameters could be used across all frequency channels. These simulations show the response of a CNSM model neuron at the centre of the network to tones corresponding to its CF, broadband noise and a combination of tones and noise. Responses of all model neurons across the network (one cell type for each frequency channel) were recorded during the verification procedure. The stimuli presented to the CNSM model included:

1. Rate-level response to short pure tone bursts at the frequency matching the CF at the centre channel of the network, 4.31 kHz. The sound level was varied from 0 to 90 dB sound pressure level (SPL).
2. Rate-level response to white noise at levels 0 to 100 dB SPL.

Figure 3.4 shows the output of the HSR and LSR ANFs in the CNSM model to the verification stimuli (modified~ Zilany and Carney 2010, AN model). The V-shaped tuning of the HSR ANFs to pure tone bursts (Figure 3.4A) has no inhibitory areas and is classified in EIRA as Type I. The equivalent Q_{10} , bandwidth measured in individual units at 10 dB above threshold, can be measured across different units. The HSR units were active over 4 channels (CF range of 880 Hz) around the central unit (CF 4.513 kHz) at 20 dB SPL (threshold at 10 dB SPL) and the equivalent Q_{10} was 0.195 octaves. The noise response area of the HSR ANFs is shown in Figure 3.4B. The HSR unit's on-CF rate level response in Figure 3.4C has a spontaneous rate (SR) = 45 sp/s, a Dynamic range (DR) between 25 and 30 dB and a maximum rate of 233.2 sp/s at 65 dB SPL. The maximum rate of the LSR ANF was 77.1 sp/s and an acoustic threshold at 25 dB SPL. The noise rate level of the central unit (Figure 3.4D) had a higher threshold at 25 dB SPL

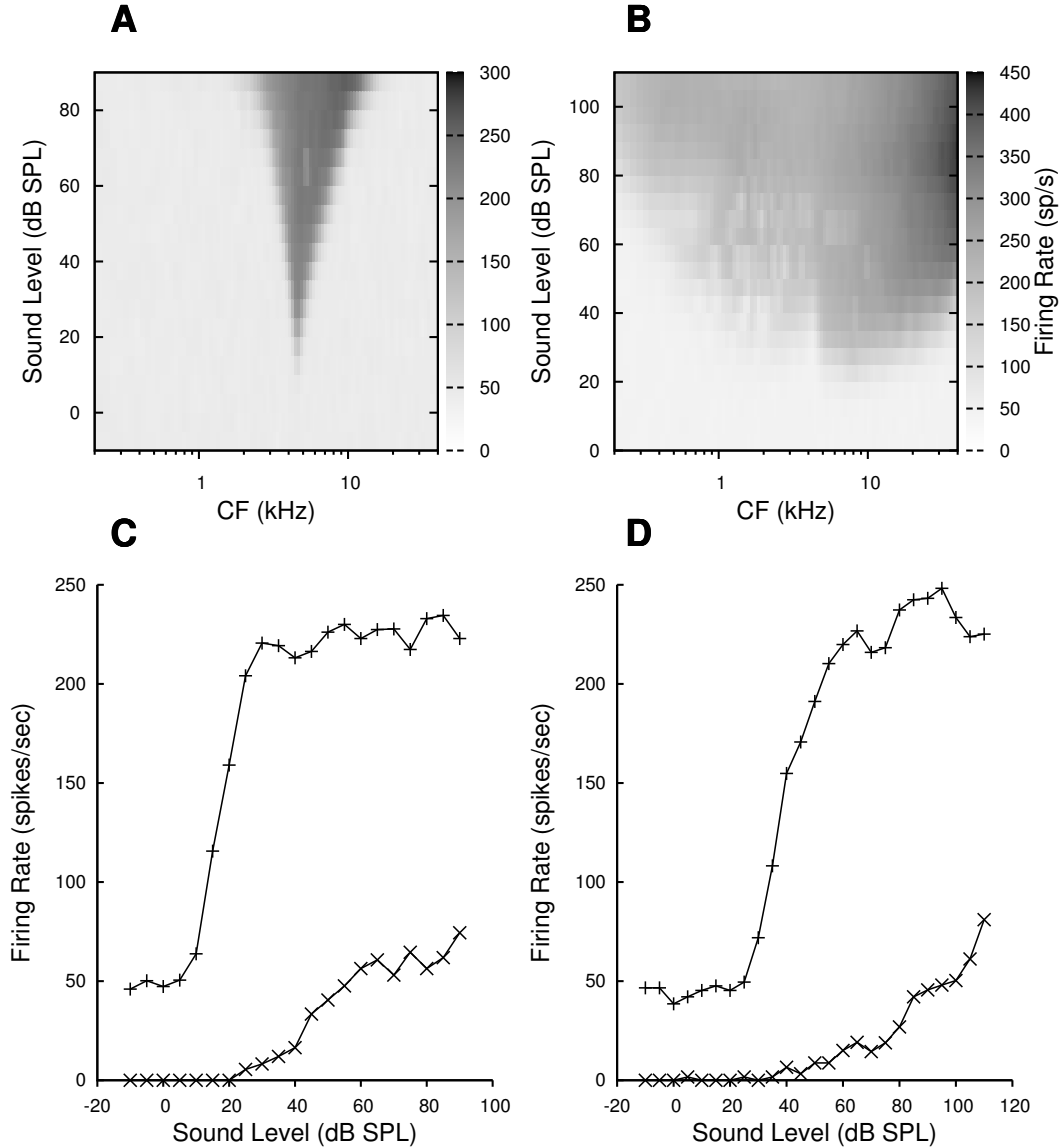


Figure 3.4: Response of ANF models across the whole network to pure tone at centre of network and broad-band noise (BBN). A. Rate level response map of the HSR ANFs to a pure tone burst (4.31 kHz, 50 msec, 100 repetitions). B. Noise rate level response map of the HSR ANFs to a short BBN burst (frozen noise, 50 msec, 100 repetitions). C. Rate level responses of the central HSR and LSR units to pure CF tone bursts (CF 4.31 kHz, 50 msec, 100 repetitions). D. Noise rate level response of the central HSR and LSR units to BBN bursts (CF 4.31kHz, 50 msec, 100 repetitions).

and two stages of dynamic range firing rate increase before a maximum rate of 243.5 sp/s at 90 dB SPL. The LSR unit's noise rate level was monotonic with a maximum rate of 76.6 sp/s at 110 dB SPL.

3.3 Golgi Cell Model

The next part of this chapter introduces the specific attributes of the GLG cell model used in the CNSM model. It then reports on the optimisation of the model parameters based on rate level information.

3.3.1 Background

3.3.1.1 Morphology of Golgi Cells

GLG cells are distinguishable from the numerous smaller granule cells in the GCD by their larger cell body and surrounding plexus of dendritic and axonal neurites. The soma diameter of GLG cells is approximately 15 μm (Ferragamo et al. 1998a), while the diameter of granule cells is 8 μm in cats (Mugnaini et al. 1980) and 6 μm in rats and mice (Alibardi 2003a; Mugnaini et al. 1980). Smooth, tapering dendrites, between 50 and 100 μm long, emanate in all directions (Cant 1993; Ferragamo et al. 1998a; Mugnaini et al. 1980). A dense, axonal plexus, limited to the plane of the GCD, extends approximately 250 μm from the soma in all directions (Benson and Brown 2004; Ferragamo et al. 1998a).

The dendrites of VCN GLG cells are mitochondria-rich and make glomeruli complexes with long synaptic junctions, with mossy fibre boutons (Mugnaini et al. 1980). The somata generally have few boutons of the flat or pleomorphic vesicle type that are characteristic of glycinergic and GABAergic terminals. Along with inhibitory boutons, the dendrites also receive excitatory input with large (Type I ANF) and small (Type II ANF and granule cell) vesicles (Ferragamo et al. 1998a; Mugnaini et al. 1980; Ryugo 2008).

The contribution of the circuits of granule cell areas of the CN to the processing of the acoustic signal is poorly understood (for a review of non-auditory inputs to the GCD see Ohlrogge et al. 2001). Ferragamo et al. (1998a) confirmed the excitation of Golgi cells from granule cells with NMDA glutamatergic synapses.

3.3.1.2 Cellular Mechanisms of Golgi Cells

In a single study in mice, intracellular recordings of GLG cells showed a classic repetitively-firing response to current clamp and an inward rectifying response to voltage clamp (Ferragamo et al. 1998a). GLG cells are classified as Type I current-clamp neurons and act as simple integrators of synaptic input (Ferragamo et al. 1998a). Responses to AN shocks in GLG cells were found to be delayed by approximately 0.7 msec relative to the core VCN units, with minimum delay in most cells around 1.3 msec (Ferragamo et al. 1998a).

3.3.1.3 Acoustic Response of Golgi cells

Extracellular recordings from labelled GLG cells are not available in the literature; however, electrophysiological studies of the GCD (or marginal shell of the VCN in cats) have been done without direct labelling of recorded units (Ghoshal 1997; Ghoshal and Kim 1996a,b, 1997). Any extracellular spikes recorded in the GCD are most likely from Golgi cells since granule cell somata are less than $10 \mu\text{m}$ and their narrow axons are unlikely to elicit electrical activity in the electrodes (Ferragamo et al. 1998a; Ghoshal and Kim 1997).

Figure 3.5 shows an example of the acoustically-driven marginal shell units in the VCN. Strongly driven units in the anterior VCN shell exhibit non-saturating rate-level functions to pure tones, noise or both with dynamic ranges as wide as 89 dB (Ghoshal and Kim 1997). The majority of GCD units recorded by Ghoshal and Kim (1997) were classified as Type I/ III or III EIRA units, showing a monotonic increase in firing rate to tones and noise. One unit was classified as Type II due to its poor response to noise but it did not show a reduction of response to tones at high SPL, typical of DCN Type II units (Ghoshal and Kim 1997). Two units with low CF ($< 1.5 \text{ kHz}$) were classified as Type II (Ghoshal and Kim 1997). The PSTH of the units included wide chopper, On_C, and pause-build; however, nearly one third of units did not fit into the known classifications and were called “unusual” (Ghoshal and Kim 1997).

The latency of acoustically driven GCD recorded units ranges from 2.4 msec to over 10 msec, with a mean of 3.75 msec. The acoustic latency closely matches the minimum

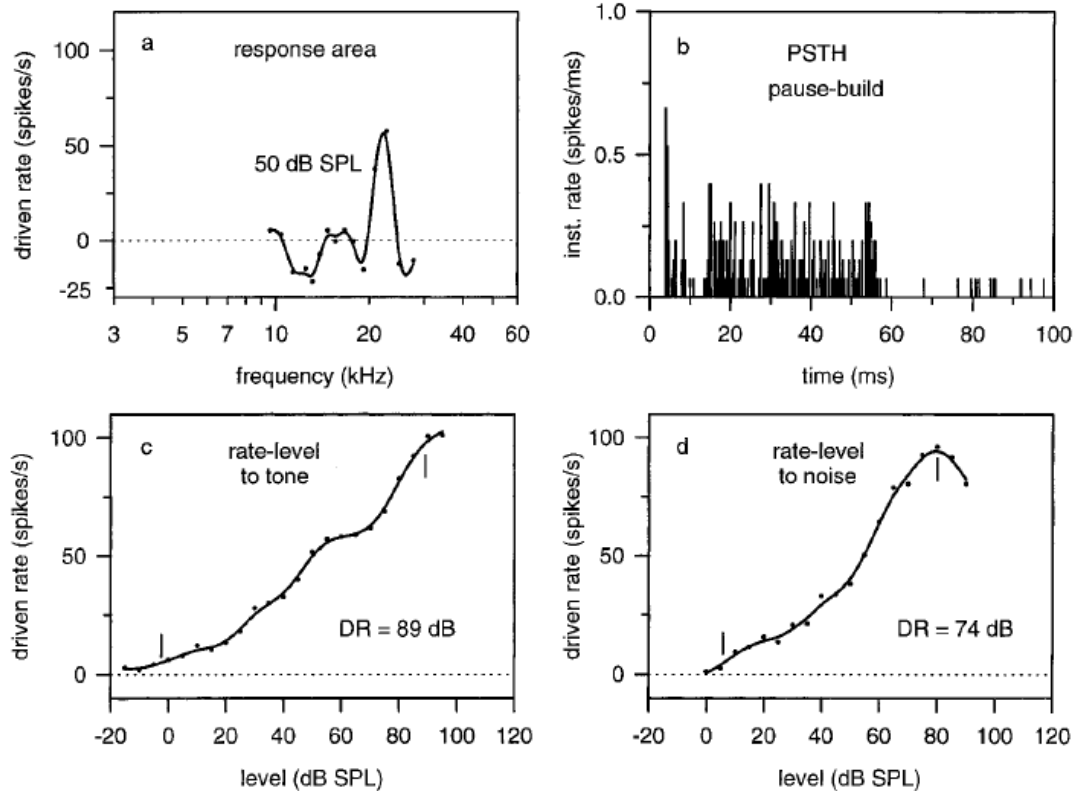


Figure 3.5: Marginal shell neuron (Unit S03-07, CF 22.7 kHz, Ghoshal and Kim 1997) with monotonic rate-level response to pure BF tones and broad-band noise. This unit was chosen as the exemplar GLG cell for optimisation purposes. Figure reproduced from Ghoshal and Kim 1997.

latency of EPSPs to AN shocks recorded in mice *in vitro* preparations (1.3 msec, Ferragamo et al. 1998a). EPSPs with longer latencies may be due to Type II ANFs, which have an estimated theoretical latency of 10 msec (Brown 1993), or from polysynaptic excitation by granule cells.

The assumed functional role of GLG cells is to regulate granule cells. They may also provide automatic gain control to the principal VCN units, primarily DS and TS cells (Ferragamo et al. 1998b; Ghoshal and Kim 1997). The presence of GABAergic inputs to VCN and DCN neurons has been verified by labeled terminals adjacent to the soma and dendrites (Awatramani et al. 2005; Babalian et al. 2003; Smith and Rhode 1989) and release from inhibition in their response areas with iontopopheretic application of the GABA_A antagonist, bicuculline (Backoff et al. 1999; Caspary et al. 1994; Evans and Zhao 1998; Ferragamo et al. 1998b). The source of GABAergic inputs to cells in

the mammalian CN is somewhat contentious. Studies show that GABAergic inputs to the CN generally arise in the peri-olivary regions of the medulla in cats (Ostapoff et al. 1997) and birds (Lachica et al. 1995; Yang et al. 1999). Slice preparations of the isolated murine VCN show strong and immediate sensitivity to bicuculline in TS and DS cells from a source within the CN complex (Ferragamo et al. 1998b). The only known source of GABA intrinsic to the VCN is the GLG cells of the GCD overlying the VCN (Ferragamo et al. 1998a; Mugnaini 1985).

Inputs to GLG cells are more complicated than the inputs to core VCN neurons. GLG cells are sparse in the GCD, surrounded by the many smaller excitatory granule cells that form small en-passant endings. Type II ANFs create diffuse glutamatergic release sites in the GCD (Benson and Brown 2004; Hurd et al. 1999) that may stimulate NMDA glutamate receptors in GLG cells (Ferragamo et al. 1998b).

3.3.2 Implementation

The key cell attributes that informed the creation of the GLG cell model for use in the CNSM model were as follows:

1. GLG cells are classic integrator neurons, as shown by their Type I current clamp response (Ferragamo et al. 1998a).
2. The minimum EPSP in GLG cells to an electric shock of the AN (Ferragamo et al. 1998a) and mean first spike latency to acoustic stimuli (Ghoshal and Kim 1997) are significantly different from the core VCN units.
3. GLG cells have a low maximum rate and large dynamic range to tone and noise stimuli (Ghoshal and Kim 1997).
4. The low threshold in GLG cells cannot be solely due to LSR fibre inputs that have high thresholds (Ghoshal and Kim 1997). This suggests medium and high spontaneous rate Type I or Type II ANFs (that project to the GCD) may provide weak inputs to GLG cells. The lack of extensive experimental data regarding Type II ANF units and granule cell response to acoustic input, reward an inhomogeneous Poisson rate neural model over the Hodgkin-Huxley type neural model in the GLG

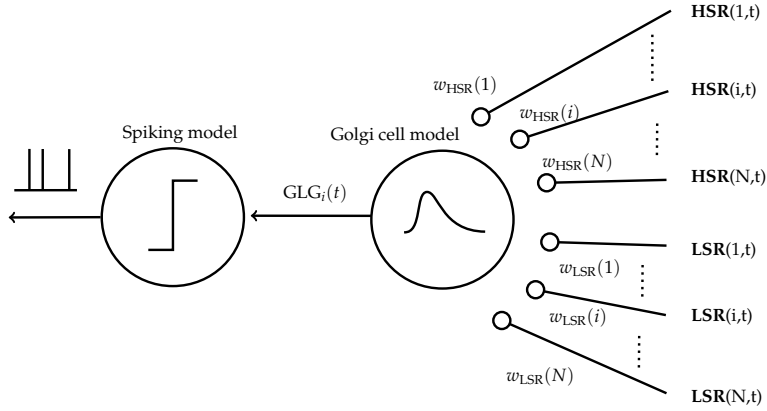


Figure 3.6: The GLG cell model’s instantaneous-rate profile was generated using a weighted sum of ANF profiles. The Gaussian spread of connections is independent for HSR and LSR auditory filters, with the mean equal to the CF channel of the unit. An alpha function smoothing kernel was used to mimic dendritic and synaptic filtering.

cell used in the CNSM model. Although HSR ANF terminals do not generally project into the GCD, they were included in the CNSM model to provide some low level spontaneous activity.

The GLG cell model was implemented as an instantaneous-rate Poisson rate model, as shown in Table 3.2D and in Figure 3.6. The primary inputs were from the HSR and LSR ANF models’ instantaneous rate outputs with connections across frequency channels. The strength of HSR and LSR ANF inputs to GLG cells was determined by a Gaussian distribution in units of channel separation in the network. The weight vectors, $\mathbf{w}_{\text{HSR} \rightarrow \text{GLG}}$ and $\mathbf{w}_{\text{LSR} \rightarrow \text{GLG}}$, span the CNSM model’s channels with size N_{channels} , with a normal curve centred on the position in the channel and variance $s_{\text{ANF} \rightarrow \text{GLG}}$. For example, for LSR inputs to GLG cells, at position i in the frequency channels, the weight vector was modified by the weight parameter $w_{\text{LSR} \rightarrow \text{GLG}}$, and the spread parameter $s_{\text{LSR} \rightarrow \text{GLG}}$, which is the variance in a standard Gaussian function

$$\mathbf{w}_{\text{LSR} \rightarrow \text{GLG}}(i, x) = w_{\text{LSR} \rightarrow \text{GLG}} \frac{1}{\sqrt{2 \pi s_{\text{LSR} \rightarrow \text{GLG}}}} \exp \left(\frac{-(x - i)^2}{2 s_{\text{LSR} \rightarrow \text{GLG}}} \right), \quad (3.3)$$

where $x = 1, \dots, N_{\text{channels}}$.

The intermediate step in the GLG cell model, $g_i(t)$, combines the weighted sum of HSR and LSR instantaneous-rate and corrects the output rate for the desired sponta-

neous activity, SR_{GLG} , and is given by

$$g_i(t) = \sum_{j=1}^{N_{\text{channels}}} \mathbf{w}_{\text{LSR} \rightarrow \text{GLG}}(j) \text{LSR}_j(t) + \mathbf{w}_{\text{HSR} \rightarrow \text{GLG}}(j) \text{HSR}_j(t) - \text{SR}_{\text{GLG}}. \quad (3.4)$$

The length of the instantaneous rate profiles of HSR and LSR models (and consequently GLG models) was determined by the stimulus duration and sampling rate ($N_{\text{stim}} = \text{stimulus duration} / \text{sampling rate}$). Profiles were calculated for each channel in the network (size= N_{channels}) and stored for use during repeated simulations.

The weighted sum of HSR and LSR instantaneous-rate vectors was convolved with a smoothing kernel, mimicking synaptic and dendritic properties of the GLG cell model. The smoothing kernel is an alpha function, $\alpha_{\text{GLG}}(t)$, given by

$$\alpha_{\text{GLG}}(t) = t \exp\left(\frac{-t}{\tau_{\text{GLG}}}\right), \quad t \geq 0. \quad (3.5)$$

The smoothing kernel was normalised by setting the area under the function to 1. For a large enough filter length, the alpha function integral

$$\int_0^\infty \alpha(t) dt = (-\tau_{\text{GLG}}^2 - t \tau_{\text{GLG}}) \exp\left(-\frac{t}{\tau_{\text{GLG}}}\right) \quad (3.6)$$

equals τ_{GLG}^2 as t approaches infinity. The convolution of the weighted inputs, g with normalised smoothing kernel, used a discrete convolution method and was cropped to the length of the input stimulus,

$$\text{GLG}_i(t) = \sum_{u=0}^{u=N_\alpha} \frac{1}{\tau_{\text{GLG}}^2} \alpha_{\text{GLG}}(u) g_i(t-u), \quad (3.7)$$

where $N_\alpha = 10 \Delta t \tau_{\text{GLG}}$ is the length of the smoothing kernel and $\Delta t = 0.05$ is the time step of the ANF input rate vectors. The inhomogenous Poisson spiking model with refractory effects (as used for the ANF models (Jackson 2004)) was used to generate the output spike times for the GLG cell model.

Table 3.2 summarises the model used to optimise the GLG cell model. The topology of the VCN follows the same tonotopic organisation of the AN, with 100 evenly-spaced

Table 3.2: Golgi cell model summary

A Model Summary	
Populations	ANF (HSR, LSR) and Golgi (GLG) cells
Topology	Tonotopic - 100 frequency channels (0.2–40 kHz); cat model; Greenwood function centre frequencies (Greenwood 1990)
Connectivity	ANF to GLG filter inputs, Gaussian spread centred on channel
Input model	ANF model: Version 4 and 5 Zilany model (Zilany and Bruce 2007; Zilany et al. 2009)
Neuron model	GLG cell model: Instantaneous-rate Poisson neuron model
Synapse model	Synapto-dendritic smoothing filter (alpha function)

B Populations		
Name	Elements	Number
HSR	ANF model (Zilany and Bruce 2007; Zilany et al. 2009)	Rate models only, 1 per channel
LSR	ANF model (Zilany and Bruce 2007; Zilany et al. 2009)	Rate models only, 1 per channel
GLG	Instantaneous-rate Poisson neuron model	1 unit (CF 22.7 kHz, channel 76)

C Connectivity			
Name	Source	Target	Pattern
ANF→GLG	HSR	GLG	Gaussian spatial convergence, centred on CF, spread parameter ($s_{\text{HSR} \rightarrow \text{GLG}} = 2$). Weight ($w_{\text{HSR} \rightarrow \text{GLG}}$) to be optimised.
	LSR	GLG	Gaussian spatial convergence, centred on CF. Spread ($s_{\text{LSR} \rightarrow \text{GLG}}$) and weight ($w_{\text{LSR} \rightarrow \text{GLG}}$) to be optimised.

D Neuron and Synapse Model	
Name	Golgi cell model
Type	Instantaneous-rate Poisson neural model
Model Dynamics	See Figure 3.6 and the GLG rate filter model Equations 3.3–3.7.
Spiking	Renewal Poisson process given instantaneous rate, $\text{GLG}_i(t)$, with refractory effects (Jackson 2003; Zilany and Bruce 2007)

E Optimisation	
Input Stimulus	Rate Level function, 22.7 kHz tone at SPL -15 to 90 dB (50 msec duration, 2 msec cosine squared on/off ramp, 20 msec delay)
Parameters	$s_{\text{ANF} \rightarrow \text{GLG}}$, τ_{GLG} , $w_{\text{HSR} \rightarrow \text{GLG}}$, $w_{\text{LSR} \rightarrow \text{GLG}}$, SR_{GLG}
Fitness function	RMS squared error between rate-level functions of Golgi model (channel 76, CF=22.7 kHz) and unit S03-07 (CF=21 kHz) from Ghoshal and Kim (1996a). Mean rate of Golgi model spikes sampled from 25 repetitions.

frequency channels. As Table 3.2B shows, the ANFs were not required because only the instantaneous profile of each AN frequency channel was used in the GLG cell model. In the CNSM model, the connectivity between ANFs and GLG cells (Table 3.2C) was a simple place-based Gaussian spread (as explained in Section 2.3).

The experimental data used to optimise the GLG cell model was the rate level response of the marginal shell unit shown in Figure 3.5. This unit was chosen due to its monotonic response to pure best frequency (BF) tones and its moderate maximal firing rate (100 spikes per second). The closest frequency channel to the experimental unit's CF (21 kHz) was used for the GLG cell model (channel 76, CF 22.7 kHz). The fitness function for the GLG cell model optimisation used 22.7 kHz pure tones at 22 sound levels to compare the experimental and model units. The GLG cell model parameters used in the optimisation are shown in Table 3.2E.

3.3.3 Optimisation Results

Figure 3.7 shows the rate-level output of the GLG cell model with its optimal combination of parameters as shown in Table 3.2E. Twenty two sound levels from -15 dB SPL to 90 dB SPL were used in the fitness function to compare the GLG cell model (CF 22.7 kHz) with the experimental unit S03-07 (CF 21 kHz, Ghoshal and Kim 1996b) representing the target response. The mean firing rate, generated from 25 repetitions at each level, was used in the fitness function to produce a square root of the mean squared difference between the model response and the target response. The optimal parameters of the GLG cell model had a fitness score of 4.48 spikes per second using the RMS error. A normalised metric that takes into account the different firing rate magnitudes at each sound level relative to the target response showed a MAR error of 21.5%. The discrepancies at low SPL contributed the most to the MAR error despite a reasonably good fit by observation.

The parameters in Table 3.3 were within the range of expected values. LSR inputs to the GLG cell model outweighed HSR inputs by a factor greater than 10. The monotonic response of LSR fibres at high sound levels was necessary to create the large dynamic range in the GLG cell model. Equally, the HSR fibres were necessary to provide spon-

Table 3.3: Best-fit parameters of the Golgi cell model optimisation

Parameters (Units)	Range	Best Values
$s_{\text{ANF} \rightarrow \text{GLG}}$ (channel)	[0,10]	2.48
τ_{GLG} (msec)	[0,20]	5.01
$w_{\text{LSR} \rightarrow \text{GLG}}$ (μS)	[0,5]	0.517
$w_{\text{HSR} \rightarrow \text{GLG}}$ (μS)	[0,5]	0.0487
SR_{GLG} (spikes/s)	[0,50]	3.73

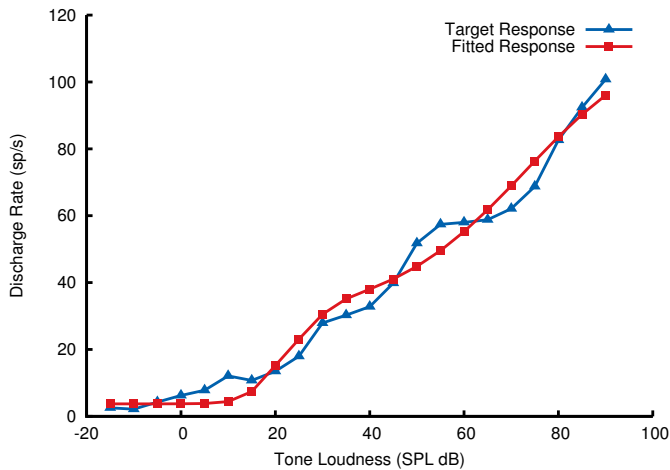


Figure 3.7: GLG cell model optimisation result trials against unit S03-07 (CF 21 kHz) from Ghoshal and Kim (1996b). Root mean squared error over 22 sound levels between the target and fitted response curves was 4.48 spikes/s.

taneous rate activity at low SPL. The spontaneous rate parameter matches the base response of unit S03-07 in Figure 3.7. The smoothing filter time constant of 5 msec is a typical value in membrane time constants for neural models and fits with the input resistance in intracellular recordings of GLG cells (Ferragamo et al. 1998a).

The input spread parameter was not well constrained by the optimisation fitness routine with a pure tone input and a single neuron, but the result was satisfactory given the uncertainty in LSR fibres' axonal organisation in the GCD. The dendritic widths in GLG cells are around 100 μm and the frequency separation laminae in the VCN core are approximately 70 μm , giving an expected spread of 1.5 channels in the 100 channel CNSM model. Consequently, the optimal spread parameter of 2.48 channels in the GLG cell model allowed added frequency spread from LSR fibres in the CNSM model.

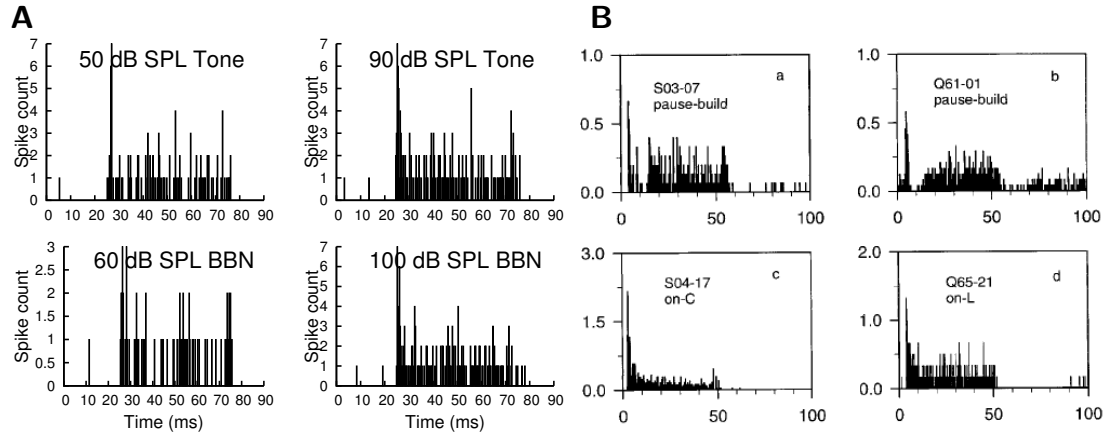


Figure 3.8: Response of optimised GLG cell model at the centre of the network (CF 5.8 kHz). A. Four simulated PSTHs of the GLG cell model to tones at 50 and 90 dB SPL and broadband noise (BBN) at 60 and 100 dB SPL (50 msec duration, 20 msec delay). B. Four experimental PSTHs from marginal shell units (from Figure 12, Ghoshal and Kim 1996b).

3.3.4 Verification of the Golgi Cell Model

After setting the optimised parameters in Table 3.3, the GLG cell model was run with tone and noise inputs to determine its behaviour to a battery of tests. The GLG cell model was tested across the entire CNSM model network, using tones, noise, and tones plus noise stimuli. Figure 3.8 shows a comparison of PSTHs to tone bursts between the optimised GLG cell model and recorded marginal shell units. The PSTH of the GLG cell model was classified as unusual and did contain the prominent onset responses of the recorded units. The merging of LSR profiles at different CFs and the convolution of the smoothing filter was thought to contribute to the reduction of the onset response to tones and noise, but the results show a prominent onset response in the GLG cell model.

Figure 3.9 shows the tone and noise rate level responses of six marginal shell units observed by Ghoshal and Kim (1996b). The unit at the top of Figure 3.9, S03-07 (CF 22.7 kHz), was chosen to optimise the GLG cell model as it is monotonic and has the median maximum rate of all the units shown (101 sp/s for tones and 96 sp/s for BBN). The typical properties of GLG units were derived from the marginal shell units recorded in the Ghoshal and Kim (1996b) study.

Figure 3.10 shows the response of optimised GLG cell models at each frequency

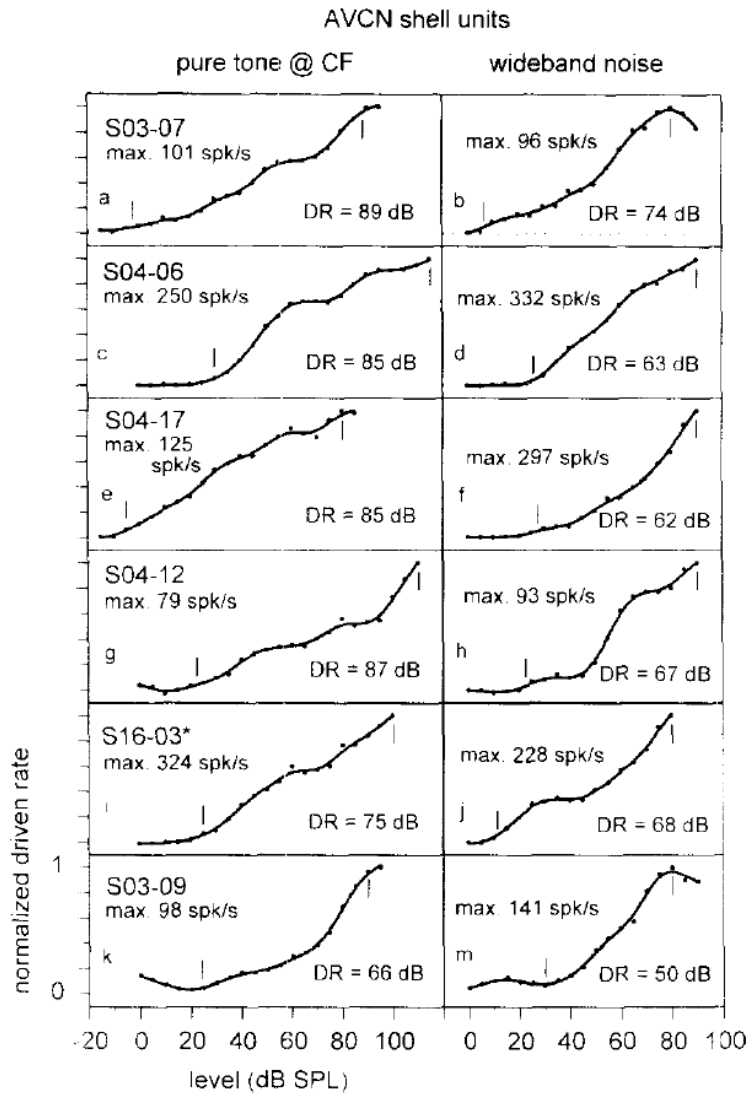


Figure 3.9: Rate level response of 6 AVCN marginal shell units (Figure reproduced from Ghoshal and Kim 1996b).

channel in the CNSM model to a 4.31 kHz tone and broadband noise over a wide range of sound levels. The GLG cell model had a monotonic response to tones and noise similar to other experimental units (Ghoshal and Kim 1996a,b, 1997). Figure 3.10A shows the response of all GLG cell units in the CNSM model to a 5.8 kHz tone. At 10 dB above the threshold (30 dB SPL) units with CFs from 4.98 kHz to 7.48 kHz were above threshold, which equates to a receptive field of 2.5 kHz or Q_{10} of 0.41. The GLG unit with CF 6.43 kHz had the highest rate at 30 dB SPL and was closest to the middle of activated units in the network. The range of activated units was 4.6 kHz at 50 dB SPL (30

dB relative to the acoustic threshold) and 10 kHz for 80 dB SPL. Figure 3.10C shows the rate level response of the central GLG unit generated using the optimised parameters. Using a sigmoidal function, the rate level curve had a theoretical spontaneous rate of 0 spikes/s (3.77 spikes/s calculated from 0 to 15 dB SPL), a threshold at 19 dB SPL, and a dynamic range of 68 dB. The theoretical maximal rate for the curve was 120.8 spikes/s and reached half maximum rate at 53 dB SPL. Figure 3.10B shows the noise rate level response of all GLG units. The non-uniform response to a linear broadband input reflects the species-specific audiogram compression in the AN model. The noise rate-level curve for the central GLG unit in Figure 3.10D was monotonic. The average gradient of the noise rate level curve between 70 and 120 dB SPL was 2.02 spikes per second per dB.

3.3.5 Discussion of the Golgi Cell Model

The GLG cell model reproduces the monotonic rate-level response observed in experimental data of a single unit in the marginal shell of the VCN (Ghoshal and Kim 1997) to a high degree of accuracy. Moderately-driven, monotonic behaviour was found in a majority of recorded units *in vivo* (Ghoshal and Kim 1997). A simple classic type 1 current clamp neural model (Type 1c RM model), similar to the *in vitro* recordings by Ferragamo et al. (1998a), was the first choice for the GLG cell model. The lack of evidence surrounding the distribution of ANFs, particularly HSR fibres, in the region of the GCD and the limited physiological data led to the use of a filter-based neural model for the GLG cell. This model is computationally faster without minimising the physiological output of the model.

Non-auditory excitatory inputs to the GLG cell were not included as this was not relevant to a strong sensory-driven input and the purpose of the CNSM model (namely to recreate acoustically-driven outputs). Inhibitory synapses are known contact Golgi cells in a number of mammalian species (Cant 1993; Mugnaini et al. 1980). Inhibitory inputs to the GLG cell model, such as other GLG cells or DS cells, were excluded due to the limited experimental evidence and the additional problems this would add to the sequential optimisation process.

Given these limitations and the results of the optimisation, the GLG cell model

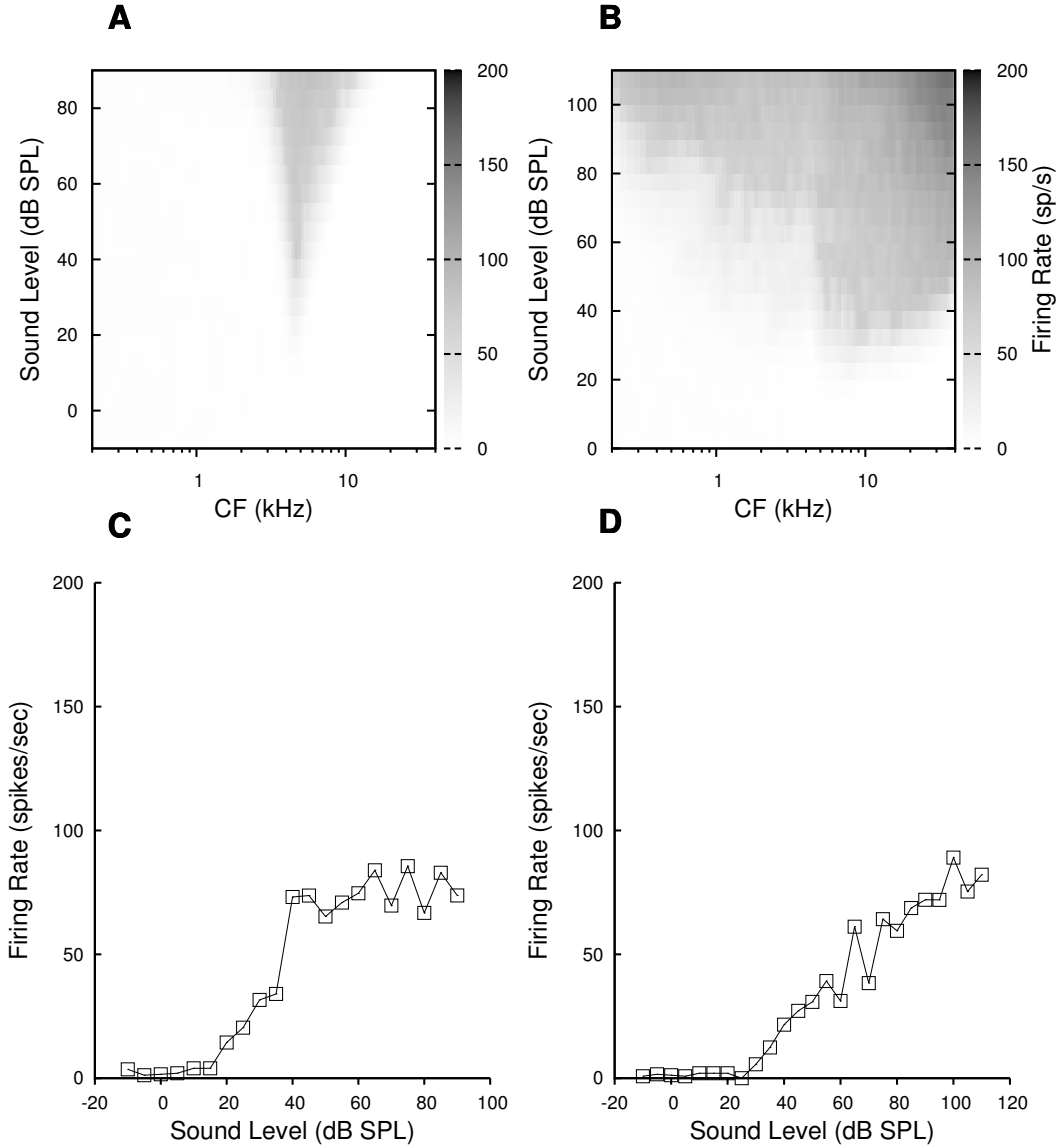


Figure 3.10: Response of GLG cell models across the whole network (CF 5.8 kHz) to pure tones and noise. A. Rate level response map of the GLG cells to a pure CF tone (5.81 kHz, 50 msec, 100 repetitions). B. Noise rate level response map of the GLG cells to broad-band noise (frozen noise, 50 msec, 100 repetitions). C. Rate level responses of the central GLG unit to a pure CF tone (5.81 kHz, 50 msec, 100 repetitions). D. Noise rate level response of all GLG units to BNN stimuli (50 msec, 100 repetitions).

using the novel filter-based neural model was deemed sufficient to proceed with the optimisation of the DS cell network parameters. The filter-based neural model, with no inhibitory component, still produces an efficient and accurate rate-level responses in the GLG cell as observed in experimental data of a single unit in the marginal shell

of the VCN (Ghoshal and Kim 1997).

3.4 D Stellate Cell Model

This section introduces the major wide-band onset inhibitor of the CNSM model, the DS cell.

3.4.1 Background

DS cells have a wide ranging influence on almost all primary cells in the mammalian CN. Glycinergic terminals of the DS cell contact TS and bushy neurons in the VCN (Rhode et al. 1983b), and fusiform and TV neurons in the ipsilateral DCN (Type II and Type IV EIRA units)(Spirou et al. 1999). Some DS cells exit the CN, forming commissural connections with the contralateral CN (Needham and Paolini 2007). *In vitro* studies have shown that DS cells are strongly inhibited by the neurotransmitter GABA, predominantly at GABA_A receptor synapses (Ferragamo et al. 1998b). GLG cells are the only GABA-ergic neuron in the VCN, but their axonal plexus does not extend into the magnocellular core. Doucet and Ryugo (1997) found that all DS cells labelled with BDA staining in the DCN had dendritic projections that entered the GCD, as shown in Figure 3.11.

This section identifies network parameters and intrinsic cell properties that influence the behaviour of DS cells. In the first optimisation, Section 3.4.3, click recovery responses are used to optimise the GABA_A synapse of the DS model. In the second optimisation, Section 3.4.4, rate-level responses to tones and noise are used to optimise the parameters controlling level of ANF excitation in the DS model.

3.4.1.1 Morphology of D Stellate Cells

Morphologically, DS cells typically have 3–4 long dendrites stretching one third of the VCN and receiving ANF inputs over a wide frequency range. DS cell axon terminals contain the inhibitory neurotransmitter glycine and synapse with a fast acting receptor (GlyR) with other cells in the CN (Alibardi 2003b; Babalian et al. 2002; Doucet et al.

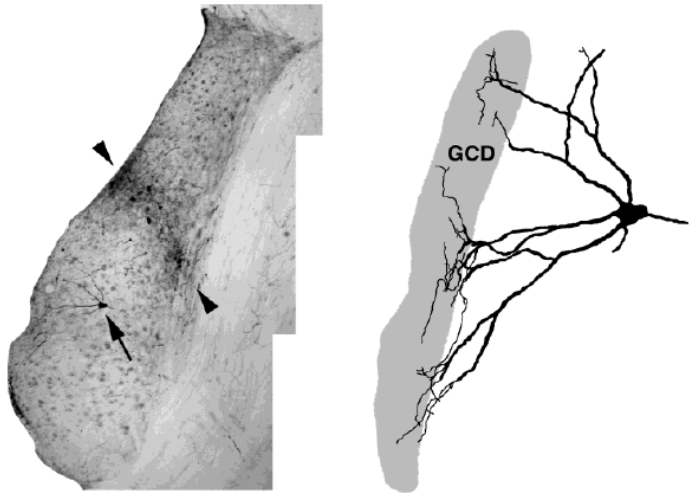


Figure 3.11: (Left) VCN stellate cells that were retrogradely stained with BDA injections in the DCN. TS cells (arrowhead) lie in the narrow frequency band corresponding to the presumed frequency band of the injection site in the DCN. The larger DS cell (arrow) lies outside the frequency band in a region with lower CF. The visibly stained dendrites of the DS cell are directed toward the GCD. (Right) Reconstructed DS cell with dendritic processes in the GCD. Images reproduced from Figure 3C in Doucet and Ryugo (1997).

1999; Harty and Manis 1996, 1998; Mahendrasingam et al. 2000, 2004; Piechotta et al. 2001; Rubio and Juiz 2004). Their axonal collaterals cover the same region in the VCN, and almost one half of the DCN (Cant 1981, 1992; Cant and Benson 2003; Needham and Paolini 2007; Paolini and Clark 1999; Schofield and Cant 1996). Some DS cells also send a commissural projection to the contralateral CN that mediates fast inhibition between the nuclei (Needham and Paolini 2003, 2006; Oertel 1997). Smith et al. (2005) combined evidence from studies in different animals to suggest that radiate neurons in rats, large Type II multipolar neurons in cats and guinea pigs, and DS neurons in mice have the closest resemblance to glycinergic labeled neurons and physiologically classified On_C and onset with latent response (On_L) units (Alibardi 2000a; Altschuler et al. 1993; Arnott et al. 2004; Cant and Gaston 1982; Doucet and Ryugo 1997; Doucet et al. 1999; Kolston et al. 1992; Needham and Paolini 2003; Palmer et al. 2003; Paolini and Clark 1999; Schofield and Cant 1996; Shore et al. 1992; Wenthold 1987).

3.4.1.2 Cellular Mechanisms of D Stellate Cells

Figure 3.12 shows the depolarising and hyperpolarising responses of DS cells *in vitro* in mice (Fujino and Oertel 2001; Oertel et al. 1990). Depolarising currents produce regular action potentials (APs) with double-exponential undershoots. Weak depolarisation produces an action potential at the onset of the stimulus (Figure 3.12A). Hyperpolarising current responses show strong inward rectification with rapid return to stable levels (time constants under 15 msec). In this way, DS cells are different from the slowly integrating TS cells which are Type I current clamp units with single exponential undershoot APs and less prominent hyperpolarising sag.

3.4.1.3 Acoustic Properties of D Stellate Cells

DS cells have been classified as having an On_C PSTH to CF tones across many species (Arnott et al. 2004; Blackburn and Sachs 1989; Feng et al. 1994; Palmer et al. 2003; Paolini and Clark 1999; Pfeiffer 1966a; Rhode et al. 1983b; Smith et al. 2005; Smith and Rhode 1989). Their high threshold to CF tones and increased response to noise show that DS cells receive inputs from many weak ANFs across a wide frequency range (Palmer et al. 2003; Rhode and Smith 1986). Electrophysiological intracellular responses *in vivo* to sounds indicate that the bandwidth of ANF inputs to DS neurons is asymmetric, with an estimated range of two octaves below the DS cells' CF and one octave above CF (Arnott et al. 2004; Palmer et al. 2003; Paolini and Clark 1999).

Post-onset GABAergic inhibition in DS cells is a major influence on the PSTH of On_C neurons (Ferragamo et al. 1998b). Iontophoretic investigations *in vivo* using bicuculline have shown that the firing rate increases to tones and noise (Caspary et al. 1994). Application of bicuculline in the VCN has the effect of changing the temporal behaviour in DS cells (Evans and Zhao 1998), which also affects amplitude modulation (AM) responses in the IC (Caspary et al. 1997, 2002). With click pairs, Backoff et al. (1997) showed strong GABA inhibition does not allow full click recovery in onset choppers until 16 msec separation of the probe and mask clicks.

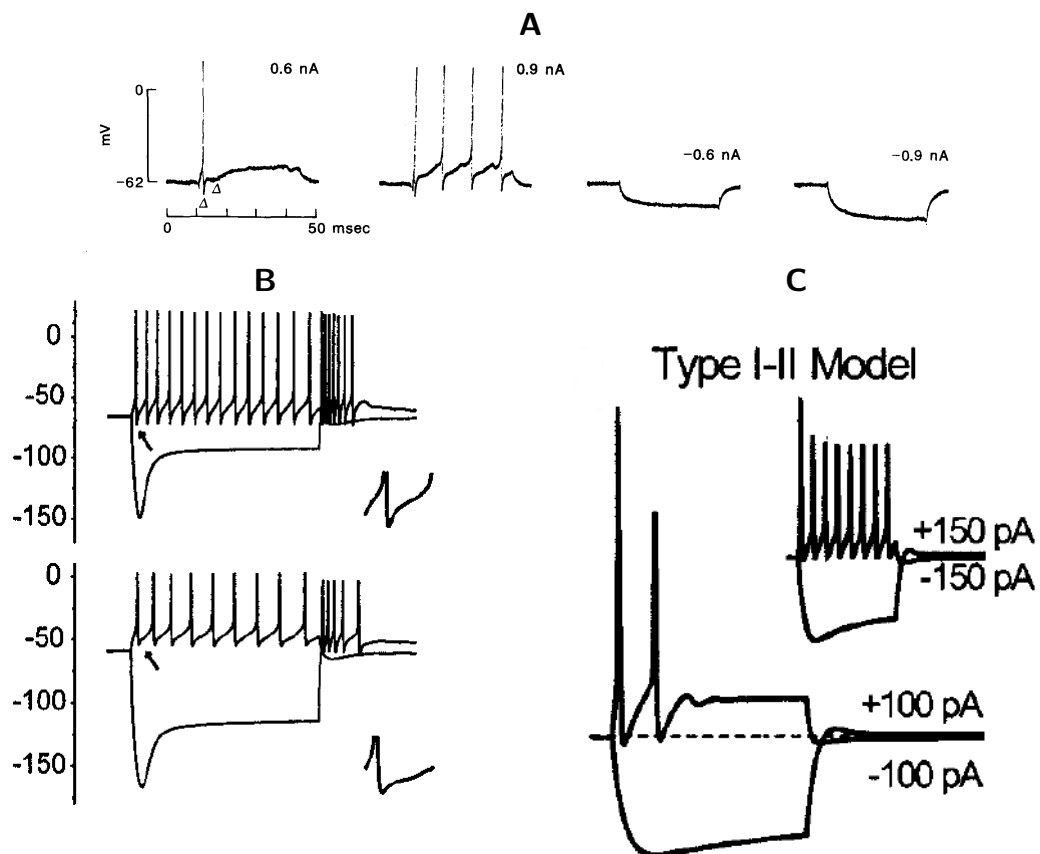


Figure 3.12: Intracellular membrane current clamp response of DS cells to depolarising and hyperpolarising current. A. Intracellular current clamp response of a mouse DS cell to different levels of current injection (reproduced from Oertel et al. 1990). B. Current clamp responses of two DS cells in an *in vitro* slice preparation to 0.1 nA and 0.6 nA current injections. Both DS cells show a prominent hyperpolarising sag and double exponential AP (reproduced from Figures 1E and 1F Fujino and Oertel 2001). C. Simulated current clamp response in a Type I-II RM model (reproduced from Rothman and Manis 2003c).

3.4.2 Implementation

The DS cell model was implemented with a single-compartment, Type I-II RM model (Rothman and Manis 2003c). The Type I-II RM model is unique to DS cells due to the presence of low-threshold potassium currents. The Type I-II model was chosen so that at high levels of intracellular current injection the model produces a regular firing pattern, whereas near threshold the model responds with a spike at the onset of the stimulus. A larger cell body diameter, average 25 μm (Arnott et al. 2004; Smith and Rhode 1989), was included in the model and conductance parameters were adjusted accordingly to keep total-compartment conductance the same as the original values (Rothman and Manis 2003c). Synaptic inputs to the DS cell model come from ANFs (HSR and LSR fibres) and GLG cells. The CNSM model assumes that GABA-ergic input to DS cells was only from local, acoustically-driven Golgi cells. Other synaptic inputs to DS cells are ignored in the CNSM model.

In order to specify how ANF and GABA-ergic inputs regulate the rate and temporal behaviour of DS cells, two optimisation routines were performed. The temporal response of GLG cells to AM is unknown; therefore clicks, as used in Backoff et al. (1997), were deemed the most suitable for optimisation. The first optimisation, described in Section 5.4.3, used the mask recovery response to click pairs observed in On_C units (Backoff et al. 1997). The click pair optimisation tested the DS cell model's response with and without GABA-ergic inputs, simulating the presence of GABA_A antagonists. The second optimisation, Section 5.4.4, used rate level responses to tones and noise from extracellular recordings of DS cells (Arnott et al. 2004). Using tones and noise at many sound levels helped to optimise the parameters controlling the level of ANF excitation in the DS cell model.

Key elements in the creation of the DS cell model are shown in the Nordlie Table 3.4A. A Type I-II single compartment neuron by Rothman and Manis (2003c) has the characteristics of an onset chopper unit and has previously been used to simulate a DS cell model. The selection of a large multipolar neuron without dendrites was based on computational efficiency and the need to ensure that the model fitted within the criteria for DS cells. DS cells have electrotonic dendrites and the filtering in DS cells controls the height of excitatory post-synaptic potentials (PSPs) reaching the soma (White et al.

Table 3.4: D stellate cell model summary

A Model Summary			
Populations		ANF (HSR, LSR), GLG, and DS cell models	
Topology		Tonotopic, auditory system of the rat, 100 frequency channels	
Connectivity		Gaussian spread dependent on morphology and afferent connections	
Input model		ANF model: Instantaneous-rate Poisson neural model (Zilany et al. 2009)	
Neuron model		GLG cell: GLG neural model (see Section 3.3). DS cell model: Type I-II RM single compartment neural model	
Channel models		I_{Na} , I_{KHT} , I_{KLT} , I_{KA} and I_{h} (Rothman and Manis 2003c)	
Synapse model		Excitatory: AMPA glutamatergic receptor (single-exponential) Inhibitory: GABA _A GABAergic receptor (double-exponential), GlyR glycinergic receptor (double-exponential)	
B Populations			
Name	Elements	Number	
HSR	Auditory nerve fibre (Zilany et al. 2009)	$N_{\text{HSR}} = 50$ per channel	
LSR	Auditory nerve fibre (Zilany et al. 2009)	$N_{\text{LSR}} = 20$ per channel	
GLG	Instantaneous-rate Poisson neuron	$N_{\text{GLG}} = 1$ per channel	
DS	Type I-II RM model	Click Recovery: 1 unit at channel 50, CF= 5.6 kHz Rate Level: 1 unit at channel 76, CF = 11.1 KHz	
C Connectivity			
Name	Source	Target	Pattern
ANF → DS	HSR, LSR	DS	Skewed Gaussian convergence, centred on-CF, spread below CF $s_{\text{ANF} \rightarrow \text{DS}}^- = 40$, spread above CF $s_{\text{ANF} \rightarrow \text{DS}}^+ = 20$, delay $d_{\text{ANF} \rightarrow \text{DS}} = 0.8$ msec. Weight and number for HSR and LSR connections ($w_{\text{HSR} \rightarrow \text{DS}}$, $n_{\text{HSR} \rightarrow \text{DS}}$, $w_{\text{LSR} \rightarrow \text{DS}}$, $n_{\text{LSR} \rightarrow \text{DS}}$) optimised.
GLG → DS	GLG	DS	Gaussian convergence, centred on-CF, spread $s_{\text{GLG} \rightarrow \text{DS}} = 3$, delay $d_{\text{GLG} \rightarrow \text{DS}} = 0.4$ msec. Weight ($w_{\text{GLG} \rightarrow \text{DS}}$) and number ($n_{\text{GLG} \rightarrow \text{DS}}$) parameters optimised.
ANF→GLG from previous section, see Table 3.2C.			

Table 3.4: D stellate cell model summary - continued

D Neuron and Synapse Model	
Name	DS cell model
Type	Type I-II (Rothman and Manis 2003c), conductance synapse input
Subthreshold dynamics	Na, KLT, KHT, Ih, and leak currents
Spiking	Emit spike when $V(t) \geq \theta$
E Optimisation - Click Recovery	
Input Stimulus	Mask and recovery click pairs, with delay 16, 2, 8, 4, and 3 msec (in this order), separated by 50 msec
Parameters	$w_{GLG \rightarrow DS}$, $w_{HSR \rightarrow DS}$, $w_{LSR \rightarrow DS}$, τ_{GABA-1} , τ_{GABA-2} , DS \bar{g}_{leak}
Fitness Function	Weighted mean squared error between masker-probe rate ratios of DS cell model and experimental DS cell (Backoff et al. 1997) to pairs of clicks. Idle rates were recorded for spontaneous activity and levels of ANF excitation were used as additional penalties.
F Optimisation - Rate Level	
Input Stimulus	1. Tone rate Level function, 11.1 kHz tone at 30 to 100 dB SPL in 5 dB intervals (50 msec duration, 2 msec cosine squared on/off ramp, 20 msec delay). 2. Noise rate level, broad-band noise at 40 to 95 db SPL in 5 dB intervals (50 msec duration, 2 msec cosine squared on/off ramp, 20 msec delay).
Parameters	$w_{HSR \rightarrow DS}$, $n_{HSR \rightarrow DS}$, $w_{LSR \rightarrow DS}$, $n_{LSR \rightarrow DS}$, $w_{GLG \rightarrow DS}$, $n_{GLG \rightarrow DS}$
Fitness Function	RMS error between DS cell model (CF 11.1 kHz) and experimental On _C unit (CF 10.9 kHz, Arnott et al. 2004) at each input stimulus in tone and noise rate levels.

1994). Accordingly, a single compartment with graded weights was sufficient for the DS cell model.

The synaptic connections onto the DS cell model, shown in Table 3.4C, were simplified to excitatory ANF inputs (HSR and LSR) and GABAergic input from GLG cells in the GCD. The DS cell model's input parameters were pre-emptively fixed. These included the number of GLG to DS synapses ($n_{\text{GLG} \rightarrow \text{DS}} = 25$), the spread of ANFs to DS cells ($s_{\text{ANF} \rightarrow \text{DS}}^+$ and $s_{\text{ANF} \rightarrow \text{DS}}^-$), and the conduction delay from the AN ($d_{\text{ANF} \rightarrow \text{DS}}$). The ANF spread onto DS cells is well documented (Arnott et al. 2004; Jiang et al. 1996; Palmer et al. 1996, 2003; Paolini and Clark 1999). Due to the large computational task of calculating an optimisation routine for DS cell input bandwidth across the whole network, the spread of ANF to DS cells was set using a Gaussian distribution with spread below ($s_{\text{ANF} \rightarrow \text{DS}}^- = 40$) and spread above CF ($s_{\text{ANF} \rightarrow \text{DS}}^+ = 20$). This approach assumed average octave separation between channels of 0.4 octaves, approximating the calculated response area (Paolini and Clark 1999).

The physiological effect of GABAergic inputs on onset choppers is primarily on CF, but the bandwidth is difficult to ascertain (Caspari and Palombi 1993; Caspari et al. 1979, 1993, 1994; Palombi and Caspari 1992). The dendrites of DS cells cover one third of the nucleus (approximately 3 octaves of tonotopic frequencies) and occasionally project into the GCD (Arnott et al. 2004). GLG cells' axonal collaterals are confined to 200 μm in the GCD. The GLG to DS cell model connection within the CNSM model was set to a spread of 2 channels (i.e. $SD = \sqrt{2}$) with zero offset, which corresponds to a DS cell receiving synapses from GLG cell models in a narrow range of frequency channels.

The additional delay parameter for ANF terminals on the DS cell model ($d_{\text{ANF} \rightarrow \text{DS}}$) was shown in Section 3.2.6. The first spike latency in high CF DS cells (2.8 ± 0.09 msec) is precise and faster than other stellate neurons in the VCN (Rhode and Smith 1986). The additional delay of 1.2 msec from ANF to DS input connections is a product of axonal conductance and dendritic delay.

3.4.3 Results of Click Recovery Optimisation

In order to specify how GLG cells regulate the click recovery response in DS cells, a parameter optimisation routine was performed using data from Backoff et al. (1997).

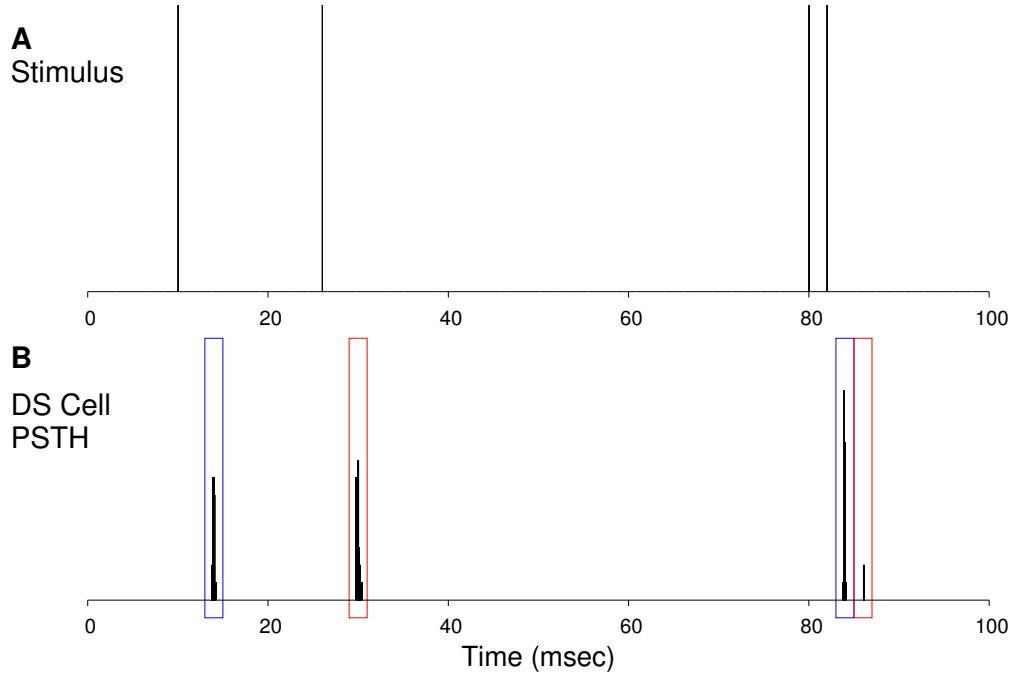
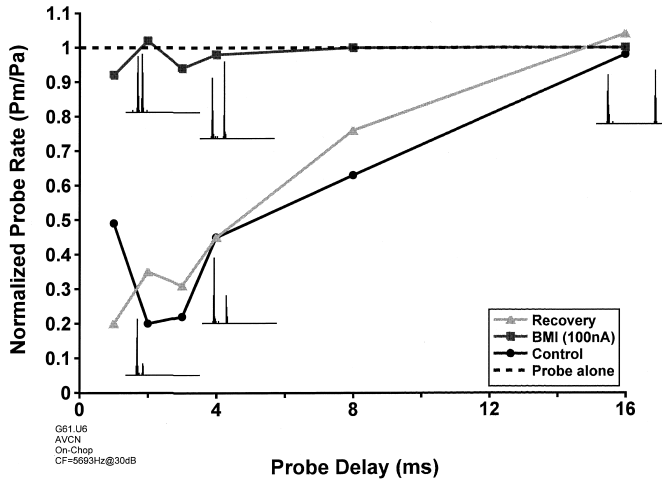


Figure 3.13: Sample of the fitness function stimulus and recording procedure for the DS cell model click recovery optimisation. A. Two pairs of clicks (0.3 msec width) with delays of 16 msec and 2 msec. B. PSTH response of a default DS cell unit (high CF, Type 1-2 RM neural model, soma diameter 21 μm) with 2 msec boxes indicating the window of response for the mask and probe periods. Windows began 3 msec after the stimulus click to account for the FSL in DS units.

Table 3.4E describes the fitness function stimulus as six pairs of masker-probe clicks separated by 50 msec. Spike outputs of the DS cell model were recorded in 2 msec windows following the clicks, accounting for the effective minimum FSL in DS cells (consistent with the experimental design of Backoff et al. (1997)). Figure 3.13 shows the stimulus and output of the first two click pairs of the fitness function stimulus (16 msec and 2 msec separation between mask and probe clicks). Two millisecond windows immediately after the mask and probe clicks were used to record the DS cell model's output.

The six parameters to be fit by the routine were the weights of the HSR ANFs, LSR ANFs and GLG cell model synapses on DS cells ($w_{\text{HSR} \rightarrow \text{DS}}$, $w_{\text{LSR} \rightarrow \text{DS}}$, $w_{\text{GLG} \rightarrow \text{DS}}$); the GABA_A synapse for fast and slow decay constants ($\tau_{\text{GABA-1}}$, $\tau_{\text{GABA-2}}$); and the DS cell maximum leak conductance (\bar{g}_{leak}). Initial optimisation procedures were not successful at constraining the short delay recovery responses (2, 3, 4 msec), so the DS cells' \bar{g}_{leak}



conductance parameter was included in the optimised parameters to allow the DS cell model's input resistance to fit fast-acting behaviour in the cell.

Figure 3.14 shows the click recovery response of unit G61.U6, an AVCN On_C unit (CF 5.69, threshold 30 dB SPL), and the effects of the GABA_A blocker bicuculline (Backoff et al. 1997). The normal probe click response of this unit only reached 100% of the mask click response until 16 msec separation. With iontopopheretic application of bicuculline, the On_C unit had full response to the probe click at 1 msec separation. From these results, Backoff et al. (1997) showed the strong effects of GABA on On_C units in the VCN, effectively DS cells. The DS cell model used in the optimisation had a CF of 5.8 kHz, the closest CF channel to the exemplar On_C unit. Spontaneous activity in idle periods was used for additional weighted penalty measures of spontaneous activity and to restrict over-excitation by ANFs.

Figure 3.15 presents the results of the optimised parameters, shown in Table 3.5, from the DS cell model click recovery optimisation routine. The optimisation parameters demonstrate a clear favouritism toward the LSR ANF input rather than the HSR input to DS cells. The large number of HSR synapses compensates for the small weight that was obtained in the optimisation.

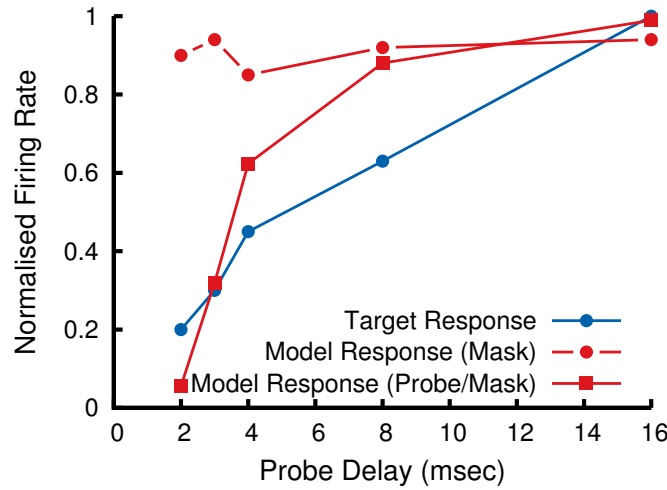


Figure 3.15: Optimisation results for click recovery behaviour in the DS cell model (CF 5.8 kHz). The optimal response (blue circle) was obtained from Figure 3 in Backoff et al. (1997). The red squares represent the best-fit parameter results for the DS cell model.

Table 3.5: Best-fit parameters for the DS cell model in the click recovery optimisation

Parameters (Units)	Range	Best Values
$w_{GLG \rightarrow DS}$ (nS)	[0.01,50]	0.532
$w_{HSR \rightarrow DS}$ (nS)	[0.01,50]	0.167
$w_{LSR \rightarrow DS}$ (nS)	[0.01,50]	13.1
τ_{GABA-1} (msec)	[0.01,10.0]	5.43
τ_{GABA-2} (msec)	[0.1,50.0]	0.262
\bar{g}_{leak} (mS cm ⁻²)	[1e-5,0.05]	0.0163

3.4.4 Results of Rate Level Optimisation

Rate level curves to CF tones and noise have been used as a physiological measure of neurons in the auditory system since the earliest experiments (Rose et al. 1959; Sachs and Young 1978). Rate level curves are used to determine the threshold, dynamic range and saturation rate in response to acoustic stimuli. The dynamic range of DS cells (On_C and On_L units) is much larger than their primary afferent inputs (DS > 50 dB SPL, ANFs < 25 dB SPL) (Joris 1998; Rhode 1994; Rhode and Smith 1986). Figure 3.16 shows two On_C unit rate level responses to CF tones and broadband noise (Arnott et al. 2004). Both units have higher acoustic thresholds to broadband noise than pure tones and higher maximum rate to broadband noise. Unit 284, from Figure 3.16A, was used as the target data to fit the DS cell model.

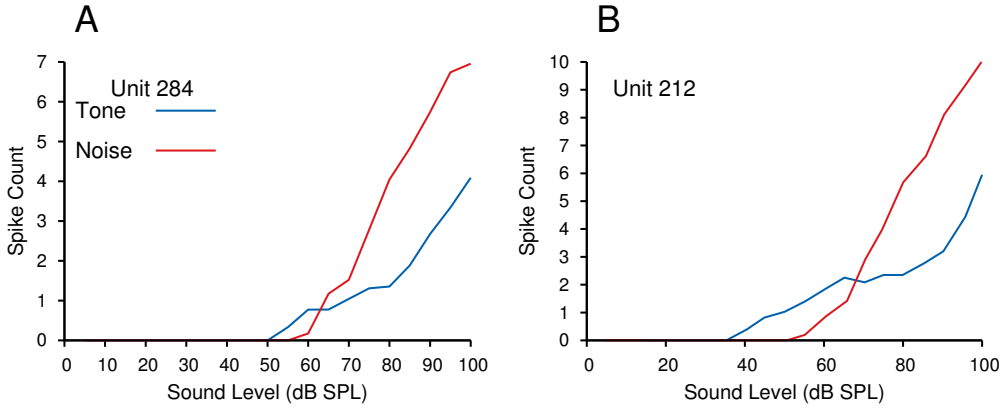


Figure 3.16: Tone and noise rate level response of OnC units used in the DS cell model rate-level optimisation. A. OnC unit 284 (CF 10.9kHz, data reproduced from Figure 3 Arnott et al. (2004)). B. OnC unit 212 (CF 5.9 kHz, data reproduced from Figure 12 in Arnott et al. (2004)).

Table 3.6: Best-fit parameters for DS cell model using the rate-level optimisation

Parameters (Units)	Range	Final Value
$w_{LSR \rightarrow DS}$ (nS)	[0.01,50]	11.03
$n_{LSR \rightarrow DS}$	[1,500]	84
$w_{GLG \rightarrow DS}$ (nS)	[0.01,50]	0.531
$n_{GLG \rightarrow DS}$	[1,50]	5
$w_{HSR \rightarrow DS}$ (nS)	[0.01,50]	0.167
$n_{HSR \rightarrow DS}$	[1,500]	125

Table 3.4F describes the DS cell model rate-level optimisation routine. Weight and number parameters for the three input connections to DS cells were optimised in the procedure. The ANF weight parameters show a clear favouritism toward the LSR input over HSR fibres, but the HSR synapses outnumber the LSR synapses by a ratio of 2:1. A small number of GLG cell synapses (5), each with a strong GABAergic weight (0.531 nS), are the only inhibitory input to the DS cell model in the CNSM model.

The output of the DS cell model in the optimisation was strongly determined by its input responses, as shown in Figure 3.17A and B. HSR fibres (all with SR =50 spikes/s) have low threshold to sounds and saturate at moderate sound levels, as shown by the stable rate level responses to tones and noise (orange circles in Figure 3.17). These flat

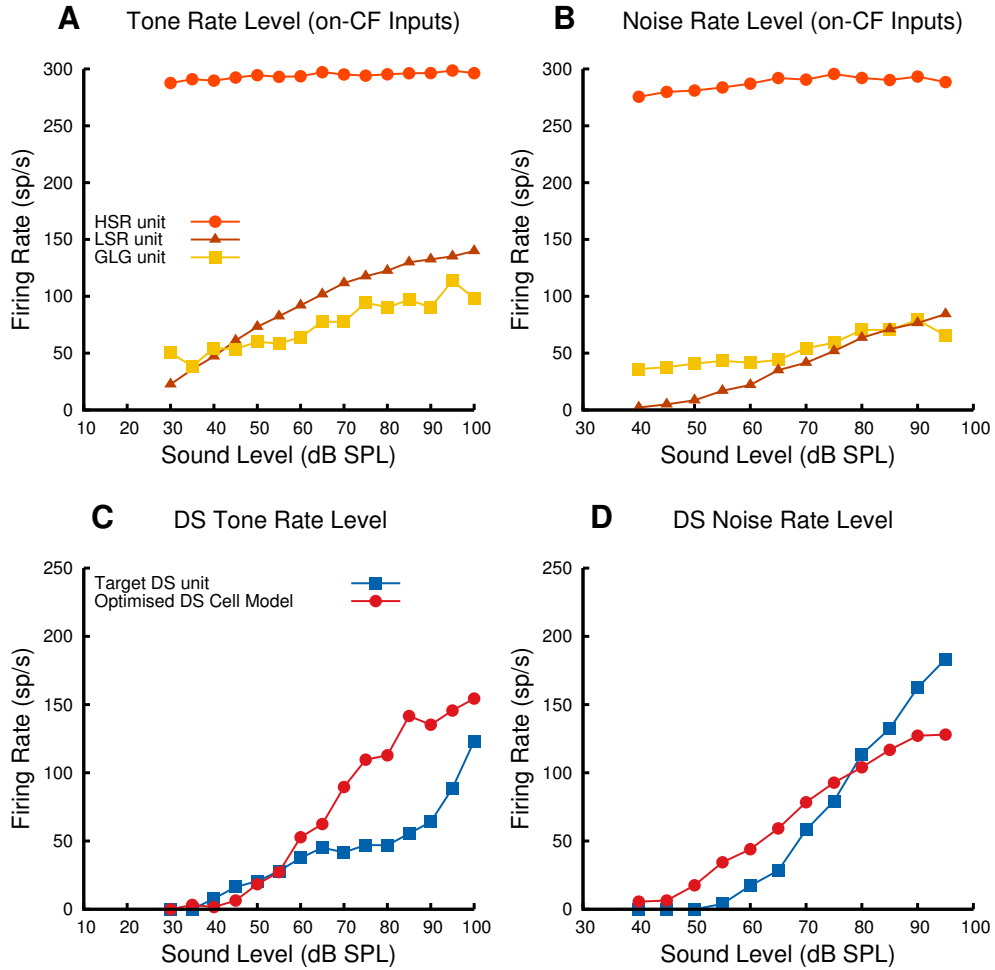


Figure 3.17: Tone and noise rate level responses in the DS cell model (CF 11.1 kHz, channel 67, red circles) were optimised to an OnC unit (CF 10.9 kHz, in figure 12 of Arnott et al. (2004)). A. Tone rate level responses of HSR, LSR and GLG unit inputs to the DS cell model at frequency channel with CF 11.1 kHz. B. Noise rate level responses of HSR, LSR and GLG units at same CF as in A. B. Tone rate level responses of DS cell optimised model (CF 11.12 kHz) and target unit (CF 10.9 kHz). D. Noise rate level responses of optimised DS cell model and target unit.

responses at a high rate (approximately 250 spikes/s) were not able to manipulate the DS cell model in the optimisation other than to set an excitation threshold for tone and noise sounds. LSR fibres ($SR=0.1$ spikes/s) and GLG units have much higher thresholds and wider dynamic ranges, which are contributors to the output response of the DS cell model.

Figure 3.17C shows the output CF tone rate level responses of the optimised DS cell model (using the best fit parameters in Table 3.6) and the reference target's rate level

response. Figure 3.17B shows the noise rate level responses of the optimised DS cell model and the reference DS unit. At 50 repetitions per stimulus, the best parameters produced a combined RMS error of 36.58 spikes per second (tone RMS 43.1 sp/s, noise RMS 26.1 sp/s). The optimisation routine used the MAR error (between the reference and model response) divided by the reference DS cell's response. The combined relative mean relative error (optimised DS cell model relative to the reference DS cell excluding non-zero elements) in Figure 3.17 was 58.59%. The poor fit of the tone rate level response (73.36% MAR error) at higher sound levels is compensated for by the good fit to the experimental target response at low levels, especially around the acoustic threshold. The noise rate level response had a lower RMS error (26.1 sp/s) and lower MAR error (37.25%) across the sound levels; however the DS cell model was active to noise at 40 dB (well below the threshold of the target DS unit, around 60 dB SPL).

3.4.5 Verification of the DS Cell Model

The optimised parameters for inputs to the DS cell model were applied to DS cells across the whole network using tones, noise and tones plus noise stimuli. The PSTH responses of the DS cell model in the centre frequency channel (CF 4.513 kHz) of the network is shown in Figure 3.18. The PSTH responses to a CF tones is classified as On_C (50 and 90 dB SPL Figure 3.18A and B) with a precise first onset spike followed by one to two regularly spaced spikes and a smaller number of irregularly spaced spikes throughout the stimulus. The mean first spike latency of the DS cell model reduced from 24.3 msec at 50 dB SPL to 23.40 msec at 90 dB SPL. The onset PSTH responses to frozen broadband noise did not have the second chopping spike but did have other peaks determined by the spectral peaks in the unit's receptive field. (Figure 3.18C and D). For comparison, on and off-CF PSTH tones responses in three rat DS cells are shown in Figure 3.19 (Paolini and Clark 1999). The on-CF tones were 30 dB above their acoustic threshold and each show two prominent spikes at onset with the unit's in A and B having few spikes in the remainder of the stimulus.

Figure 3.20 shows the optimised DS cell model's response to tones and noise. Figure 3.20A shows the wide response of all DS units in the network to a 4.5 kHz tone with increasing sound level. The on-CF unit (Figure 3.20C) had monotonic increase in rate

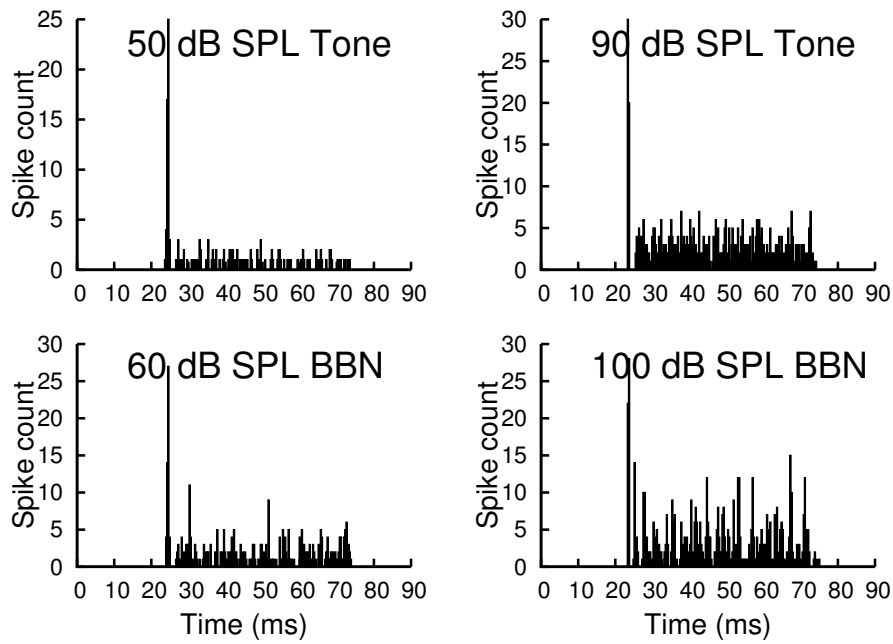


Figure 3.18: Response of optimised DS cell model at the centre of the network (CF 5.8 kHz). Four simulated PSTHs of the DS cell model to CF tones at 50 (A) and 90 dB SPL (B) and broadband noise (BBN) at 60 (C) and 100 dB SPL (D). (Stimuli duration 50 msec, 20 msec delay, 100 repetitions, 2 msec cosine on-off ramp).

from an acoustic threshold of 30 dB SPL. The response to noise was spread throughout all DS cells (Figure 3.20B). The variation in acoustic threshold at different frequency channels is due to the cat audiogram compression in the AN model.

3.4.6 Discussion of the DS Cell Model

The DS cell model within the CNSM model adopted the rate level and click recovery characteristics of a typical On_C unit of the VCN. The network topology and synapto-physiology of inputs to DS cells complement the intrinsic characteristics of the neuron. Assumptions and optimisation design choices were made to generate a biophysically-realistic neuron with physiological behaviour to tones, noise and click pairs that closely matched the experimental data.

Some cell and network parameters were fixed based on solid assumptions. To accurately reflect the neural properties, the DS cell model used a modified Type I-II RM neural model. The cell's intrinsic behaviour contributed to its rapid response at onset and transient phasic response as shown *in vitro* (Ferragamo et al. 1998b; Fujino and

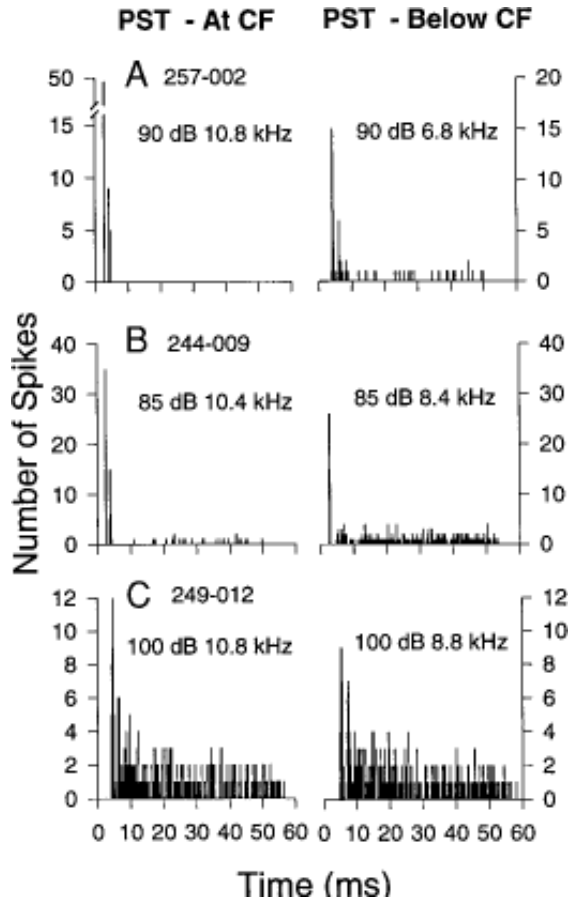


Figure 3.19: A-C. PSTHs in 3 rat OnC neurons to 50 msec tones on CF and below CF (Figures reproduced from Paolini and Clark 1999).

Oertel 2001; Oertel et al. 1988, 1990; Rothman and Manis 2003a). Similarly, the synaptic inputs to the DS cell model reflected the network properties of the DS cell. The morphology of DS cells allows them to integrate a wide BF range of excitatory ANF inputs, with physiological responses to sounds 1 octave above and 2 octave below their BF (Arnott et al. 2004; Palmer et al. 1996, 2003). The CNSM model uses a skewed Gaussian distribution of ANF inputs onto DS cells centred on CF with a fixed spread parameter, $s_{\text{ANF} \rightarrow \text{DS}} = 40$ channels (equivalent to a standard deviation of 4.47 channels in the 100 channel network), for inputs below CF and spread reduced by a factor of 2 for inputs above CF.

The discrepancy in the rate level optimisation show a limitation in fitting a DS cell model to exemplar cell data and has implications for the design of the CNSM model. These discrepancies can be explained by the homogeneity of inputs to the

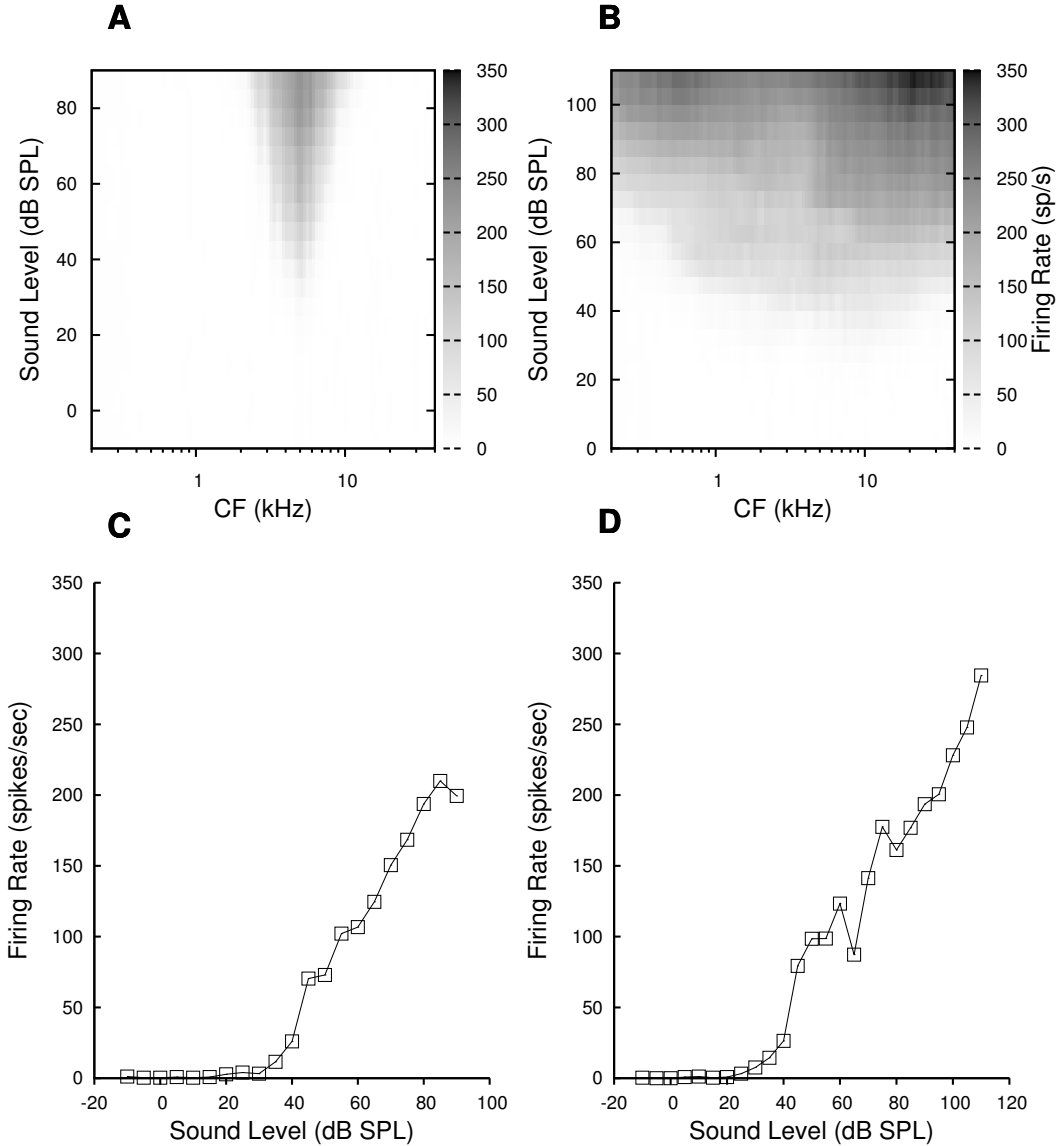


Figure 3.20: Response of the DS cell model across the whole network to a pure tone (on centre unit's CF, 4.513 kHz) and frozen broadband noise. A. Rate level response map of the DS cells to a pure CF tone (4.513 kHz, 50 msec, 100 repetitions). B. Noise rate level response map of the DS cells to broad-band noise (50 msec, 100 repetitions). C. Rate level responses of the central DS unit to a pure CF tone. D. Noise rate level response of the central DS unit to BNN.

DS cell model. The large number of ANFs (125 HSR and 84 LSR fibres) contact the DS cell model with the same synaptic weight (HSR: 0.531 nS, LSR: 8.25 nS) and narrow distributions of SR (HSR: 50 sp/s, LSR: 0.1 sp/s). The limitations in the ANF spontaneous rates has direct impact on the distribution of acoustic thresholds (CF tone HSR: approx. 0 dB SPL, LSR: approx. 30 dB SPL), which varies greatly in HSR units in

cats and other mammals (Heil et al. 2007; Liberman 1978, 1993; Schmiedt 1989; Wang et al. 1997). Variation in acoustic thresholds and rate level responses is introduced to the DS cell model through wide distribution (skewed Gaussian process) of ANFs across a wide section of the nucleus. The same goes for GLG cell inputs to DS cells. The combination of ANFs and GLG cell inputs achieved a good match to acoustic threshold for CF tones and noise; however, the DS cell model's responses at high sound levels diverged from the experimental unit's response. The errors in the DS cell model's rate level optimisation are a consequence of parameterisation in the CNSM model and, so long as the DS cell model characteristics are categorically similar to experimental DS cell responses any further development of the model is not necessary.

The click recovery optimisation was used to modify the physiological dynamics of the GLG cells' GABA_A synapses with DS cells, particularly the GABA_A decay constant. GABAergic inputs to DS cells are well documented in the literature; in synaptic contacts and intracellular pharmacological studies, however, their distribution and network properties are unknown. Electrophysiological evidence shows that GABA influence on DS cells is mediated by a neuron within the local vicinity of DS cells. Ferragamo et al. (1998b) found that DS cells were sensitive to the GABA_A blocker bicuculline and that their IPSPs were not visible at the soma. GLG cells in the GCD are the likely candidates for GABA_A synapses on the distal dendrites of DS cells.

Two important results came out of the click recovery optimisation. First, the GABA_A synapse onto DS cells needs to have a fast onset. The initial response of the DS cell model to click pairs separated by 2 msec required a probe response 20% less than the masker response. The onset of inhibition is limited by the delay from GLG cells and the rise time of the GABA_A synapse. The optimisation found a decay constant of 5.6 msec achieved the best results. In MNTB neurons of mature rats, the fast decay time constant of GABA_Ainhibitory post-synaptic potentials (IPSPs) had a mean of 7 msec and standard deviation of 2 msec (Awatramani et al. 2005). Slower components of the GABA_A synapse with slower decays and synapse depletion were ignored in the CNSM model but may be important in more complex stimuli.

The rate level optimisation used tone and noise responses from an exemplar OnC unit to fit the weights and number of inputs of HSR, LSR and GLG cells. Of note in the

optimised parameters was the difference between synaptic strengths of LSR and HSR ANF inputs (HSR 0.167 nS, LSR 11.03 nS). For this differential to occur in an actual DS cell or in a morphologically detailed neural model, LSR fibres would have to contact the DS cell on the soma or near to the site of activation and the HSR fibres would be on distal dendrites. The optimal DS cell model also received five GLG cell synapses with a synaptic weight of 0.532 nS. The acoustic threshold for both the tone and noise responses was well fitted; however, the responses of the optimised model were unable to match the target at higher sound levels. At higher levels, HSR fibres are saturated; therefore, the balance of LSR and GLG cell inputs is important for maintaining the monotonic rate level response for both tones and noise. The importance of acoustic threshold accuracy becomes critical in later simulations of TV and TS cells. While it is acknowledged that a large discrepancy in the rate-level response occurs at high sound levels, the optimised DS cell model's accuracy at low sound levels was regarded as satisfactory to provide a basis for progression to optimising the TV cell model.

3.5 Tuberculoventral Cell Model

The following section introduces, defines and optimises the neural model of TV cells of the DCN.

3.5.1 Background

3.5.1.1 Morphology and Cellular Properties of Tuberculoventral Cells

TV cells are glycinergic, inhibitory cells found in the deep layers of the DCN. They form local synaptic circuits with pyramidal cells and also send axon collaterals to the VCN. The dendrites of TV cells are aligned with ANFs; consequently, they are also known as 'vertical' cells, and are tuned similarly to ANFs (Rhode 1999). TV cells are characterised as having unique cell bodies and synaptic characteristics that distinguish them from other cells in the deep layer, namely giant cells and Golgi-stellate cells (Alibardi 1999, 2000b; Saint Marie et al. 1991; Wickesberg and Oertel 1993).

TV cells receive weak mono-synaptic excitatory input, mainly on their dendrites, from ANFs (Oertel and Wu 1989; Zhang and Oertel 1993). The intracellular response of TV cells to injected currents are linear, regularly-spaced APs, indicating TV cells are simple integrators (Zhang and Oertel 1993). The input resistance of TV cells ranges from 80 to 125 MΩ (Manis 1990; Zhang and Oertel 1993).

Anterograde labeling in the DCN suggests TV cells project tonotopically to the VCN not just on-CF, but also to the low and high frequency side bands (Munirathinam et al. 2004; Ostapoff et al. 1999). Three types of ventro-tubercular units in rats were identified with retrograde labelling in the DCN (Friedland et al. 2003), compared with only two types in cats (Oertel et al. 1990; Smith and Rhode 1989). These units are identified as TS and DS cells, with the third in rats identified as small adendritic neurons.

Ultra-structural labeling of synapses in the rat DCN suggests that TV cells are inhibited by glycinergic DS cells and from GABA and mixed GABA-Gly sources in the DCN (Rubio 2005). Intracellular responses from labeled TV cells in the mouse show clear diffuse inhibitory input from DS cells (Wickesberg and Oertel 1993; Zhang and Oertel 1993). Evidence in the mouse suggests TV cells also receive excitation from TS cells (Wickesberg and Oertel 1993); however, Rubio (2005) found no TS terminals on rat TV cells.

3.5.1.2 Acoustic Response of Tuberculoventral Cells

TV cells have low spontaneous rates and variable PSTHs (pauser, chopper, wide-chopper or onset/sustained) have been recorded (Rhode 1999; Shofner and Young 1985; Spirou et al. 1999). The complex physiological characteristics of DCN neurons are categorised into EIRA types, first in cats (Evans and Nelson 1973) then refined (Shofner and Young 1985; Spirou et al. 1999; Young and Brownell 1976; Young and Voigt 1981, 1982). Type I EIRA units reflect the excitatory response area of single ANFs. TV cells have a non-monotonic response to tones with increasing sound level, respond poorly to broadband noise, and are categorised as Type II EIRA units (Davis and Voigt 1997; Nelken and Young 1997; Reiss and Young 2005; Spirou et al. 1999; Voigt and Young 1980). Units with Type II EIRA responses are sharply tuned and have thresholds 10 dB higher than other units with which they are intermingled and do not respond to

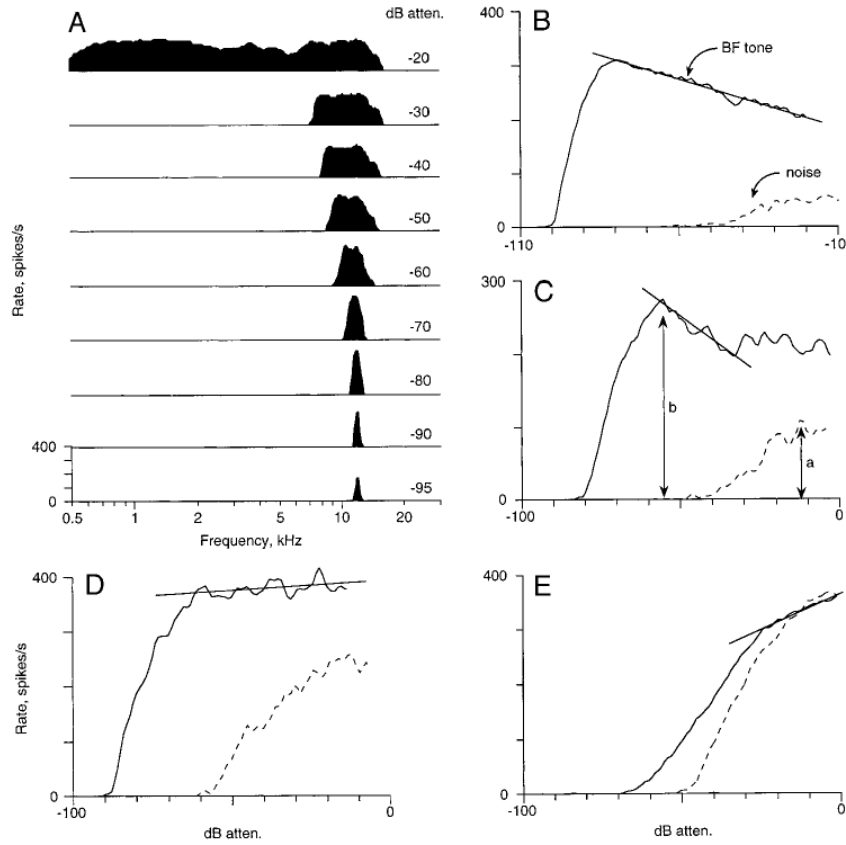


Figure 3.21: Response area and rate-level responses to tones and noise of a single Type II DCN unit. Reproduced from Figure 1 in Spirou et al. (1999).

broad-band noise (Rhode 1999; Sachs and Young 1980; Shofner and Young 1985; Spirou et al. 1999; Voigt and Young 1990; Young 1980; Young and Brownell 1976; Young and Voigt 1982; Young et al. 1992). Figure 3.21 shows the recording of a single TV cell, with narrow tuning and weak response to noise (Spirou et al. 1999).

Recorded PSTHs of TV cells *in vivo* are variable (pause-build, unusual chopper, or onset with sustained activity) (Shofner and Young 1985; Spirou et al. 1999). Recordings *in vitro* show that TV cells respond with regular chopper-like APs to current injection (Zhang and Oertel 1993). The strong input from DS cells across behaviour to voltage-clamped current injection frequencies contributes little or no response to wide band noise and firing rates to CF tones that are non-monotonic functions of intensity. The low SR and high sound thresholds of Type II DCN units might be caused by a high intrinsic electrical threshold (Hancock et al. 1997); this is consistent with the responses of TV cells to intracellular current injection (Ding and Voigt 1997; Zhang and Oertel

1993).

Pharmacological studies into the effects of neurotransmitter blockers have shown that TV cells (Type II DCN units) are strongly regulated by glycinergic and GABAergic inputs. TV cells' zero spontaneous activity is still maintained on application of glycinergic or GABA_A blockers (Davis and Young 2000). In response to sounds, strychnine and bicuculline enable TV cells to respond more vigorously to noise and lower the threshold for tones (Davis and Young 2000; Young and Davis 2002).

Taken together with histological studies, the results suggest that ANFs (predominantly LSR fibres) form the major excitatory input to Type II DCN units along with other excitation from TS cells. Type II units also supply an inhibitory input to the VCN (Wickesberg and Oertel 1990), but the role of Type II terminals in the VCN is less clear. Three hypotheses have been proposed. Wickesberg and Oertel (1990) suggest that the role of Type II units in spectral processing may be that of a delayed narrowband inhibitor in the VCN, with important echo-suppression characteristics. Paolini and Clark (1998) argue that this projection modulates the response thresholds of VCN neurons. Spirou et al. (1999) propose that the responses of DCN principal cells are strongly inhibited by this narrowband source, especially at sharp spectral peaks close to their BF.

3.5.1.3 Modelling of Tuberculoventral cells

Modelling of Type II units in the DCN has been thoroughly investigated by Davis and colleagues (Davis and Voigt 1991, 1994, 1996; Davis and Young 2000; Hancock et al. 1997, 2001; Spirou et al. 1999; Young and Davis 2002). To create a neural model with low spontaneous rate requires either increasing the intrinsic spiking threshold or lowering the synaptic strength of the inputs. Intracellular observations in decerebrate gerbils show higher thresholds in Type II units (Ding and Voigt 1997) and intracellularly recorded Type II units. Another explanation for the absence of spontaneous activity is the greater prevalence of LSR ANFs compared with HSR fibres. It is yet to be confirmed whether LSR fibres preference the deep layers of the CN (Babalian et al. 2002; Meltzer and Ryugo 2006; Ryugo 2008; Ryugo and Parks 2003).

The intrinsic mechanism is more favourable in Type II units, provided there is suf-

ficient inhibition and excitation (Hancock et al. 1997). Consistent with previous TV cell models (Hancock et al. 1997), the CNSM model used the wide-band inhibition of DS cells onto TV cells. Studies of the circuitry of the DCN have shown that wide-band inhibition is necessary for accurate modeling of the principal cells of the DCN including Type II units (Blum and Reed 1998; Blum et al. 1995; Reed and Blum 1995, 1997). The most recent TV cell models have focused on refining the Davis model of the DCN circuit (Lomakin and Davis 2008; Reiss and Young 2005).

3.5.2 Implementation

The implementation of the TV cell model used in the CNSM model and its optimisation routines are described in Table 3.7. The TV cell model was implemented with a single-compartment conductance Type I-c RM neural model, a classic regular firing unit (Rothman and Manis 2003c). The reversal potential of TV cells (E_{Rev}) was set to a lower RMP (-70 mV) to increase the AP threshold. The synaptic inputs to the TV cell model included excitation from HSR and LSR ANFs, and inhibition from DS cells and GLG cells. GLG cell inputs represent characteristic GABAergic inhibition of TV cells from local neurons (Golgi-stellate and cartwheel cells) that are not included in the CNSM model. These units have a similar Type I/III EIRA characteristic to GLG cells. The weights ($w_{\text{LSR} \rightarrow \text{TV}}, w_{\text{HSR} \rightarrow \text{TV}}$) of ANF synapses were used in the optimisation procedures to allow for fine adjustments to the strength of excitation. The numbers of synapses ($n_{\text{LSR} \rightarrow \text{TV}} = 20, n_{\text{HSR} \rightarrow \text{TV}} = 20, n_{\text{DS} \rightarrow \text{TV}} = 30, n_{\text{GLG} \rightarrow \text{TV}} = 10$) were fixed at appropriate values. The TV cell model received ANF inputs on-CF from only one frequency channel at the same CF ($s_{\text{ANF} \rightarrow \text{TV}} = 0$). The strength of inhibition in the TV cell model was controlled by the weight of DS and GLG cell inputs ($w_{\text{DS} \rightarrow \text{TV}}, w_{\text{GLG} \rightarrow \text{TV}}$). The parameters controlling the distribution of DS cell inputs to TV cells were fixed ($s_{\text{DS} \rightarrow \text{TV}} = 30, o_{\text{DS} \rightarrow \text{TV}} = 0$) in the rate level optimisation. The offset parameter, $o_{\text{DS} \rightarrow \text{TV}}$, is the focus of the notch optimisation in Section 3.5.4.

Figure 3.22 shows the rate level output behaviour of two TV cells in control environments and environments that block important neurotransmitters (Spirou et al. 1999). Figure 3.22A shows a Type I/III EIRA unit in the deep layer of the DCN. The suppressed noise response in Figure 3.22B categorises this neuron as a typical Type II EIRA

Table 3.7: Tuberculoventral cell model summary

A Model Summary			
Populations	HSR and LSR ANFs, Golgi, DS, and TV cells		
Topology	Tono-topicity of the rat AN and CN		
Connectivity	ANF → {GLG, DS, TV}, GLG → DS, DS → TV, GLG → TV		
Input model	ANF model: Instantaneous-rate Poisson neural model (Zilany et al. 2009)		
Neuron model	GLG cell: GLG neural model (see Section 3.3) DS cell: Type I-II RM model (see Section 3.4) TV cell: classic Type I RM model		
Channel models	I_{Na} , I_{KHT} , I_{KLT} , I_{KA} and I_{h} (Rothman and Manis 2003c)		
Synapse model	Excitatory: AMPA glutamatergic receptor (single-exponential) Inhibitory: GABA _A GABAergic receptor (double-exponential), GlyR glycinergic receptor (double-exponential)		
B Populations			
Name	Elements		Size
HSR	Poisson generator		$N_{\text{HSR}} = 50$ per freq. channel
LSR	Poisson generator		$N_{\text{LSR}} = 30$ per freq. channel
GLG	Poisson generator		$N_{\text{GLG}} = 1$ per freq. channel
DS	Type I-II RM model		$N_{\text{DS}} = 1$ per freq. channel
TV	Type I-classic RM model		$N_{\text{TV}} = 2$ at centre channel
C Connectivity			
Name	Source	Target	Pattern
ANF → TV	LSR, HSR	TV	Narrowband connection on-CF, zero spread, number $n_{\text{LSR} \rightarrow \text{TV}} = 20$ and $n_{\text{HSR} \rightarrow \text{TV}} = 20$, delay $d_{\text{ANF} \rightarrow \text{TV}} = 2.0$ msec. Weight parameters ($w_{\text{HSR} \rightarrow \text{TV}}$ and $w_{\text{LSR} \rightarrow \text{TV}}$) optimised.
GLG → TV	GLG	TV	Gaussian convergence, centred on-CF, spread $s_{\text{GLG} \rightarrow \text{TV}} = 20$, number $n_{\text{GLG} \rightarrow \text{TV}} = 10$, delay $d_{\text{GLG} \rightarrow \text{TV}} = 0.5$ msec. Weight parameter $w_{\text{GLG} \rightarrow \text{TV}}$ optimised.
DS → TV	DS	TV	Off centred Gaussian convergence, spread $s_{\text{DS} \rightarrow \text{TV}}$, number $n_{\text{DS} \rightarrow \text{TV}} = 30$, delay $d_{\text{DS} \rightarrow \text{TV}} = 0.5$ msec. Offset ($o_{\text{DS} \rightarrow \text{TV}}$) set to zero in rate level routine and optimised in notch routine. Weight parameter ($w_{\text{DS} \rightarrow \text{TV}}$) optimised in rate level routine.
ANF → GLG, ANF → DS, and GLG → DS from Table 3.4.			

Table 3.7: Tuberculoventral cell model summary - continued

D Neuron and Synapse Model	
Name	TV cell model
Type	Type I-classic RM model (Rothman and Manis 2003c), conductance synapse input
Subthreshold dynamics	Na, KHT, Ih, and leak currents
Spiking	Emit spike when $v(t) \geq \theta$
E Optimisation	
Input Stimulus	Tone Rate Level: 4.5 kHz tone at SPL 0 to 95 dB SPL in 5 dB steps (50 msec duration, 2 msec cosine squared on/off ramp, 20 msec delay) Noise Rate Level: BBN at 20 to 95 dB SPL in 5 dB steps (50 msec duration, 2 msec cosine squared on/off ramp, 20 msec delay)
Parameters	$w_{LSR \rightarrow TV}$, $w_{HSR \rightarrow TV}$, $w_{DS \rightarrow TV}$, $w_{GLG \rightarrow TV}$
Fitness Function	Mean squared error of noise rate-level responses between TV model (channel 50, CF=4.5 kHz) and target TV cell in Figure 8A in Spirou et al. (1999). PSTH of TV units calculated for mean firing rate at different sound levels for tones and BBN stimuli.

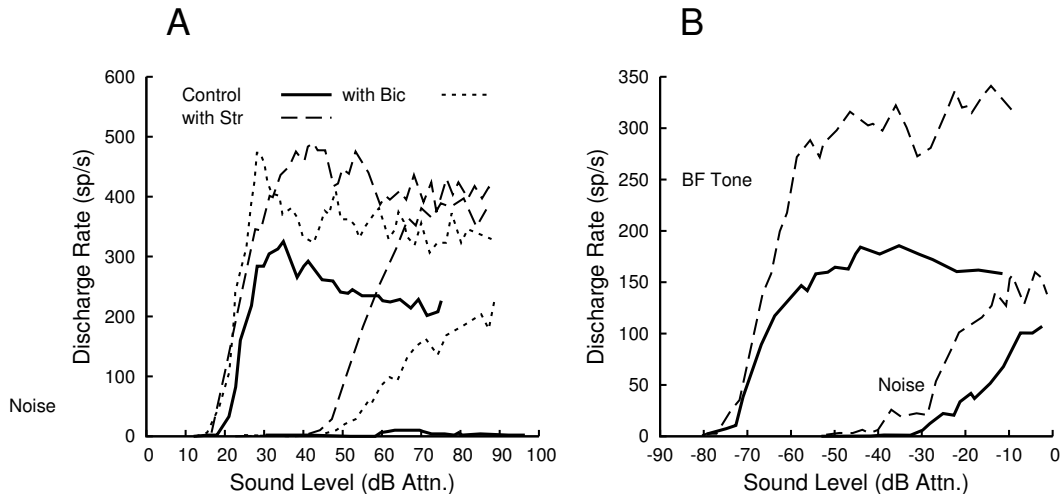


Figure 3.22: Physiological effects of neurotransmitter blockers strychnine and bicuculline on the rate level response of TV cells (Spirou et al. 1999). A. Type II EIRA unit. B. Type I/III EIRA unit. Data reproduced from Figure 8 in Spirou et al. (1999). Sound levels are attenuated from a reference acoustic calibration

unit. The TV cell in Figure 3.22B was used as the reference in the TV cell model optimisation. The reference TV unit was recorded with iontopopheretic application of strychnine and bicuculline, which directly affect synaptic connections relevant to the CNSM model, e.g. glycinergic DS cell connections and GABA_A-ergic GLG cell connections. For the TV cell model's rate level optimisation, three TV cell models were

simulated. The first TV cell model was simulated with all connections active and was compared against the control responses. The second TV cell model was simulated without DS cell connections and compared against the strychnine responses. The final TV cell model was simulated without DS or GLG connections and compared against bicuculine responses. The sound level units (dB Attenuation) were drawn from an acoustic calibration technique close to the ear drum of the animal (Rice et al. 1995; Spirou and Young 1991), where 0 dB attenuation is approximately 100 dB SPL.

3.5.3 Results of Tone and Noise Rate Level Optimisation

Figure 3.23 shows the best fitted output behaviour of the optimised TV cell model (Table 3.8) and the target data from the unit in Figure 8A in Spirou et al. (1999) (see Figure 3.22). Figures 3.23A and B show the tone and noise rate level response of each of the inputs to the TV cell model.

The optimised TV cell model response in Figure 3.23C shows a poor fit for the control tone rate-level output, especially at high SPL. The RMS of the tone rate level response in the experimental control and optimised TV cell model was 149.8 sp/s. This response was non-linear and showed strong inhibitory effects without recovery to a stable firing rate. The discrepancy is problematic for this particular experimental data, but the TV cell model's response is similar to other Type II DCN units in Figures 3.21B and C which also showed strong suppression of CF tones at high level. The acoustic threshold in the HSR on-CF unit was 10 dB less than the experimental TV unit and was almost saturated at 20 dB SPL where the target TV cell was just beginning to fire. The noise rate level RMS error was significantly better at 6.8 sp/s, an important factor in the Type II EIRA response of the TV cell model. For the strychnine-affected experimental data and response of the TV cell model without DS cell inputs (Figures 3.23E and F), the RMS error for the tone and noise rate level was 97.4 and 61.7 sp/s, respectively. The model's response was well fitted, with only a limited amount of error in mid-level tones and a shift in threshold by 15 dB in noise stimuli. For the bicuculine-affected experimental data and equivalent TV cell model (Figures 3.23G and H), the RMS errors were 181.4 and 109.9 sp/s, for tone and noise rate level, respectively. The DS cell inhibition present in the bicuculine-affected scenario reduced the maximal output and

Table 3.8: Best-fit parameters of the TV cell model using the rate-level optimisation

Parameters (Units)	Ranges	Final Value
$w_{\text{LSR} \rightarrow \text{TV}}$	(nS) [0.01,100]	5.17
$w_{\text{HSR} \rightarrow \text{TV}}$	(nS) [0.01,100]	0.355
$w_{\text{DS} \rightarrow \text{TV}}$	(nS) [0.01,100]	1.97
$w_{\text{GLG} \rightarrow \text{TV}}$	(nS) [0.01,100]	1.42

saturation rate of the model's rate level response. The timing and coincidence of onset inhibition dramatically affected the TV cell model where the activity in the model was predominantly in the second half of the 50 msec stimulus. In response to noise, the DS cell model's rate level was slightly higher but the LSR noise rate level flattened out (Figure 3.23B) contributing to a low saturation rate in the TV cell model (Figure 3.23H). The final error used in the optimisation routine was 607.0 sp/s, a summation of the six rate-level RMS errors.

Misalignment of the rate-level curve in the input on-CF HSR units had detrimental affect on the TV cell optimisation. The acoustic thresholds of the HSR units to pure tones were 10 dB lower than the target TV unit (Figures 3.23A and C for tones). The acoustic threshold of the TV cell exposed to strychnine (Figure 3.23F) was 15 dB greater than the threshold of the HSR unit (Figure 3.23B). The control tone and noise comparisons were weighted five times more than the strychnine and bicuculine comparisons in the optimisation and the $w_{\text{HSR} \rightarrow \text{TV}}$ parameter would be less favourable due to the misalignment of its rate-level response.

The optimised parameters of the TV cell model in Table 3.8 are indicative of a strongly-inhibited neuron. The excitation from ANF inputs was moderate, with stronger weighting toward LSR fibres ($w_{\text{LSR} \rightarrow \text{TV}} = 5.17$ nS, $w_{\text{HSR} \rightarrow \text{TV}} = 0.355$ nS). Each of the input cell types to the TV cell model had 30 synaptic inputs. All ANF inputs were on-CF and were chosen from different HSR and LSR fibres in the same frequency channel. The optimum inhibitory weight from DS cells was 1.97 nS. The DS cell inputs were selected from frequency channels on and around the CF of the TV cell (Gaussian distribution, spread parameter $s_{\text{DS} \rightarrow \text{TV}} = 30$). Due to the On_C response properties of DS cells, the inhibition was most effective at stimulus onset and at higher sound levels.

The weight of GLG cell inputs was comparable to DS cells' synaptic weight ($w_{GLG \rightarrow TV} = 1.42$ nS) as well as the same number of connections. The GLG cell model had a low threshold and a steady increase in firing rate with increasing level (Figure 3.23A and B), along with its longer time constant, suggesting a continuous monotonic GABA inhibition regulating the activity in the TV cell model.

3.5.4 Results of Notch Noise Optimisation

Table 3.9 shows the implementation methods used in the TV cell model notch noise optimisation. The main purpose of this optimisation was to test whether DS cell connection distribution variables (i.e. spread and offset) play a role in modifying the output of TV cells (as suggested by Reiss and Young (2005)). The experimental data in Figure 3.24 shows the average responses of Type II DCN units to notch sweeps (Reiss and Young 2005). single notch presented across the whole network of TV cells to avoid multiple notch sweeps. Accordingly, the fitness function took the relative position of cells in the network into account when comparing the experimental data. For example, when presented with a notch noise filtered between 5 kHz and 10 kHz, a unit with CF of 5 kHz will see a falling edge of a 1 octave notch, whereas a unit with CF of 10 kHz will see a rising edge of a half octave notch. Figure 3.25 shows the combination of the Type II DCN unit notch data for 1 octave.

Table 3.9: TV cell model notch noise optimisation

A	Optimisation
Input Stimulus	Notch-noise stimulus based on Reiss and Young (2005). Stop-band filtered white noise (60 dB SPL, 50 msec duration, 2 msec cosine squared on/off ramp, 20 msec delay), 30 dB half-octave stop-band width, centred on the middle of the network (5.8 kHz).
Parameters	$s_{DS \rightarrow TV}, o_{DS \rightarrow TV}, w_{HSR \rightarrow TV}, w_{LSR \rightarrow TV}, w_{DS \rightarrow TV}, n_{DS \rightarrow TV}$
Input	Stimulus induced Poisson spike trains from GLG units, HSR and LSR ANFs, and natural synaptic input from DS units.
Fitness Function	Spiking output of all 100 TV units across the network recorded over 25 repetitions. PSTH of TV cells, calculated for first spike latency and mean rate. Fitting data was compared against experimental data of a Type II DCN unit (Reiss and Young 2005, Figure 9).

The notch sweep sets used by Reiss and Young (2005) were generated with log-

Table 3.10: Best fit parameters of DS to TV cell connections using the notch optimisation.

Parameters (Units)	Range	Best Values
$o_{DS \rightarrow TV}$ (channel)	[-10,30]	2.1
$s_{DS \rightarrow TV}$ (channel)	[0,100]	13

arithmically constant notch widths and notch centre frequencies ranging from 1 octave below to 1 octave above CF in 1/50 octave steps. The single notch noise stimulus presented in this optimisation routine was generated in MATLAB/GNU Octave using frozen Gaussian noise (100 kHz sampling rate) and a Chebyshev Type II band reject filter.¹ The sound level in the Reiss and Young (2005) data added further complexity. The power spectrum was maintained at a constant level per frequency band (dB per Hz^{1/2}) and this was scaled at each point in the notch sweep. For the single presentation used in this experiment the sound level plays an important part in stimulating the ANFs and contributing interneurons. From the previous TV cell model optimisation, Section 3.5.3, the preliminary response to noise in TV cell models was linear between 40 to 80 dB SPL.

Higher thresholds in Type II DCN units (Spirou et al. 1999) and the presence of multiple inhibitory synapses (Alibardi 2006) suggest TV cells either receive a strong inhibitory influence or they have a lower RMP due to a lower leak current reversal potential. A reduced resting membrane potential may increase the AP threshold for excitatory inputs to generate action potentials. To allow for this, the reversal potential of the TV cell model (E_{Rev}) was used as a parameter in the optimisation routine with a range from -80 to -50 mV.

Figure 3.26 shows the notch noise response of the TV cell mode using the best parameters in Table 3.10. The eventual result of the DS to TV cell connection optimisation, highlighted in Table 3.10, was derived from simulations using a 70 dB SPL notch-noise stimulus. The optimisation produced a better result for the offset parameter and the overall error value of the fitness function. The offset of DS onto TV cells at 2.1 channels, equivalent to a mean of 0.14 octaves (0.34 octaves at the lowest channel and 0.13 at the highest channel), was closer to the offset predicted by Reiss and Young (2005).

¹The cheby2 function is in the octave-forge signal package and MATLAB's Signal Processing Toolbox.

3.5.5 Verification of the TV Cell Model

The TV cell model, with optimised parameters from both the rate level and notch optimisations, was tested using tones and noise stimuli across the whole CNSM network. Figure 3.27A shows the PSTH response of the central TV unit (CF 4.5 kHz) at 40 dB SPL (classified as On_L). The first spikes occur at 4.3 msec after the stimulus onset (similar to the non-optimised TV cell model's mean FSL in Section 3.2.6). The characteristic chopping response of the Type I-c RM neural model (Rothman and Manis 2003c) is restricted from repetitive firing due to GABA and glycinergic inhibition, particularly at the onset of excitation. With increasing sound intensities the PSTH become highly irregular and suppressed (Figure 3.27B). In response to noise, the PSTH of the TV cell model had minimal activity at 40 and 90 dB SPL (Figure 3.27C and D) typical of the Type II EIRA units in the deep layer of the DCN (Davis and Young 2000; Rhode 1999; Spirou et al. 1999).

Figure 3.28 shows the response of all the TV cells to the full battery of stimuli. The rate response to tones (Figure 3.28A) is limited to a narrow field around the central channel (CF 4.513 kHz). The bandwidth of active units 10 dB above threshold was only three channels with a Q₁₀ of 0.143 octaves , measured at 20 dB SPL. Due to the strong DS cell inhibition, the responses above 60 dB SPL were suppressed for all TV cells. The on-CF tone rate level response in Figure 3.28C shows a rapid rise in excitation at 10 dB SPL followed by a gradual rate reduction at 40 dB SPL and then a sudden drop in rate from 65 dB SPL. The TV cell model's response to noise was suppressed for all units (Figure 3.28B). Activity above small spontaneous rates was present only at low sound levels that follow the acoustic threshold curve in the ANF inputs. The central unit's maximum rate was 38 sp/s at 40 dB SPL (Figure 3.28D) was less than half the maximum rate for all TV cell's to noise (98 sp/s in unit 93, CF 30.8 kHz, 40 dB SPL).

The response of individual Type II DCN units to notch and band-pass sweeps in Figure 3.24 (from Figure 9 in Reiss and Young 2005) was the target data used for the optimisation of DS cell connections to TV cells. To replicate the response of a single unit to notch sweeps, notches were generated in MATLAB/GNU Octave using Chebychev II filters with a sampling rate of 100 kHz and an optimal filter number. The half octave sweep was calculated from -2 to 2 octaves away from 12.7 kHz at 1/32nd increments

with logarithmically constant notch widths. A 50 msec stimulus at 50 dB SPL was established in the AN model for use by the CNSM model.² Figure 3.29 shows the response of a unit with similar CF (TV unit 70, CF 12.76 kHz) to notch and band-pass noise.

3.5.6 Discussion of the TV Cell Model

TV cells are an important inhibitory inter-neuron in the DCN and VCN. TV cells' role in the CNSM model is to provide delayed, narrow-band inhibition to TS cells. Their limited activation to broad-band noise (Figure 3.23B) and strong activation to CF tones (Figure 3.23A) is characteristic of Type II EIRA units in the deep DCN (Spirou et al. 1999). The noise rate level output of the optimised TV cell model was a closer fit to the experimental unit's response in Figure 3.22A than the response used for the optimisation in Figure 3.22B. The strong level of wide band inhibition from DS cells diminishes the rate TV cells to stimuli with a broad spectrum. The functional role of TV cells in the CNSM model is the enhancement of peaks in the TS cell rate spectrum but only for stimuli with a narrow spectrum.

The discrepancies in the TV cell's rate level optimisation reflect the limitations of the CNSM model and the optimisation process. The acoustic threshold and rate-level response gradient in each of the input cell types play a critical role in the output responses of TV cells. The cytoarchitecture of TV cells and their synaptic inputs may be more elaborate than originally proposed (Alibardi 2006; Munirathinam et al. 2004; Rubio 2005, 2006). The TV cell also receives more complex EIRA inputs in the deep layer of the DCN than are accounted for in the model. GLG cell inputs to the TV cell model were included to replace GABA and mixed GABA-glycinergic neurons. This approach, while limited, was satisfactory for demonstrating the performance of the TV cell model with all the features of a Type II EIRA DCN unit: no spontaneous activity, non-linear rate level response to tones and no response to noise.

The results of the notch noise optimisation do not exclusively confirm or deny the hypothesis presented by Reiss and Young (2005) whether wide-band inhibitory offset

²Logarithmically constant means the notch width is calculated at the centre frequency of the notch and not the CF of the unit of interest.

of TV cells causes asymmetric responses to notch noise. The LSR ANF spectrum in Figure 3.29 shows a bias at the falling edge that closely resembles in the experimental TV cell responses, as shown in Figure 3.24. The design of the experimental target data used to fit the responses of the network of TV cells also needs further investigation.

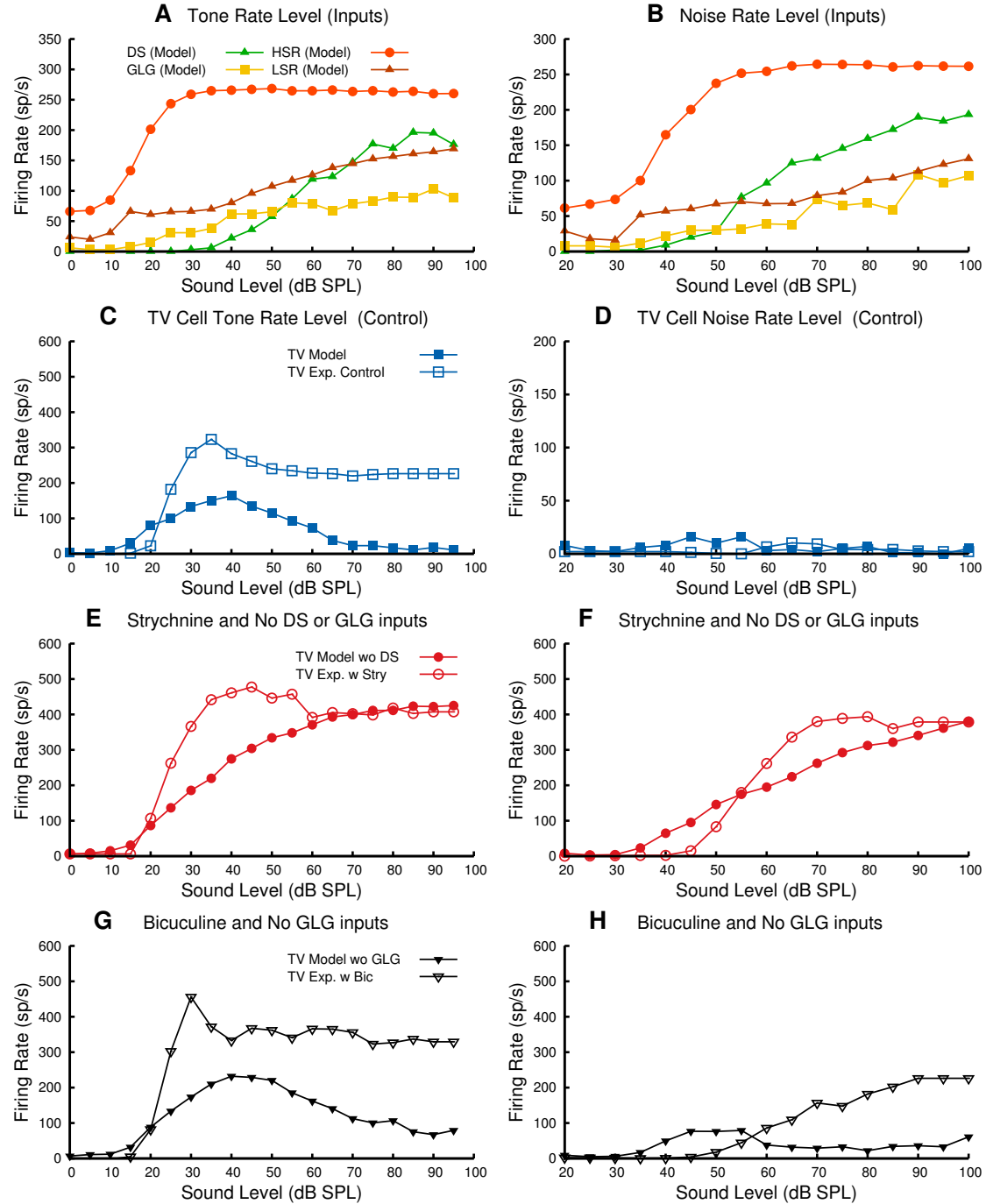


Figure 3.23: Tone and noise rate level responses in the TV cell model (CF 5.8 kHz, channel 49, red circles) were optimised to experimental data, a Type II DCN unit (CF unknown, in figure 8B of Spirou et al. (1999)). Glycinergic blocker strychnine used in the target unit was emulated in the TV cell model by removing DS cell synaptic inputs. A. Tone RL of optimised TV cell model and target unit data with and without inhibition. B. Noise RL of optimised TV cell model and target unit data with and without inhibition.

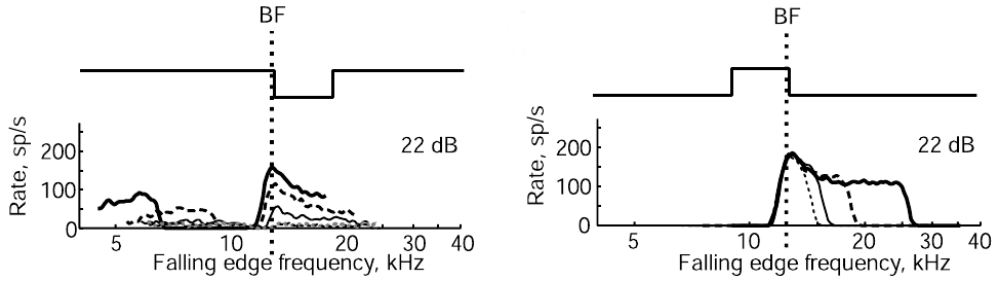


Figure 3.24: Experimental notch-noise data of a single Type-II DCN unit, reproduced from Figure 9 Reiss and Young (2005).

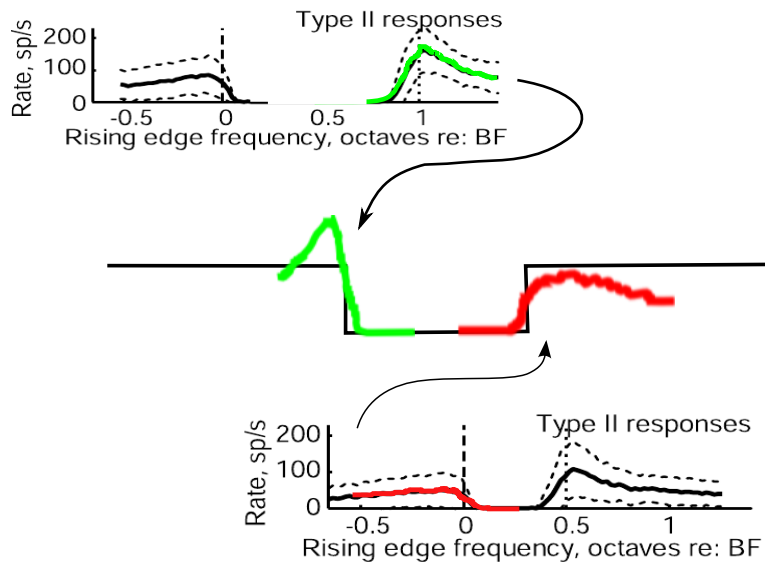


Figure 3.25: Expected mean rate response to notch noise in the TV cells, created from 1 octave notch sweeps (top) for the falling edge and from half octave notch sweeps (bottom) for the rising edge (augmented from Figure 9 in Reiss and Young (2005)).

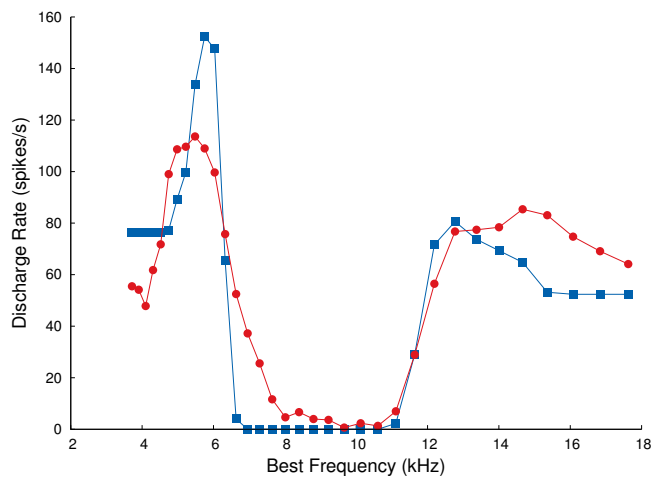


Figure 3.26: Best-fit result of TV cell model notch optimisation.

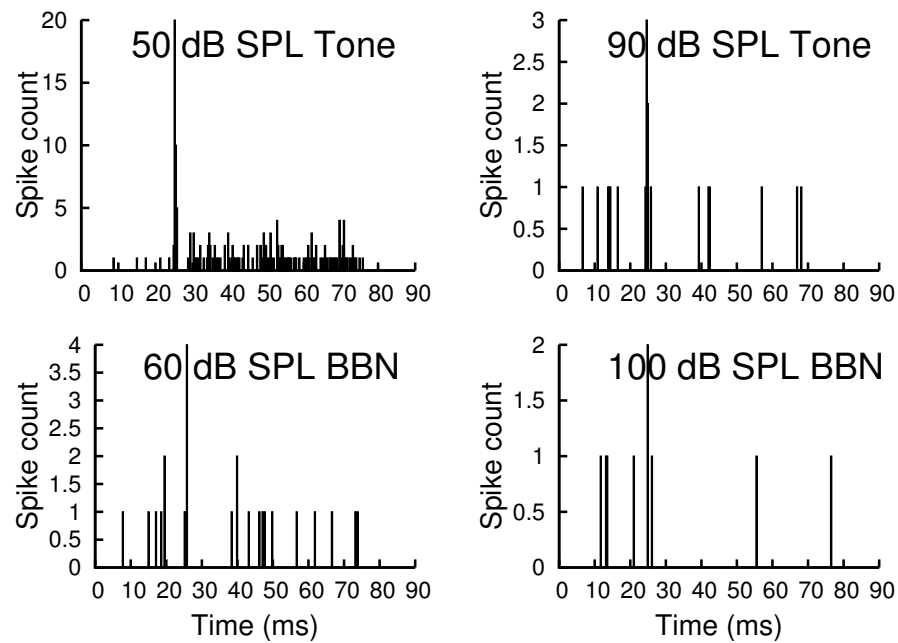


Figure 3.27: PSTH response of optimised TV cell model at the centre of the network (CF 5.8 kHz) to CF tones and noise (50 msec duration, 50 repetitions). PSTH responses to CF tones at 40 (A) and 70 dB SPL (B), and broad-band noise (BBN) at 40 (C) and 90 dB SPL (D).

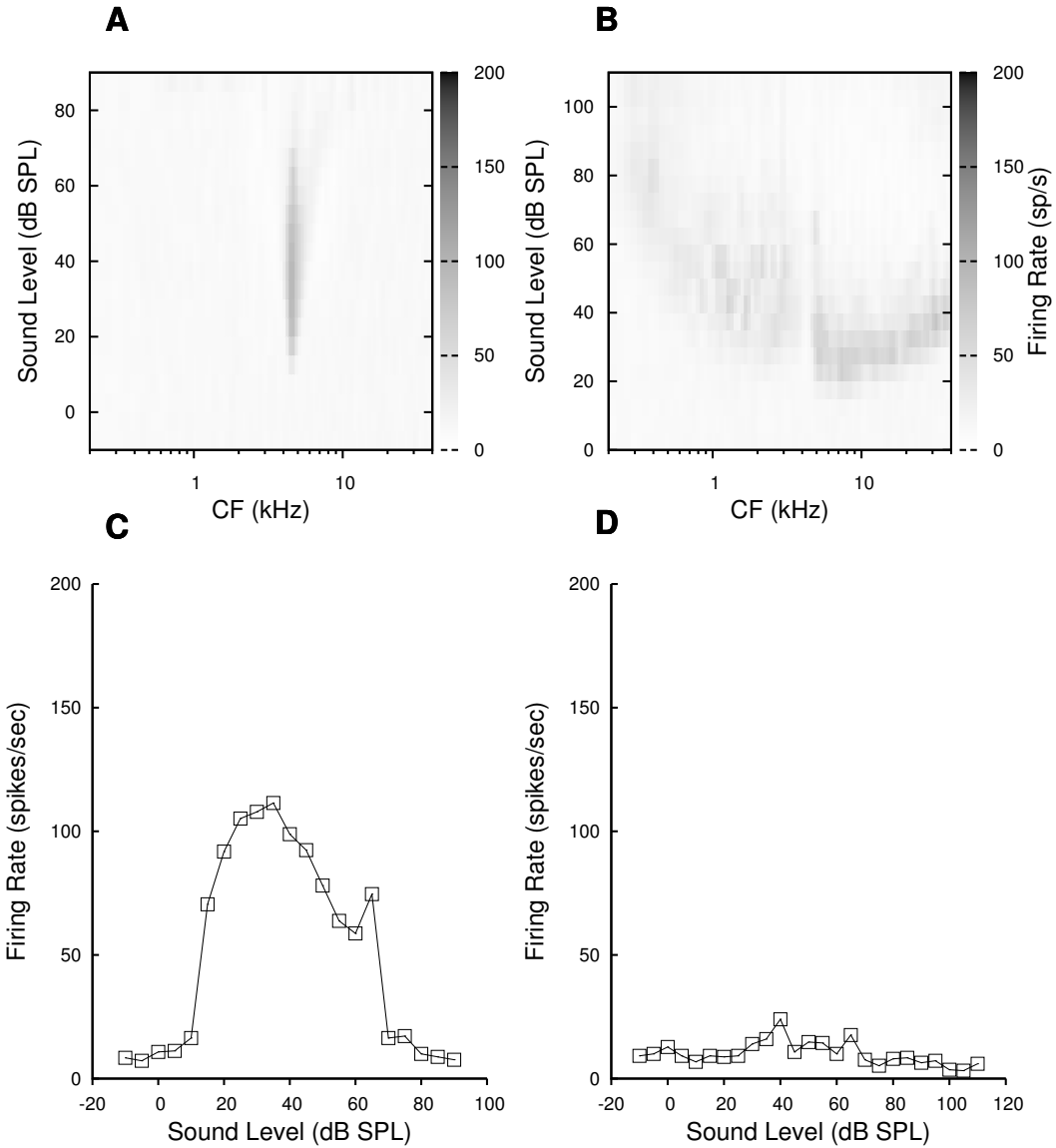


Figure 3.28: Response of the TV cell model across the whole network to a pure tone (on centre unit's CF, 4.513 kHz) and frozen broadband noise. A. Rate level response map of the TV cells to a pure CF tone (4.5 kHz, 50 msec, 100 repetitions). B. Noise rate level response map of the TV cells to broad-band noise (50 msec, 100 repetitions). C. Rate level responses of the central TV unit to a pure CF tone. D. Noise rate level response of the central TV unit to BNN.

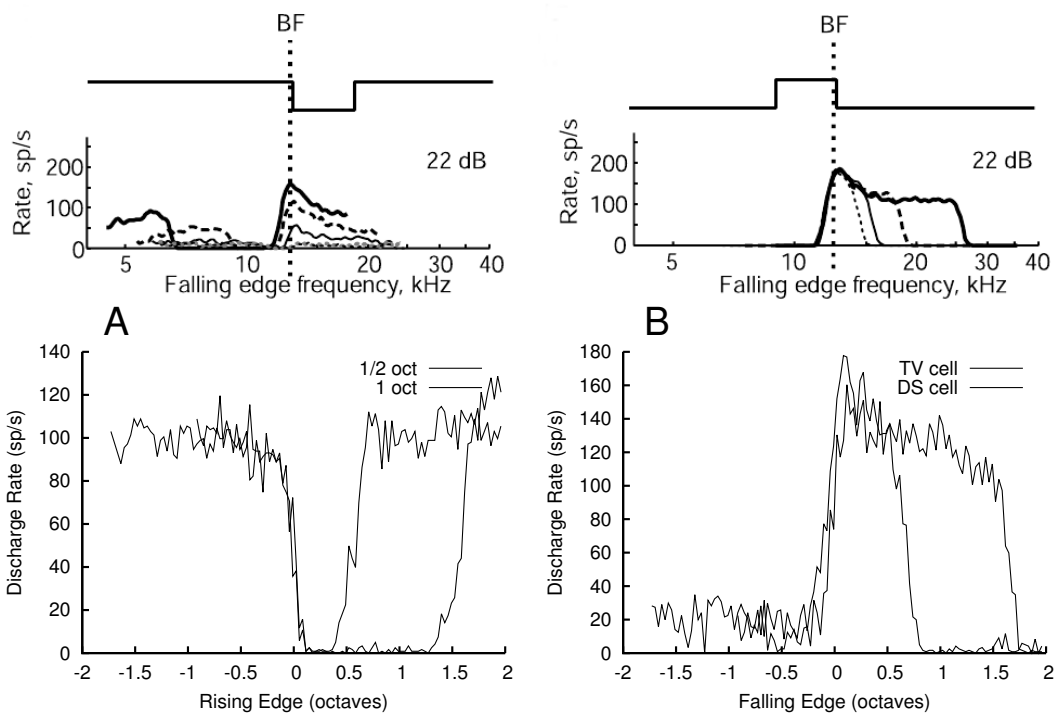


Figure 3.29: Response of optimised TV cell (CF 12.76 kHz) to notch and band-pass filtered noise sweeps with stimulus sound level at 50 dB SPL. Mean rate responses are plotted against the rising edge frequency of the notch and falling edge of the band-pass in octaves relative to 12.7 kHz. Top row is reproduced from Figure 9 E and F in Reiss and Young (2005).

3.6 T Stellate Cell Model: Three Chopper Subtypes

This section reports on the major output neurons in the CNSM model, TS cells, which are classified into three sub-types based on their regular firing or chopper characteristics.

3.6.1 Background

A considerable literature exists on the TS cells of the VCN (see Oertel et al. 2011). The first extracellular physiology studies classified supposed TS cells as regular-firing choppers (Bourk 1976; Pfeiffer 1966a). With further developments in analysis and classification techniques, TS cells were segregated into transiently adapting (ChT) and ChS sub-types (Blackburn and Sachs 1989; Young et al. 1988). In cats, Smith and Rhode (1989) were the first to perform simultaneous labelling of TS cells. They confirmed the physiological response of Type I multipolar neurons as units classified as choppers. This simultaneous classification and labelling was followed by others in gerbils (Feng et al. 1994; Ostapoff et al. 1994), guinea pigs (Arnott et al. 2004; Palmer et al. 2003), and rats (Paolini and Clark 1999; Paolini et al. 1997, 2004). In each of these studies, there were no morphological properties that segregated transient and sustained choppers, which indicates that synaptic inputs play an important role in determining the output of TS cells.

The spike-based coefficient of variation (CV) categorisation of TS cells is shown in Figure 3.30. CV is unitless and measures the regularity of interspike-intervals (by dividing the mean by the standard deviation). By accumulating intervals in time bins relative to the first spike, a time course of the neuron's regularity (mean, standard deviation and CV) throughout a stimulus is generated (Blackburn and Sachs 1989; Young et al. 1988). Sustained choppers maintain a stable CV below 0.2, throughout the entire stimulus. The transient chopper optimisation had two types defined by Paolini et al. (2005). The first transient chopper type, ChT₁, is categorised with CV starting below 0.2 then rising but staying below 0.3. The second transient type, ChT₂, is regular in the first 10 msec period, but rises to 0.3 or higher throughout the stimulus. OnC units can also be misclassified as ChT₂ due to two to three regular onset spikes followed by irregularly spaced spikes.

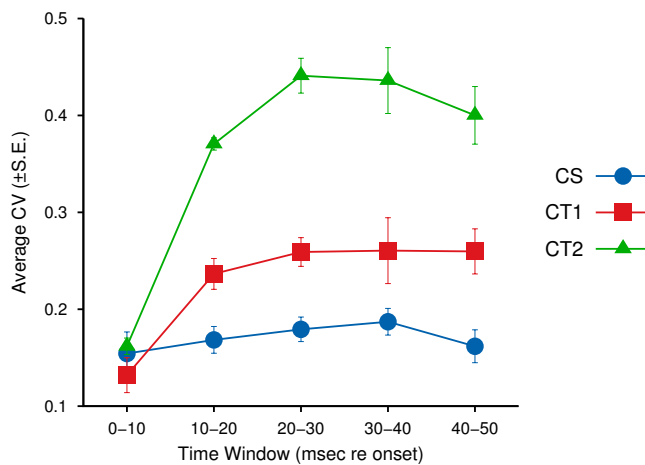


Figure 3.30: A. Regularity in chopper units measured using 10 msec interval CV at 30 dB relative to acoustic threshold. Data represents mean and standard deviation in units in each category. Data reproduced from Figure 2 in Paolini et al. (2005).

Figure 3.31 shows the average intracellular voltage (AIV) classification of chopper units in the rat into three types (Paolini et al. 2005). The technique of averaging intracellular membrane potential responses to acoustic stimuli to determine stochastic excitatory and inhibitory inputs was first used in the chopper units of gerbils (Feng et al. 1994; Ostapoff et al. 1994). Paolini et al. (2005) used similar averaging of TS and DS cell intracellular responses in rats as the basis for a thorough statistical analysis to separate chopper units into three distinct subtypes. The intracellular traces in Figure 3.31 along with the CV statistics in Figure 3.30 formed the basis for the optimisation routine of the TS cell model of each chopper type in the CNSM model. Intracellular responses provide greater details regarding the sub-threshold dynamics in neural models and the signal-to-noise ratio of synaptic inputs (Svirskis and Rinzel 2003).

3.6.1.1 Morphology of T Stellate Cells

Three to four primary dendrites emanate from the TS cell body, characteristic of stellate or multipolar neurons (Cant 1981, 1982). The dendrites and local axonal collaterals are restricted to the isofrequency lamina ($75\text{-}100\mu\text{m}$ perpendicular to ANFs) and extend between $150\text{-}300\mu\text{m}$ parallel to ANFs (Palmer et al. 2003; Smith and Rhode 1989). The cell body diameter of TS cells is typically $16\text{-}20\mu\text{m}$ in rat (Doucet and Ryugo 1997, 2006; Doucet et al. 1999), and $21.6 \pm 11.3\mu\text{m}$ in cats (Redd et al. 2002). The variation

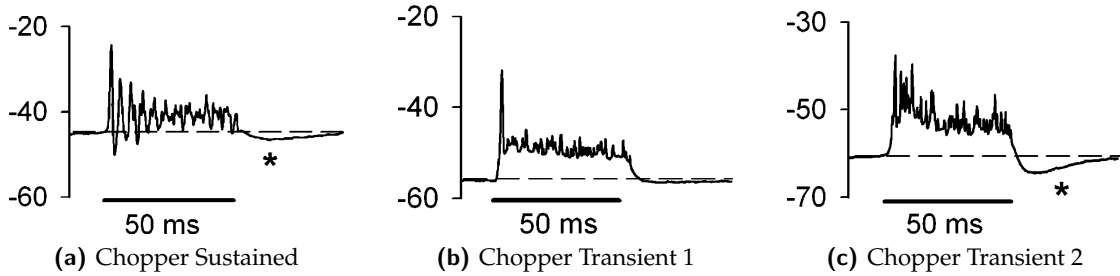


Figure 3.31: Average intracellular response to BF tone 30 dB above depolarisation threshold in chopper units (TS cells) in rats (Reproduced from Fig. 2, Paolini et al. 2005). A. Sustained chopper unit 01-864-004, CF 3.8 kHz. B. Transient chopper type 1 unit 01-857-007, CF 8.9 kHz. C. Transient chopper type 2 unit 01-305-014, CF 12.3 kHz. Hyper polarisation after tone indicated by asterisk.

is somata sizes based on chopper categorisation has been suggested in guinea pigs ($15.9 \mu\text{m}$ (ChS), $17.5 \mu\text{m}$ (ChT) Palmer et al. (2003)). Variation across the frequency regions of the VCN has also been shown in chinchilla TS cells; cell body sizes in low CF regions were 20% larger than cells in high CF regions (high CF $14.5 \pm 2.0 \mu\text{m}$, low CF $17.6 \pm 2.7 \mu\text{m}$ (Josephson and Morest 1998)). The diameter of the TS cell model's cell body was $21 \mu\text{m}$, representative of the average TS neuron in cats (Redd et al. 2002).

3.6.1.2 Cell-based Properties of T Stellate Cells

TS cells were first thought of as basic integrators with linear current-voltage relationship (type 1 current clamp) and a single exponential undershoot AP (Feng et al. 1994; Manis and Marx 1991; Oertel 1983; Oertel et al. 1988). Effective cell membrane time constant *in vitro* for different species was: (mice at room temperature) $9.1 \pm 4.5 \text{ msec}$ (Manis and Marx 1991); (rat at room temperature) $6.9 \pm 3 \text{ msec}$ (Isaacson and Walmsley 1995); and 8.8 ± 1.4 in dogs (Bal et al. 2009). TS cells do not have any low-threshold potassium channel (KLT) current channels (Manis and Marx 1991; Rothman and Manis 2003a) but do contain a specialised transient deactivating potassium current I_{KA} and hyperpolarisation-activated mixed cation current I_h (Rothman and Manis 2003a). I_{KA} is active at RMP and has a role in modulating repetitive APs and resetting when inhibition preceeds excitation Kanold and Manis (2001, 2005); Rothman and Manis (2003c). The Type 1-t RM neural model was used in TS cells due to its type 1 current-clamp property and the inclusion of I_{KA} .

3.6.1.3 Synapto-physiological properties of TS cells

The synaptic inputs to the TS cell model (as shown in Figure 3.1) include excitatory inputs from LSR and HSR ANFs; GABA-ergic inputs from GLG cells; and glycinergic inputs from DS and TV cells. Figure 3.32 shows the expected response of a TS cell to individual connections from different cells in the CNSM model. The membrane parameters for the single compartment TS cell model were default except for sodium conductance, which was set to zero. In this example, excitation from the afferent ANF inputs (LSR Figure 3.32A and HSR Figure 3.32B) show a large depolarisation. HSR inputs show a rapid onset and a slowly adapting depolarisation throughout the remainder of the stimulus. HSR fibres have a spontaneous rate of 50 Hz and recover to the same rate around 15 msec after the stimulus offset.

ANF input to TS cells is on-CF. This is due to the arrangement of their dendrites along the same direction. The number of ANF terminals on TS cells is small relative to their multipolar cousin, DS cells. An *in vivo* study in mice suggested TS cells receive as few as 5 excitatory inputs (Ferragamo et al. 1998b). ANF terminals rarely contact TS cells on their soma and are mainly on proximal dendrites (Cant 1981; Fay and Popper 1994; Josephson and Morest 1998; Redd et al. 2002; Ryugo et al. 1993; Ryugo 1992; Ryugo and Parks 2003; Smith and Rhode 1989; Tolbert and Morest 1982b). Terminals closer to the site of AP activation have a greater influence and are less likely to be shunted by inhibitory terminals along the dendrite. Josephson and Morest (1998) found some ANF terminals at the axon hillock of TS cells in chincillas. This would remove the integrative contribution of the neuron's intrinsic cell membrane properties and other synaptic inputs on the output of the neuron.

The CNSM model in Figure 3.1 shows the TS cell model receives synaptic inputs from all other neurons in the microcircuit. Glycinergic inputs to TS cells come from DS and TV cells (Oertel and Wickesberg 1993). Using the glycine-receptor blocker strychnine, Caspary et al. (1994) showed the physiological effects of glycine on the response area are within the frequency receptive field of chopper units. The distribution of DS and TV pre-synaptic cells are assumed to be centred on the post-synaptic TS cell. The timing of glycinergic inputs is important to controlling the response properties of TS cells (Needham and Paolini 2003, 2006; Paolini et al. 2004, 2005). The transient potas-

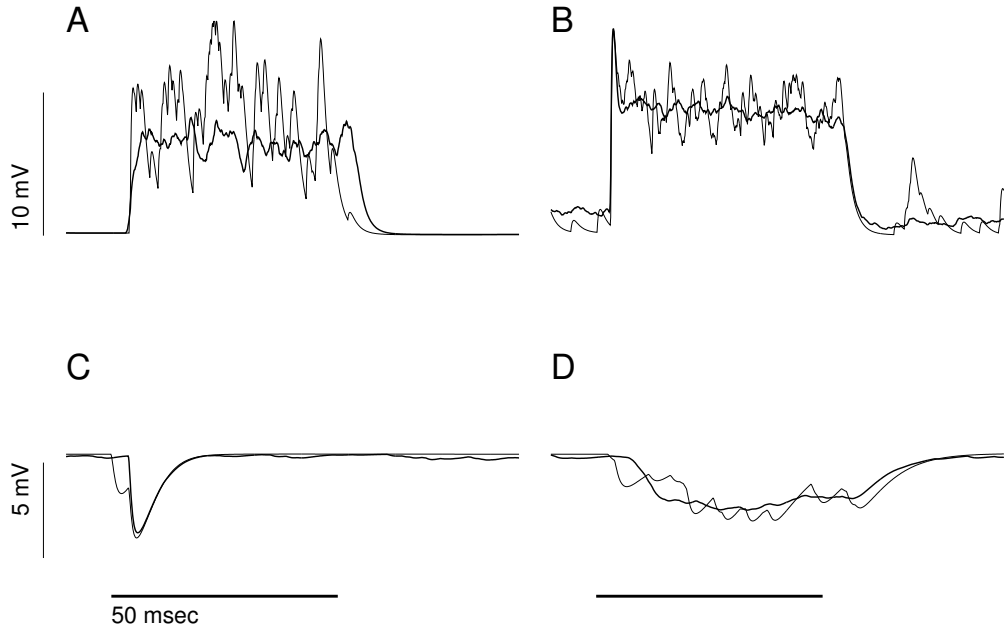


Figure 3.32: Intracellular membrane voltage response of a TS cell model to isolated synaptic inputs. A pure tone stimulus of 8.2 kHz at 85 dB SPL was presented to the CN network. The CF of the recorded TS unit was 8.267 kHz. Single stimulus responses are shown as a thin line and average response over 25 repetitions is shown as the thick line. A default Type I-t RM neural model was used and the sodium conductance (\bar{g}_{Na}) was set to zero to inhibit spike generation. All synaptic weights were set to 0.5 nS. A. 30 LSR ANFs onto AMPA synapses ($\tau = 0.36$ msec). B. 20 HSR ANFs (mean rate 250 spikes per second) onto AMPA synapses. C. 20 DS cell model glycinergic synapses ($\tau_1 = 0.4$ and $\tau_2 = 2.5$ msec). D. 15 GLG cell model GABA_A synapses ($\tau_1 = 0.7$ and $\tau_2 = 9$ msec).

sium current I_{KA} has been shown to increase the time to first spike when an inhibitory synapse input precedes an excitatory one (Kanold and Manis 2001, 2005). DS cells have a precise onset spike to load tones and broadband noise and provide fast inhibition that can reach the TS cell soma before excitation in off-CF tones (Paolini et al. 2004). TV cells do not have consistent PSTH responses to tones (Rhode 1999; Spirou et al. 1999) and their location in the DCN adds further delay to inhibiting TS cells (Wickesberg and Oertel 1990).

Figure 3.32 omits the non-linear dynamics of the action potential and the responses of the intrinsic currents in the RM neural model. The hyperpolarisation activation of I_h and I_{KA} currents due to inhibitory input are not evident. I_h influences the recovery from AP and modulates the regularity of the chopping behaviour (Rothman and Manis 2003c). I_{KA} is active at rest and is important in enhancing the first spike response across

TS cells to an oncoming stimulus (Kanold and Manis 2005; Paolini et al. 2004).

3.6.2 Implementation

Table 3.11 describes the particular design of the CNSM model and optimisation study parameters used in fitting network parameters of three TS cell model subtypes. The weights ($w_{LSR \rightarrow TV}$, $w_{HSR \rightarrow TV}$) of ANF synapses were used in the optimisation procedures to allow for fine adjustments to the strength of excitation. The number of synapses ($n_{LSR \rightarrow TS} = 30$, $n_{HSR \rightarrow TS} = 30$, $n_{DS \rightarrow TS} = 20$, $n_{TV \rightarrow TS} = 20$, $n_{GLG \rightarrow TS} = 20$), connectivity spread and delays were fixed at appropriate values.

The optimisation fitness function, F , of the TS cell model calculated the relative error between a combination of average intracellular membrane voltage measures and spike time statistics against the experimental data given by Paolini et al. (2005). Spike trains were collected for 25 repetitions of a 50 msec CF tone (5 msec on-off ramp) and analysed for PSTH and inter-spike interval characteristics (Blackburn and Sachs 1989; Pfeiffer 1966b; Young et al. 1988). CV of the inter-spike intervals were calculated over a 10 msec window, beginning at stimulus onset. Chopper units were required to have three regular intervals at the start of the stimulus otherwise the stimulus repetition was excluded from the CV calculations. Additional penalties were added to the cost function score if certain CV conditions weren't met. In all chopper units, if the CV value in the first 10 msec period was above 0.2 a penalty of 10 times the difference was applied. In the ChS model, if the CV value at any time period was above 0.3 a penalty of 100 times the difference was applied. In the ChT₁ model optimisation, for periods between 10 and 40 msec if the CV value was above 0.3 a penalty of 10 times the difference was applied. In the ChT₂ model optimisation, for periods between 10 and 40 msec if the CV value was below 0.3 or above 0.5 a flat 10 point penalty and a proportional penalty of 10 times the difference was applied.

The AIV statistics, first introduced by Paolini et al. (2005), included the onset ratio, adaptation shift and offset shift. The AIV measures highlight the balance of excitation and inhibition in TS cells and were designed to be independent of RMP and FSL. The effective stimulus onset was determined to be 2.5 msec prior to the peak in the reference AIV trace. A shift in onset peak between the reference trace and the test TS cell model's

Table 3.11: T stellate cell model summary

A Model Summary			
Populations	Six: HSR and LSR ANFs, GLG, DS, TV and TS cells		
Topology	Tono-topicity of the rat AN and CN		
Connectivity	$\text{ANF} \rightarrow \{\text{GLG}, \text{DS}, \text{TV}, \text{TS}\}$, $\text{GLG} \rightarrow \{\text{DS}, \text{TS}\}$, $\text{DS} \rightarrow \{\text{TV}, \text{TS}\}$, and $\text{TV} \rightarrow \text{TS}$		
Input model	ANF model: Instantaneous-rate Poisson neural model (Zilany and Bruce 2007)		
Neuron model	GLG cell: GLG neural model (see Section 3.3). DS cell: Type I-II RM model (see Section 3.4). TV cell: Type I-c RM model (see Section 3.5). TS cell: HH-like single-compartment Type I-t RM model		
Channel models	I_{Na} , \bar{g}_{leak} , I_{KHT} , I_{KLT} , I_{KA} , and I_{h} (Rothman and Manis 2003c)		
Synapse model	AMPA (single exponential), GABA _A and GlyR (double exponential)		

B Populations			
Name	Elements	Size	
HSR	Poisson generator	$N_{\text{HSR}} = 50$ per freq. channel	
LSR	Poisson generator	$N_{\text{LSR}} = 20$ per freq. channel	
GLG	Poisson generator	$N_{\text{GLG}} = 1$ per freq. channel	
DS	Type I-II RM model	$N_{\text{DS}} = 1$ per freq. channel	
TV	Type I-classic RM model	$N_{\text{TV}} = 1$ per freq. channel	
TS	Type I-transient RM model	$N_{\text{TV}} = 1$ per freq. channel	

C Connectivity			
Name	Source	Target	Pattern
$\text{ANF} \rightarrow \text{TS}$	ANF	TS	Narrowband connection at CF, zero spread, number $n_{\text{LSR} \rightarrow \text{TS}} = 30$ and $n_{\text{HSR} \rightarrow \text{TS}} = 30$, delay $d_{\text{ANF} \rightarrow \text{TS}} = 1.6$ msec. Weight parameters optimised ($w_{\text{LSR} \rightarrow \text{TS}}$ and $w_{\text{HSR} \rightarrow \text{TS}}$).
$\text{GLG} \rightarrow \text{TS}$	GLG	TS	Gaussian convergence, centred on-CF, spread $s_{\text{GLG} \rightarrow \text{TS}} = 20$, number $n_{\text{GLG} \rightarrow \text{TS}} = 20$, delay $d_{\text{GLG} \rightarrow \text{TS}} = 0.5$ msec. Weight $w_{\text{GLG} \rightarrow \text{TS}}$ optimised.
$\text{DS} \rightarrow \text{TS}$	DS	TS	Gaussian convergence, centred on-CF, spread $s_{\text{DS} \rightarrow \text{TS}} = 20$, number $n_{\text{DS} \rightarrow \text{TS}} = 20$, delay $d_{\text{DS} \rightarrow \text{TS}} = 0.5$ msec. Weight $w_{\text{DS} \rightarrow \text{TS}}$ optimised.
$\text{TV} \rightarrow \text{TS}$	TV	TS	Gaussian convergence, centred on-CF, spread $s_{\text{TV} \rightarrow \text{TS}} = 3$, number $n_{\text{TV} \rightarrow \text{TS}} = 20$, delay $d_{\text{TV} \rightarrow \text{TS}} = 1.0$ msec. Weight $w_{\text{TV} \rightarrow \text{TS}}$ optimised
ANF \rightarrow GLG, ANF \rightarrow DS, ANF \rightarrow TV, GLG \rightarrow DS, DS \rightarrow TV from previous CN model in Table 3.7C.			

Table 3.11: T stellate cell model summary - continued

D Neuron and Synapse Model	
Name	DS, TV and TS cell models
Type	Type I-II, I-c and I-tRM neural models (Rothman and Manis 2003c), conductance synapse input
Subthreshold dynamics	I_{Na} , I_{KA} , I_{KHT} , I_{h} , and \bar{g}_{leak} currents. See Chapter 2.
Spiking	Emit spike when $V(t) \geq \theta$

E Optimisation	
Input Stimulus	Pure tone stimuli with 50 msec duration, 2 msec cosine squared on/off ramp, and 20 msec delay. Optimisation of each chopper unit used the CF and 30 dB relative to the threshold sound level of the exemplar unit: CS (CF 3.9 kHz, thresh 40 dB SPL), CT1 (CF 8.2 kHz, thresh 85 dB SPL), CT2 (CF 12.4 kHz, thresh 35 dB SPL).
Parameters	$w_{\text{HSR} \rightarrow \text{TS}}$, $w_{\text{LSR} \rightarrow \text{TS}}$, $w_{\text{DS} \rightarrow \text{TS}}$, $w_{\text{TV} \rightarrow \text{TS}}$, $w_{\text{GLG} \rightarrow \text{TS}}$
Fitness Function	Input stimulus was presented to the CNSM model with intracellular voltage and spike timing output recorded from one TS cell model. Special AIV measures and spike statistics were calculated. CV statistics were measured in 10 msec windows from 2.5 msec after the stimulus onset. Three intracellular voltage statistic values and four CV values were compared against similarly calculated experimental data and were combined to a single fitness value through mean squares method.

AIV trace was used to compensate for differences in ANF onset delay.

Early attempts to use the original AIV measures, which used 1 msec windows, were unable to fit the model to the experimental data. The fluctuations in the TS cell model's AIV traces were mainly due to AP artifacts and only 25 stimulus repetitions. Increasing the number of repetitions would be computationally expensive, so the sampling window was set to 5 msec. The latency of the depolarisation peak was used to temporally shift the model's AIV trace for a stronger comparison with the exemplar unit.

The onset ratio measure was calculated as the ratio in peak onset AIV depolarisation (sum over the first 5 msec) relative to the sustained depolarisation (sum measured between 20 to 25 msec).

$$\text{Onset Ratio} = \bar{\mathbf{v}}|_{t=0}^{t=5} / \bar{\mathbf{v}}|_{t=20}^{t=25}. \quad (3.8)$$

The adaptation shift measurement calculates the drop in AIV depolarisation at the

end of the stimulus compared to the stable point around 20 msec after the onset

$$\text{Adaptation} = \bar{v}|_{t=18}^{t=23} - \bar{v}|_{t=43}^{t=48}. \quad (3.9)$$

Greater adaptation to a sustained stimulus is represented by a larger drop in depolarisation. Adaptation shift is caused by a combination of factors, but is mostly due to reduced excitation from ANF inputs which is caused by adaptation at the IHC-AN synapse. Due to simulation complications, adaptation measures were averaged over 5 msec rather than the 1 msec period used in the original paper (Paolini et al. 2005). The second adaptation measure was shifted from around 50 msec to 45 msec to avoid rapid AIV drop-off in some units with a delayed onset peak that shifted the AIV trace.

The offset shift measures the effects of sustained inhibition and recovery of excitation 10 msec after the stimulus offset

$$\text{Offset} = \bar{v}|_{t=-10}^{t=0} - \bar{v}|_{t=60}^{t=65}. \quad (3.10)$$

Negative values indicate post-stimulus AIV hyperpolarisation which is caused by reduced excitation or the presence of inhibition. The post-stimulus AIV was averaged over 5 msec from 60 msec to avoid errors in optimisation simulations.

Three CF tone bursts at different SPL above the exemplar units' acoustic threshold (20, 30 and 40 dB re θ) were used in all three TS cell model optimisations. Figure 3.33 shows the results of the chopper sub-groups for adaptation shift (see Equation 3.9) and average post-tone hyperpolarisation (see offset shift Equation 3.10). These data points, along with the CV data points in Figure 3.30 at 30 db re θ , were used in the fitness function as a root mean squared comparison against the TS cell model. Population data given by Paolini et al. (2005) was used where appropriate, otherwise an exemplar unit was chosen to fill remaining data points. ChS unit population data for AIV results was limited to one data point at offset shift at 30 dB re θ (1.6 ± 1.0 mV). The unfilled triangles in Figure 3.33 were measured from the average membrane voltage trace of unit 01-859-013 (Figure 3 in Paolini et al. 2005). Adaptation shift in ChT 1 and ChT 2 units increased with increasing SPL (Figure 3.33A), reaching a peak at 30 dB re θ . ChT₂ units consistently had a stronger inhibitory influence (adaptation and offset shifts) compared

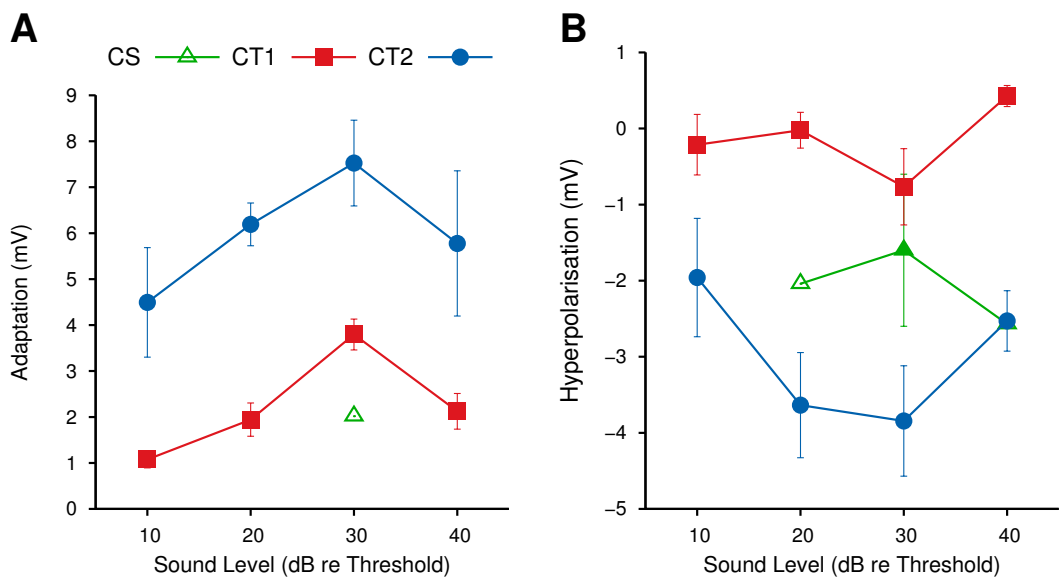


Figure 3.33: A. Adaptation shift (Equation 3.9) at different sound levels (relative to acoustic threshold, re θ). Transient chopper data, representing average within ChT₁ and ChT₂ groups (reproduced from Figure 6A in Paolini et al. 2005). B. Average membrane voltage hyperpolarisation after stimulus offset (Equation 3.10) at different sound levels re θ . Transient chopper data uses group averages from Figure 6B in Paolini et al. (2005). The offset shift in ChS units (green triangles) uses the group average at 30 dB re θ (1.6 mV, filled triangle) and measurements from ChS unit 01-859-013 (CF 3.9 kHz, Th 25 dB, see Figure 3 Paolini et al. (2005)) at 20 and 40 dB re θ (unfilled triangle).

to ChT₁ for all SPL above threshold. The variation in acoustic thresholds in the experimental data presented further challenges to generating similar stimulus and input rates for each of the TS cell subtypes. The acoustic threshold of the TS cell model was set to 20 dB SPL, so the three tone bursts in the optimisation routine were presented at 40, 50 and 60 dB SPL. In this region of the rate level curve, all input cells of the TS cell are active and the TS cell model is at the end of the DR or in the saturation region. The CF of the simulated TS cell model was set to 9.1 kHz (mean CF of chopper units in Paolini et al. (2005)) to normalise properties of the TS cell models to improve comparison of optimised parameters.

3.6.3 Optimisation Results

3.6.3.1 Sustained Chopper

Figure 3.34 shows the optimisation results for the ChS subtype of the TS cell model. The exemplar ChS unit (CF 3.9 kHz) had an intracellular depolarisation threshold, θ , at 10 dB SPL and a firing rate saturation at 75 dB SPL. The stimuli for the optimisation routine were three pure CF tones at 20, 30 and 40 dB re θ (above the acoustic threshold 20 dB SPL) of the exemplar unit (40, 50 and 60 dB SPL, respectively). A 20 msec delay was included to allow the model to reach a sustained RMP. The TS cell model used in the ChS optimisation, hereafter called the ChS model, used the Type I-t RM neural model. The output spiking and intracellular responses of the best parameters found by the optimisation are shown in Figure 3.34. The optimised ChS model had very high excitatory input ($w_{LSR \rightarrow TS} = 1.8$ nS, $w_{HSR \rightarrow TS} = 0.491$ nS) and very low inhibitory strength from all three interneurons ($w_{DS \rightarrow TS} = 0.0734$ nS, $w_{TV \rightarrow TS} = 0.173$ nS, $w_{GLG \rightarrow TS} = 0.00895$ nS). The mean rates for the optimised ChS unit at 20, 30 and 40 dB re θ were 191.6, 214.4 and 230.4 spikes per second, respectively. These results show the ChS model had a high firing rate that was still increasing, which indicates the model was highly active and the stimuli range was in the upper DR region of the rate level response.

The final error used in the ChS model optimisation routine was 26.4278. Due to the different magnitudes of the CV and AIV measures, this error has no physical units or

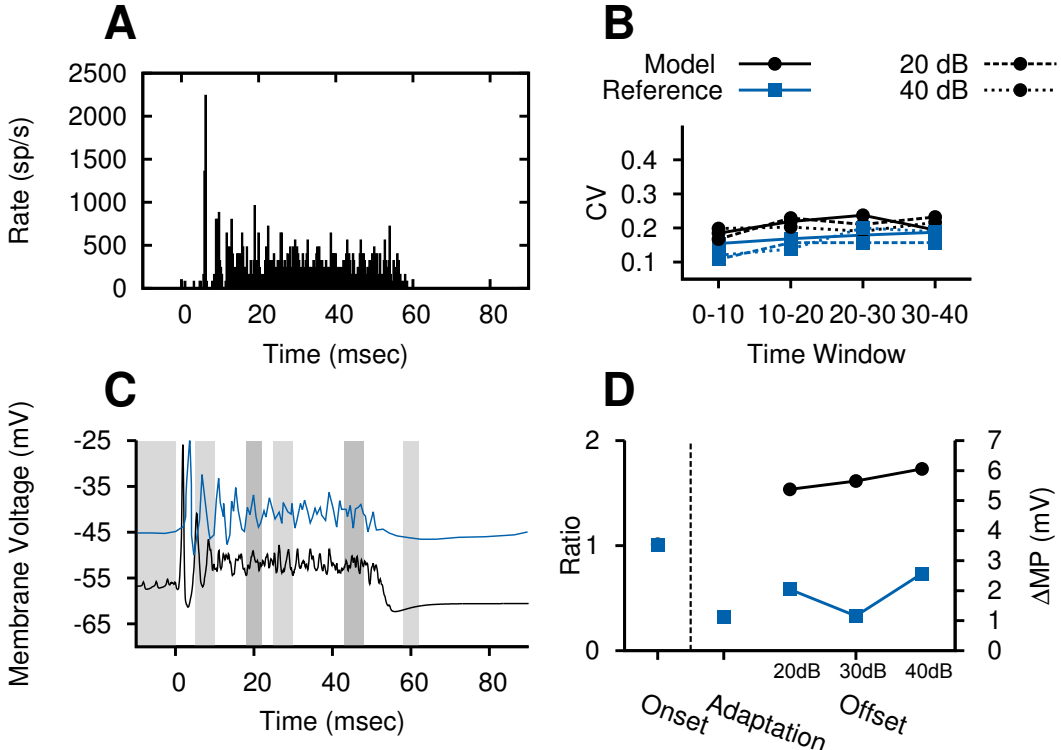


Figure 3.34: Optimisation results for the sustained chopper subtype of the TS cell model. The reference data for ChS unit 01-864-004 from Paolini et al. (2005), with CF 3.9 kHz, is shown in blue and the optimised model is shown in black (CF 9.1 kHz). The stimulus (pure tone 9.1 kHz stimulus) was repeated 50 times for this analysis but during the optimisation routine the repetition was 25. A. PSTH of the TS cell model (CF 9.1 kHz) to a pure tone at CF at 30 dB re θ (50 dB SPL). B. Coefficient of variation averaged over 10 msec periods at 20, 30 and 40 dB re θ . C. Reference (blue) and ChS cell model AIVs at 30 dB re θ . Note: shaded areas indicate AIV regions used in D. The temporal adjustment to match the onset peaks was 2.5 msec. D. AIV measures including (a) onset ratio (30 dB re θ , Equation 3.8), (b) adaptation of sustained depolarisation (20,30,40 dB re θ , see Equation 3.9), and (c) post-tone hyperpolarisation (20,30,40 dB re θ , see Equation 3.10). The RMP, calculated from -10 to 0 msec, for the reference unit and best-fit ChS model was -45.1 and -64.22 mV, respectively.

references. Weighting was used to equalise the magnitudes of the CV and AIV error metrics and additional penalties were applied when the model results were outside acceptable ranges. The best fit model received no additional penalties. The RMS error between the CV data of the optimised ChS model and the exemplar ChS unit (Figure 3.34B) was 0.034 combined (20dB: 0.027, 30dB: 0.021, 40dB: 0.047). In relative terms the mean CV at 30 dB re θ was 0.192 and 0.172 for the modelled and exemplar ChS units, respectively. Figure 3.34D shows the AIV measures used in the optimisation. The onset ratio and the adaptation AIV difference were only measured for the 30 dB re θ due to the limited availability of experimental data. The ChS model's onset ratio, 1.0125, was smaller than the exemplar unit's, 1.0417. The onset ratio was affected by the synchronisation of AP peaks and troughs at onset that cancelled each other out in the averaging of the membrane voltage. The adaptation AIV difference was 1.67 mV for the model and 0.94 mV for the exemplar unit. The drop-off in the experimental unit's AIV (Figure 3.34C) at the end of the stimulus affected the adaption measure by increasing the apparent adaption drop in the AIV. The post stimulus offset in the experimental ChS unit was below 3 mV for each of the stimuli. The ChS model's post-stimulus offset hyperpolarisation was consistently above 5 mV. This was due to spontaneous spikes preceding the stimulus (increasing the apparent RMP) and the strong hyperpolarising dip due to inhibition and post-stimulus recovery of HSR units producing reduced excitatory input to the model.

3.6.3.2 Transient Chopper 1

The optimisation results of ChT₁ are shown in Figure 3.35 along with the experimental data for the ChT₁ subtype (exemplar unit unit 01-857-007, CF 8.2 kHz Paolini et al. 2005). The depolarisation threshold for the exemplar unit was 55 dB SPL, close to the average 47.2 dB SPL for all ChT₁ units (Paolini et al. 2005). The threshold for the simulated model was 20 dB SPL so that the three stimuli to accommodate comparisons with the other chopper models and for consistency in the inputs to the model.

Excitatory synaptic weights ($w_{LSR \rightarrow TS}$ 1.62 nS, $w_{HSR \rightarrow TS}$ 0.886 nS) were balanced with moderate to low glycinergic synaptic input from DS and TV cells ($w_{DS \rightarrow TS}$ 0.405 nS, $w_{TV \rightarrow TS}$ 0.324 nS). The GABAergic input weight was very low ($w_{GLG \rightarrow TS}$ 0.142 nS),

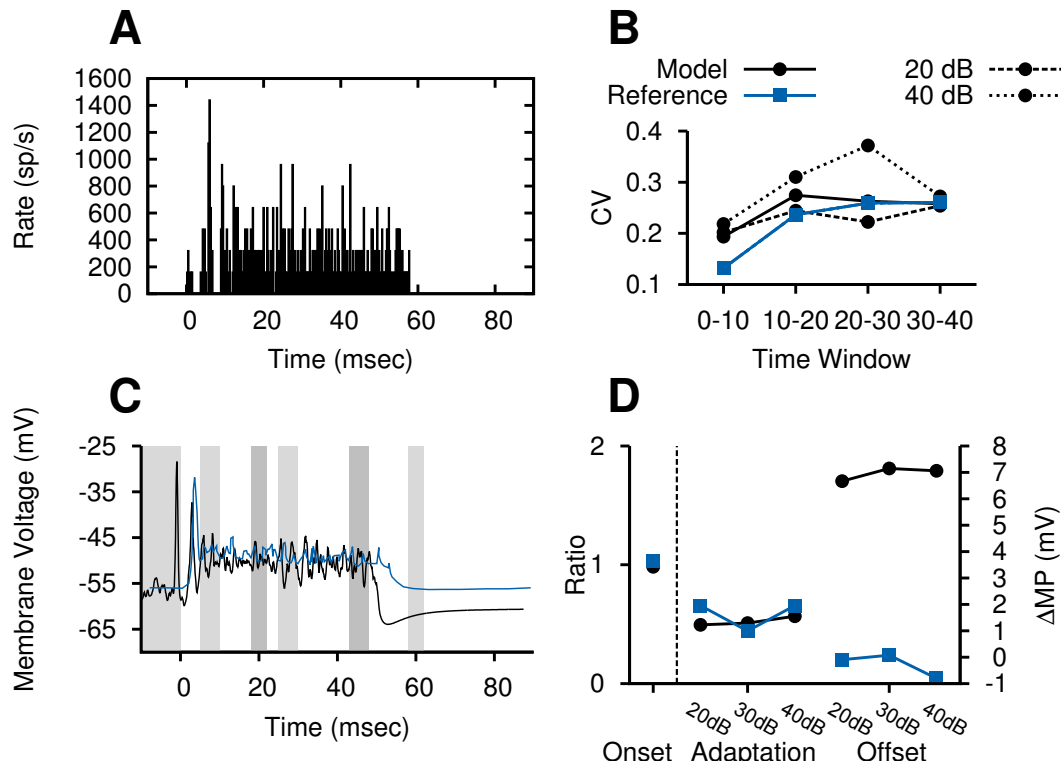


Figure 3.35: Transient chopper type 1 optimisation results of the TS cell model. Pure tones at 9.1 kHz pure tone and at 40, 50, 60 dB SPL sound levels were used in the optimisation procedure to reproduce intracellular and spiking statistics of unit 01-857-007 (CF 8.2 kHz, threshold 55 dB SPL Paolini et al. 2005). The RMP for the reference unit and best fit ChT₁ model was -55.98 and -64.97 mV, respectively. See Figure 3.34 for figure configuration. A. PSTH of the optimised ChT₁ model at 30 dB θ (50 repetitions, CF 9.1 kHz, 50 dB SPL). B. CV statistics of spike times. C. AIVs over 50 repetitions of the optimised ChT₁ model and experimental unit at 30 dB θ. The temporal adjustment of onset peaks was 2.2 msec. adjustment to match the onset peaks was 2.5 msec. D. AIV measures.

but the longer GABA_A time constant would cause reasonable inhibition to the TS cell throughout the stimulus.

Figure 3.35 shows the spike and AIV statistical measures of the optimised ChT₁ model. The PSTH of the model at 30 dB re θ (50 dB SPL) is shown in Figure 3.35A. The mean rates for the optimised ChT 1 model at 20, 30 and 40 dB re θ were 212.8, 212.8 and 209.6 spikes per second, respectively. Consequently, the optimisation stimulus levels were in the saturation region of the cell's rate level curve and not in the expected dynamic range region.

The final error of the optimised ChT₁ unit at 25 repetitions was 89.1398, an arbitrary value that is a combination of weighted CV and AIV differences. The characteristic CV response of the ChT₁ was highly regular in the first 10 msec (less than 0.2), then transiently adapted to regularity below 0.3 for the remainder of the stimulus. The combined RMS error of the CV data was 0.064. The CV at 30 dB re θ was closest fit to the reference data (RMS error 0.034). The RMS error of the 20 and 40 dB re θ CV profiles was 0.038 and 0.098, respectively. The AIV traces in Figure 3.35C show the differences in the exemplar unit and the simulated TS cell model. The repetitive firing in the first 20 msec of the ChT₁ AIV trace resulted in consistent membrane voltage fluctuation that was not present in the exemplar unit. The onset ratio statistics of the exemplar and optimised ChT₁ units were 0.983 and 1.01, respectively, at 30 db re θ . The optimised ChT₁ unit was consistently below the adaptation statistic of the exemplar unit at each of the stimulus levels. The post-offset hyperpolarisation results of the exemplar ChT₁ unit were not consistent with the inhibitory behaviour of ChT₁ units. The lack of hyperpolarisation in experimental unit recordings can be explained by one or more of (1) the position of the electrode relative to the site of AP generation, (2) the distance to inhibitory synapses on dendrites, and (3) shunting of excitatory currents from distal inhibitory synapses.

3.6.3.3 Transient Chopper 2

The ChT₂ model optimisation used average population data for CV data and unit 01-305-014 (CF 12.4 kHz (Paolini, Clarey, Needham, and Clark 2005)) for IV measure data. The reference unit had a low depolarising threshold (5 dB SPL) so the experimental stimuli (25, 35 and 45 dB SPL) were lower relative to those used in the ChT 1 model

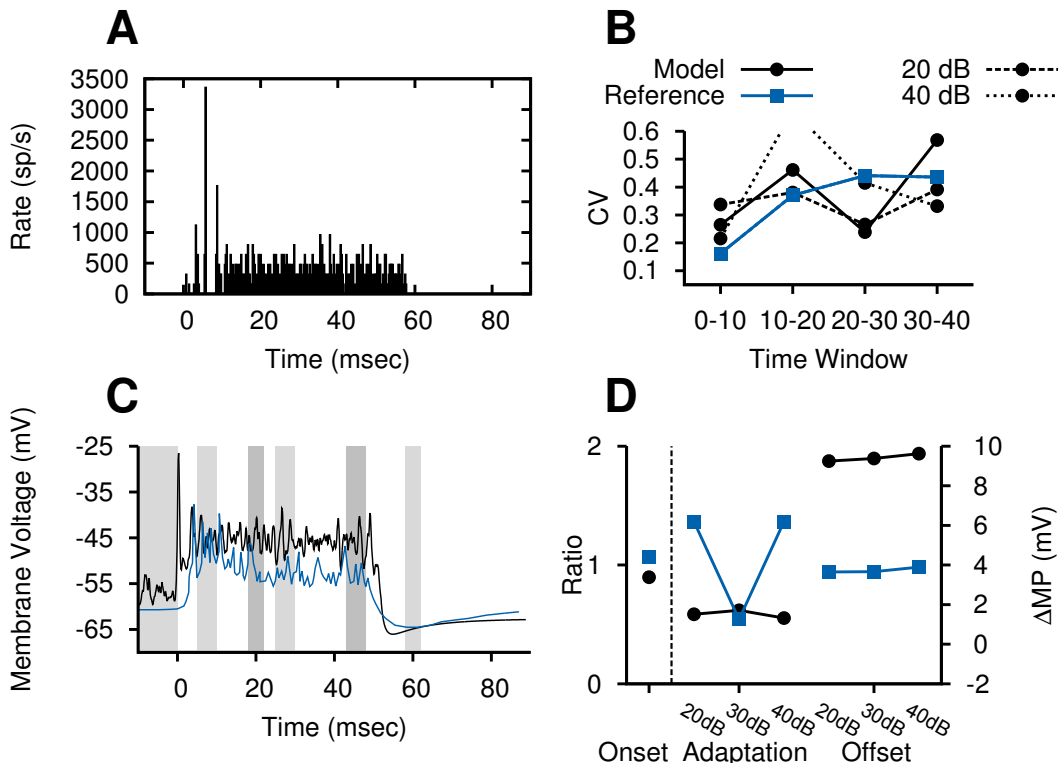


Figure 3.36: TS cell model optimisation results for the second transient chopper subtype. The experimental data was reference unit 01-305-014 (CF 12.57 kHz, threshold 5 dB SPL) (Paolini et al. 2005). The RMP for the reference unit and best ChT₁ model was -60.63 and -64.95 mV, respectively. See Figure 3.34 for figure configuration. A. PSTH of the model unit in response to a 9.1 kHz tone at 30 dB re θ (50 dB SPL). B. CV statistics of the model and reference units. C. AIVs over 50 repetitions at 30 dB re θ (50 dB SPL). D. AIV measures.

optimisation routine (40, 50 and 60 dB SPL). The main difference between the transient chopper types is their CV values after 10 msec, with the ChT 2 type becoming irregular (i.e. having a CV value over 0.3) and maintaining that irregularity for the remainder of the stimulus. ChT 2 has a higher reduction in onset depolarisation (90.2%) compared to ChT1, and post-tone inhibition is greater (+8.82 mV at 30 dB re θ) (Paolini, Clarey, Needham, and Clark 2005).

Figure 3.36 shows the results for the optimised ChT₂ model. The characteristic CV response of the ChT₂ unit was closely matched at 30 and 40 dB re θ (Figure 3.36B). The mean rates for the optimised ChT₂ unit at the three SPL tones were 274.4, 268.0 and 259.2 spikes per second, respectively. Synaptic activity from GLG, TV and DS cell model inputs reduced the regularity of the spike intervals after 10 msec and increased CV throughout the stimulus. The RMP for the experimental and model ChT₂ units was -60.63 and -64.96 mV, respectively. The experimental ChT₂ unit had a greater reduction in onset depolarisation (90.2%) compared to ChT₁ units at 30 dB re θ (Paolini et al. 2005). The adaptation statistic results of the optimised ChT₂ model did not demonstrate a similar drop (around 6 mV) to that shown in the reference data Figure 3.36D, despite reduction in firing rate and strong changes in CV. The post-tone inhibitory offset of the experimental ChT₂ unit was the greatest of all the chopper subtypes (8.82 mV at 40 dB re θ). The optimised ChT₂ unit had a stable post-offset inhibition around 4 mV at the three stimulus levels.

Excitatory synaptic weights ($w_{LSR \rightarrow TS}$ 2.11 nS, $w_{HSR \rightarrow TS}$ 1.7 nS) were balanced with moderate to low glycinergic synaptic input ($w_{DS \rightarrow TS}$ 0.412 nS, $w_{TV \rightarrow TS}$ 0.153 nS). The GABAergic input weight was very low ($w_{GLG \rightarrow TS}$ 0.383 nS), but the loud input stimulus (60 dB SPL) would cause reasonable inhibition to the TS cell throughout the stimulus. The final error of the optimised ChT₂ unit was 255.185, with the greatest weighting from the CV data.

3.6.4 Verification of the TS Cell Models

Figures 3.37, 3.38 and 3.39 show the responses of the TS cell models across the nuclei to the verification stimuli, CF tones in the central channel and broadband noise.

The ChS model's response area to tones, Figure 3.37A, show a narrow receptive field

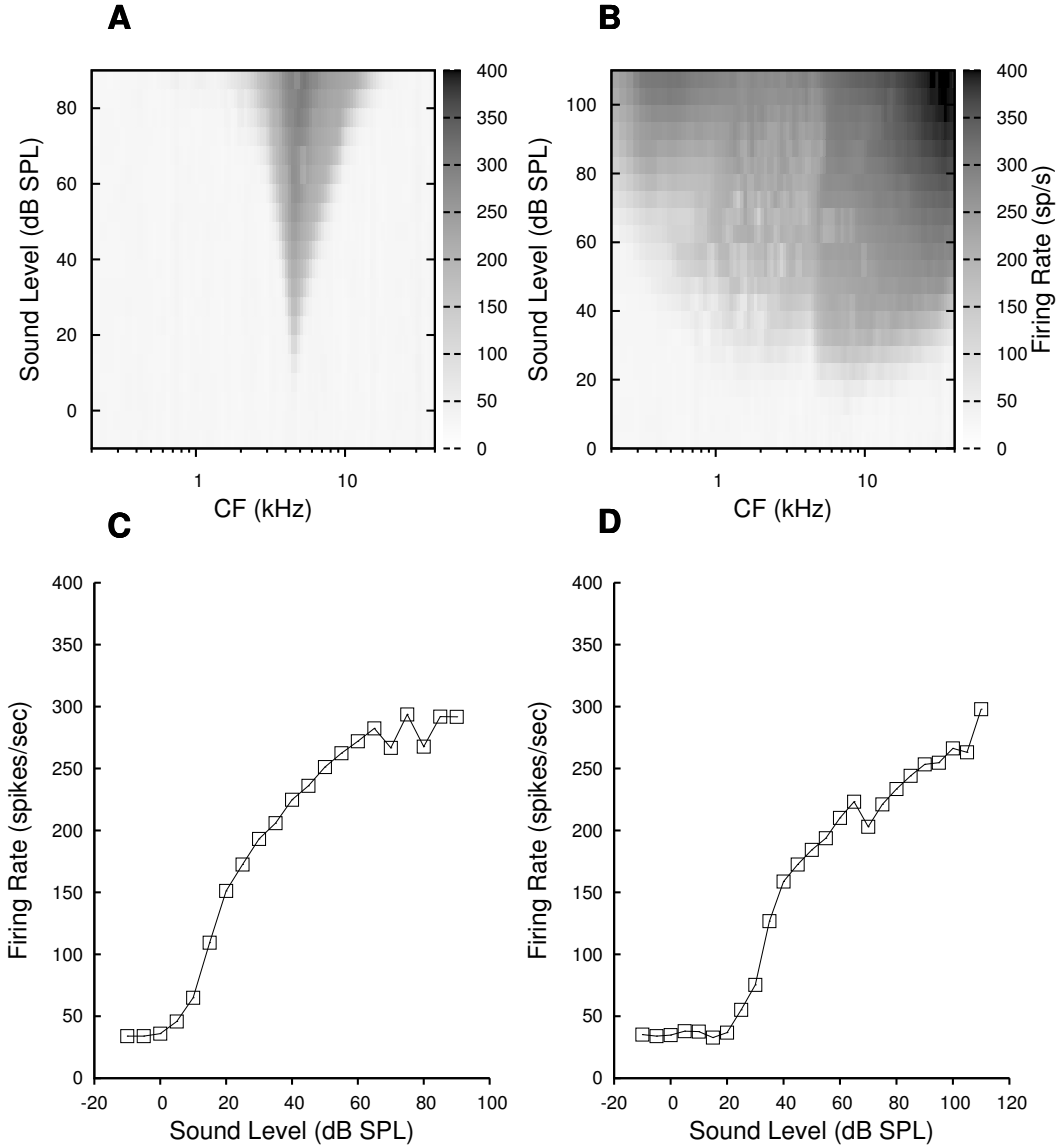


Figure 3.37: Response of the ChS subtype TS cell model across the whole network to a pure tone (on centre unit's CF, 4.513 kHz) and broadband noise. A. Rate level response map of the TS cells to a pure CF tone (4.5 kHz, 50 msec, 100 repetitions). B. Noise rate level response map of the cells to broad-band noise (50 msec, 100 repetitions). C. Rate level responses of the central unit to a pure CF tone. D. Noise rate level response of the central unit to BNN.

with a threshold at 10 dB SPL and a Q_{10} of 0.143 octaves (three active channels at 20 dB SPL). The on-CF unit had a large dynamic range to tones (± 60 dB, Figure 3.37C) due to similar strength of synaptic inputs from LSR and HSR fibres. The ChS model's response to noise, Figures 3.37B and D, were monotonic with acoustic threshold dependent on HSR inputs.

The ChT₁ model's response area to tones, Figure 3.38A, show a narrow receptive field with a threshold and Q₁₀ similar to the ChS model. The on-CF unit had a small dynamic range (around 20 dB, Figure 3.38C), saturating around 30 dB with rate just under 250 sp/s. The unit also showed slight depression of the rate-level curve at high sound levels, likely due to inhibitory influences. In response to noise, the ChT₁ model's threshold increased and its saturation rate decreased to just over 200 sp/s (Figures 3.37B and D).

The ChT₂ model's response area to tones and noise is shown in Figures 3.39A and B. The tuning of the tone response area is similar to the ChS and ChT₁ models but with higher firing rates. The on-CF ChT₂ unit had a high spontaneous rate (\$\approx\$100 sp/s) and a high maximum firing rate (over 350 sp/s) at 30 dB SPL. Its tone rate level curve (Figure 3.39C) had a small dynamic range (around 20 dB) and immediate linear depression. In response to noise, the ChT₁ model's had a compressed rate-level curve (Figure 3.37D) with increased threshold similar to the other models, reduction in its maximum firing rate and reduction of rate at high SPL similar to the ChT₁ model.

3.6.5 Overview of TS Cell Model Results

The primary purpose of the CNSM model is to regulate the output behaviour of the main projection neurons, TS cells. The diversification of the physiological responses of TS cells into three different chopper response categories required three optimisation procedures to fit unique synaptic parameters to their corresponding target responses. The TS cell optimisation study attempted to constrain the many network parameters using different modalities: intricate intracellular voltage statistics and regularity of spike interval statistics.

The CV statistics used in the chopper optimisations were the dominant modality in fitting the cell model and network parameters. The regularity of inter-spike intervals in TS cells creates its typical chopper PSTH and is best highlighted by the time varying CV. The ChS model matched the sustained regular firing of the exemplar unit, performing best at 30 dB re θ with RMS error of 0.034. The ChT₁ model had an RMS error of 0.074 at 30 dB re θ , which was stimulated at a lower level than the experimental unit (50 dB SPL against 85 dB SPL), which may have had more active inputs from the other cells

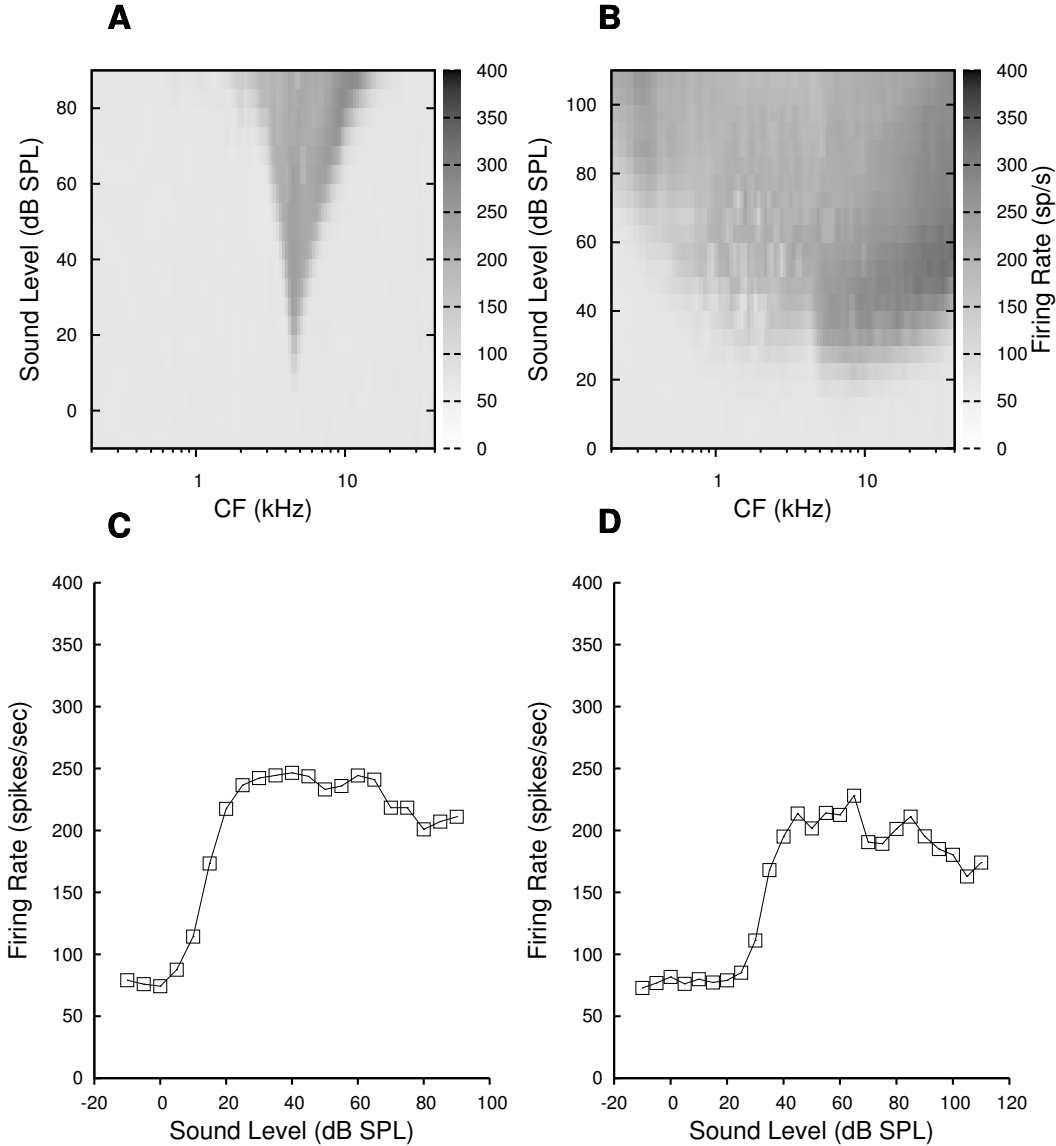


Figure 3.38: Response of the ChT₁ subtype TS cell model across the whole network to a pure tone (on centre unit's CF, 4.513 kHz) and broadband noise. A. Rate level response map of the TS cells to a pure CF tone (4.5 kHz, 50 msec, 100 repetitions). B. Noise rate level response map of the cells to broad-band noise (50 msec, 100 repetitions). C. Rate level responses of the central unit to a pure CF tone. D. Noise rate level response of the central unit to BNN.

in the CNSM model. The CV data of the ChT₂ model satisfied the expected responses at 20 and 30 dB re θ , but failed to generate regular onset spikes at 40 dB re θ . Along with stringent penalties to constrain the CV response output in the TS cell optimisation procedure, the CV measure was an effective tool in the optimisation of the TS cell model.

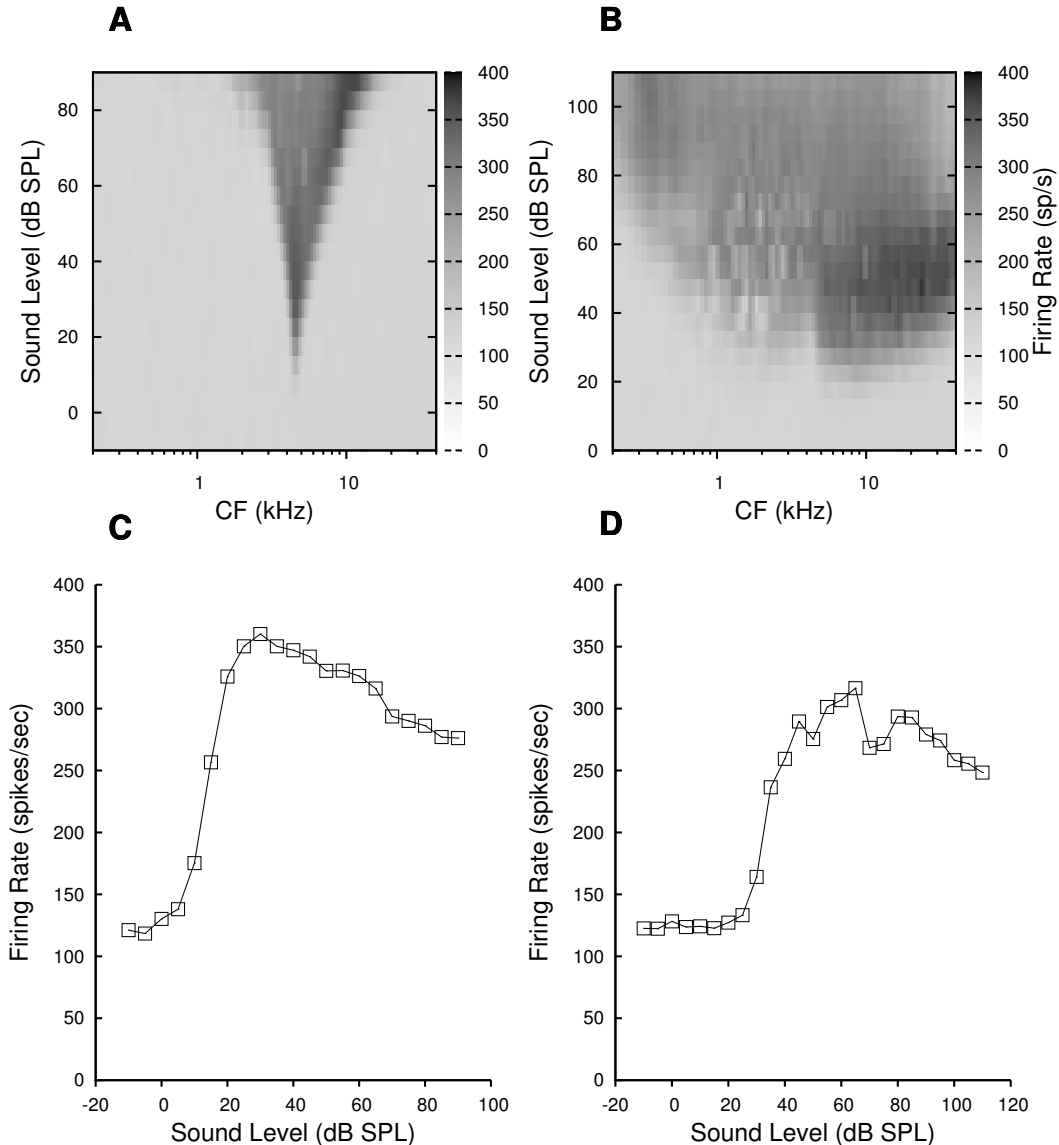


Figure 3.39: Response of the ChT₂ subtype TS cell model across the whole network to a pure tone (on centre unit's CF, 4.513 kHz) and broadband noise. A. Rate level response map of the TS cells to a pure CF tone (4.5 kHz, 50 msec, 100 repetitions). B. Noise rate level response map of the cells to broad-band noise (50 msec, 100 repetitions). C. Rate level responses of the central unit to a pure CF tone. D. Noise rate level response of the central unit to BNN.

Intracellular voltage data contains more information regarding synaptic inputs and sub-threshold membrane dynamics than mere spikes alone. The AIV statistics of (Paolini et al. 2005) were modified to 5 msec sampling to allow for less repetitions in the optimisation routines. For both the offset ratio and adaptation MP difference measures, the optimal neurons' responses were within the accepted bounds for noise.

The results of the post-stimulus MP offset difference show the limitations of comparing real and simulated intracellular recordings. In the single-compartment neural model, the depression and recovery at the end of a stimulus is due to the recovery properties of the ANF model and inhibition from IPSPs with longer time constants than the EPSPs of ANFs. The experimental recordings in the exemplar TS cell have a high RMP and minimal post-tone offset. TS cells of mammals are known to have very few somatic contacts (Cant 1981, 1992; Josephson and Morest 1998; Smith and Rhode 1989). Inhibitory inputs on the dendrites act by shunting excitatory current and may not be visible at recording sites in the soma. This may be the cause of the weaker optimisation results for adaptation and post-stimulus offset membrane difference measures. Increasing the morphological complexity of the neural model (i.e. using a passive dendrite segment) could help to improve the TS model and improve the optimisation match for the chopper subtypes.

The expected output of gradual increase in the strength of inhibition from ChS to ChT₁ to ChT₂ is only present in GLG cell inputs to the TS cell models. DS cell inhibition is strongest in each of the TS models and the weights of TV cell inputs are considerably lower. The SPL of the three CF tones used in each optimisation was set based on an acoustic threshold of 10 dB SPL that differed from the exemplar units'. In this case the input inhibitory cells (GLG, DS and TV cells) were all moderately active and may have differed from the range of possible input rates and dynamics of the experimental data.

3.7 Discussion

The T stellate cells featured in the CNSM model form one of the major ascending auditory pathways through the brainstem. They enable a high fidelity sensory input to be passed to higher order centres, by reproducing the spectrum in a robust fashion (Blackburn and Sachs 1990; May 2003) and synchronisation to significant periodic frequencies (Keilson et al. 1997). The CNSM model facilitates the investigation of the neural network processing properties and capabilities of the stellate microcircuit. This section sets out the limitations of the CNSM model and its implications for optimisation methods in other BNN models.

Table 3.12: Optimised synaptic weight and number of connections in the CNSM model. The units of synaptic weight are in 10^{-9} Siemens with the exception of GLG cell inputs that are unitless.

	GLG	DS	TV	ChS	ChT ₁	ChT ₂
HSR	0.0487×1	0.1672×125	0.6451×20	0.4908×30	0.8856×30	1.699×30
LSR	0.5166×1	11.03×84	5.172×20	1.799×30	1.62×30	2.112×30
GLG	0×0	0.5315×5	1.293×20	0.0089×20	0.1418×20	0.3827×20
DS	0×0	0×0	1.793×30	0.07337×20	0.4053×20	0.4116×20
TV	0×0	0×0	0×0	0.1732×20	0.3243×20	0.1532×20

3.7.1 Optimised Parameters of the CNSM Model

Table 3.12 show the aggregated optimised parameter values of the synaptic strength in the CNSM model. One important point for the table is that the synaptic weights of LSR fibres in the CNSM model appears to have a stronger value than HSR ANFs in each of the CN units. Their large dynamic range was beneficial to the GLG and DS cell models that were fitted to experimental data with monotonic rate level responses. For TS and TV cell models, LSR ANFs are the only excitatory source that counters the increasing inhibitory sources, GLG and DS cells, at high SPL. TV cells have a particularly high level of DS and GLG cell inhibition compared to the different TS cells models. The expected output of gradual increase in the strength of inhibition from ChS to ChT₁ to ChT₂ is only present in GLG cell inputs to the TS cell models. DS cell inhibition is strongest in each of the TS models and the weights of TV cell inputs are considerably lower.

The number of connection, connectivity spread and delay parameters were assigned values based on evidential and physiologically plausible guesses. The exceptions were the number of connections in the GLG cell optimisation and the DS cell rate level optimisation. These assumptions are necessary to remove the burden of coarse granular steps so that the optimisation can focus on the fine-grained detail of synaptic weights. Further investigation of optimisation processes and routines will help understand the neural network dynamics in the stellate microcircuit and help to identify its key components.

3.7.2 Limitations of the CNSM Model

A number of limitations need to be considered when evaluating the CNSM model and optimisation results. Most fundamentally, accurate replication of realistic responses to acoustic stimuli in the CNSM model is dependent on the capabilities of the input AN model. The CNSM model used the most detailed phenomenologically-realistic AN model available at the time of the model's development. The fractional Gaussian noise component in the IHC-AN synapse was removed to ensure consistency in the SR of the ANF models. Future work in this field may benefit from using the complete Zilany et al. (2009) AN model and any future improvements.

In the CNSM model, we elected to use 100 frequency channels, which established an average separation of 0.4 octaves in the middle of the network. This approach is suitable for on-CF connections, but may limit the realistic responses from connections in adjacent frequency channels. While an increase in the number of channels would have improved the accuracy of the model's output behaviour, it would have been computationally expensive.

The connectivity properties (number, weight, spread and delay) were uniform across frequency channels in the CNSM model. This uniformity excluded natural variations in synaptic connections in order to minimise the number of network parameters, and reduced the variation of output responses within cell types. This approach is justifiable for synaptic connections to the GLG, DS and TV cells in the CNSM model because of their within-type homogeneity. In light of the three different physiological output responses of TS cells, unique parameters were used to separate each TS cell type.

The microcircuit described in Figure 3.1 is incomplete (see Section 1.2.5 and background sections of each cell in this chapter). Some feed-back connections within the CNSM model (for example TV cells to DS cells, TS cells to TV cells, and TS cells to TS cell connections) create nonlinear pathways that would unduly complicate the sequential optimisation process. This problem was addressed in the CNSM model by excluding connections based on weak experimental support. The alternative, namely the addition of new cell types, was beyond the scope of the model, and needs to be pursued in future research.

The CNSM model is constrained by the level of detail in its constituent neural models. Single-compartment conductance neural models and spiking filter-based models do not adequately account for the morphology of dendritic trees, and the shunting and filtering properties of their synaptic inputs. Other stellate microcircuit models have used ball-and-stick neural models to introduce dendritic filtering (Wang and Sachs 1995; Wiegrebé and Meddis 2004), and to investigate selective filtering of ANFs (Lai et al. 1994b). The RM conductance neural model was chosen because it contains three potassium current channels (I_{KHT} , I_{KLT} , and I_{KA}) and the mixed cation hyperpolarisation current (I_h) that were fitted precisely from intracellular recordings in mouse VCN neurons (Rothman and Manis 2003a,b,c). The use of more complex multi-compartment conductance models was beyond the scope of the thesis, and also requires investigation in future research.

Finally, the direct generalisability of the CNSM model and the optimisation results is limited to small mammal or rodent species. This is a product of the data drawn upon in the development of the model. Data from a range of small mammals and rodents was chosen to overcome the challenge of data scarcity. Further analyses are required to determine whether the model and results can be replicated either in a singular species, or generalised across different species.

3.7.3 Implications for BNN Optimisation

The development and optimisation of the CNSM model in this chapter has wider implications for BNN models and their optimisation procedures. Through the development and optimisation of the CNSM model, this chapter demonstrated that understanding the limitations of experimental data facilitates better fitness function design. It also showed that optimisation methods can provide valuable evidence in developing valid and reproducible BNN models; and that the design and execution of sequential optimisation stages can prevent parameters negatively influencing previous results. Whether it best to optimise cell types based on population responses or exemplar unit responses is an open question in BNN modelling. In the development and optimisation of the CNSM model, exemplar unit responses were preferred and generated sound results.

The development and optimisation of the CNSM model demonstrates the impor-

tance of close attention to the specific properties of data used in BNN models. Experimental devices and methods differ across laboratories and species, and technologies change over time. Cochlear frequency mapping and acoustic thresholds differ between species (Greenwood 1990; Heffner et al. 2001). Additionally, choice of anaesthesia can change the response properties of neurons, especially in CN units (Anderson and Young 2004; Rhode and Kettner 1987). Understanding these difference is important when deciding upon which data to use in BNN optimisation. The CNSM model provides a valuable example of good practice in having due regard for the potential impact of these data inconsistencies on model performance.

Finally, the CNSM model illustrates an appropriate treatment of noise in BNNs. Sources of noise in a BNN model have critical implications for the network output and the optimisation of the model's parameters. Noise is present in BNNs at the level of ion channels, in synaptic jitter, in local variation of synaptic strengths, and in variation of synaptic properties across nuclei. The sources of noise in the CNSM model were the spike generators of the ANF and GLG cell models and the connectivity allocation scheme between cell types. Also, output responses of neurons were averaged over multiple repetitions of the same stimuli to encompass stochasticity of the neuron's inputs. As seen in the CNSM model, optimisation of synaptic parameters also requires a gradient in the search space, otherwise it risks overfitting parameters to noise. Limiting or parameterising the sources of noise is therefore essential in the development of BNN models and their optimisation routines.

3.8 Conclusion

The purpose of the optimisation experiments was to develop a biophysically-realistic model of the stellate microcircuit in the cochlear nucleus. The methods used in this chapter are a practical and realistic means for constructing microcircuits with sensory or feature-based topography. They exploit extensive experimental evidence that describes the behaviour of each interneuron in the network. The tabular reporting format for neural network modelling, as suggested by Nordlie et al. (2009), was followed so that other researchers can easily reproduce and improve upon this work.

The next chapter investigates the optimised CNSM model with the more complex, biologically-realistic stimuli involved in amplitude modulation.

Chapter 4

Amplitude Modulation Coding in the Cochlear Nucleus Stellate Microcircuit Model

4.1 Introduction

Amplitude modulation (AM) is the periodic modulation of the sound amplitude of a carrier frequency (see Figure 4.1 (Joris et al. 2004)). It is a key feature of speech and other biologically relevant sounds (Bregman 1990). Investigating AM coding is a useful way of understanding how temporal information is processed and encoded in the auditory system. The cochlear nucleus (CN) is a major processing stage between the auditory nerve (AN) and higher auditory centres, and modelling and numerical analysis of its processes are important ways to develop insight into its operation.

This chapter presents the AM coding behaviour of the cochlear nucleus stellate microcircuit (CNSM) model. It focuses specifically on the microcircuit's rate and temporal behaviour in response to sinusoidal AM stimuli. The outputs of the CNSM model are the T stellate (TS) cells, which provide a robust spectral representation of auditory information and enhanced coding of temporal information, especially the pitch in complex environments (Keilson et al. 1997). Despite rate saturation of auditory nerve fibres (ANFs) – the input to the CNSM model cells – their ability to code temporal information is not disabled. The optimal coding of AM is still provided across the network, more specifically in lateral sidebands around the edges of the response area.

The analysis in this chapter investigates the responses of the CNSM model to variation in sound level and modulation frequency (f_m) using measures of envelope syn-

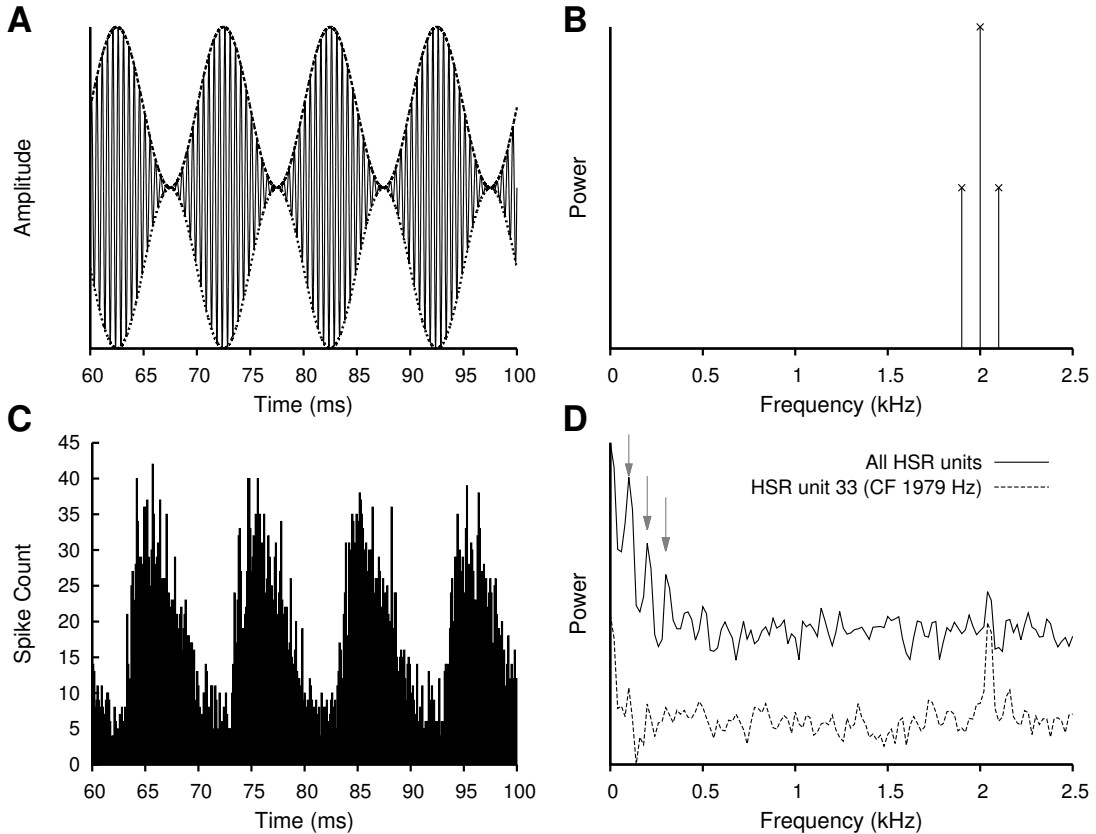


Figure 4.1: Amplitude modulation and its response in the auditory system. A. Sinusoidal amplitude modulated stimulus with carrier frequency 2 kHz and modulation frequency 100 Hz. The period of the envelope is 10 msec. B. Theoretical spectrum of AM stimulus. C. Post-stimulus time histogram of all HSR ANF units to a 60 dB SPL AM stimulus (Zilany and Carney (2010) AN model, 100 frequency channels from 0.2 to 40 kHz, 20 fibres per channel, stimulus duration 150 msec, onset delay 20 msec). D. FFT spectrum of PSTH for all HSR units and the HSR unit with a CF closest to the f_c (unit 33, CF 1.979 kHz). The modulation frequency harmonics are prominent in the FFT spectrum of all HSR units, especially the first (100 Hz) which is also the fundamental frequency.

chronisation and average rate. The analysis measures of AM encoding are introduced in the next section.

4.1.1 Definition of Amplitude Modulation

Figure 4.1 shows the general properties of a sinusoidal AM stimuli and the response of an AN model filterbank. The general formula for an AM tone is

$$s(t) = [1 + m \sin(2\pi f_m t)] \sin(2\pi f_c t) \quad (4.1)$$

where m is the modulation height. A portion of an AM stimulus is shown in Figure 4.1A, which is a 100% modulated sinusoidal AM tone ($m = 1$), with f_c 2 kHz and f_m of 100 Hz. When transformed to the frequency-domain, the frequency components of an AM tone are a dominant spike at f_c and two components $f_c \pm f_m$ with half the height of the component at f_c (Figure 4.1B). In the CNSM model, the Zilany and Carney (2010) AN model was processed using an AM tone (150 msec 65 dB sound pressure level (SPL)) with 100 frequency channels from 200 Hz to 40 kHz (centre frequencies determined by the cat Greenwood function, see Section 2.1.1) and 20 HSR fibres per frequency channel. Figure 4.1C shows a portion of the spike time histogram of 2000 HSR ANFs to a 150 msec AM stimulus as shown in Figure 4.1A. A Fast Fourier transform (FFT) was applied to the all-unit histogram (excluding the first 20 msec) and a spike time histogram of the unit with CF closest to f_c . The peaks in the all-unit FFT spectrum (arrows in Figure 4.1D) are the f_m (100 Hz) and its harmonics. The frequency components of HSR fibres with CF closest to f_c (dotted line in Figure 4.1D) show synchronisation to f_c , which is typical of low CF ANFs.

4.1.2 Temporal Measures of Amplitude Modulation

Temporal information in neural outputs is measured using the synchronisation index (SI) (also known synchronisation coefficient or vector strength) (Goldberg and Brown 1969; Joris et al. 2004; Mardia and Jupp 1999; Shannon et al. 1995). SI measures phase-locking relative to the f_m or envelope of the stimuli. The SI measure was calculated 20 msec after the onset of the stimulus:

$$S = \frac{1}{N} \sqrt{\left(\sum_{i=1}^{i=N} \cos \theta_i \right)^2 + \left(\sum_{i=1}^{i=N} \sin \theta_i \right)^2} \quad (4.2)$$

where N is the number of spikes (Joris et al. 2004; Kajikawa and Hackett 2005). Each spike was treated as a vector of unit length with phase θ_i between 0 and 2π measured as the spike time modulo of the stimulus period, $1/f_m$. Perfect synchronisation will give SI equal to 1 and occurs when all spikes lock to the same phase. An SI measure of zero occurs when spikes have a uniform phase distribution. Bi-phasic or multi-phasic responses (i.e. phase-locking to harmonics of the fundamental) degrade the SI

value but the temporal information pertaining to f_m is still retained for higher auditory centres. Further measures of temporal information, i.e. phase-locking to any frequency, is performed using a FFT as in Figure 4.1.

The statistical test used to verify the non-uniformity of circular data is the Rayleigh test (Fisher 1996; Jammalamadaka 2001; Shannon et al. 1995; Zar 1999). The null hypothesis states that the population of phases is uniformly distributed around the circle. This test assumes the distribution is unimodal around a particular phase. SI and the Rayleigh test are dependent on the number of spikes and the resolution of the spike recordings (in simulations this is the integration time step). For SI values below 0.1, a high spike count is required to obtain a statistically significant result. The p-value for the Rayleigh test is computed using the approximation by Zar (1999, p. 617):¹

$$p = \exp \left(\sqrt{1 + 4N + 4(N^2 - R^2) - (1 + 2N)} \right) \quad (4.3)$$

where $R = N \times S$. In this analysis, SI and Rayleigh tests were also calculated using a FFT of the period histogram to verify the procedure.

4.1.3 Amplitude Modulation Coding in the Auditory Pathway

The auditory pathway transforms the high-fidelity, metabolically intensive, temporal-place encoding of AM signals in the AN into a more efficient rate-place encoding in the inferior colliculus (IC) and higher auditory nervous system centres (Joris et al. 2004). Temporal coding of AM relies on the precise timing of spikes relative to the envelope of the stimulus, otherwise called phase locking or synchrony. Rate coding of AM signals can take the form of pure rate-place, rate-responder or feature-based encoding. Pure rate-place encoding is where neurons encode the stimulus' energy spectrum in their receptive field through simple firing rate changes. In rate-responder encoding, neurons fire in each envelope cycle and as the cycle gets shorter the rate increases up to a certain limit - this is common in low CF units in the AN and CN, and onset units (octopus cells) in the posteroventral cochlear nucleus (PVCN). Specialised feature-based rate encoding encodes particular features of AM signals, especially f_m in IC neurons.

¹The code was converted for use in NEURON from the CircStat Matlab Toolbox (Berens 2009).

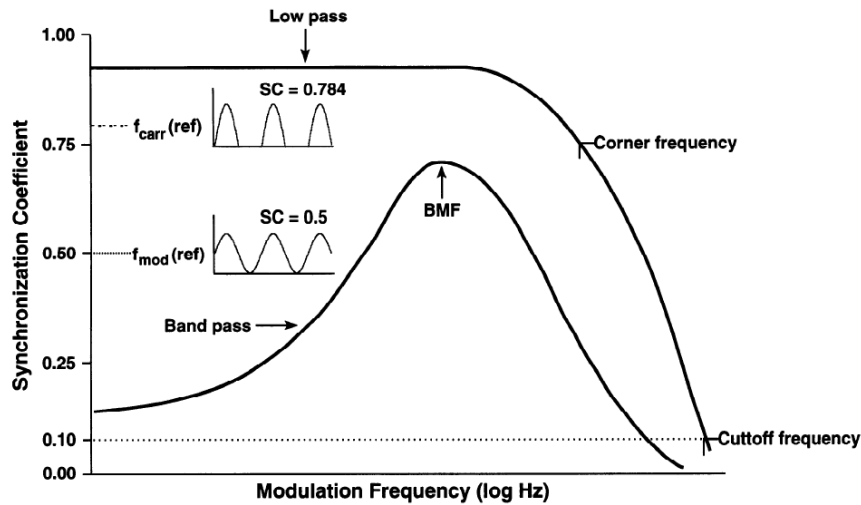


Figure 4.2: Temporal modulation transfer function. Figure reproduced from Rhode and Greenberg (1994a). Response synchronisation in the figures is analogous to SI.

To investigate the response of CNSM model neurons to AM tones, we tested variations in sound level and variations in f_m . The fundamental frequency (f_0) response illustrates the encoding with respect to the stimulus sound level, typically measured with a fixed f_m and a carrier frequency at a neuron's CF. Modulation transfer function (MTF) is used in auditory neuroscience to measure the output of neurons in response to variation in f_m . The rate MTF (rMTF) measures the output in terms of firing rate. Temporal encoding of modulation, tMTF, is measured using SI at each f_m . Figure 4.2 shows the filter characteristics of low-pass and band-pass tMTF responses (Rhode and Greenberg 1994a). Low-pass filters have a stable SI response to low f_m stimuli that degrades when f_m increases above the corner frequency. Band-pass filters increase their synchrony to the f_m envelope to a peak SI response, called its best modulation frequency (BMF), after which their synchrony deteriorates. The inset figures in Figure 4.2 provide more information on the nature of the SI statistic. A half-wave rectified sinusoidal plot, where spikes occur in only half of the cycle period around a single phase, has an SI of 0.784. The modulation envelope, where spikes occur across the whole period with one dominant phase, has a theoretical SI of 0.5.

Temporal information is critical for vocal communication in the mammalian auditory system. In humans, AM is essential for distinguishing vowels and for segregation of streams of sounds with different fundamental frequencies (Bregman 1990). Firing

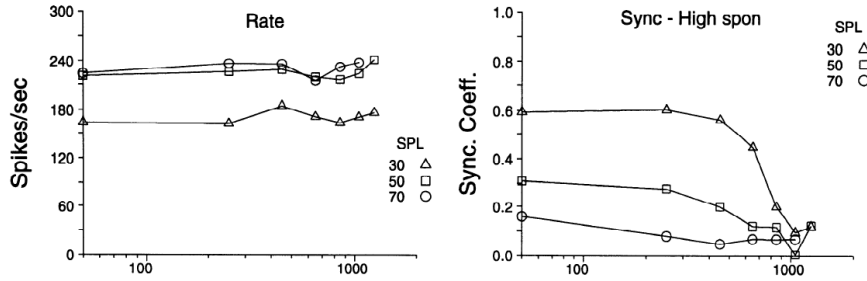


Figure 4.3: Rate (left) and temporal (right) MTF response properties of a single HSR ANF to AM stimuli at 30, 50 and 70 dB SPL. The rMTF of the HSR ANF unit is an all-pass filter and saturates at 230 spikes per second. The tMTF is a low pass filter at 30 dB SPL and strength of synchronisation reduces dramatically with increase in sound intensity (Sync. Coeff. is the same as SI). Figure reproduced from Rhode and Greenberg (1994a).

rate is an efficient way of indicating a specific quality or stimulus feature, as shown in other sensory pathways. Rate coding in the individual ANFs and spectral coding across all ANFs give a poor representation of modulated signals (Frisina 1983; Joris and Yin 1992; Joris et al. 2004). Neural encoding and transformations of sound-envelope information in the CN and higher auditory centres have been studied extensively due to the fundamental importance of temporal information in animal communications (see reviews Frisina et al. (1994) and Joris et al. (2004)).

The temporal coding of AM in auditory neurons uses fine timing of spikes locked to the stimulus envelope. Individual ANFs can encode temporal information of CF tones up to 5 kHz and AM tones up to 2 kHz. Figure 4.3 shows the characteristic rate and temporal MTF response of an HSR ANF to on-CF AM tones. The HSR ANF rate responses are flat and saturate at moderate sound levels. The temporal MTF response in HSR ANFs is low-pass and moderate in maximum synchrony, and the synchronisation deteriorates with increasing sound intensity. The Zilany et al. (2009) AN model has shown accurate replication of experimental AM responses in cat ANFs (Joris and Yin 1992) including synchronisation changes to modulation depth, sound level and modulation frequency.

The encoding of AM tones in the mammalian CN is well documented (Frisina 1984, 2001; Frisina et al. 1990a,b; Rhode and Greenberg 1994a). Figure 4.4 shows the typical temporal MTFs of TS cells (sustained chopper (ChS) and transient chopper (ChT)) in cats (Rhode and Greenberg 1994a). Sustained choppers are characterised as changing

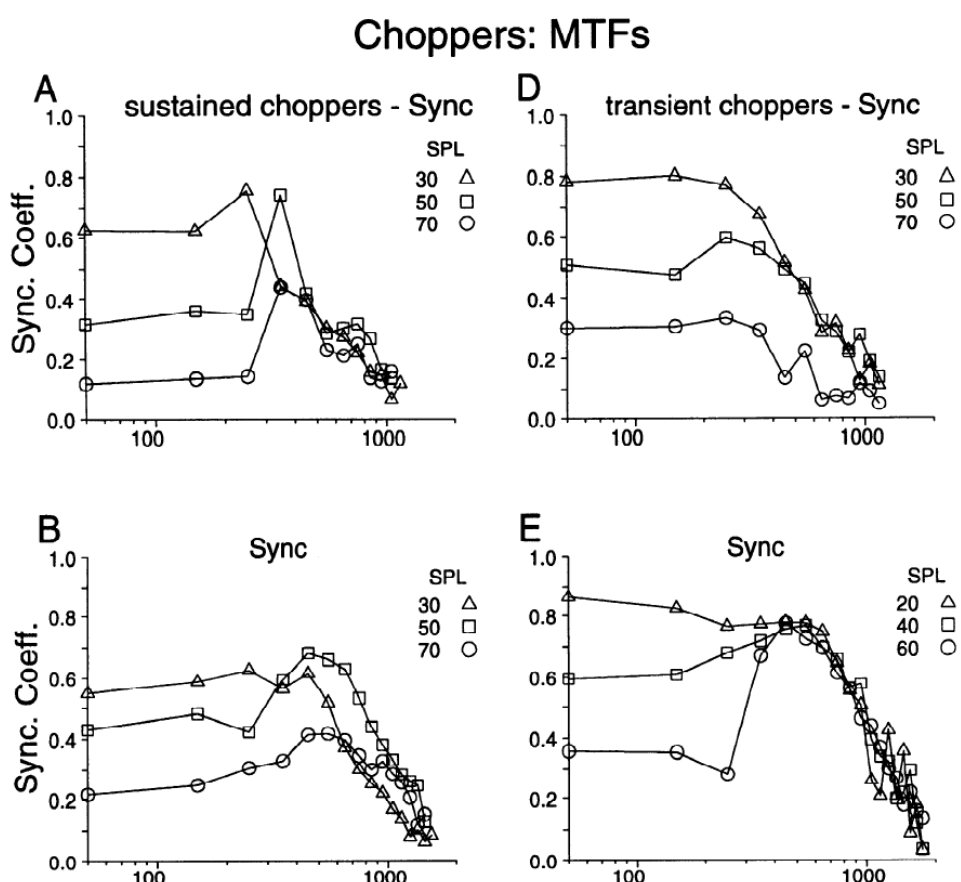


Figure 4.4: Rate and temporal response properties of sustained and transient chopper units (TS cells). Figure reproduced from Rhode and Greenberg (1994a).

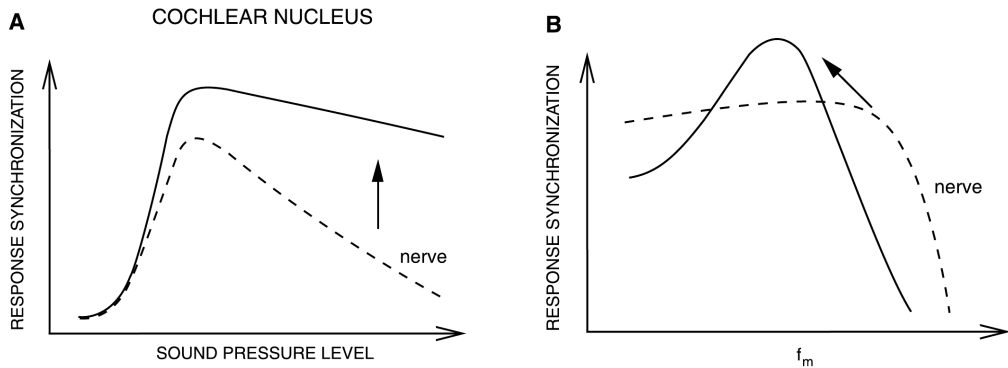


Figure 4.5: Schematic temporal responses of ANFs and TS cells with respect to variations in intensity and modulation frequency. TS cells have enhanced synchronisation at high SPL (A) and a band-pass tMTF with peaks greater than ANFs (B). Figures reproduced from Joris et al. (2004).

from low-pass tMTF to band-pass tMTF with increasing sound levels. Transient choppers have a greater enhancement in synchronisation to the modulation envelope and are more robust to increases in sound level. All chopper units have a reduced tMTF cut-off frequency due to slower membrane dynamics and integration of inputs. The variations in BMFs in TS cells are possibly due to a resonance in either their neuron's intrinsic oscillation frequency (Manis et al. 2003; Wiegert and Meddis 2004) or recurrent network connections between other TS cells (Bahmer and Langner 2006a; Manor et al. 1997). The temporal encoding of AM tones in CN neurons is preserved in noise, but like pure AM tones, deteriorates at high stimulus intensities (Frisina et al. 1996; Joris and Yin 1992). Temporal encoding in CN units is also greatly affected by changes in GABA and glycinergic synapses (Backoff et al. 1999; Caspary et al. 2002).

Figure 4.5 shows the simplified temporal f_0 and MTF responses in ANFs and the comparative transformation of temporal responses in chopper units (Joris et al. 2004). The general enhancement of synchronisation to the stimulus envelope aids in the translation of this information to higher auditory centres. Conversion of temporal MTFs from low-pass filters to band-pass filters also aids in BMF selectivity and pitch sensitivity in the central nucleus of the IC (Caspary et al. 2002; D'Angelo et al. 2003; Depireux and Shamma 1996; Joris et al. 2004; Krishna and Semple 2000; Langner et al. 2002; Zhang and Kelly 2003). The robustness of AM coding to sound level is important for loud conversational speech and speech in noisy environments. The AN and CNSM mod-

els encode sound from one ear and the spectro-temporal processing performed in the network is important for detecting pitch, variations in phase and harmonic differences (Carlyon and Shamma 2003; Millman et al. 2003).

4.2 Methods

4.2.1 Stimulus

The stimulus generation followed Rhode and Greenberg's encoding of AM in cats (Rhode and Greenberg 1994a). AM signals were generated by modulating a carrier signal of specified frequency, amplitude, and phase by a sinusoidal modulator with amplitude and phase equal to that of the carrier (100% modulation). The f_m ranged from 50 to 1200 Hz and was stepped up by 50 Hz. The f_c was set to 4.513 kHz, the central channel CF of the CNSM model.

4.2.2 Simulations and Analysis

The simulations were performed using the neural simulation package NEURON (Carnevale and Hines 2006), as described in Chapter 2. NEURON's Crank-Nicholson integration method was used in the simulations with time step 0.05 msec, stimulus duration 150 msec and total duration 170 msec. Stimuli were repeated 50 times and the spike times of all ANF and CN units recorded.

To avoid onset adaptation effects in auditory neurons, simulations or recordings preferred long stimuli so that the units' responses were in a steady-state. Rate analysis in each neuron was calculated from the average firing rate from 20 ms after onset to the end of the stimulus. Temporal analysis used the same post-stimulus spikes in the calculation of SI and the Rayleigh statistics.

4.2.3 CNSM model

Table 4.1 shows the summary of the model used in this study. As described in Chapter 2, the Nordlie approach to reproducible neural network simulations (Nordlie et al. 2009) was followed. The cell types of the CNSM model (Golgi (GLG) cells, D stellate

Table 4.1: CNSM model summary for AM tone study

i		Model Summary
Populations		HSR and LSR ANFs, GLG, DS, TV and three TS cells
Topology		Tonotopicity of the cat AN and CN
Connectivity		ANF → GLG, DS, TV, TS, GLG → DS, TS, DS → TV, TS, and TV → TS
Input model		ANF model: instantaneous-rate Poisson model (Zilany and Bruce 2007)
Neuron model		GLG cell: instantaneous-rate Poisson model DS cell: HH-like single-compartment Type I-II RM model (Rothman and Manis 2003c) TV cell: HH-like single-compartment Type I-c RM model (Rothman and Manis 2003c) TS cell: HH-like single-compartment Type I-t RM model (Rothman and Manis 2003c)
Channel models		I_{Na} , I_{KHT} , I_{KLT} , I_{KA} and I_h (Rothman and Manis 2003c)
Synapse model		AMPA (<i>ExpSyn</i>), GABA _A (<i>Exp2Syn</i>), Glycine (<i>Exp2Syn</i>)
Input		Amplitude modulated tones, $f_c = 8.91$ Hz (f_m and SPL varied according to stimulus paradigm)
Measurements		Spikes recorded over 50 repetitions. Mean rate and SI measured from the spike times 20 msec after stimulus onset.

ii			Populations
Name	Elements	Size	
HSR	ANF model (SR=50 Hz)	$N_{HSR} = 50$ per freq. channel	
LSR	ANF model (SR=0.1 Hz)	$N_{LSR} = 20$ per freq. channel	
GLG	GLG neural model	$N_{GLG} = 1$ per freq. channel	
DS	Type I-II RM model	$N_{DS} = 1$ per freq. channel	
TV	Type I-classic RM model	$N_{TV} = 1$ per freq. channel	
TS *	Type I-transient RM model	$N_{TS} = 1$ per freq. channel	

* Three chopper subtypes were simulated at different times.

(DS) cells, Tuberculoventral (TV) cells, and the chopper subtypes of TS cells) and network parameters of the microcircuit were developed and optimised in Chapter 3 to fit the experimentally observed behaviour of each of the cell types in the model.

CNSM Model Summary for AM tones – continued

iii Connectivity			
Name	Source	Target	Pattern
ANF→GLG	HSR, LSR	GLG	Gaussian convergence, spread $s_{\text{LSR} \rightarrow \text{GLG}}$, weight $w_{\text{HSR} \rightarrow \text{GLG}}$ $w_{\text{LSR} \rightarrow \text{GLG}}$, delay $d_{\text{ANF} \rightarrow \text{GLG}}$
ANF → DS	HSR, LSR	DS	Skewed Gaussian convergence, 2 octave spread below CF and 1 octave spread above CF, weight $w_{\text{HSR} \rightarrow \text{DS}}$ $w_{\text{LSR} \rightarrow \text{DS}}$, number $n_{\text{HSR} \rightarrow \text{DS}}$ $n_{\text{LSR} \rightarrow \text{DS}}$, delay $d_{\text{ANF} \rightarrow \text{DS}}$
ANF → TV	LSR, HSR	TV	Narrowband connection, weight $w_{\text{LSR} \rightarrow \text{TV}}$ and $w_{\text{HSR} \rightarrow \text{TV}}$, number $n_{\text{LSR} \rightarrow \text{TV}}$ and $n_{\text{HSR} \rightarrow \text{TV}}$, delay $d_{\text{ANF} \rightarrow \text{TV}}$
ANF → TS	LSR, HSR	TS	Narrowband connection, weight $w_{\text{LSR} \rightarrow \text{TS}}$ and $w_{\text{HSR} \rightarrow \text{TS}}$, number $n_{\text{LSR} \rightarrow \text{TS}}$ and $n_{\text{HSR} \rightarrow \text{TS}}$, delay $d_{\text{ANF} \rightarrow \text{TS}}$
GLG → DS	GLG	DS	Gaussian convergence, spread $s_{\text{GLG} \rightarrow \text{DS}}$, uniform weight $w_{\text{GLG} \rightarrow \text{DS}}$, number $n_{\text{GLG} \rightarrow \text{DS}}$, delay $d_{\text{GLG} \rightarrow \text{DS}}$
DS → TV	DS	TV	Gaussian convergence with offset $o_{\text{DS} \rightarrow \text{TV}}$, with spread $s_{\text{DS} \rightarrow \text{TV}}$, weight $w_{\text{DS} \rightarrow \text{TV}}$
GLG → TS	GLG	TS	Gaussian convergence, spread $s_{\text{GLG} \rightarrow \text{TS}}$, weight $w_{\text{GLG} \rightarrow \text{TS}}$, number $n_{\text{GLG} \rightarrow \text{TS}}$, delay $d_{\text{GLG} \rightarrow \text{TS}} = 0.5$ msec
DS → TS	DS	TS	Gaussian convergence, spread $s_{\text{DS} \rightarrow \text{TS}}$, weight $w_{\text{DS} \rightarrow \text{TS}}$, number $n_{\text{DS} \rightarrow \text{TS}}$, delay $d_{\text{DS} \rightarrow \text{TS}} = 0.5$ msec
TV → TS	TV	TS	Gaussian convergence, spread $s_{\text{TV} \rightarrow \text{TS}}$, weight $w_{\text{TV} \rightarrow \text{TS}}$, number $n_{\text{TV} \rightarrow \text{TS}}$, delay $d_{\text{TV} \rightarrow \text{TS}} = 0.5$ msec

iv Neuron and Synapse Model	
Name	DS, TV and TS cell models
Type	I_{Na} , I_{KHT} , I_{KLT} , I_{KA} , I_{h} , and \bar{g}_{leak} currents (Rothman and Manis 2003c), conductance synapse input
Subthreshold dynamics	$I_{\text{Na}}(t, V) = \bar{g}_{\text{Na}} m^3 h(V - E_{\text{Na}}) ,$ $I_{\text{KA}}(t, V) = \bar{g}_{\text{KA}} a^4 b c(V - E_K) ,$ $I_{\text{h}}(t, V) = \bar{g}_{\text{h}} r(V - E_{\text{h}})$ $I_{\text{KHT}}(t, V) = \bar{g}_{\text{KHT}} \left(\frac{n^2 + p}{2} \right) (V - E_K) ,$ $I_{\text{KLT}}(t, V) = \bar{g}_{\text{KLT}} w^3 z(V - E_K)$
Spiking	Emit spike when $V(t) \geq -20$ mV

CNSM Model Summary for AM tones – continued

v	Input/Ouput
Input Stimulus	AM stimuli with fixed parameters for all paradigms: f_c 8.91 kHz and 100% modulation depth ($m = 1$), 150 msec duration, 2 msec cosine squared on/off ramp, and 20 msec delay. f_0 response paradigm: $f_m = 100$ Hz, with 5 dB SPL increments from 0 to 90 dB SPL. MTF paradigm: f_m varied from 50 to 1200 Hz in 50 Hz increments at sound levels 20, 40, 60 and 80 dB SPL.
Input	Stimulus induced Poisson spike trains from GLG units, HSR and LSR ANFs.
Measurements	Mean rate and synchronisation index were calculated from each AN and CN unit for each stimuli over 50 repetitions.

4.3 Results

4.3.1 Responses to Changes in Stimulus Intensity

Sinusoidal AM tones with fixed carrier and modulation frequencies ($f_c = 4.513$ kHz and $f_m = 150$ Hz) were presented to the CNSM model to measure the f_0 response across the model's cell types. The f_0 response illustrates the effects of synchrony to the stimulus envelope (f_m) with respect to the stimulus sound level, typically measured with the f_c at a neuron's CF. The stimulus paradigm is similar to experimental methods; however, the CNSM model allows the inspection of a whole network of units with different CFs. The fixed f_m in this study, 150 Hz, is within the range of human speech fundamental frequencies (women 150–300 Hz, men 75–150 Hz). The f_c is not in the human speech range (most speech is between 200–3400 Hz with other relevant information up to 8 kHz) but is in the human audibility range (64 Hz to 23 kHz) (Bregman 1990). This study uses the cat AN model which has an audibility range up to 64 kHz (Fay and Popper 1994; Simmons et al. 2002). The carrier frequency of 4.5 kHz was chosen to be close enough to the speech range and away from low frequency harmonics of f_m which interfere with the lateral side-bands of the stimulus and in range of DS cell inputs. The AM stimulus paradigm is described in Table 4.1v. Spiking outputs 20 msec after the stimulus onset were used to calculate the firing rate and SI of each of the CNSM model units.

The temporal f_0 response maps for each cell in the CNSM model are shown in

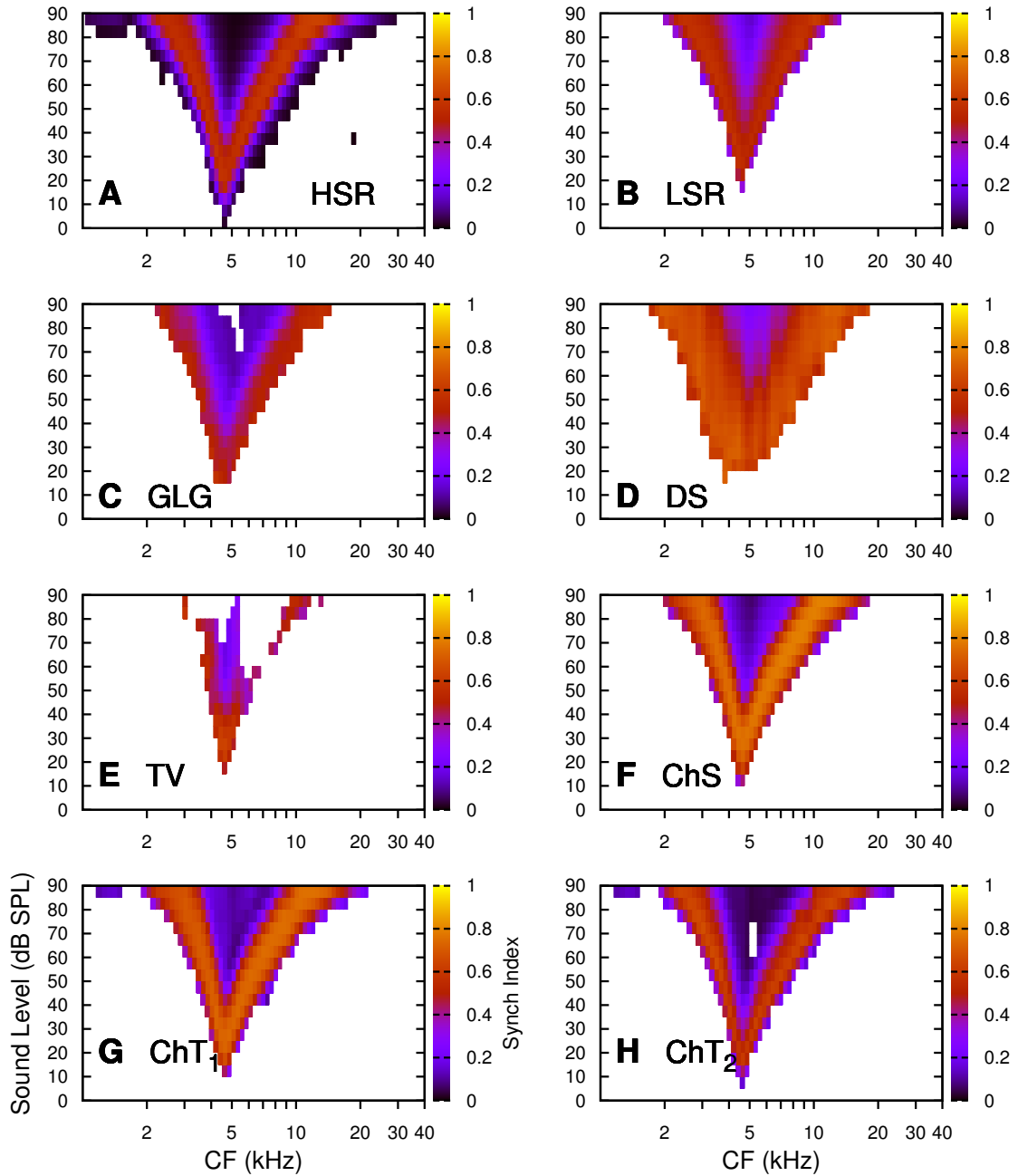


Figure 4.6: The f_0 response map of each cell in the CNSM model to AM tones of different stimulus intensities and units with different CFs. The colour bar shows the synchronisation index from 0 to 1, with white representing areas with Rayleigh test not statistically significant ($p\text{-value} < 0.05$). The stimuli were AM tones with $f_c = 4.5$ kHz, $f_m = 150$ Hz, duration 150 msec, 20 msec delay, and 2 msec on-off ramp. SI calculations used spikes in the last 130 msec of the stimulus. A. HSR ANFs. B. LSR ANFs. C. GLG cells. D. DS cells. E. TV cells. F. ChS type TS cells. G. ChT₁ type TS cells. H. ChT₂ type TS cells.

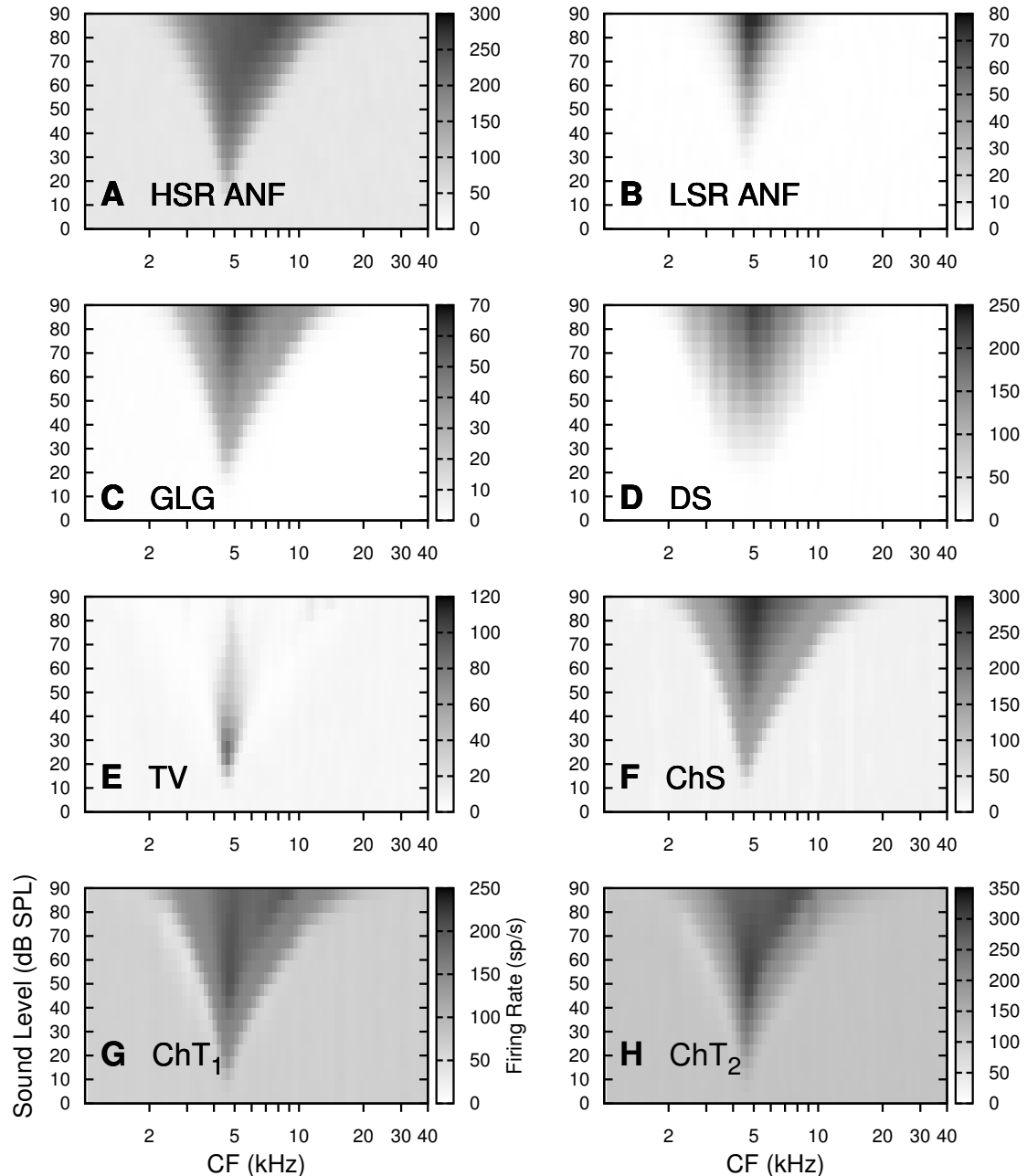


Figure 4.7: The rate level response map of each cell in the CNSM model to AM tones with a fixed f_m and different stimulus intensities. The stimuli are the same as in Figure 4.6. A. HSR ANFs. B. LSR ANFs. C. GLG cells. D. DS cells. E. TV cells. F. ChS type TS cells. G. ChT₁ type TS cells. H. ChT₂ type TS cells.

Figure 4.6. Each column represents a single unit's f_0 response to the AM stimulus, where, traversing on the y axis from bottom to top, the stimulus level varies from 0 to 90 dB SPL. Each row in the f_0 response maps represents the temporal response (SI) of units in adjacent frequency channels to a single presentation of the stimulus to the CNSM model at a fixed intensity. The rate level response maps for the same stimuli are shown in Figure 4.7.

Figures 4.6A and B show the f_0 response map of the HSR and LSR cell types in the CNSM model. The rate level response maps of ANFs are shown in Figure 4.7A and B. HSR ANFs have a non-linear f_0 response, with SI peaking around 0.6 at intensities 20-30 dB above threshold, then reducing to below 0.2 for intensities 60 dB above rate threshold (Joris and Yin 1992). Loss of f_0 response in ANFs is typically due to saturation at the inner hair cell to AN synapse or the encoding of higher harmonics rather than the envelope. The Zilany et al. (2009) AN model was designed to replicate AM responses and the f_0 response. The V-like f_0 response map of the HSR fibres (Figure 4.6A) shows the strong non-linear temporal behaviour at each frequency channel surrounding the f_c . For the on-CF unit (4.513 kHz), the peak SI was 0.775 at 15 dB SPL and then subsequently fell below the Rayleigh test of statistical significance (p -value < 0.05) when the unit reached maximum firing rate at 40 dB SPL. Adjacent network channels showed similar behaviour with an adjustment in rise and fall of SI based on excitation from the cochlea filter. These results are similar to the model results presented by Zilany et al. (2009). The peak SI in the map was 0.777 by unit 84 (CF 20.7 kHz) at 90 dB at approximately 50% of maximum firing rate.

In LSR ANFs (Figure 4.6B) the f_0 response map maintained moderate temporal information throughout the response area. The f_0 response of the on-CF unit had its peak temporal response at rate threshold then slowly reduced to a moderate temporal response at high intensity. The rate level map is the exact opposite (Figure 4.7B) with the peak response on-CF at high sound levels. Across frequency channels and intensities, active units near the edges of the response area provided high (around 0.8 SI) temporal information. At high intensities, units with CFs near the carrier frequency maintained moderate (0.5 – 0.6 SI) temporal information that was lacking in the HSR units in this area.

The rate f_0 response map of GLG cells in Figure 4.7C was broader and had a higher firing rate output relative to LSR inputs. GLG cells receive a majority of their inputs from LSR fibres that have high temporal information throughput across their active response area (Figure 4.6B). Figure 4.6C shows the GLG cells' temporal f_0 response map. The GLG cells' temporal encoding performance was moderate near the edges of their response area and deteriorated at high SPL to levels below 0.3 SI. The diminished temporal information is a result of the smoothing kernel in the GLG neural model. Despite this, the GLG cell model was still capable of passing temporal information to other cells in the microcircuit (mean SI = 0.52, $p < 0.05$); however, the GLG cells' monotonic rate-level response shows that they are very good at encoding stimulus intensity in AM tones and using their slower GABAergic synapses to control excitability within the CNSM model.

Figures 4.6D and 4.7D show the DS cells' temporal and rate f_0 response maps, respectively. Both the rate and temporal responses had a broad activation and the temporal information was enhanced at every level-CF point on the map relative to HSR and LSR ANFs. Onset chopper (On_C) units recorded from the dorsal acoustic stria in cats have shown high SI maintained above 0.8 up to 60 dB SPL then sloping down to 0.6 at 80 dB SPL (Joris and Smith 1998). The on-CF unit peaked at 20 dB SPL with SI of 0.937 and steadily declined with increasing level to 0.443 SI at 90 dB SPL. The lowest point in the DS cell f_0 response map was 0.417 at 90 dB SPL (unit 71, CF 11.7) and the mean for all points below 0.05 in the Rayleigh test was 0.77 SI. The maximum phase response for the DS cell model (results not shown) was linear over SPL similar to experimental results (Joris and Smith 1998).

The f_0 response of TV cells (Figure 4.6E) shows an enhanced temporal response but due to the cell's non-linear rate response (Figure 4.7E) its activity was only effective at sound levels below 50 dB SPL. TV cells receive strong inhibition from DS cells, especially at higher sound levels. At lower sound levels, TV cells process only HSR and LSR ANF inputs. This implicates intrinsic mechanisms in the TV cell model and integration of ANF inputs within the dynamic range that contribute to this enhancement.

Figure 4.6F shows the f_0 response map of ChS subtype TS cell models. ChS model cells receive inputs from all the other cell types in the CNSM model with greater ex-

citation relative to the other chopper subtypes. The ChS model's f_0 response map has a narrower V-shape compared to the HSR response map with elevated temporal responses over the whole map (mean 0.70, min 0.366, max 0.973). The f_0 response of the unit with CF at f_c has a sharp rise in SI at rate threshold then falls to 0.216 SI at 50 dB SPL, and steadily rises to 0.800 SI at 90 dB SPL. The characteristic robustness of the TS cell on-CF f_0 response, summarised in Figure 4.5, is appropriately matched by the ChS model with strong enhancement of temporal information at high SPL. The rate response (Figure 4.6F) is not stable at sound levels above 60 dB (as shown by the white patches in the temporal response) where the firing rate is low. The inhibition to the ChS model is stronger for units with CFs below f_c . Figure 4.6G shows the f_0 response map of ChT₁ subtype TS cell models. The strong firing rate after threshold is equally matched by the strong inhibition at high SPL on the ChT₁ model, seen in its rate-level response map (Figure 4.7G). The f_0 responses of the final TS cell in the CNSM model, ChT₂, were more robust in its rate response (Figure 4.7H) with enhanced synchronisation in the lateral sidebands (Figure 4.6H). The on-CF ChT₂ unit peaked at 15 dB SPL with SI 0.873 before falling to 0.35 with some irregularities at higher sound levels.

4.3.2 Responses to Changes in Modulation Frequency

The figures in this section show the rate and temporal MTF response maps, across the entire network, of the CNSM model to an AM tone with carrier frequency 4.513 kHz. Modulation frequency ranged from 50 to 1200 Hz in 50 Hz steps and the SPL was set to four appropriate levels (20, 40, 60 and 80 dB SPL). Each figure shows the rMTF on the left and tMTF on the right. The SI values were masked in white if the Rayleigh coefficient was not statistically significant (p -value < 0.05).

4.3.2.1 ANF Model Results

Figure 4.8 shows the rate and temporal MTF maps of HSR ANFs to AM tones with $f_c = 4.513$ kHz. HSR fibres saturate to pure CF tones at 40 dB SPL, whereas their response to AM tones was dependent on the carrier and modulating frequencies. Figures 4.8A, C and E show the average rate response to AM tones of varying f_m at stimulus intensities

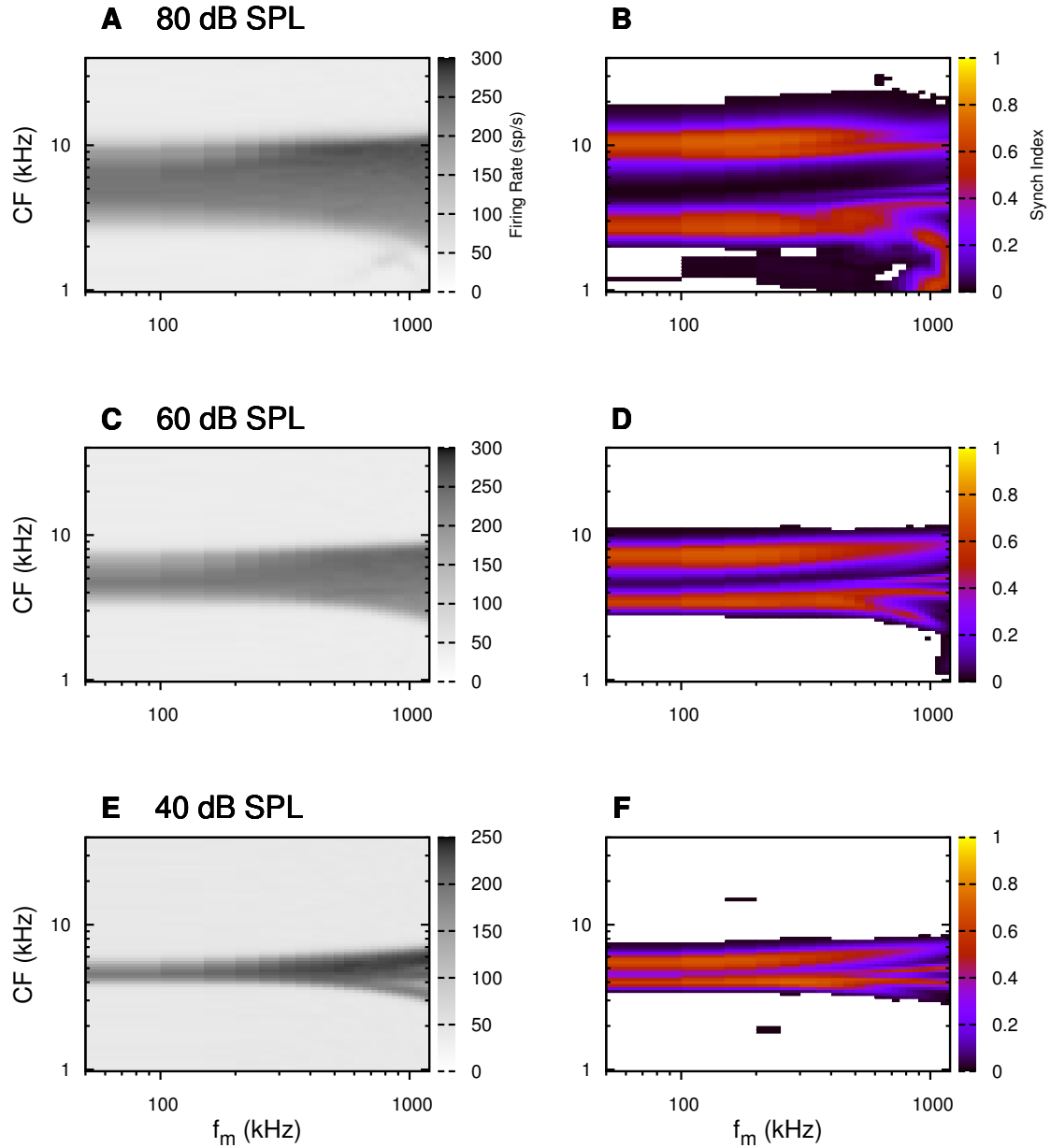


Figure 4.8: Rate and temporal modulation transfer functions (MTF) maps of HSR ANFs at 40, 60 and 80 dB SPL to AM tones with carrier frequency 4.513 kHz. Rate (left column) and temporal (right) MTF maps of modulation frequency (f_m) against the CF of the HSR units are shown. The corresponding temporal MTF maps show their SI with range 0 to 1. The white regions on the tMTF figures show where the Rayleigh test was insignificant ($p\text{-value} > 0.05$). A. rMTF map at 80 dB SPL. B. tMTF map at 80 dB SPL. C. rMTF map at 60 dB SPL. D. tMTF map at 80 dB SPL. E. rMTF map at 40 dB SPL. F. tMTF map at 40 dB SPL.

80, 60 and 40 dB SPL, respectively. The spread of excitation is consistent across f_m at each intensity. For HSR units with CFs above f_c , rate increases with f_m and peaks around 600 Hz. The rate peak occurs in unit 75 (CF 14 kHz) with rate 30% greater than the unit closest to f_c (CF 4.513 kHz).

Temporal information in HSR units at each of the corresponding stimulus intensities (Figures 4.8B, D and F) is strongest near the edges of excitation with a low-pass tMTF extending beyond 1.2 kHz (the maximum range f_m is this study). At 80 dB SPL (Figure 4.8B), units with CFs above the centre channel had mean SI of 0.75 with a peak of 0.814. Moving toward f_c , the HSR units lose low modulation frequency information to become band-pass tMTF filters until 7 kHz where the salient temporal information ceases. Units between 7 kHz and 3.8 kHz (two frequency channels below the centre unit) show a rapid deterioration of temporal information despite being at the centre of the stimulus' energy. Below the centre channel, band-pass tMTF responses increase in mean and peak values further away from the centre with the apex at unit 39 (CF 2.67 kHz, mean SI = 0.608, max SI = 0.785). Synchronisation for units below the centre channel at high f_m showed anomalous behaviour due to the low frequency tail in the AN tuning curve and harmonics of the f_m .

The tMTF response observed at 60 dB SPL (Figure 4.8D) looks similar to the 80 dB SPL response with a reduced number of frequency channels reflecting the reduced rate excitation range in Figure 4.8C. The dominant frequency channels below (unit 44, CF 3.4 kHz, mean SI 0.666, max SI 0.805) and above (unit 61, CF 7.47 kHz, mean SI 0.741, max SI 0.787) are at the border of rate threshold, showing a gradual increase of temporal information in units further from the centre CF unit. At 40 dB SPL, the two salient information bands begin to merge as the range of excited frequency channels gets closer to the centre CF.

LSR fibres' rate responses to AM tones were non-saturating and centred on the f_c (Figures 4.9A, C and E). The rMTF of the on-CF unit was typically low-pass but did fluctuate at modulation frequencies above 400 Hz for each stimulus intensity. Figures 4.9B, D and F show that LSR fibres in the AN model were better at encoding temporal information than HSR ANFs. This has been observed previously in cat ANFs (Joris and Yin 1992). The low-pass tMTF is typical of ANFs and can be seen at each stimulus intensity,

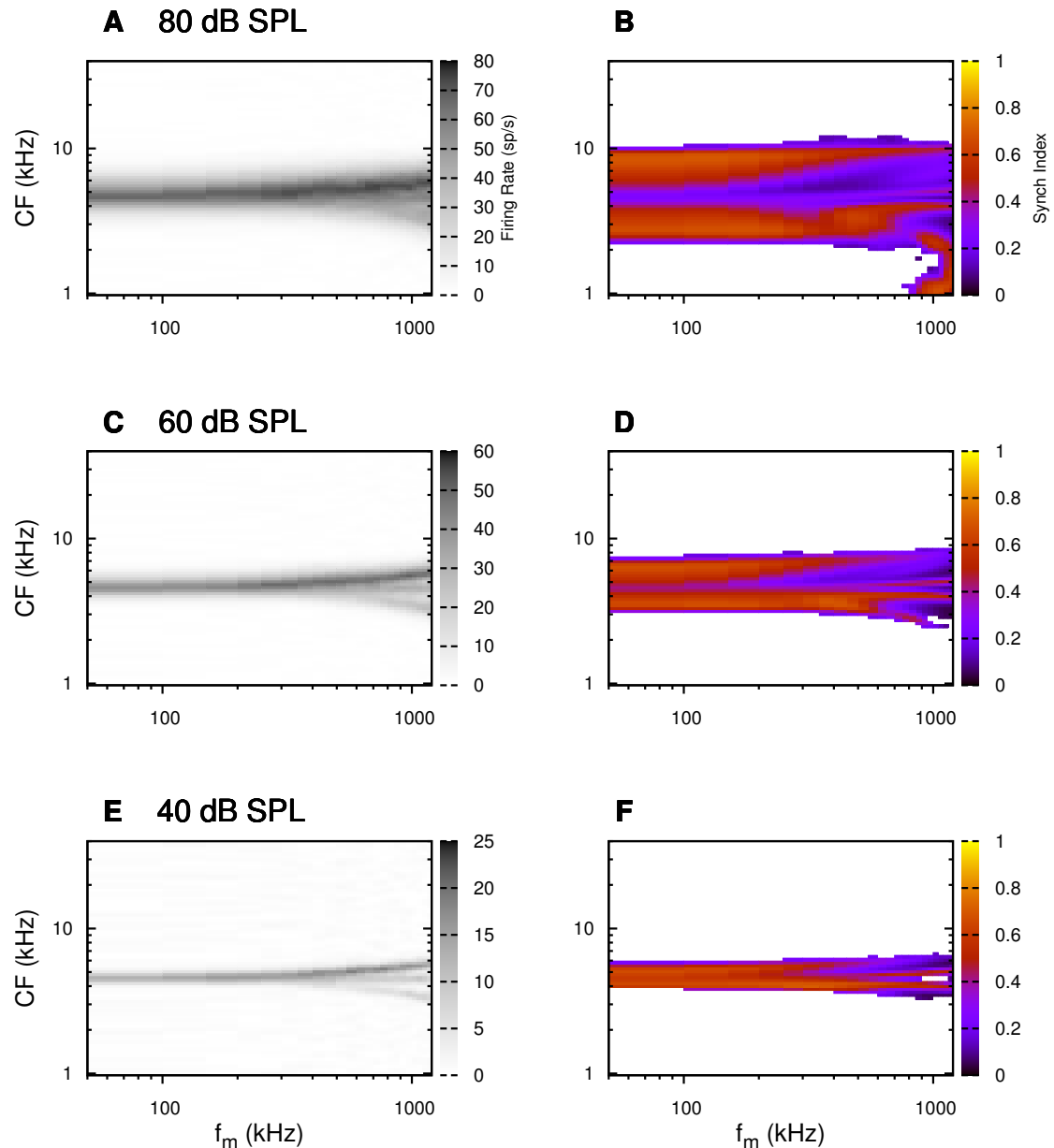


Figure 4.9: Rate and temporal modulation transfer functions (rMTF and tMTF) of LSR ANFs at 40, 60 and 80 dB SPL to AM tones with carrier frequency 4.5 kHz. A. rMTF map at 80 dB SPL. B. tMTF map at 80 dB SPL. C. rMTF map at 60 dB SPL. D. tMTF map at 80 dB SPL. E. rMTF map at 40 dB SPL. F. tMTF map at 40 dB SPL.

particularly in units above the f_c . The f_m cut-off frequency for LSR units was beyond the 1.2 kHz range used in this study. At 80 dB SPL (Figure 4.9B), LSR units had higher mean and peak SI values than HSR units (mean 0.74, max 0.937) above f_c and the low-pass tMTF response was maintained. For the on-CF unit (unit 50, CF 4.5 kHz), its mean SI 0.415 with a peak of 0.673 was the lowest of all salient temporal response channels. Below f_c , an unusual temporal response at high f_m may relate to the rate fluctuations in Figure 4.9A or a reduction in the f_m cut-off frequency. The high gain, low-pass tMTF responses were observed at 60 and 40 dB SPL stimulus intensities (Figures 4.9D and F).

Figures 4.10A and B show the on-CF rate and temporal MTF responses of HSR ANF experimental data (Rhode and Greenberg 1994a). All stimulus levels but the lowest (20 dB SPL) showed saturated rate responses in the on-CF rMTF response of the HSR ANF (Figure 4.10C). The sensitivity to f_m at 20 dB SPL shows the typical rate-following characteristic by phase-locking to each cycle and following the increase in the number of cycles. Temporal information was also more substantial at 20 dB for the on-CF HSR fibres' tMTF response (Figure 4.10D). As shown in Figure 4.8, the on-CF tMTF response becomes insignificant with increasing sound level. The LSR ANF model's rate responses increased with sound level but were insensitive to changes in f_m with flat rMTF responses (Figure 4.10E). The on-CF tMTF responses of simulated LSR ANFs were low-pass and linearly decreased with increasing sound levels but still maintained moderate temporal information (Figure 4.10F). The irregular errors in HSR and LSR ANF responses at high SPL and high f_m are an artefact of the Zilany et al. (2009) AN model.

4.3.2.2 Golgi Cell Model

Figure 4.11 shows the GLG cell rate and temporal MTF across the whole network to AM tones centred at 4.5 kHz. The GLG cell model's rMTF on-CF was typically flat or low-pass, mimicking the rate behaviour of LSR fibres, its primary source of excitation. The rMTF maps of GLG cell responses, Figures 4.11A, C and E, show a wider activation of units compared to LSR fibres (Figure 4.9) with no discernible saturation. The GLG cell units had a flat rMTF response for all sound levels, indicating GLG cells provide consistent spike output independent of changes in f_m .

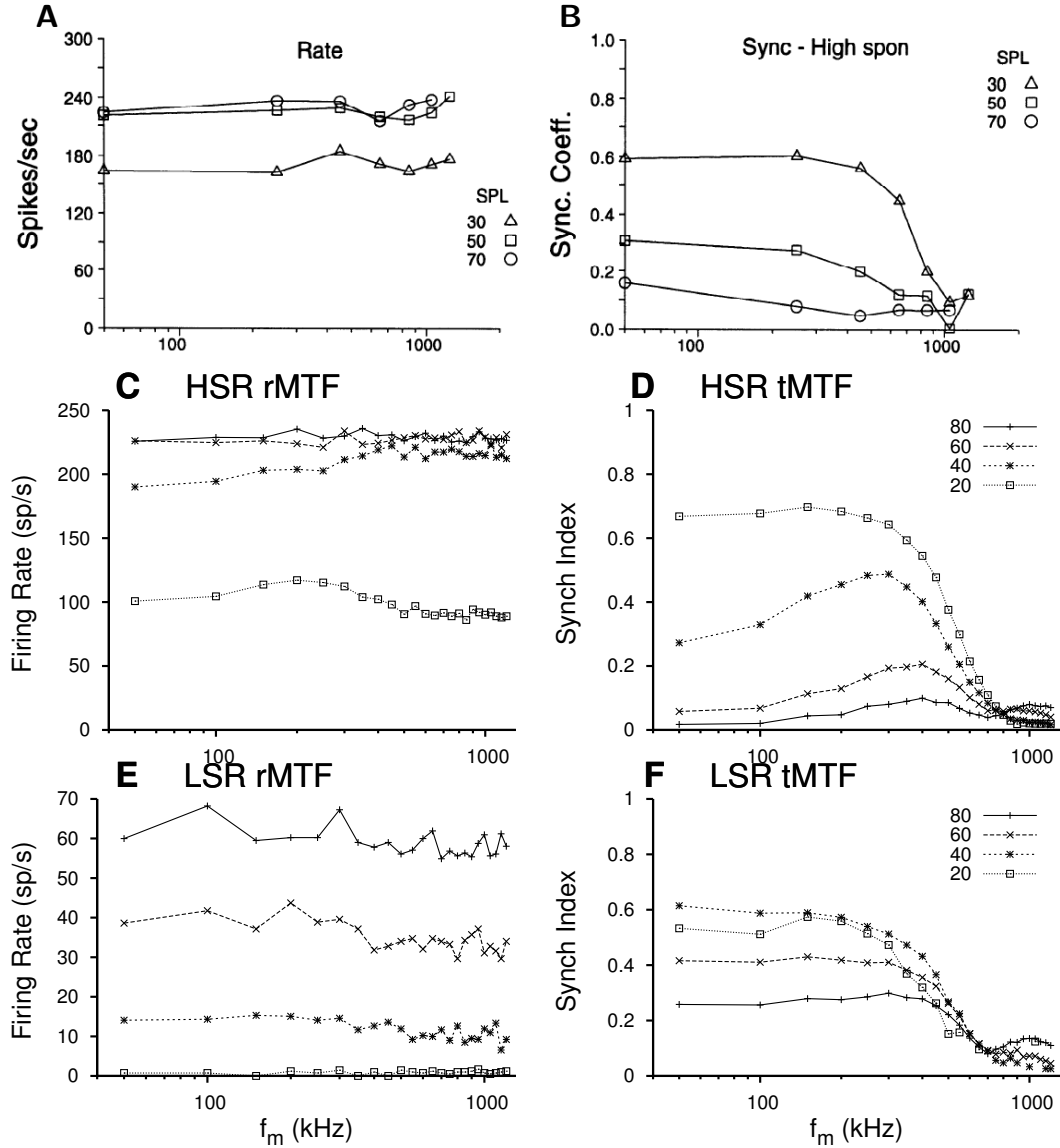


Figure 4.10: Rate and temporal response properties of HSR units with the carrier frequency on or nearest to its CF. A and B (reproduced from Rhode and Greenberg (1994a)) show the experimental rMTF and tMTF responses of a HSR ANF at 30, 50 and 70 dB SPL. C. Simulated on-CF rMTF response of HSR unit 50 (CF 4.513 kHz) in the CNSM model at 20, 40, 60 and 80 dB SPL. C. Simulated on-CF tMTF response of HSR unit 50. C. Simulated on-CF rMTF response of LSR unit 50 (CF 4.513 kHz). C. Simulated on-CF tMTF response of LSR unit 50.

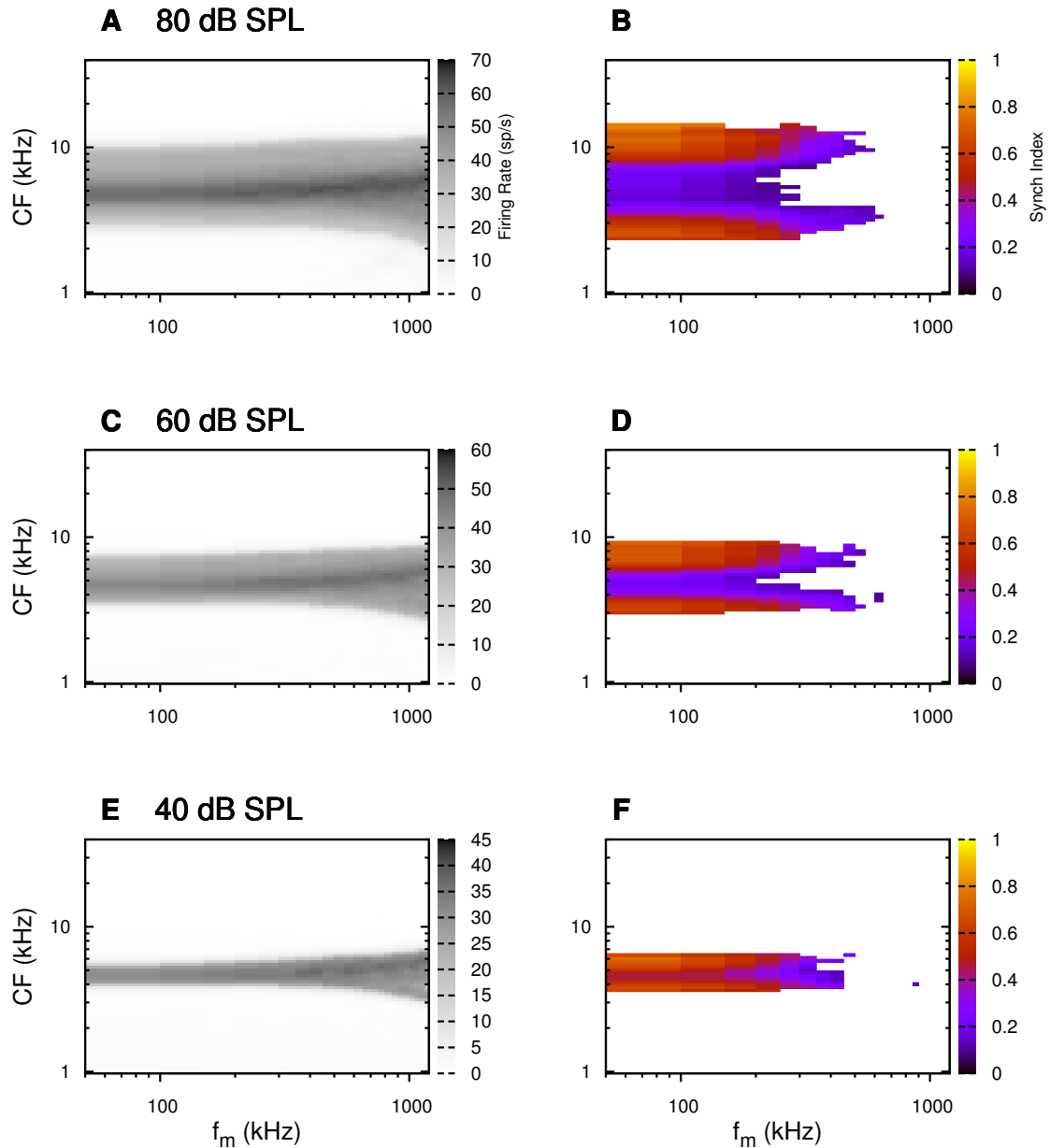


Figure 4.11: GLG cell rate (rMTF, left column) and temporal (tMTF, right column) modulation transfer function response maps for AM stimulus sound levels at 40, 60 and 80 dB SPL. A. rMTF map at 80 dB SPL. B. tMTF map at 80 dB SPL. C. rMTF map at 60 dB SPL. D. tMTF map at 60 dB SPL. E. rMTF map at 40 dB SPL. F. tMTF map at 40 dB SPL.

The temporal information contained in the tMTFs of GLG cell units was diminished relative to LSR fibres. The smoothing filter used in the GLG cell model contributes to the reduction of temporal information, particularly the cut-off frequency. The peak temporal responses of the GLG cell model occurred at low f_m with a rapid drop off in SI around 350 Hz. The on-CF unit had a flat low-pass tMTF before its Rayleigh test dropped below the threshold. Its mean SI from 50 to 1200 Hz (excluding values when the Rayleigh test was below threshold) was 0.39, 0.275, 0.146, and 0.11 at stimulus intensities 20, 40, 60, and 80 dB SPL, respectively. The cut-off frequency for the on-CF unit was consistently at 250 Hz, after which the GLG cells output was unsynchronised to the envelope of the stimulus. At the highest intensity, 80 dB SPL in Figure 4.11B, units furthest from the f_c and active had greater temporal information with the maximum SI value 0.828 at CF = 11.2 kHz and f_m = 50 Hz. With firing rates near threshold in high SI regions and the low cut-off frequencies, the temporal effects of GLG cells on other neurons in the CNSM model are predominantly at low f_m .

4.3.2.3 DS Cell Model

The broad CF range of ANF inputs to DS units allows for a greater likelihood of co-incidence detection and an increase in synchronisation relative to the inputs. The rate responses of DS units (Figure 4.12) were wider for 40 and 60 dB SPL stimuli relative to the narrow band TS units. For 40 dB SPL stimuli, most DS units had a band-pass rMTF. For higher SPL, a greater number of spikes occurred between 100 and 500 Hz for units above CF (band-pass rMTF), but the rest of the active units remained stable (low-pass rMTF). Figure 4.13A shows the consistent linear increase in rate MTF responses at low f_m , a peak between 300-400 Hz and falling off to a stable rate at high f_m . This behaviour is called “rate-responder” due to the linear increase in firing-rate being dictated to by shortening of the f_m envelope period. This is similar to ideal onset units (octopus cells) in the PVCN but the corner- and cut-off frequencies of the DS cell’s rMTF are typically lower.

The temporal responses of DS units were predominantly band-pass, with higher SI values than ANFs. For lower SPL, the responses were consistent across active units with a falling cut-off frequency with falling CF. For high SPL, the DS units were divided

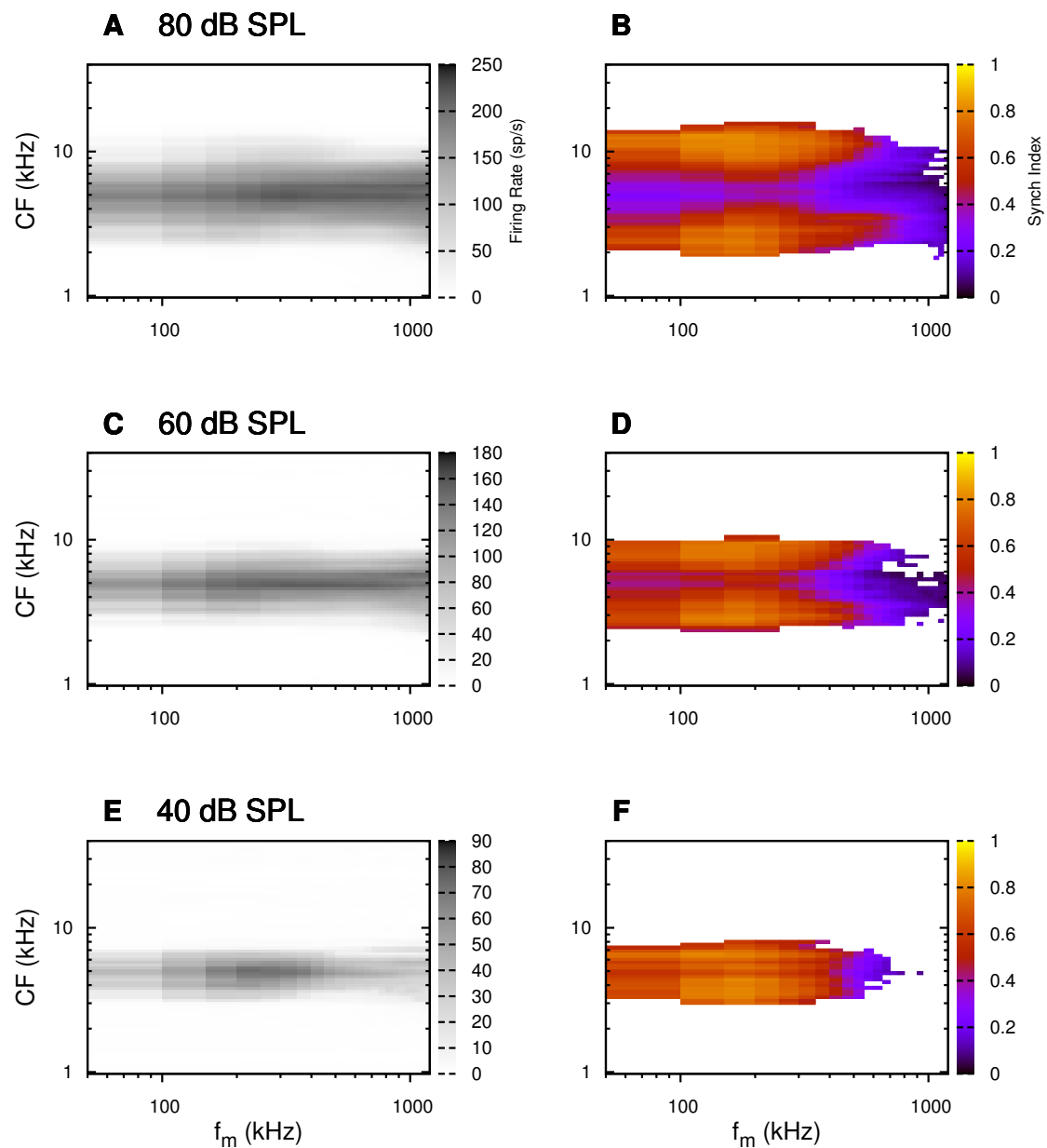


Figure 4.12: Rate and temporal MTF responses for DS cells at three stimulus sound levels. A. rMTF map at 80 dB SPL. B. tMTF map at 80 dB SPL. C. rMTF map at 60 dB SPL. D. tMTF map at 60 dB SPL. E. rMTF map at 40 dB SPL. F. tMTF map at 40 dB SPL.

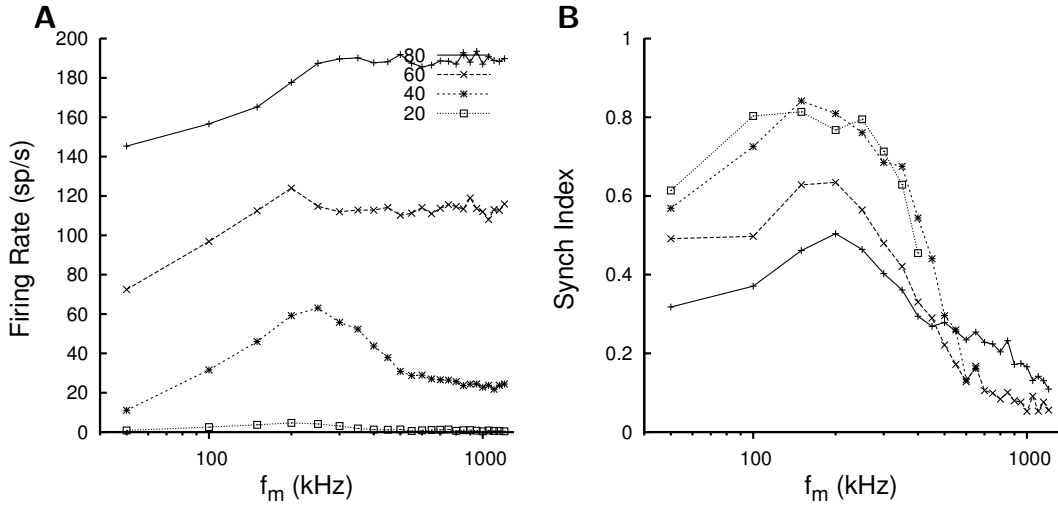


Figure 4.13: Rate and temporal MTF response properties of DS cells with the carrier frequency on or nearest to its CF. A. Simulated on-CF rMTF response of DS unit 50 (CF 4.513 kHz) in the CNSM model at 20, 40, 60 and 80 dB SPL. C. Simulated on-CF tMTF response of DS unit 50.

along the central channel. The central unit (Figure 4.13B, with CF closest to the carrier frequency) had mean SI values of 0.827, 0.566, 0.41 and 0.485 for tMTF responses at 20, 40, 60 and 80 dB SPL, respectively. The cut-off frequency for significant SI values (Rayleigh test, $p < 0.05$) was above the maximum f_m we used in this study (1200 Hz). The maximum SI values in the on-CF CS cell were strongly synchronised and decreased slightly with increasing SPL (0.814 at $f_m = 150$ Hz, 0.841 at $f_m = 150$ Hz, 0.634 at $f_m = 200$ Hz, 0.504 at $f_m = 200$ Hz for 20, 40, 60 and 80 dB SPL, respectively). The DS units above the central channel had the strongest synchronisation and cut-off frequencies near the upper limit of the AN model. The maximum unit across all DS cells at 80 dB SPL was 0.834 at CF =12.8 kHz and $f_m = 200$ Hz. The DS units below the central channel had cut-off frequencies around 400 Hz.

4.3.2.4 TV Cell Model

The rate and temporal responses of TV units (Figure 4.14) showed the non-linear effects of strong inhibition from DS cells. TS and TV units received similar ANF inputs, but the inhibition limited the activity at low sound level and then to a narrow range at higher SPL. The temporal responses of TV units had enhanced synchronisation and sharper

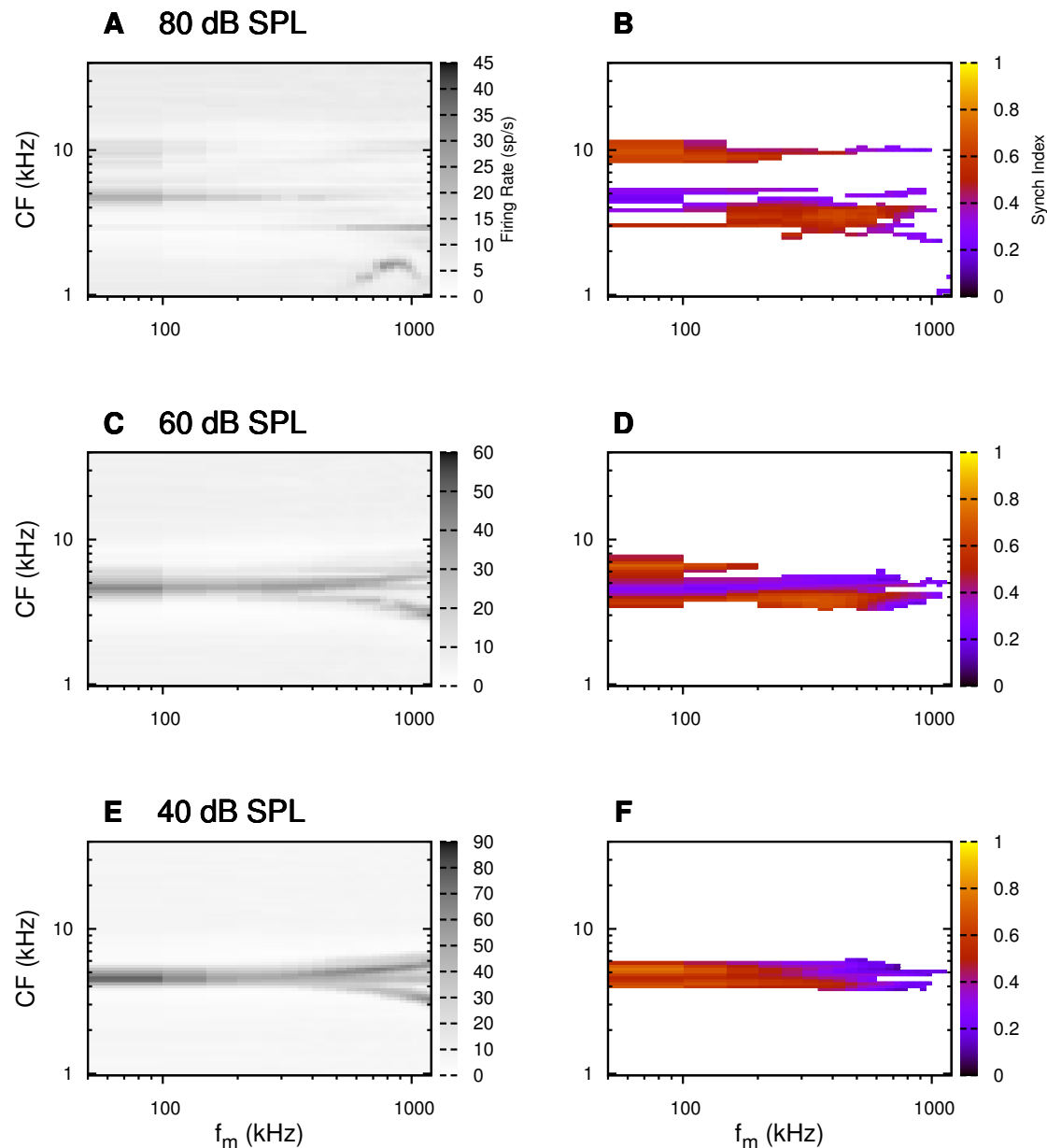


Figure 4.14: Rate (rMTF) and temporal (tMTF) responses for three stimulus sound levels of the TV cell model. A. rMTF map at 80 dB SPL. B. tMTF map at 80 dB SPL. C. rMTF map at 60 dB SPL. D. tMTF map at 60 dB SPL. E. rMTF map at 40 dB SPL. F. tMTF map at 40 dB SPL.

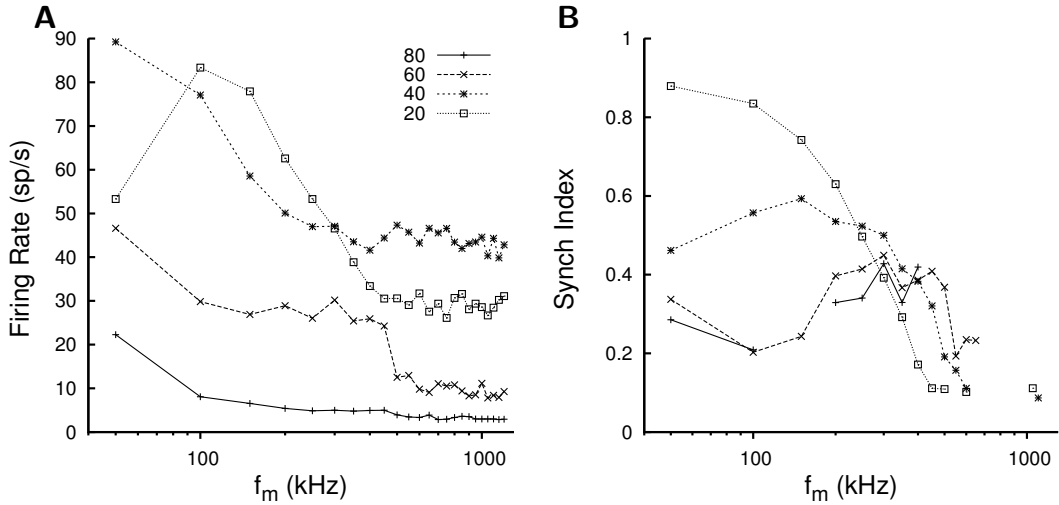


Figure 4.15: Rate and temporal MTF response properties of TV cells with the carrier frequency on or nearest to its CF. A. Simulated on-CF rMTF response of TV unit 50 (CF 4.513 kHz) in the CNSM model at 20, 40, 60 and 80 dB SPL. C. Simulated on-CF tMTF response of TV unit 50.

cut-off. The outer edges of active units provided the best temporal response with little to no temporal information at the f_c units. The rate MTF responses on the on-CF TV cell in Figure 4.15A showed a marked drop in spike output after 20 dB SPL. This non-linearity in TV cell responses to AM tones reflects the inconclusive status of the relevant experimental data (Frisina et al. 1990a; Neuert et al. 2004; Spirou et al. 1999; Zhao and Liang 1997).

Where significant, the temporal MTF responses of TV cells were either low-pass or band-pass typically at low sound levels. With firing rates in stimuli above 40 dB SPL, the temporal responses of all TV cell's in Figure 4.14 and the on-CF TV cell in Figure 4.15B show irregular temporal information. The maximum SI values in the on-CF TV cell were moderately synchronised at 20 dB SPL ($=0.879$ at $f_m = 50$ Hz=[:results replace raw]) and decreased to a stable level and higher intensities (0.593 at $f_m = 150$ Hz, 0.449 at $f_m = 300$ Hz, 0.428 at $f_m = 300$ Hz for 40, 60 and 80 dB SPL, respectively). The TV units below the central channel had stronger synchronisation for high sound levels (maximum SI at 80 dB SPL 0.727 at CF =11.2 kHz and $f_m = 50$ Hz and 60 dB SPL maximum SI 0.743 at CF =6.83 kHz and $f_m = 50$ Hz). The maximum unit across all TV cells at lower intensities had a CF above the central channel (40 dB SPL maximum SI 0.81 at CF =3.92 kHz and $f_m = 50$ Hz, 20 dB SPL maximum SI 0.879 at CF =4.51 kHz and

$f_m = 50$ Hz).

The central channel had corner-frequencies less than 500 Hz (Figure 4.15B), indicating a limitation in the intrinsic cell properties that integrate ANF inputs or strong phasic inhibition for this input modulation. The low firing rate and few temporally active TV cell units above 40 dB SPL but shows a neural group that is strongly inhibited across the network primarily from DS cells.

4.3.2.5 TS Cell Model

Figure 4.16 shows the final MTF responses of the ChS type TS units in the network. The spread of excitation in ChS units was narrow around the central channel, with greater excitation above CF around $f_m = 300$ Hz. For higher sound levels, the spread of excitation was wider but the rate was steadier for each stimuli. The significant features of the temporal responses in the right of the figure are the very poor synchronisation in the central channel and dominant synchronous responses at the outer edge of excitation. For 40 dB SPL, most active units showed a band-pass tMTF; however, the dominant units above CF had low-pass tMTFs. For 60 dB SPL, most active units showed band-pass MTFs except for the central units, which showed limited results or a low-pass MTF. The maximum SI values in the on-CFChS model were strongly synchronised and decreased with increasing SPL (0.883 at $f_m = 100$ Hz, 0.767 at $f_m = 200$ Hz, 0.439 at $f_m = 200$ Hz, 0.333 at $f_m = 250$ Hz for intensities 20, 40, 60 and 80 dB SPL, respectively). Outermost active units (above and below f_c) had the highest synchronisation across the TS cell population, similar to HSR and LSR excitatory input responses and the phasic inhibitory inputs from GLG and DS cells.

Figure 4.17 shows the on-CF unit rate and temporal MTF responses of the three TS cell model subtypes that are otherwise hidden in the MTF response maps. Figures 4.17A and B show the ChS model's responses from the rMTF and tMTF response maps in Figure 4.16. The on-CF unit's rMTFs (Figure 4.17A) are all-pass at 60 and 80 dB SPL. The on-CF response at 20 dB SPL was band-pass (BMF = 150 Hz) up to 500 Hz where the ChS model follows the input response of the on-CF HSR unit (Figure 4.10C).

The non-linearity in the tMTFs at 40 and 60 dB contrasts with the similarity of the 20 and 80 dB responses (high SI at low f_{ms} and a BMF at 350 Hz).

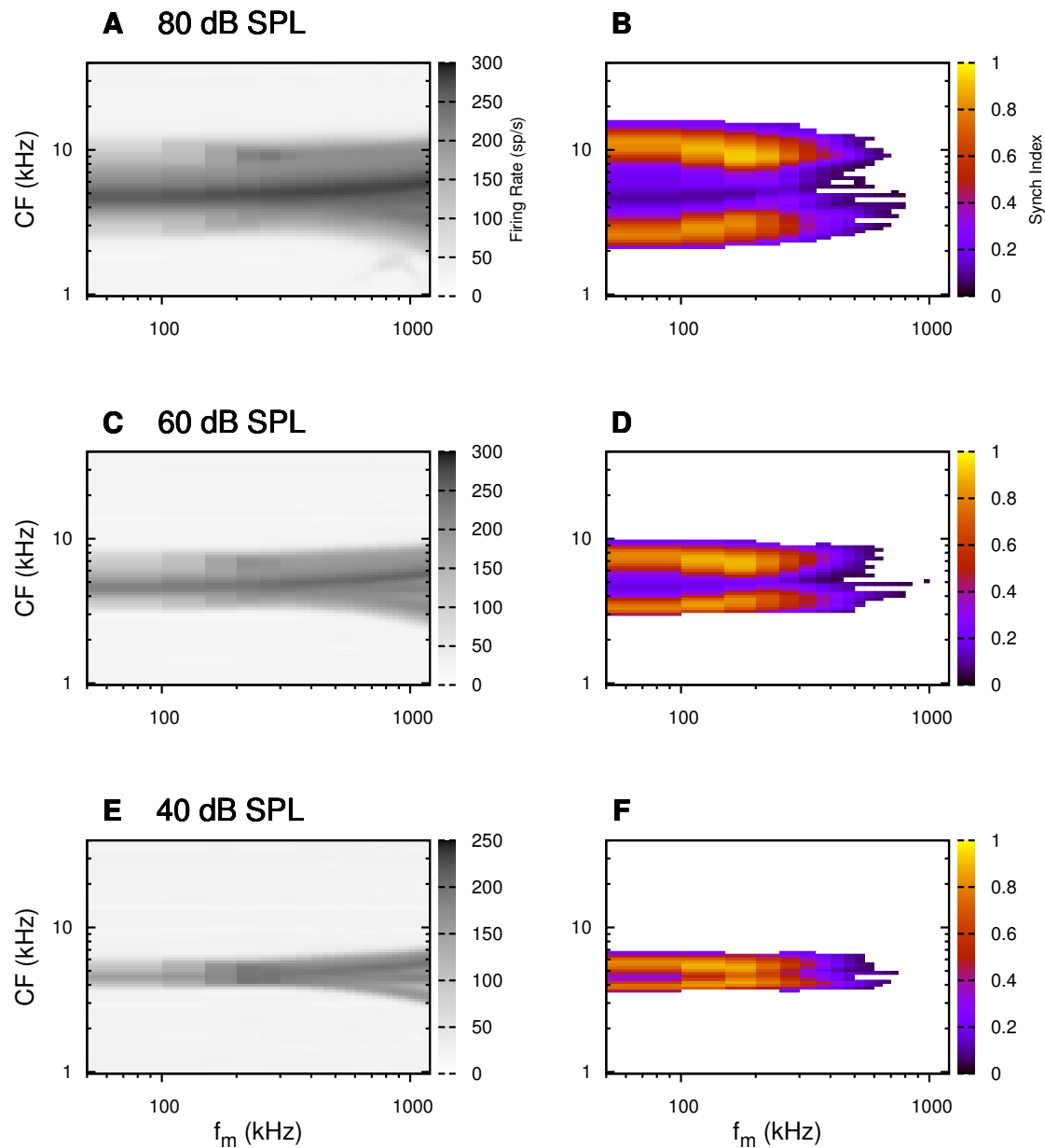


Figure 4.16: Rate and temporal MTF responses for the ChS TS cell model. A. rMTF map at 80 dB SPL. B. tMTF map at 80 dB SPL. C. rMTF map at 60 dB SPL. D. tMTF map at 60 dB SPL. E. rMTF map at 40 dB SPL. F. tMTF map at 40 dB SPL.

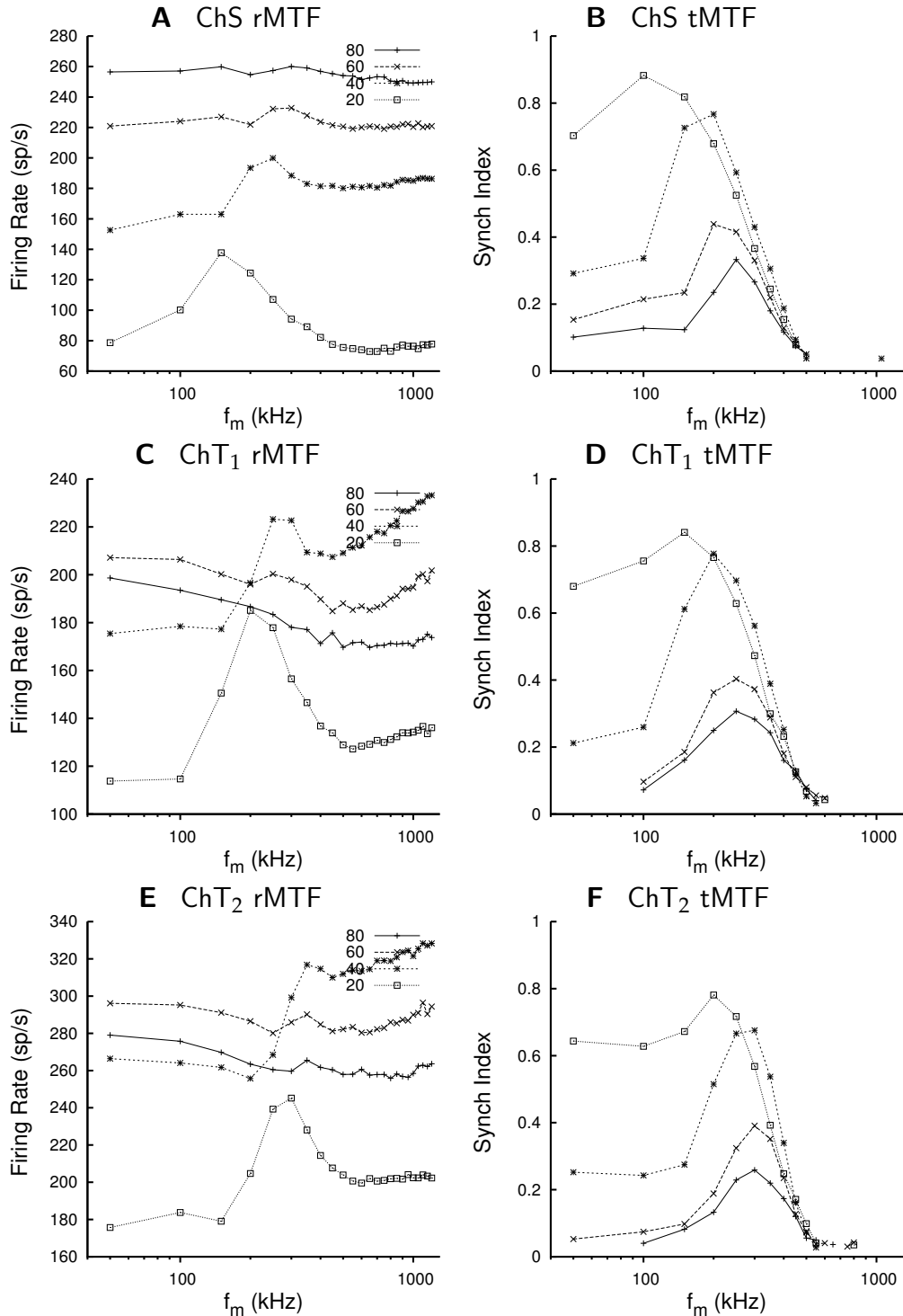


Figure 4.17: A. Rate MTFs of sustained chopper (ChS) model (unit 50, CF 4.513 kHz) on-CF to sound levels 20, 40, 60 and 80 dB SPL. B. Temporal MTFs of the ChS model on CF (unit 50, CF 4.513 kHz) at four different sound levels. C. rMTFs of the on-CF ChT₁ model. D. rMTFs of the on-CF ChT₁ model. E. rMTFs of the on-CF ChT₂ model. F. tMTFs of the on-CF ChT₂ model. tMTF data points that failed the Rayleigh test (p -value < 0.05) were not plotted.

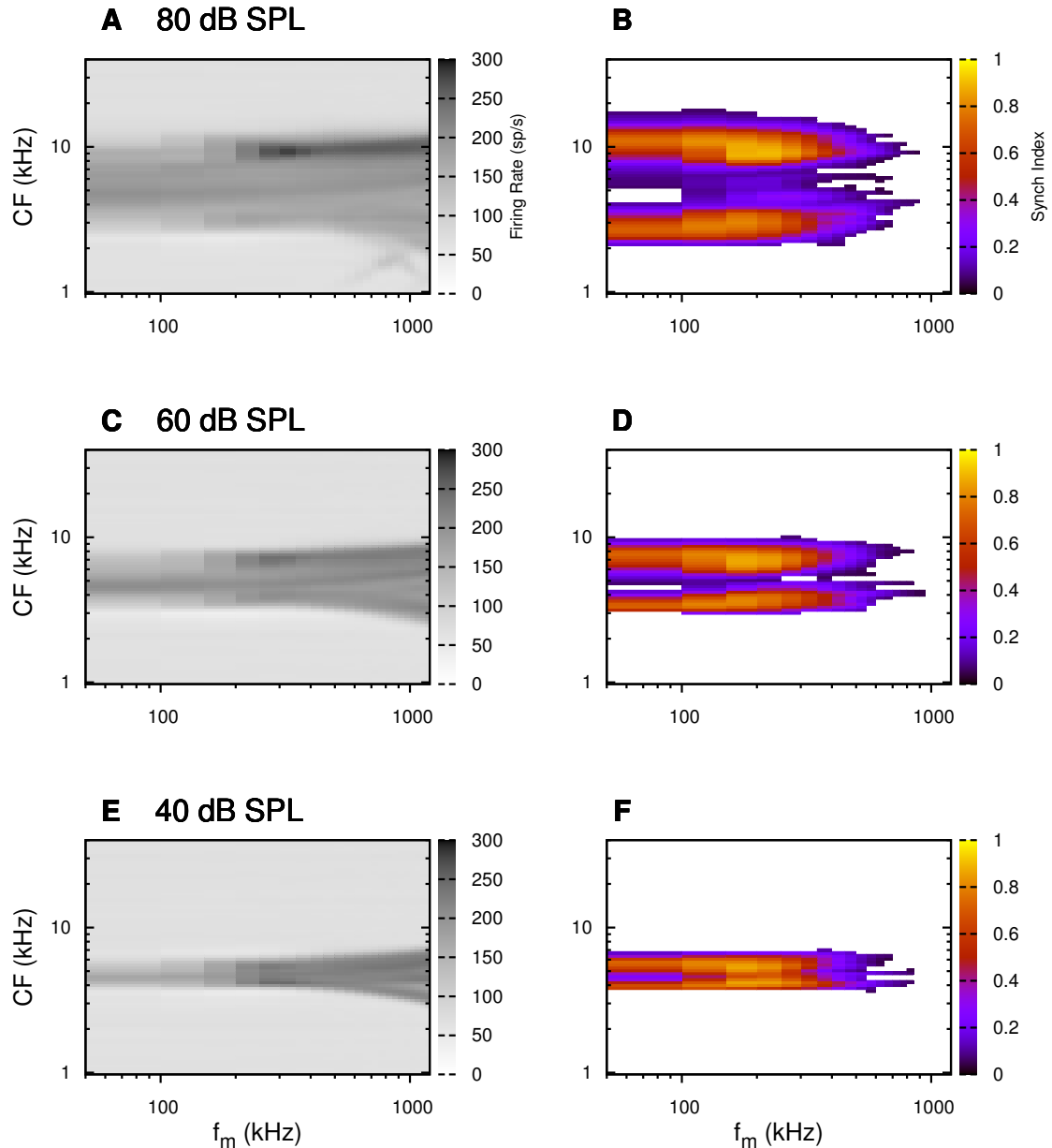


Figure 4.18: Rate and temporal MTF responses for the ChT₁ TS cell model. A. rMTF map at 80 dB SPL. B. tMTF map at 80 dB SPL. C. rMTF map at 60 dB SPL. D. tMTF map at 60 dB SPL. E. rMTF map at 40 dB SPL. F. tMTF map at 40 dB SPL.

The Rhode and Greenberg (1994a) sustained choppers in Figures 4.4A and B had similar band-pass tMTF responses to the ChS model (Figure 4.17B). The SI of the BMF in the on-CFChT₁ model decreased from a peak at 20 dB SPL (0.841 at $f_m = 150$ Hz) before degrading the SI value and increasing the BMF (0.777 at $f_m = 200$ Hz, 0.403 at $f_m = 250$ Hz, 0.307 at $f_m = 250$ Hz for intensities 40, 60 and 80 dB SPL, respectively).

Figure 4.18 shows the MTF response of the ChT₁ subtype TS cell. The rate response of the ChT₁ model is low-pass and is greatly diminished due to its mixture of strong inhibitory inputs. The low firing rate is not visible at higher f_m , but can be seen in the range of activated units in the tMTF maps. The temporal MTF response maps of the ChT₁ model have a high degree of synchrony to the envelope and cut-off frequencies above 1200 Hz. The mean synchronisation of the on-CF unit was very high (mean 0.713, 0.771, 0.721, 0.79) across the range of levels tested (20, 40, 60, and 80 dB SPL). The filter characteristics of the on-CF unit changed from band-pass at 40 and 60 dB SPL (Figure 4.18D and F) to low-pass at 80 dB SPL (Figure 4.18B). The BMF of the on-CF band-pass filters at 350 Hz at 40 dB SPL and 300 Hz at 60 dB SPL had SI values 0.979 and 0.971, respectively. The BMF of the on-CF unit in Figure 4.4D followed a similar pattern to the ChS (0.841 at $f_m = 150$ Hz, 0.777 at $f_m = 200$ Hz, 0.403 at $f_m = 250$ Hz, 0.307 at $f_m = 250$ Hz at sound levels 20, 40, 60 and 80, respectively).

Figure 4.19 shows the MTF responses of the ChT₂ model of the TS cell. The ChT₂ model's rMTF responses were similar the ChT₁ model, with the central units having moderate firing rates for all f_m at each sound level and rate-responder behaviour in the lateral side bands. The units with CF above f_c were more active and the peak response was at $f_m = 450$ Hz, 100 Hz greater than the ChT₁ model, predictably where DS cells become more active. The on-CF rate response was band-pass at 20 dB (BMF at 100 Hz) and at 40 dB (BMF at 150 Hz), however due to uncertainties in the rates at higher sound levels, the rate MTF profiles on-CF were flat or low-pass. The temporal MTF response maps (Figures 4.19B, D and F) had band-pass characteristics for most active units and were strongest in the lateral side bands.

The BMF of the central unit was around 350 Hz for each of the stimulus levels above 40 dB SPL (0.777 at $f_m = 200$ Hz, 0.403 at $f_m = 250$ Hz, 0.307 at $f_m = 250$ Hz for 40, 60 and 80 dB SPL, respectively). The subtle variation in synaptic strength to the ChT₂ model increased the BMF by 100 Hz relative to the ChT₁ model. The simplified band-pass tMTF in Figure 4.5 with an enhanced resonant peak at BMF had limited comparability with the band-pass tMTF of the ChT₂ model. The transient chopper tMTF response in Figure 4.4E was more comparable with the ChT₂ model with a broader band-pass peak at high sound levels and higher cut-off frequencies.

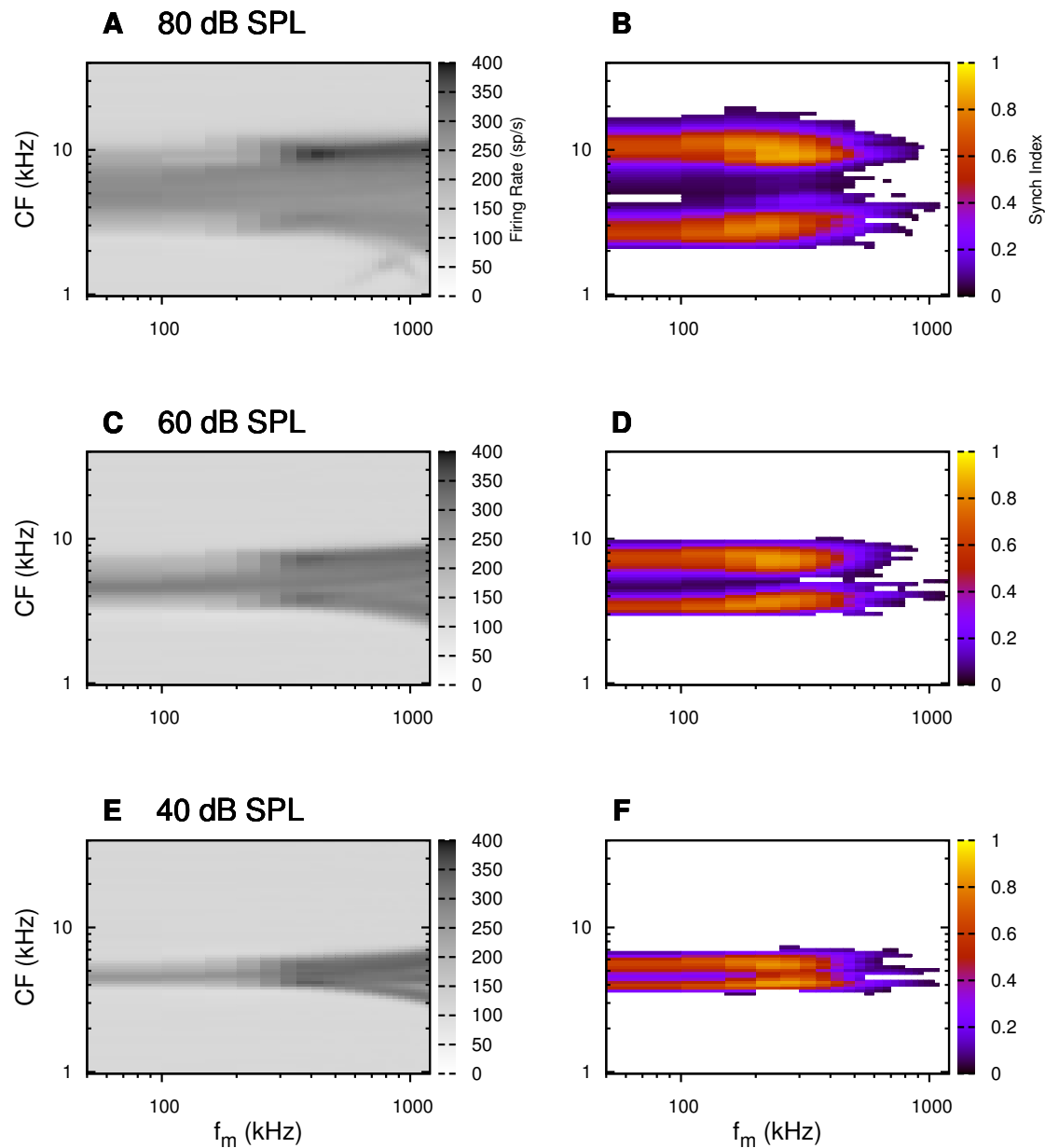


Figure 4.19: Rate and temporal MTF responses for the ChT₂TS cell model. A. rMTF map at 80 dB SPL. B. tMTF map at 80 dB SPL. C. rMTF map at 60 dB SPL. D. tMTF map at 60 dB SPL. E. rMTF map at 40 dB SPL. F. tMTF map at 40 dB SPL.

4.4 Discussion

The results in this chapter demonstrate the successful simulation of AM coding over the whole CNSM model. The primary physiological mechanisms for AM detection and envelope encoding lie in the inner ear or cochlea (Viemeister 1979; Zwicker and Fastl 1999). The cochlea consists of the basilar membrane, the tectoral membrane-outer hair cell mechanism, and the inner hair cell-AN synapse. The signal processing mechanism involves a filterbank of band-pass filters, an active-feedback filter, and a half-wave rectifier followed by a low-pass filter. The Zilany and Carney (2010) AN model used in this chapter includes all these mechanisms and has been shown in this chapter to provide consistent and phenomenologically accurate output in the HSR and LSR units. Irregularities were only observed in responses to high f_m AM tones at 80 dB SPL.

The temporal responses of cells in the CN depend on, and are limited by, the capabilities of the ANF input responses. Intra-nuclei synaptic interactions within isofrequency microcircuits and across frequency channels, and the intrinsic properties of each of the cell types, are best understood by observing responses across the whole network. The next sections discuss the results and their implications for each cell type simulated in this chapter.

4.4.1 Golgi Cells

The demonstration of the response of GLG cells in the CNSM model to AM tones in this chapter is limited by the absence of experimental data with which to make a comparison. The results in Figure 4.7C and Figure 4.11 show that the spectro-temporal response of the GLG cell model to AM tones was mainly dependent on the sound level and the spectral component of the stimulus. The temporal component of GLG cell output information was located toward the edges of its response area and was diminished relative to its primary input, LSR fibres. Intrinsic mechanisms in the cell membrane play a significant role in limiting temporal information. The envelope of synaptic input is drowned out by the synaptic-dendritic smoothing function of the model. The low-pass filter limits the post-synaptic neuron's ability to phase-lock to the modulating frequency, especially at high f_m .

The functional influence of GLG cells on the CNSM model in response to AM tones is the automatic gain regulation of DS and TS cells. GLG cells' monotonic rate-level responses and their GABAergic subtype A (GABA_A) inhibitory synapses control the excitability in both stellate cells in a way that is linearly dependent on stimulus intensity. At high SPL, HSR fibres are rate-saturated and their temporal MTF response diminishes with increasing sound level, producing background synaptic noise in the microcircuit. GLG cell inputs to DS and TS cells during AM tones aid in suppressing elevated, unsynchronised, continuous excitation and enhance their synchronous response to modulated inputs.

4.4.2 D Stellate Cells

DS cells are critical to the CNSM model's ability to encode temporal information at high sound intensity levels. The cumulative results in this chapter show the typical rate-responder behaviour in the DS cell model's rMTF and enhanced, robust tMTF responses (Figures 4.12 and 4.13). The enhanced synchronisation of the DS cell model's on-CF tMTF changed from low-pass to band-pass with increase in sound level. Consistently, DS cell responses in adjacent frequency channels increase their temporal information further from f_c up to the limit of their response area.

The functional role of DS cells in the CNSM model is to provide wide-band, phasic inhibition to TV and TS cells. More specifically, they enhance the entrainment of the TS cells to complex stimulus envelopes through precisely timed inhibition (Frisina et al. 1990b; Joris and Smith 1998; Needham and Paolini 2006; Paolini et al. 2005; Rhode and Greenberg 1994a). DS cells receive a large number of HSR and LSR units from a wide range of frequency channels; consequently, the number of active inputs increases with intensity. Correlated on-CF LSR units and HSR inputs from upper and lower sidebands with high SI help to encode the stimulus envelope; however, dendritic smoothing and uncorrelated on-CF HSR units are capable of diminishing the entrainment of DS cells to the envelope. The DS cell model does not have dendritic compartments or an equivalent smoothing filter as in other models (Kalluri and Delgutte 2003; Wang and Sachs 1995). This model does have a jitter (0.1 ms standard deviation) in the ANF inputs to emulate the variable distance of synapses for the site of activation at the axon hillock.

4.4.3 Tuberculoventral Cells

The results of the TV cell model show a general enhancement of temporal information in response to AM tones relative to ANF inputs at low sound levels. The strong enhancement is likely due to a combination of intrinsic mechanisms, afferent excitation and inhibition by DS units. The f_0 response map of TV cells in Figure 4.6E showed high SI values near boundaries of its response area. Intrinsic mechanisms in the TV cell model (Type I classic RM model) contribute to a high input resistance at the resting membrane potential (RMP). The lower leak potential (E_{leak}) in the TV cell model also increases the difference between RMP and action potential (AP) threshold. These mechanisms remove the DC component of uncorrelated inputs and enhance the AC component of HSR and LSR excitatory inputs.

At high sound levels, the strong inhibitory inputs from DS cells create a non-monotonic response in TV cells. TV cells' temporal response properties in experimental studies have been shown to be complex and non-linear (Joris and Smith 1998; Rhode 1999; Spirou et al. 1999). TV cells are thought to be responsible for delayed inhibition or echo-suppression (Wickesberg and Oertel 1990) in ventral cochlear nucleus (VCN) units, but can also be involved in tuning the temporal behaviour in TS cells at low sound levels. In general, knowledge of the role of TV cells has been further expanded through the CNSM model but further investigation is required to explain inconsistencies in temporal processing of TV cells.

4.4.4 T Stellate Cells

Intrinsic membrane properties and fast, synaptic connections enable TS units to be tuned to important temporal features of the acoustic input (Paolini et al. 2005). The behaviour of TS units is influenced by all three interneurons in the stellate microcircuit. AM rate responses of on-CF TS cell models were fairly weak but temporal information was still present. In the f_0 and MTF analysis, the response of the TS cell subtypes showed insights into the complex spectro-temporal processing being performed in the stellate microcircuit.

In the literature, robustness of temporal information to increased intensity or in

background noise was greatest in ChT units compared to ChS units (Frisina 2001; Frisina et al. 1990a,b, 1993; Joris et al. 2004; Rhode and Greenberg 1994a). The f_0 (Figures 4.6, 4.7) and MTF (Figures 4.16, 4.18 and 4.19) figures show snapshots of the response characteristics in TS cell models across all cells in the network. In the f_0 response analysis, the ChS type TS cell models near the centre of the AM response area had moderate rate and moderate enhancement at high SPL centred around f_c . The temporal response of the ChT₁ model was robust to increases in sound level. This unit did have high firing rates and high SI response near its response area edges, a V-shaped response similar to the HSR units. The ChT₂ models's f_0 response was less robust at higher SPL on-CF but had similar V-shaped enhanced temporal output across different CFs.

Experimental data has shown TS cells generally have low-pass MTF at low sound level and band-pass MTF for higher sound levels for on-CF AM tones (Frisina et al. 1990a; Rhode and Greenberg 1994a). The band-pass temporal responses of different types of TS cells aid in the transformation from a low-pass, temporal encoding of AM in ANFs to a more robust rate encoding in the IC based on preference for different BMFs (Frisina 2001; Joris et al. 2004). At 20 dB SPL (only shown in Figure 4.17), the on-CF tMTF responses were similar for each subtype with high synchronisation at low SPL, a dip in SI at 300 Hz and a second peak above 0.8 SI at 500 Hz. At higher sound levels, the MTF response characteristics of the chopper subtypes diverged. ChS models had lower cut-off frequencies than both the ChT type models. The ChT₁ model had primarily low-pass tMTF responses, but strong inhibition on-CF and suppression of its rate at higher f_m limit the conclusiveness of this model. The ChT₂ had a more consistent rate response and tMTF responses that varied from band pass on-CF to strongly enhanced low-pass in its lateral sidebands.

Given the TS cell subtypes' network parameters were optimised to chopping characteristics for pure CF tones, the results of the CNSM model must be viewed from that perspective. Current TS cell models have investigated AM responses (Bahmer and Langner 2006b; Wiegreb and Meddis 2004) but their inaccurate physiological design is not a good basis to fully understand temporal encoding in the CN stellate microcircuit. An exploration of the parameter space in the TS cells of the CNSM model and their ef-

fектs on the temporal characteristics was not in the scope of this chapter but is an open prospect for future research.

4.4.5 Limitations of the CNSM Model in Modelling AM Encoding

The limitations of the CNSM model discussed in Chapter 3 are equally relevant to the study of AM encoding presented in this chapter. The performance of the Zilany and Carney (2010) AN model has been verified against AM responses in cat ANFs (Joris and Yin 1992; Zilany et al. 2009) and the model remains the most phenomenologically-realistic in terms of AM encoding for use in this study.

A further set of limitations are specifically relevant to AM encoding as studied in this chapter. Most importantly, synaptic delays in the CNSM model are known to play a role in modulating the delay of responses. The CNSM model includes a topographical delay from ANFs to CN neurons, as well as intrinsic connection delays within the stellate microcircuit. Timing of inhibitory synaptic inputs has a major role in regulating the latency of responses in CN neurons, particularly in TS cells with the transient I_{KA} current (Kanold and Manis 2001, 2005). Further work is required to investigate the effects of synaptic parameters in the CNSM model in response to AM tones and stimuli, particularly with respect to highly synchronised DS cell inhibition of TS cells.

The major limitation of this chapter arises out of the fixed network parameter set generated in Chapter 3. The output of TS cells in this chapter were routinely suppressed at high SPL by strong inhibition from DS cells. Whether the design of the optimisation stimuli used in Chapter 3 fully encompassed the influence of DS cells or the phasic responses of DS cells to AM tones provides more effective inhibition is still an open question. Also, the homogeneity of cell-type parameters and their responses in the CNSM model limit its realism and further work is required to understand variability within cell types of the stellate microcircuit.

4.4.6 Implications for Temporal Processing in BNN Models

Paradoxically, the complex temporal processing dynamics in a biophysically-realistic neural network (BNN) model with excitatory and inhibitory connections can be both a

benefit and a detriment to the synchronised output of post-synaptic neurons. A mixture of modulated inputs is beneficial when they are in phase with each other, but can be detrimental when they are uniformly out of phase. Unsynchronised excitation (like that seen in HSR fibres on-CF in moderate to loud AM tones) can saturate temporal information and raise firing rates in the post-synaptic unit. Simultaneously, it can be entrained to the envelope with fast, phasic, highly-synchronised inhibition (like that seen in DS cells) (van Vreeswijk et al. 1995). Unsynchronised inhibition (like that seen in GLG cells on-CF) can be beneficial to a saturated post-synaptic neuron by reducing the DC component of synaptic inputs. Unsynchronised inhibition can also enhance the temporal output by rectifying the AC component. Phase lags, irregularities in synaptic delays and dendritic smoothing all contribute to reductions in temporal processing, especially at the upper limits of f_m .

4.5 Conclusion

By drawing on the CNSM model's strong bio-physiological realism, this chapter has demonstrated a viable approach for generating improved insight into AM encoding in the stellate microcircuit. The CNSM model provides a more realistic representation of AM coding in the output of GLG, DS and TV cells than previous models. While the results of the three TS cell analyses were less convincing, they nonetheless provide a valid example of the diversity in AM encoding by chopper units.

AM representation in lateral sidebands within the CN is essential in communicating valuable temporal information to higher auditory centres. The whole-network approach used in this chapter provides a stronger basis for understanding temporal coding of AM than an approach based solely on CF. This chapter has demonstrated the need to model detailed neural microcircuits away from basic receptive fields of individual units. The CNSM model has been used for detailed optimisation so that it can best illustrate the physiological properties in TS cells and the CN stellate microcircuit. Further exploration of the CNSM model's parameters could cast further light on the role of intrinsic cell properties and synaptic connectivity in the signal transformations performed within the stellate microcircuit.

Chapter 5

Simultaneous Optimisation of Microcircuits Using Genetic Algorithms

5.1 Introduction

Innovative methodologies, such as multi-unit recording (Brown et al. 2004) and optical recording using voltage-sensitive dyes (Grinvald and Hildesheim 2004; Yang et al. 2000), enable neuroscientists to monitor the simultaneous activity of networks of neurons with a higher degree of spatial and temporal accuracy than has previously been achieved at the network level. Concurrently, modern computing power is increasing the speed of modelling biophysically-realistic neural networks (BNNs). Despite these considerable advances, uncertainty remains about the best means to reliably constrain the many free parameters in a model where experimental data are limited. This chapter seeks to address this issue using the cochlear nucleus stellate microcircuit (CNSM) model as an example of simultaneous BNN parameter optimisation and surrogate data in place of experimental data.

One set of approaches to constraining BNNs, denoted as “bottom-up”, use detailed knowledge of specific neurons and their membrane current properties in model construction. Bottom-up approaches to neural modelling have proven successful for representing single cell models, generally relying on hand-tuning parameters. They are, however, insufficiently sophisticated when it comes to constraining the free parameters in small networks of neurons (Grillner et al. 2005; Koch and Segev 1998). In contrast, top-down approaches to constraining neural network models uses the output of the

network activity to infer the underlying model parameters. Such networks were originally developed to be abstract feature detectors (Malsberg 1973) or simple nerve field projections (Amari 1980) based on general principles of neural processing. Optimisation and training algorithms for top-down network constraint are highly efficient and generally involve a gradient-descent search with a training method called back-propagation, where the output error is calculated back through the network (Rumelhart et al. 1986). These algorithms are not applicable to BNNs, however, because the input/output relationships of Hodgkin-Huxley (HH)-type models are not mathematically suitable for error back-propagation.

The particular challenges of constraining network parameters in BNNs or ensembles of spiking neural networks, which have been discussed previously (Brette 2007; Egger and van Hemmen 2001), focus on the analytical methods characterising the spike output (Brown et al. 2004; Kostal et al. 2007). Inferring the connectivity within a network requires a cost analysis or metric of the spiking output (Brette et al. 2007; Victor 2005). Developments in this area have progressed from ensemble feature-based methods (Dahlhaus et al. 1997; Sameshima and Baccala 1999; Theunissen et al. 2000), to information theoretical approaches using maximum likelihood (Chichilnisky 2001; Okatan et al. 2005; Paninski et al. 2004; Yamada et al. 1996), evolutionary algorithm methods (Takahama and Sakai 2005; Yao 1999), and other non-linear approaches (Eblen-Zajjur et al. 1999). Most of these efforts, however, have been restricted to single neuron models or networks of integrate-and-fire neural models, rather than BNNs.

Genetic algorithms (GAs) belong to a class of optimisation algorithms that mimic the process of evolution through natural selection. The primary strength of GAs relative to other optimisation techniques, such as gradient-descent, is that GAs can avoid becoming caught in local minima (Goldberg 1989; Whitley 1995). Since Holland (1975) first used GAs to evolve the connectivity and synaptic weights of artificial neural networks, a range of other hybrid methods have been proposed (Whitley 1995; Yao 1999). Existing examples of biophysically-based neural models constrained using GAs are limited to single and multi-compartmental single cell models (Keren et al. 2005; Van Geit et al. 2008; Vanier and Bower 1999) or small microcircuits (Taylor and Enoka 2004). They are generally regarded as effective in automated parameter-searches.

Keren et al. (2005) used intracellular recordings from a cortical pyramidal cell to constrain the membrane conductances of a multi-compartmental model. The synaptic input noise was filtered out, enabling the model data to be fit to experimental recordings. Additionally, Taylor and Enoka (2004) used a microcircuit of spinal motor units that was trained using feature-based analysis of the output to fit the membrane and synaptic parameters. Ongoing work in BNN modelling (Van Geit et al. 2008; Vanier and Bower 1999) is making headway in removing the hand-tuning of parameters, but the application to medium and large-scale networks may require more techniques from the top-down methods in cost analysis and optimisation algorithms.

This chapter of the thesis reports on an investigation of the application of GAs in constraining synaptic parameters in a topographically-ordered BNN, using the CNSM model as an example of a network in the auditory brainstem. The design of the GA, described below in Section 5.2, includes the specification of a cost function that measures how well the model network reproduces the target data. It assesses three alternate cost functions derived from the outputs of neural responses in the network. Each cost function was based on measures of (1) spike-timing, (2) instantaneous firing rate (IFR), or (3) average intracellular voltage (AIV). Surrogate data from a randomly generated network model served as our target and the ability of the algorithms to find the known neural parameters was assessed. To analyse the robustness of the cost functions to synaptic noise and the effects of trial-to-trial variability, we incorporated these effects into the model.

5.1.1 Stellate Microcircuit of the Cochlear Nucleus

As described in Chapter 1, the cochlear nucleus (CN) is the gateway between the peripheral auditory system and the central nervous system, with six distinct pathways to higher auditory nuclei (Cant and Benson 2003). The exemplar network used in this chapter is a simplified version of the CNSM model.

The tonotopic organisation of the auditory pathway (i.e. the continuous mapping of sound frequency to place of resonance in the cochlea) is transferred to the CN through the population of ANFs (Lorente de Nó 1981). As Figure 5.1 shows, ANFs enter the brainstem ventrally and bifurcate, so that each fibre sends axonal collaterals to the ven-

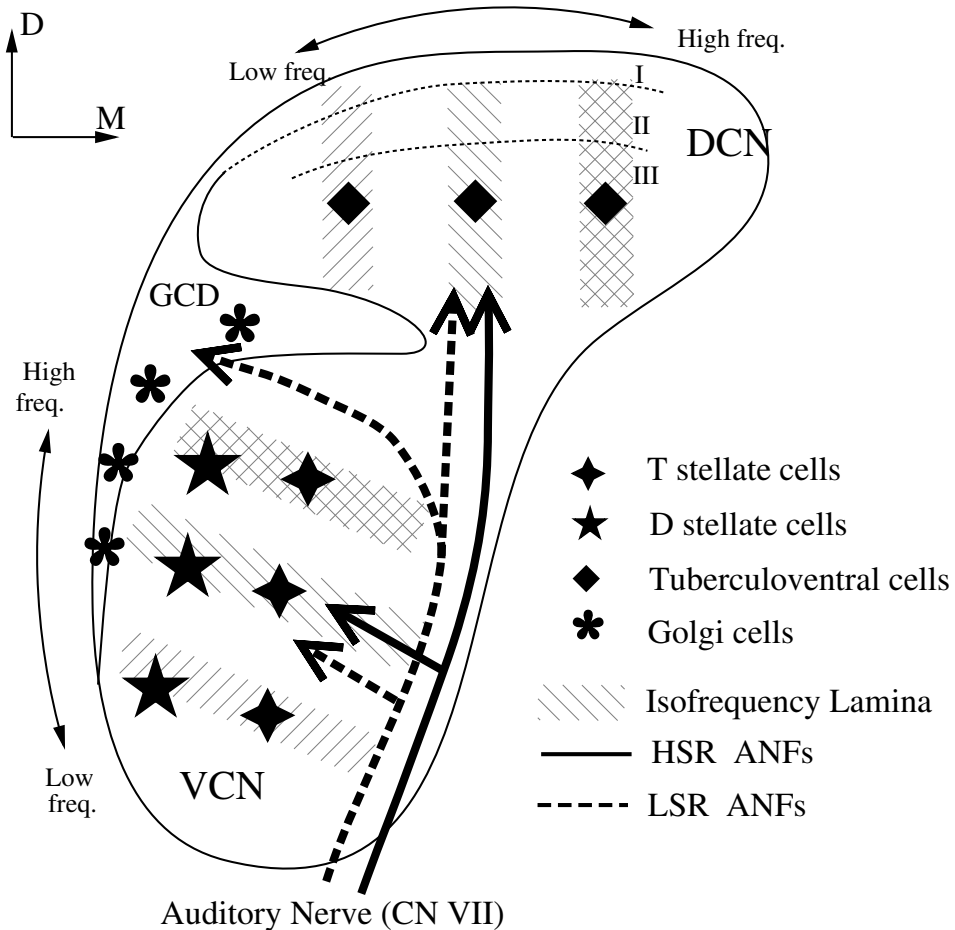


Figure 5.1: Synaptic connections in the mammalian stellate microcircuit of the CN. ANFs sensitive to particular frequencies project to the CN in a tono-topically organised fashion and bifurcate to innervate both the VCN and DCN. The CN comprises two main divisions, VCN and DCN, plus the GCD. Type I ANFs are categorised into two groups based on their spontaneous rate: high (HSR, solid line) and low (LSR, dashed line). Only LSR and smaller type II ANFs project to the GCD. Golgi cells in the GCD are the only known source of GABAergic cells within the VCN, and it is presumed that they synapse with TS and DS cells (Ferragamo et al. 1998a). Glycinergic DS cells project to wide areas of the VCN, DCN, and contralateral CN. DS cells are broadly tuned and respond best at the onset of a tone, with a small number of precisely timed spikes, and respond strongly to broad-band noise. In the deep layer of the DCN, TV cells provide a narrow-band on-frequency source of glycinergic inhibition to the VCN. These neurons respond poorly to clicks and broad-band noise, due to wide-band inhibition from DS cells (Spirou et al. 1999).

tral and dorsal sections of the CN, to organised isofrequency lamina. ANFs are categorised into high spontaneous rate (HSR) (Figure 5.1 solid line) and low spontaneous rate (LSR) fibres (Figure 5.1 dashed line). LSR fibres have a higher threshold than HSR

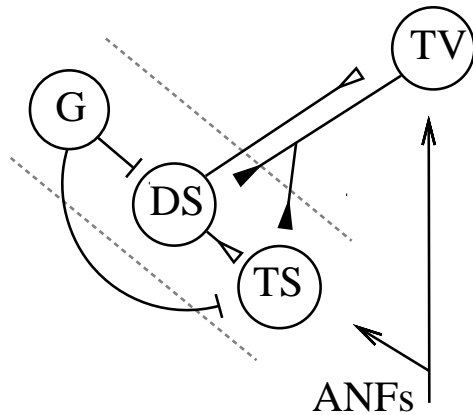


Figure 5.2: Stellate microcircuit showing synaptic interaction within one isofrequency lamina of the ventral CN (dotted lines) and TV cells of the DCN. Excitatory synapses from ANFs (arrows) are modulated within the network by glycinergic (triangle) and GABAergic (bar) inputs.

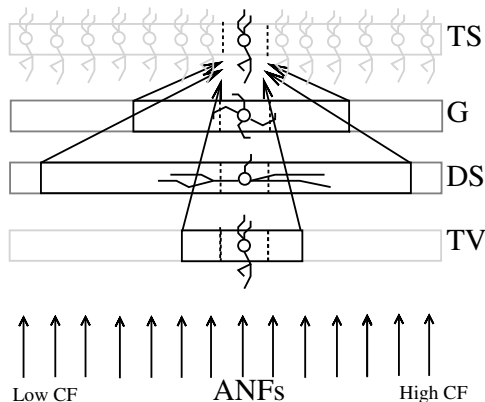


Figure 5.3: ANFs are ordered into a wide range of frequency channels that are mapped to the VCN and DCN in a tonotopic fashion. Topographic organisation of lateral connections in the CN stellate network shows the range of inputs to TS cells from Golgi, DS and TV cells. Dendritic cell morphologies characterise the range of ANF inputs and hence determine their frequency response. ANF inputs to TS and TV cells are restricted to one isofrequency lamina, whereas DS dendrites span one third of the VCN. Axonal plexi of DS cells typically cover one third of the CN and one half of the DCN, giving them a strong influence throughout the CN (Arnott et al. 2004).

fibres and do not saturate in response to loud sounds.

The connectivity of the cell types in the stellate microcircuit is shown in Figure 5.2. Fast, glycinergic inhibition from Tuberculoventral (TV) and D stellate (DS) cells (Figure 5.1) is involved in modulating the firing rate and spike interval variability in T stellate (TS) cells (Ferragamo et al. 1998a; Wickesberg and Oertel 1993). TV cells in the deep

layer of the DCN provide a delayed narrowband inhibition to TS and DS cells in the VCN. The dendrites of DS cells cover one third of the cross-frequency axis in the CN, contributing to this cell's wide frequency response. In turn, this cell is responsible for altering the frequency responses in TS and TV cells (Spirou et al. 1999). DS cells are coincidence detectors and have a precisely timed onset response that affects the temporal properties of TS cells (Paolini et al. 2005; Rhode and Greenberg 1994b) and completely inhibit TV cell responses to loud clicks (Spirou et al. 1999). GABAergic inhibition from Golgi cells (Figure 5.1) modulates the level of excitation necessary to reach threshold for all CN cells (Caspry et al. 1994; Ferragamo et al. 1998a). Feedback circuits from the olivary complex to the VCN are also known to use gamma-aminobutyric acid (GABA) as a neurotransmitter (Saint Marie et al. 1989); however, this was not included in our model.

5.2 Methods

5.2.1 Genetic Algorithm Implementation

GAs work to constrain models by searching across successive generations for the model that is “fittest” in the sense that it best reproduces the supplied data. Each generation of models is obtained from the previous one by using fitness-based selection criteria to create new models from existing members of the population. In this process, a model is represented by a genome, which is the result of mapping the model parameters into binary strings and concatenating them together. Each population of genomes is evaluated for fitness using a carefully tailored cost function. The basic principle of genetic reproduction, namely that fitness increases the probability that a genome will contribute to the crossover operation and mutation, is used to generate new genomes from selected existing genomes. A crossover operation breaks two genomes at a random location and swaps their tail portions to create two new genomes. A mutation is a random bit reversal in a genome. Crossover operations ensure that there is adequate mixing of the best performing genomes in the population and mutations are introduced to ensure diversity. The best members of the population are usually copied (cloned) in the new population.

In this analysis, all GA simulations ran with 100 genomes in each population and evolved for 200 generations. From each population, a new population was created by cloning the five best genomes and performing the following procedure for the remaining 95 genomes. Candidate genomes for crossover were randomly selected based on their fitness, using the roulette-wheel selection probability function, where each score was linearly scaled so that the probability of selection, P_i , was:

$$P_i = 1 - \frac{c_i}{\mathbf{c}} \quad (5.1)$$

where c_i is the genome's cost function score, and \mathbf{c} is the sum of all genome scores in the current population (note that the sign in front of c_i is negative here, instead of the conventional positive, because we used cost functions corresponding to an error term, so that smaller values of c_i imply greater fitness). Following selection of a genome, crossover occurred with a strictly different selected genome, with probability 0.95. Alternatively, the selected genome was cloned, with probability 0.05. For the group of 95 genomes, a random bit mutation was implemented with probability 0.01. The best performing genome string at the end of the 200th generation was declared the winner.

The optimised parameters were the synaptic weights, number of synaptic connections per neuron and a parameter describing the spatial variance of connections (see details in Section 5.2.6 below). The genome encoding scheme, shown in Table 5.1, describes the number of bits used for each parameter and the range of values that each parameter could take. For example, the first parameter in Table 5.1, $w_{\text{ANF} \rightarrow \text{TS}}$, models the strength of synapses from ANFs to TS cells. It was encoded over the range 0.0–0.0051 μS using 8 bits by assigning 0b00000000 to 0.0 and 0b11111111 to 0.0051, and linearly interpolating all values within the range. This procedure was used for all parameters where the unit step was either 0.0001 μS for weight parameters or 1 (synaptic connection or frequency channel) for all others. The number of bits representing each parameter was chosen so that the maximum value lay outside of known physiological values. Genomes were formed by concatenating the parameter bit strings in the order given in Table 5.1.

To test the application of GAs for optimising parameters of a BNN, a network with a known set of parameters was created (the target network). This approach assessed

Table 5.1: Network parameter-to-genome encoding scheme

	Parameter	Binary Bits	Range		Target Value
1	$w_{\text{ANF} \rightarrow \text{TS}}$	8	0.0	0.0051	0.00270
2	$n_{\text{LSR} \rightarrow \text{TS}}$	5	0	31	7
3	$n_{\text{HSR} \rightarrow \text{TS}}$	5	0	31	22
4	$w_{\text{ANF} \rightarrow \text{DS}}$	8	0.0	0.0051	0.00178
5	$n_{\text{ANF} \rightarrow \text{DS}}$	6	0	63	27
6	$n_{\text{HSR} \rightarrow \text{DS}}$	6	0	63	59
7	$w_{\text{ANF} \rightarrow \text{TV}}$	8	0.0	0.0051	0.00091
8	$n_{\text{LSR} \rightarrow \text{TV}}$	5	0	31	13
9	$n_{\text{HSR} \rightarrow \text{TV}}$	5	0	31	16
10	$w_{\text{LSR} \rightarrow \text{GLG}}$	8	0.0	0.0051	0.00150
11	$n_{\text{LSR} \rightarrow \text{GLG}}$	5	0	31	16
12	$w_{\text{DS} \rightarrow \text{TS}}$	8	0.0	0.0051	0.00028
13	$n_{\text{DS} \rightarrow \text{TS}}$	5	0	31	14
14	$s_{\text{DS} \rightarrow \text{TS}}$	6	0	63	15
15	$w_{\text{TV} \rightarrow \text{TS}}$	8	0.0	0.0051	0.00040
16	$n_{\text{TV} \rightarrow \text{TS}}$	5	0	31	12
17	$s_{\text{TV} \rightarrow \text{TS}}$	5	0	31	3
18	$w_{\text{GLG} \rightarrow \text{TS}}$	8	0.0	0.0051	0.00022
19	$n_{\text{GLG} \rightarrow \text{TS}}$	5	0	31	7
20	$s_{\text{GLG} \rightarrow \text{TS}}$	5	0	31	3
21	$w_{\text{DS} \rightarrow \text{TV}}$	8	0.0	0.0051	0.00042
22	$n_{\text{DS} \rightarrow \text{TV}}$	6	0	63	18
23	$s_{\text{DS} \rightarrow \text{TV}}$	6	0	63	8
24	$w_{\text{TV} \rightarrow \text{DS}}$	8	0.0	0.0051	0.00016
25	$n_{\text{TV} \rightarrow \text{DS}}$	6	0	63	7
26	$s_{\text{TV} \rightarrow \text{DS}}$	6	0	63	3
27	$o_{\text{DS} \rightarrow \text{TV}}$	5	0	31	3
28	$w_{\text{GLG} \rightarrow \text{DS}}$	8	0.0	0.0051	0.00246
29	$n_{\text{GLG} \rightarrow \text{DS}}$	5	0	31	7
30	$s_{\text{GLG} \rightarrow \text{DS}}$	5	0	31	5

Units of weights are μS . n and s parameters are unitless integers. The resolution of weight parameters was set to 0.0001 μS and other parameters to 1.

the GA by the algorithm's ability to recover the target parameters. The target parameters were randomly selected from within the physiological range of values given in Table 5.1. Target data were generated from the target network and used as training data for the GA by incorporating them in an error-based cost function. A notch noise stimulus (described in Section 5.2.3) was chosen to present to the network as it produced a spectrally rich response that was spread over the whole frequency range of the target network. Figure 5.4A shows a spike raster plot for the response of all TS cells to the notch noise stimulus. The vertical axis is arranged according to the frequency to which the neuron is most sensitive (the centre frequency). There was a clear reduction in the firing rate corresponding to the stop band in the notch noise. Figure 5.4B shows the responses to 100 repetitions for a single TS cell in the centre of the network, at the rising edge of the notch (arrow in Figure 5.4A).

5.2.2 Cost Functions

At the core of a GA optimisation is a cost function, which is given here by an error measure of an observable output of a trial network against the output of the target network. In this analysis, the total cost function score was calculated using the output of all cells in the network. Three different cost functions were investigated, based on experimental observables: spike times, instantaneous firing rates, and intracellular voltages.

5.2.2.1 Spike Timing Cost Function

Temporal information is critical for communication and segregation of sounds in the mammalian auditory system (Bregman 1990). Spike times give accurate temporal information but are limited by their focus on individual stimulus presentations, which may contain various sources of noise and trial-to-trial variability. The metric we used for comparing trial and target spike trains applied a cost based on relative timing of spikes (see Victor (2005)).

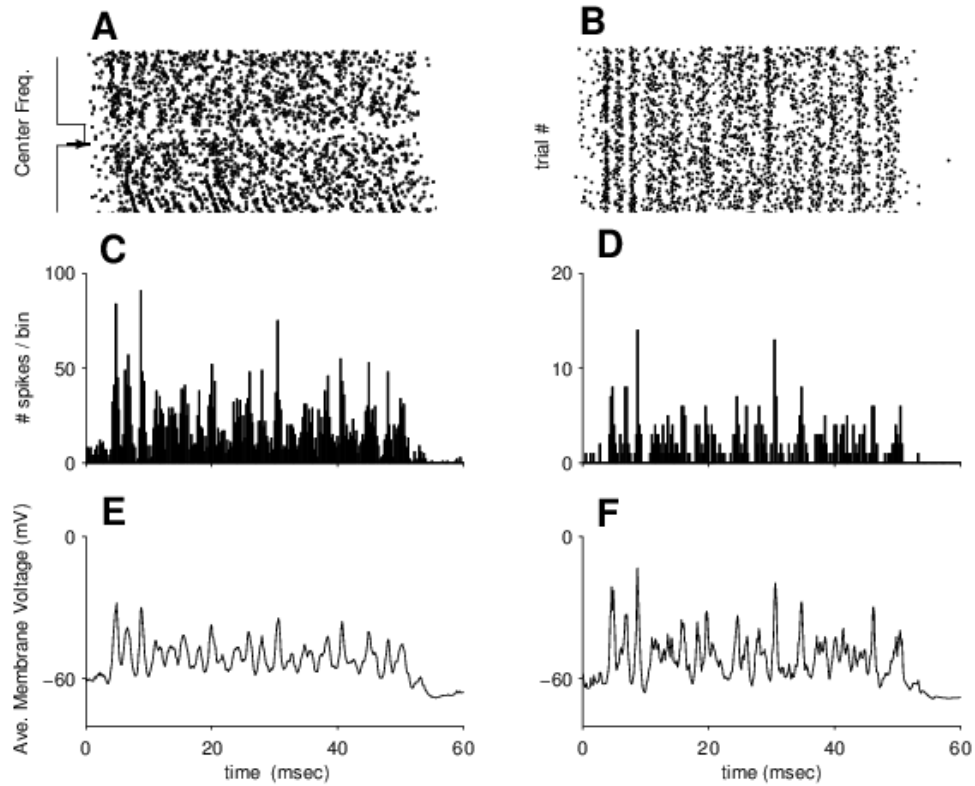


Figure 5.4: Cost function measures derived from the output of the CN stellate network. (A) Dot raster of TS cell spikes during a presentation of the notch noise stimulus. A rough trace shows the relative location of the 30-dB notch in a broadband spectrum from 0.2 to 30 kHz. Frequency scale was determined by the Greenwood function for the cat (Greenwood 1990). (B) The reference spikes for a TS cell in the middle of the 'target' network (CF 3.45kHz) from 100 repetitions of the stimulus are shown. This cell was placed at the edge of the spectral notch (arrow in (A)). (C) PSTH response of the same TS cell used in (B) (bin width 0.25 msec, 100 repetitions). Note the regularly-spaced peaks at the start of the stimulus due to the TS cells' chopper response characteristics. Irregular peaks throughout the stimulus are due to temporal features of the notch noise captured by the auditory filter at this frequency. (D) PSTH of the same cell as in (C) using only 25 repetitions. The IFR cost function normalises the reference PSTHs and calculates a mean squared error between reference and test PSTHs for every cell in the network. (E) Average intracellular voltage, smoothed from 100 repetitions, for the same TS cell. There was some similarity with the PSTH in (C), particularly the location of the peaks, but (E) demonstrates subthreshold effects. (F) Average intracellular voltage using 25 repetitions was more variable than (E) since single action potentials can distort the trace.

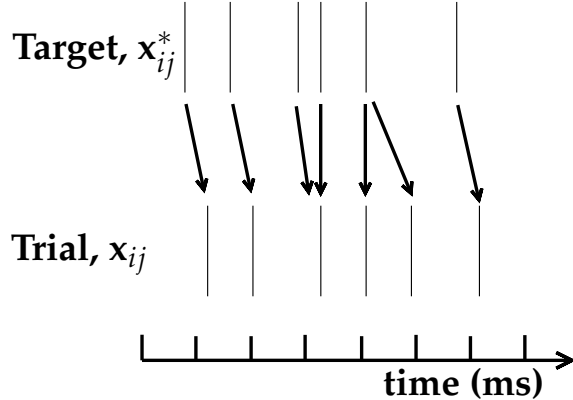


Figure 5.5: Spike timing cost function measure computed using a dynamic programming algorithm. A minimum distance matrix between the *target* set of spike times and a *trial* set of spike times (from the same cell in the network, i) was traversed to find the minimum cumulative path of timing errors. Arrows indicate the possible combinations of spike time errors. For every cell, each repetition in the trial set, j , was compared against 25 repetitions, k , in the training data to find the best fit and to minimise penalties for missing or additional spikes.

The spike timing (ST) cost function was defined as:

$$\Psi_{\text{ST}} = \frac{1}{N_{\text{ST}}} \sum_{i=1}^M \sum_{j=1}^R \min_k (D(x_{ij}, x_{ik}^*)) \quad (5.2)$$

where $N_{\text{ST}} = R \times M$ is a normalisation factor, $M = 240$ is the number of neurons in the network, $R = 25$ is the total number of stimulus repetitions, x_{ij} is the vector containing the spike times of the trial network for stimulus repetition j produced by neuron i , and x_{ik}^* is the vector containing the spike times of the target network for the stimulus repetition k produced by neuron i . The units for Ψ_{ST} are msec per cell per spike train for 60 msec duration spike trains, but are milliseconds in the remainder of the study. $D(x_{ij}, x_{ik}^*)$ is the difference measure between trial and target network spike trains as found by dynamic programming. Dynamic programming is a method for analysing sequential processes (Denardo 1982) and was applied to find the minimum distance between two spike trains, as illustrated in Figure 5.5. In this process, a trial spike train, x_{ij} , was mapped onto a target spike train, x_{ik}^* , by a process of realignment, without specifically considering insertion or deletion of spikes. Insertion and deletion of spikes require additional penalties and have been used in single spike trains (Aronov 2003; Victor et al. 2007). The cost associated with a spike in the trial network and a spike in

the target network was measured as the time difference between the spikes. The spikes were selected for comparison in order to minimise the overall cost.

We chose the minimum value of $D(x_{ij}, x_{ik}^*)$ over 25 target network spike-time vectors, $x_{ik}^*, k = 1, \dots, 25$, to reduce the effect of output randomness. We imposed a limit of 25 repetitions to obtain a reasonable computational load. In the case where a trial network produced no output spikes, $D(x_{ij}, x_{ik}^*)$ was the sum of the target spike times; no target neurons produced empty spike trains.

To illustrate the behaviour of this cost function in the ideal case, where ANF inputs to the trial network are identical to those used in the 25 repetitions of the target data and the target network parameters are used, the value of Ψ_{ST} is zero. The maximum value of Ψ_{ST} observed in this study was approximately 360 msec. For an example trial network that produces the correct number of spikes for each neuron but with an average spike timing error of 1 msec, given that the average number of spikes per train is 9, the cost function would be $\Psi_{ST} = 9$ msec per spike train.

5.2.2.2 Instantaneous Firing Rate (IFR) Cost Function

The PSTH has been an effective tool for classifying the stimulus-induced time-varying firing rate in many neurons including auditory neurons (Blackburn and Sachs 1989; Smith and Rhode 1989). When measured using very short time bins (< 1 msec), the PSTH is an estimate of the IFR. The IFR cost function was obtained from the mean squared error between each neuron's PSTH, r_i , and the corresponding target neuron's PSTH, r_i^* , and was normalised to obtain a firing rate (spikes per msec) error per stimulus.

The IFR cost function was defined as:

$$\Psi_{IFR} = \frac{1}{T_{IFR}} \sqrt{\frac{1}{M} \sum_{i=1}^M \frac{1}{B} \left(\sum_{n=1}^B (r_i(n) - r_i^*(n))^2 \right)}, \quad (5.3)$$

where B is the number of bins in the PSTH, M is the number of cells in the network, $T_{IFR} = R \times W$ is a normalisation factor, R is the number of trial repetitions ($R = 25$ was used in this study), and W is the bin width of the PSTH. The unit for Ψ_{IFR} is spikes per millisecond per stimulus per neuron, spikes per millisecond were used for

the remainder of this study.

To increase the robustness of the IFR cost function to input and trial-to-trial variability, target data from 100 repetitions was used to generate a higher resolution set of target PSTHs, r_i^* , and was scaled by 0.1 to match the trial PSTH repetition number. Figure 5.4D shows an example of a TS cell's PSTH produced from 100 repetitions of a notch noise stimulus. Similarly, Figure 5.4E shows the same cell but with 25 repetitions. The smoother PSTH of r_i^* is evident in Figure 5.4D when compared to the 25 repetitions in Figure 5.4E. Each PSTH is 60 msec in duration (50 msec stimulus then 10 msec silence) and discretised using a bin width of $W = 0.25$ msec (total number of bins $B = 241$).

While the minimum value that Ψ_{IFR} can attain is zero, in practice it will be greater than zero even when the trial network exactly matches the target because the numbers of repetitions used to create r_i^* and r_i are different (100 and 25 respectively). The maximum Ψ_{IFR} value observed in this study was approximately 0.5 spikes/msec per stimulus per neuron. For a trial network, if the average PSTH error is 10 spikes over all bins, then Ψ_{IFR} is approximately 0.2 spikes/msec.

5.2.2.3 Average Intracellular Voltage (AIV) Cost Function

AIV responses reflect the influence of excitatory and inhibitory inputs on a neuron. This may be a more reliable way of determining the strength of synaptic inputs, since spike times and PSTHs do not convey any information about the subthreshold activity of a neuron. The intracellular membrane potential waveform has been used to constrain single neural models with deterministic current inputs and no synaptic noise (Keren et al. 2005; Vanier and Bower 1999). Recordings in real neurons are more varied, with background noise, thermal noise in synapse and membrane channels and non-linear effects of action potentials (APs). AIV alleviates this noise by averaging membrane potential recordings over multiple repetitions. Previous studies in the CN have used experimental AIV to categorise physiological responses, especially different stellate cells (Paolini et al. 2004, 2005).

The AIV cost function was defined using the mean-squared error between averaged voltage waveforms of each trial neuron, \bar{v}_i , and the corresponding target AIV waveform, \bar{v}_i^* . It was normalised to obtain a voltage (mV) error per neuron per stimulus

(mV is used as an abbreviation). The AIV cost function is defined as:

$$\Psi_{\text{AIV}} = \frac{1}{R} \sqrt{\frac{1}{M} \sum_{i=1}^M \frac{1}{N} \sum_{n=1}^N (\bar{v}_i(n) - \bar{v}_i^*(n))^2} \quad (5.4)$$

where N is the number of points in the AIV waveform, M is the number of cells in the network, and R is the number of repetitions.

Figures 5.4F and 5.4G show examples of AIV waveforms, \bar{v} , from a TS cell averaged over 25 and 100 repetitions, respectively, illustrating the reduction in trial-to-trial variation with more repetitions. Action potentials were clipped at 0 mV so that irregular peak heights did not affect the average waveform.

The minimum value of Ψ_{AIV} is zero. Similar to Ψ_{IFR} , in practice the minimum value of Ψ_{AIV} was greater than zero because of the different numbers of repetitions used to create \bar{v}_i and \bar{v}_i^* (25 and 100, respectively). The maximum Ψ_{AIV} value observed in this study was approximately 0.5 mV per cell per stimulus, where no spikes were generated and each cell's AIV was flat.

Table 5.2: CNSM model and simulation parameters

Parameter	Value	Comment
Auditory Model Parameters		Cat model, normal hearing (Heinz et al. 2001)
Channels	60	Centre frequencies determined by Greenwood function (See Eq. 5.5)
Low Freq. (kHz)	0.2	
High Freq. (kHz)	30	
$s_{\text{ANF} \rightarrow \text{TS}}, s_{\text{ANF} \rightarrow \text{TV}}$ (channels)	0	All ANF inputs to TS and TV cells come from their own CF channel
$s_{\text{ANF} \rightarrow \text{DS}}$ (channels)	Above CF: 3 Below CF: 6	Approx. 1 octave above, 2 octaves below CF (Palmer et al. 1996)
$s_{\text{ANF} \rightarrow \text{GLG}}$ (channels)	3	
ANF latency function		
A_0 (ms)	8.3	Eq. 2.16, Cat model (Carney and Yin 1988)
A_1 (cm)	6.49	
Synaptic Delay adjustment		Conduction delay adjustment calculated from mean FSL in CN units
$d_{\text{ANF} \rightarrow \text{TS}}$ (ms)	1.6	Mean FSL 3.6 ms (Rhode and Smith 1986)
$d_{\text{ANF} \rightarrow \text{DS}}$ (ms)	1.2	Mean FSL 3.2 ms (Rhode and Smith 1986)
$d_{\text{ANF} \rightarrow \text{TV}}$ (ms)	2.0	Mean FSL 4.0 ms (Oertel and Wickesberg 1993)
$d_{\text{ANF} \rightarrow \text{GLG}}$ (ms)	2.3	0.7 ms more than VCN core units (Ferragamo et al. 1998a)
Membrane Current Model Parameters		
C_m ($\mu\text{F}/\text{cm}^2$)	0.9	Specific membrane capacitance
Temperature ($^\circ\text{C}$)	37	Rothman and Manis (2003c) used 22°C for <i>in vitro</i> slice experiments.

Continued on next page

Table 5.2 – continued from previous page

Parameter	Value	Comment
Q_{10}	3	Membrane current model temperature quality factor affects the activation and deactivation functions' time constants. $Q = Q_{10}^{((37^\circ - 22^\circ)/10)}$
E_K (mV)	-72	Potassium reversal potential
E_{Na} (mV)	0	Sodium reversal potential
E_h (mV)	-43	Mixed-cation (Ih) reversal potential
Synapse Parameters		
τ_{AMPA} (ms)	0.36	VCN neurons, mature guinea pig (Gardner et al. 1999)
E_{Exc} (mV)	0	Excitatory reversal potential
τ_{Gly1} (ms)	0.4	
τ_{Gly2} (ms)	2.5	GlyR time-constants, MNTB neurons, mature guinea pig (Leao et al. 2004)
τ_{GABA1} (ms)	0.7	
τ_{GABA2} (ms)	9.0	GABA _A time-constants, MNTB neurons, mature guinea pig (Awatramani et al. 2005)
E_{Inh} (mV)	-75	Chlorine reversal potential in GlyR and GABA _A receptors
NEURON Simulation Parameters		
dt (ms)	0.1	Integration time step
<i>secondorder</i>	2	Crank-Nicholson method
R	25	Stimulus repetition
M	240	Total number of cells
W (ms)	0.2	PSTH bin width

5.2.3 Stimulus Generation

Frozen notch noise was used as the stimulus for all simulations. Notch noise is white noise that has been filtered by a narrow band-stop filter. Gaussian white noise was generated in MATLAB/GNU Octave with a 50 kHz sampling frequency and filtered with a quarter octave, 30 dB band-stop, 100-tap FIR filter centred at 5 kHz. A 50 msec

stimulus was presented at 60 dB sound pressure level (SPL) with 5 msec onset/offset ramps, a 20 msec delay and 10 msec pause after the stimulus. Notch noise stimuli have been used in experimental studies of the CN to measure the asymmetric, wide-band suppression of TV cells by DS cells (Reiss and Young 2005) and to estimate the frequency range of ANFs converging on DS cells (Palmer et al. 1996).

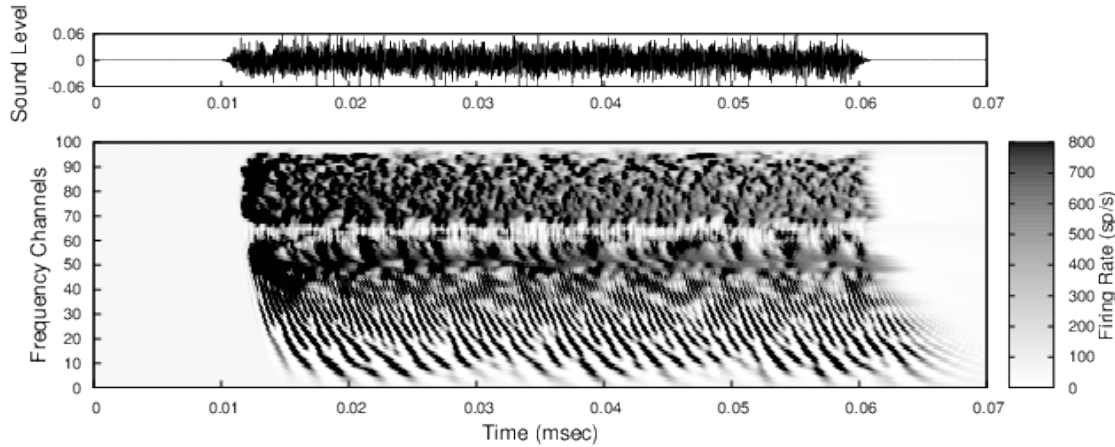


Figure 5.6: Notch stimulus and HSR ANF filterbank output. The stimulus is in Pascals (dB SPL is defined as $20 \mu\text{Pa}$).

5.2.4 Auditory Nerve Model

Figure 5.6 shows the notch stimulus and the output responses of the filterbank of HSR ANF frequency channels. The input to the stellate microcircuit was provided by the phenomenological auditory nerve (AN) model of Heinz et al. (2001) and originally developed by Carney and colleagues (Carney 1993; Zhang and Carney 2001). The model reproduces all significant ANF phenomena including non-linear compression and two-tone suppression over a wide range of frequencies in the normal hearing cat model (see review Lopez-Poveda 2005). The auditory filterbank used in this study consisted of sixty frequency channels with centre frequencies between 0.2 and 30 kHz, with other simulation parameters as listed in Table 5.2. Centre frequencies of the channels were spaced logarithmically according to the basilar membrane frequency-place map of cats (Greenwood 1990):

$$f(x) = 456.0 \times 10^{\frac{x}{11.9}} - 0.8, \quad (\text{Hz}) \quad (5.5)$$

where x is the distance in centimetres from the apex.

The level of spontaneous activity in HSR and LSR AN fibres was set to 50 and 0.5 Hz, respectively. The stimulus was passed through the AN model for each frequency channel for both LSR and HSR fibres, producing an IFR response that was down-sampled to 10 kHz. Twenty HSR and ten LSR AN fibres were simulated for each frequency-channel. Spike times were generated independently for each fibre from the IFR using a pseudo-random spike generator (Jackson and Carney 2005), with refractory effects similar to those present in ANFs.

5.2.5 Neural Models

HH single compartment conductance neural models (Rothman and Manis 2003c) and current-based synapses were used to model the CNSM, as described in Chapter 2. Type I neurons respond to current injection with regularly spaced APs. TV (Zhang and Oertel 1993) and Golgi cells (Ferragamo et al. 1998b) are classic type I, and have I_{Na} , I_{KHT} and I_h currents. While TS cells are regular-firing neurons typical of type I, they have additional A-type transient potassium channels, I_{KA} (Ferragamo et al. 1998a; Rothman and Manis 2003c). Type II responses have only one phasic AP at the start of the stimulus, characteristic of ventral CN bushy cells, which enables them to rapidly follow ANF input events (Oertel et al. 1988; Smith and Rhode 1989). I_{KLT} is present in type II units and is active at resting membrane potential, which allows for rapid changes depending on the input. DS cells respond with a single AP for injected current levels near threshold, then discharge regularly for higher current levels (Oertel et al. 1988; Paolini and Clark 1999), corresponding to an intermediate type I-II response. DS cells have a small amount of I_{KLT} current to reduce the cells' input resistance and enhance coincidence detection. The Golgi cell model used in this chapter was a type I-c single compartment Rothman and Manis (RM) model as distinct from the filter based spiking Poisson neural model, used in Chapter 3.

Table 5.3 shows the maximum conductances, \bar{g} , for each cell type in the CN network. The membrane parameters were fixed after we established the *in vitro* characteristics of each cell type from the literature (Ferragamo et al. 1998a,b; Oertel et al. 1988; Zhang and Oertel 1993) at 37°C, and matched them to the model types in Rothman and Manis

Table 5.3: Cell-type membrane current parameters

Cells Current Clamp Model	TS I-t	DS I-II	TV I-c	Golgi I-c
$\bar{g}_{\text{Na}}, \text{S/cm}^2$	0.235	0.235	0.235	0.235
$\bar{g}_{\text{KHT}}, \text{S/cm}^2$	0.018	0.02	0.019	0.019
$\bar{g}_{\text{KLT}}, \text{S/cm}^2$	0	0.0047	0	0
$\bar{g}_{\text{KA}}, \text{S/cm}^2$	0.0153	0	0	0
$\bar{g}_h, \text{mS/cm}^2$	0.0618	0.247	0.06178	0.6178
$\bar{g}_{\text{leak}}, \text{mS/cm}^2$	0.471	0.471	0.471	0.962
Soma Diameter, μm	21	25	19.5	15
Input Resistance, $\text{M}\Omega$	163	73	170	130

(2003c).

5.2.6 Connectivity

The connectivity and network parameters were described in detail in Section 2.3. The synapse models and their delay parameters in this analysis are unchanged from those reported in Section 2.3.3, in Chapter 2. Topographical connectivity in this model was based on position within the CN (Figure 5.2B), but is easily interchangeable with frequency-specific connectivity. Connection parameters that were fixed are shown in Table 5.2 and parameters used in the optimisation are shown in Table 5.1.

CN cells were spatially organised into 60 isofrequency laminae or channels, as described by the ANF organisation. TS and TV cells' dendrites are located within isofrequency laminae, so ANF inputs were chosen from fibres in the same channel (zero spread, $s = 0$, see Table 5.2). DS cells have many dendritic arborisations extending perpendicular to ANF axons and have a typical physiological response to frequencies 2 octaves below and 1 octave above their characteristic frequency (CF) (Palmer et al. 1996; Paolini and Clark 1999) (see fixed parameters in Table 5.2). Physiological evidence in the analogous granule cell domain of the VCN, the marginal shell in cats, shows units with monotonic, non-saturating rate-level curves, similar to LSR ANFs (Ghoshal and Kim 1996b). ANF labeling evidence shows the absence of HSR ANFs in the Golgi cell domain of the CN (Liberman 1991; Rhode et al. 1983a; Ryugo 2008), so the strength of Golgi cells' excitation is given solely by LSR ANFs ($w_{\text{LSR} \rightarrow \text{GLG}}$ and $n_{\text{LSR} \rightarrow \text{GLG}}$). Wide-

band inhibition of TV cells by DS cells includes an additional channel offset, $o_{DS \rightarrow TV}$, to account for the asymmetry of wideband suppression found in TV cells (Reiss and Young 2005). In this model, the offset was added to the Gaussian mean in the random allocation process.

5.2.7 Simulation Environment

Membrane current models, neural models and network connections were generated using the neural simulation package NEURON (Carnevale and Hines 2006), as described in Chapter 2. Numerical integration was performed using the Crank-Nicholson method with second order accuracy and fixed time step of 0.1 msec. GAs and sensitivity analyses were implemented in C++ using GAlib (Wall 2006) and PVM libraries (Geist et al. 1994). GA simulations were distributed on a cluster of nine PCs (3 GHz Pentium4) and a 64-CPU SGI Altix¹ with a master-slave paradigm.

5.2.8 Analysis of Genetic Algorithms and Cost Functions

To test the performance of the cost functions in GA optimisations, sets of target data were produced using a target CN network with parameters shown in Table 5.1. The GA was run with each cost function using two conditions: (1) with identical ANF spike times as used in creating the target data, and (2) with different ANF spike times, derived from the same IFR function but where the spike times were recalculated for each evaluation. The performance of the GA was evaluated by examining the behaviour of the best genomes in relation to the scores of other genomes with small parameter deviations, the relative parameter difference between the best genome and target genome (parameters of the target network), and the robustness of the optimisation when using different ANF inputs.

We used two analytical techniques to test the sensitivity and robustness of the cost functions to parameter variation. Sensitivity was defined as the relative change in cost function when one or more parameters were varied. Robustness was the relative change of a cost function in response to different instances of noise, in this case different

¹Computer system named soma at the Department of Electrical and Electronic Engineering and Neuroimaging Group, University of Melbourne in 2006.

instances of randomly generated spike inputs from the AN model for each fibre. The sensitivity measure for uniform parameter variation was provided by the degree of variation of cost function scores near the global optimum when performing random deviations of all parameters about their target values. One thousand genomes were generated and each parameter was randomly varied by -1, 0 or +1 unit steps (0.001 for weight parameters and 1 for other parameters) with equal probability. This procedure was repeated for 1000 genomes with unit steps between -5 and 5. Robustness was measured by re-evaluating the two genome sets above with different ANF input spikes regenerated for every genome.

The sensitivity analysis of the cost functions to individual parameter variation at the global optimum is described in Section 5.3.2. Parameter values were stepped up and down independently (steps were determined from the gene resolution in Table 5.1) to determine the cost function learning gradient on either side of the target value. Gradients were calculated using a least-squares linear regression in MATLAB and two-sided t-tests were performed to determine whether each gradient was significantly different from zero. This was done for the identical and the different ANF inputs, and robustness was evaluated by comparing the ratio of V-shaped to non-V-shaped cost function gradients for different inputs.

5.3 Results: Optimisation of Biophysically-Realistic Neural Networks Using Different Inputs

This section presents the results and analysis of GA optimisation on network parameters of the CN stellate microcircuit model.

5.3.1 Genetic Algorithm Performance

5.3.1.1 Evolution of Cost Functions

The performance of the GA optimisation is demonstrated by the evolution of the best score in each generation for three independent GA runs (Figure 5.7). The best genome score in each generation (solid line) shows the progress of the optimisation by the GA,

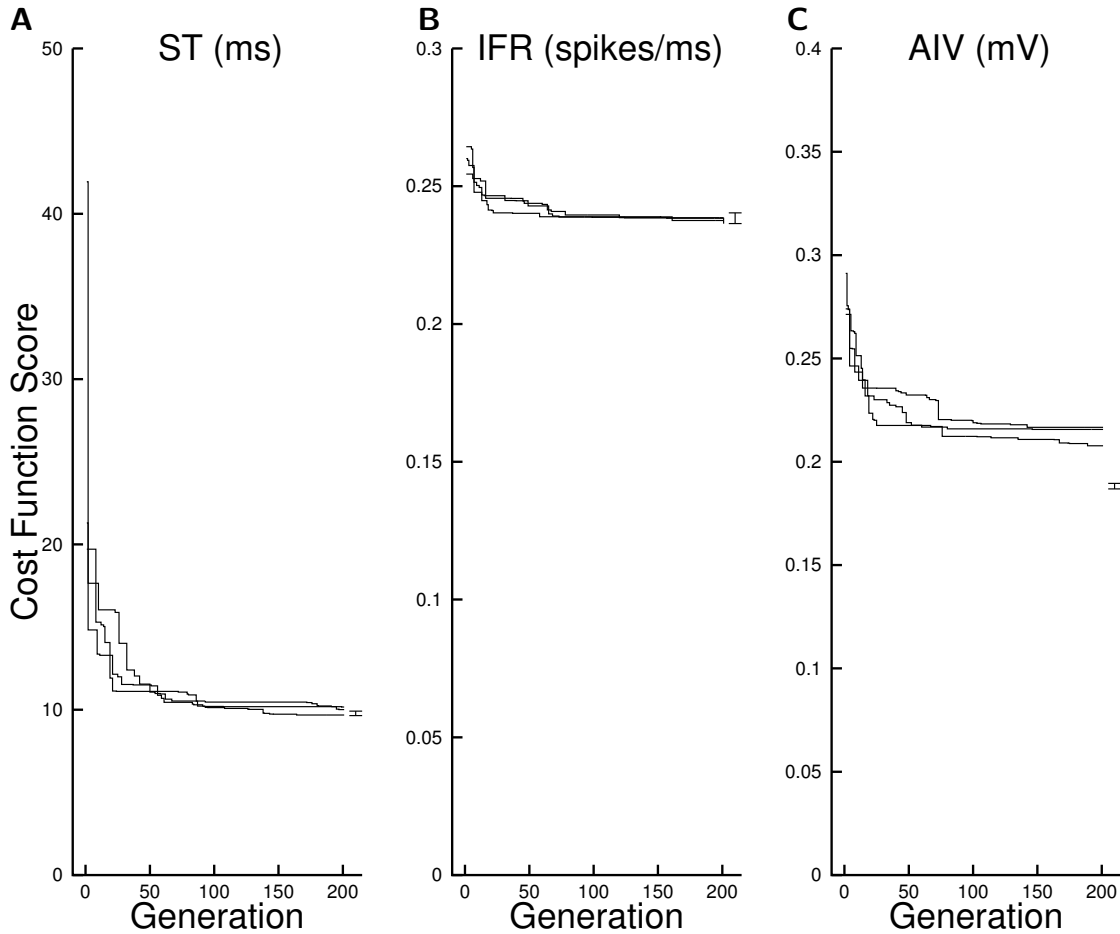


Figure 5.7: Performance of the GA's best performing genome in each generation is shown for each simulation. The error bar to the right of each graph is the mean score and 95 percentile range of the target genome.

from large steps initially to more incremental improvements as the score tends towards an asymptote. During the later generations, the best genome score showed relatively little variability between different GA runs, suggesting that GA performance was consistent across runs. The relative improvement between initial and final scores was greater for the ST and AIV cost functions than for the IFR cost function.

For all three cost functions, the best score obtained by the GA was considerably above an error of zero. This does not imply poor performance by the GA, because a perfect score of zero would require not only an exact match to the target parameters, but also a precise match to the AN input spike trains used in the target data. Experimentally, the spike times of the AN vary stochastically based on an instantaneous rate function for any given stimulus. This stochasticity was incorporated into our model

and led to non-zero scores, even for the target network. The mean target score is shown by the error bars on the right of each plot in Figure 5.7.

For the ST and IFR cost functions, the best genome score was within the range of scores found for the target network, indicating that the GA was able to find a network that gave the same behaviour as the target network, as measured by the cost function. For the AIV cost function, the best genome had a score that was greater than the range of scores found for the target network, indicating a discrepancy between the behaviour of the best network and that of the target, as measured by the cost function.

5.3.1.2 Cost Function Cross Comparison

To facilitate the comparison of cost function performance, we used the best genome from GA runs trained with one of the cost functions to evaluate the remaining cost functions. This also allowed us to gauge how well that genome was able to generalise to reproduce network behaviour, as measured by the other cost functions. The results are shown in Figure 5.8, which compares the mean score evaluated using the ST, IFR and AIV cost functions (top to bottom, respectively) for each of the three best genomes obtained from GA runs trained with the different cost functions. In general, the lowest scores were obtained when using the same cost function for evaluation as was used for training of the best genome.

One AIV-trained best genome generated ST scores around the target distribution; however, the top graph in Figure 5.8 shows that overall the IFR and AIV best genomes performed relatively poorly when evaluated against the ST cost function. The opposite pattern was observed when the best genomes were evaluated with the IFR cost function (middle plot), in which the ST best genomes performed poorly relative to the IFR and AIV best genomes. All the best genomes gave similar scores for the AIV cost function (bottom plot), but did not reach the target genome scores.

5.3.1.3 Match to Target Parameters

An additional way to evaluate GA performance is to compare the parameter values between the best and target genomes by evaluating the relative error between parameters

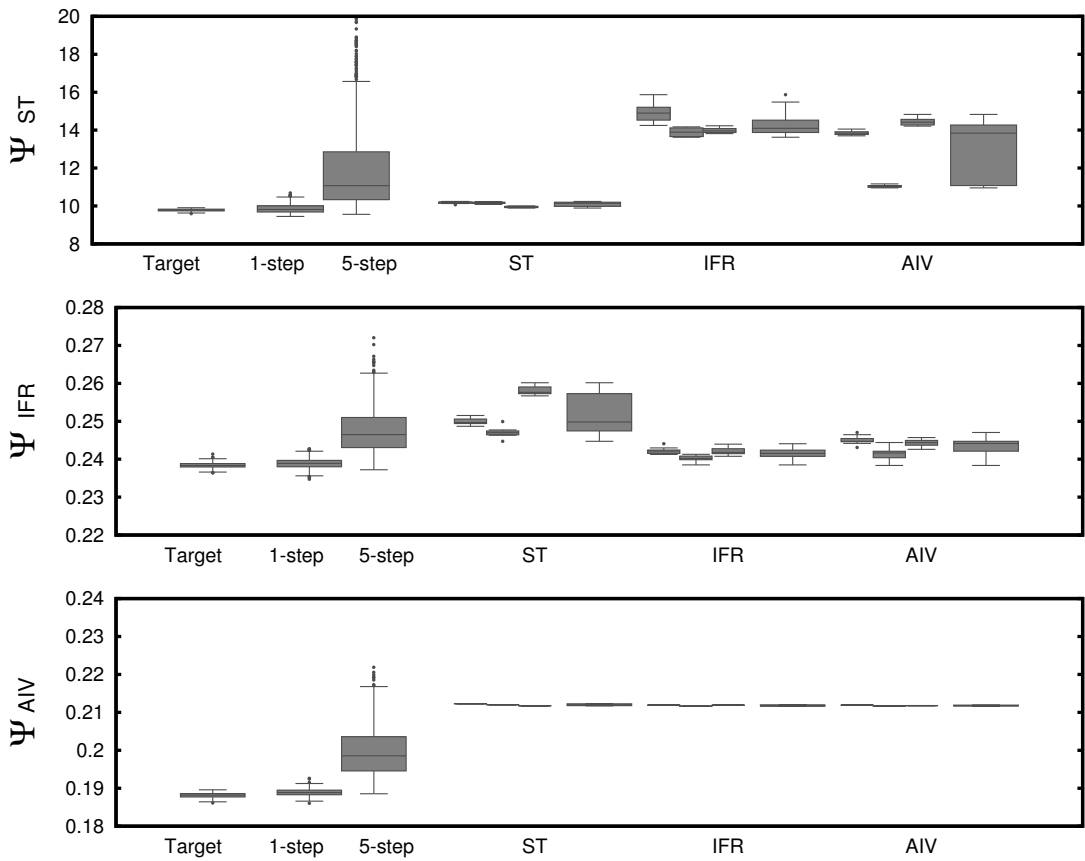


Figure 5.8: Cross comparison of best genomes generated using GA with 25 repetitions, measured against the target, 1-step and 5-step parameter perturbation distributions. The box plots show the three best genomes evaluated ten times for each cost function, plus an accumulation box plot of all three. 100 evaluations of the target genomes were evaluated and 1000 parameter perturbations were evaluated for the 1-step and 5-step distributions.

(i.e. $|g_i^* - g_i| / g_i^*$). Individual relative parameter errors are shown in Figure 5.9 for each of the best genomes trained on a particular cost function. Parameters were ordered by increasing mean relative error across all best genomes and all cost functions.

The plot shows a similar level and pattern of performance across genomes trained with the three different cost functions. Parameters were either reasonably or poorly constrained independent of the cost function being used in training. In terms of parameter type, all bandwidth parameters were in the upper half of genome errors whereas synapse number parameters were predominantly in the lower half. Weight parameters were spread over the whole range.

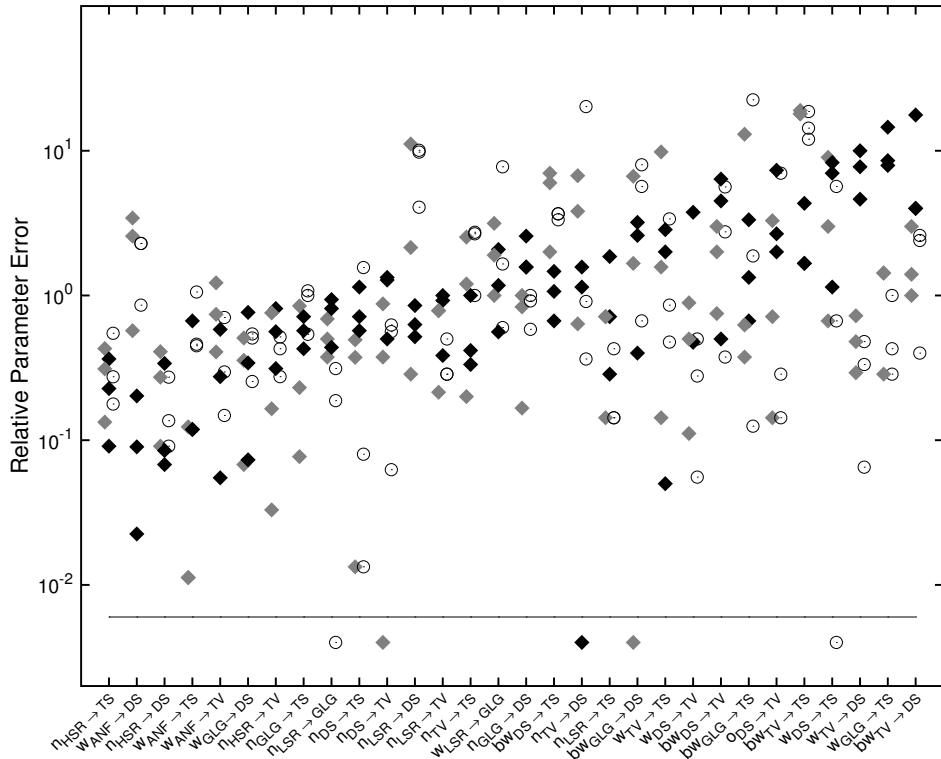


Figure 5.9: Parameter errors of the best genomes in 3 GA simulations for each cost function: ST (grey diamond), IFR (block diamond), and AIV (unfilled circle). Errors were normalised in terms of the target parameter values. Points below the line were fit perfectly to the target value.

5.3.2 Parameter Sensitivity

5.3.2.1 Simultaneous Parameter Perturbation Analysis

We performed a parameter sensitivity analysis to better understand the relationship between cost function scores and the match to target parameter values. This involved measuring the change in the cost function due to simultaneous perturbations in all parameters. Figure 5.10 shows the distribution of cost function scores for different degrees of random simultaneous parameter perturbation. Two populations of 1000 genomes were generated, one with parameter values allowed to vary uniformly by 1 unit step either side of the target (i.e. -1, 0 or 1 step), and a second population varied uniformly up to 5 unit steps. In the 5 unit step experiment, one parameter covers 11 combinations, including the target value.

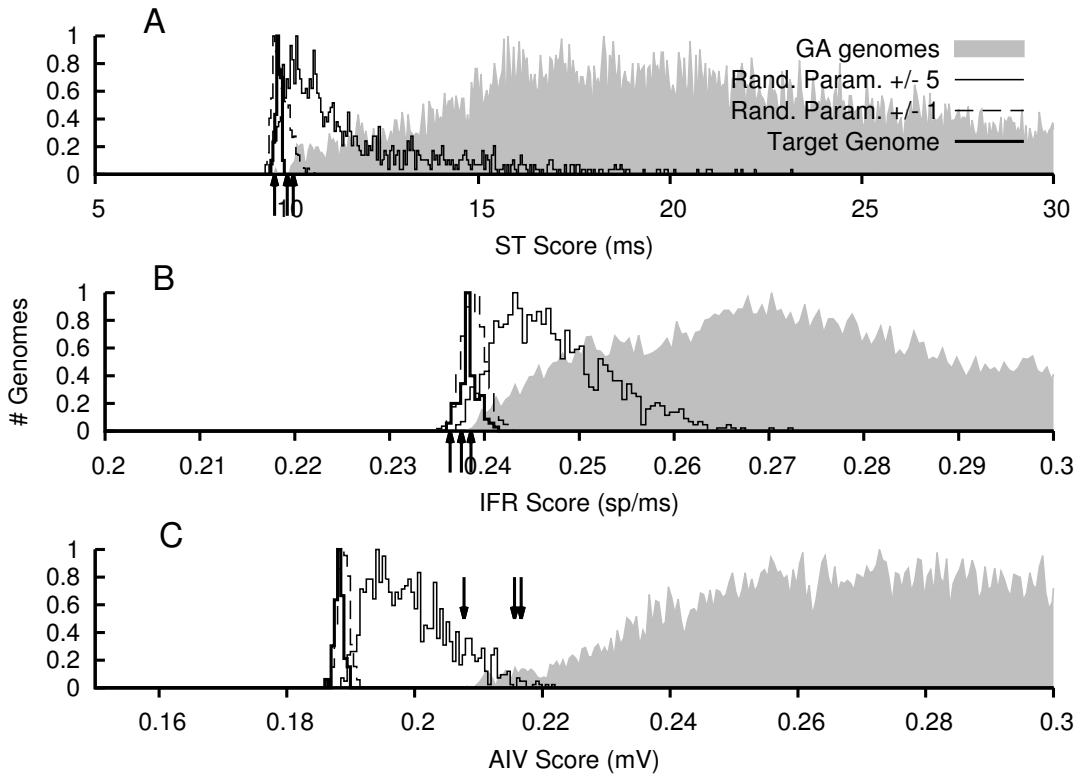


Figure 5.10: Histograms of simultaneous parameter perturbation of each cost function. The distribution of genomes in grey were all evaluated by the GA that obtained the lowest score. The best scores of 3 GA simulations are pointed to by the arrows. The histograms show the distributions of 100 target genome scores (thick line), 1000 genomes deviated by 1 unit step away from the target value (dashed line), and 1000 genomes deviated by 5 steps (thin line) from the target. The input spike generation and network connections for each parameter set (genome) were randomly generated for each evaluation. All graphs are normalised to the peak value in each histogram.

In general, 1 unit step perturbations produced cost function scores that were slightly above and slightly below the range produced by the target network (compare dashed and bold lines in Figure 5.10A). Five unit step perturbations produced cost functions scores that were largely above the target network range (compare thin solid and bold lines in Figure 5.10A). This pattern was consistent across the three cost function types. The shift of cost function scores to progressively higher values with progressively larger perturbations was expected and desirable. It forms the basis upon which the GA performs optimisation by comparing candidate genomes to the target.

Best genome scores from GA runs trained with either the ST or the IFR cost function lay inside the range produced by the 1 unit step perturbation, whereas best genome

scores from the GA runs trained with the AIV cost function were at the upper limit of the range produced by 5 unit step perturbations. In fact, Figure 5.9 shows that all best genomes scored equally badly when evaluated 100 times with the AIV cost function. Given this difference in AIV cost function scores, it is worth noting again that the pattern of change in cost function distributions with perturbation size was fairly consistent across cost function types. This suggests that the AIV cost function is equally well behaved in the vicinity of the target compared to the other two cost functions. In this case, the reason that the best genomes trained with any cost function were unable to attain a score in the target range (bottom plot of Figure 5.9) was not due to a poorly behaved cost function.

It was surprising that the 1 unit step perturbations produced a network with lower cost function scores than the target network, albeit marginally. This effect is the result of noise in the cost function, introduced by the stochastic AN input: the 1 unit step perturbations involved 1000 separate instances of ANF input, compared to only 100 instances for the target, so it was likely that a better match to the precise target ANF input was found amongst the former rather than the latter. This effect is only expected for values of the cost function around the target score, where systematic reduction of the cost function becomes increasingly marginal. This finding is consistent with the observation that for larger, 5 unit step perturbations the effect was much diminished or absent.

5.3.3 Effects of Noise

Noise from AN inputs could have a significant impact on the GA optimisation, with noise potentially preventing the GA from attaining a good match to target. A simple way to reduce noise is to use a larger sample of stochastic realisations of the AN input when evaluating target and candidate genomes. This can reduce noise through an averaging process, in the case of IFR and AIV cost functions, or through allowing more choice in matching spike trains in the ST cost function. This would require using more stimulus repetitions when collecting target data experimentally, and when simulating candidate networks in the GA computationally. In this section, we examine the utility of this approach by comparing GA performance for 100 instead of 25 stochastically

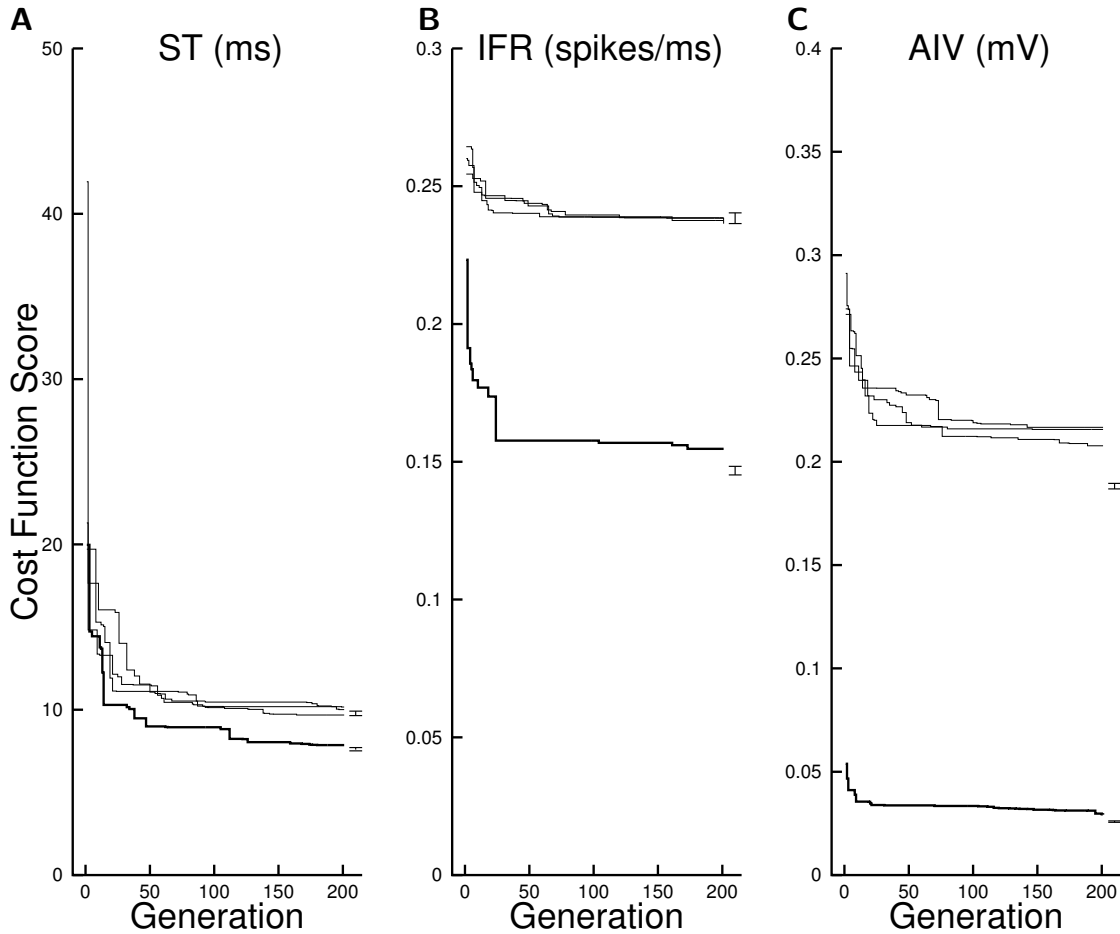


Figure 5.11: Performance of the GAs best performing genome run with 100 repetitions in the fitness function. GA simulations run with 25 repetitions are shown in grey. The mark to the right of each graph is the mean score and error bars showing the range of 2 times standard deviation away from the mean target genome score.

distinct repetitions of the ANF input for both target and candidate genomes.

5.3.3.1 Effects of Increasing Stimulus Repetitions

Figure 5.11 shows the evolution of best genome scores when 100 repetitions were used for the target and candidate genomes instead of 25 (as used in the results presented thus far). Overall, the use of increased repetitions of the stimulus resulted in reduced cost function scores but did not result in better GA performance (see Figure 5.12).

Similar to Figure 5.9, Figure 5.11 compares scores across best genomes trained with different cost function types (ST, IFR or AIV) and different numbers of repetition (25 or 100) giving a total of six different best genomes types: ST-25, ST-100, IFR-25, IFR-

100, AIV-25 and AIV-100. The three different graphs (Figure 5.11A-C) correspond to evaluation of these best genomes using the three different cost function types. The top of the lighter bars give the mean score when 100 repetitions were used for evaluation, while the top of the (appended) dark bars give the mean score when only 25 repetitions were used for evaluation.

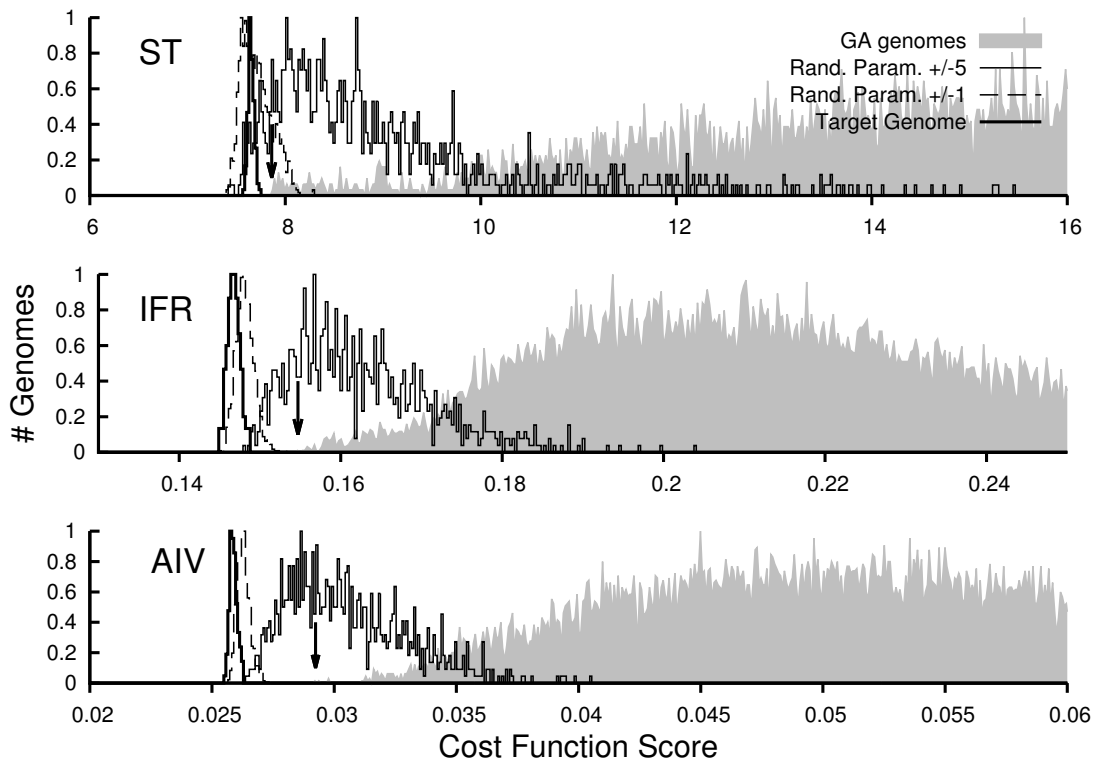


Figure 5.12: Cost function histograms of simultaneous parameter perturbation using 100 repetitions. The distribution of genomes evaluated during the GA is shown in grey and the eventual best score is pointed to by the arrow. The histograms show the distributions of 100 target genome scores (thick line), 1000 genomes deviated by 1 unit step away from the target value (dashed line), and 1000 genomes deviated by 5 steps (thin line) from the target. The input spike generation and network connections for each parameter set (genome) were randomly generated for each evaluation.

In all cases the use of 100 repetitions to evaluate the cost function resulted in lower scores than when 25 repetitions were used (i.e. the top of the dark bar lies above the top of the light bar). This did not show that genomes trained with 100 repetitions attained lower scores than those trained with 25 repetitions once the comparison was made using the same cost function (i.e. same type, same number of repetitions). In nearly all cases, scores for genomes trained using different numbers of repetition (25 or 100), but

the same type of cost function (ST, IFR or AIV), obtained similar scores, regardless of the details of the cost function used to evaluate them (i.e. ST-25, ST-100, IFR-25, IFR-100, AIV-25 and AIV-100 cost functions). The exception was the AIV-100 trained genome when evaluated by the ST cost function. This suggests that, although the increased number of repetitions reduced noise (and, therefore, cost function scores), this was not a factor limiting GA performance.

Table 5.4: Best genomes obtained from GAs run with 100 repetitions. * PE = mean relative parameter error.

Cost function	PE*	Final GA Score	Mean (S.D)
ST (msec)	1.977	7.86038	7.89 (0.04)
IFR (spikes/msec)	2.169	0.154698	0.1557 (8.6e-4)
AIV (mV/msec)	2.325	0.0292369	0.0292 (9.8e-5)

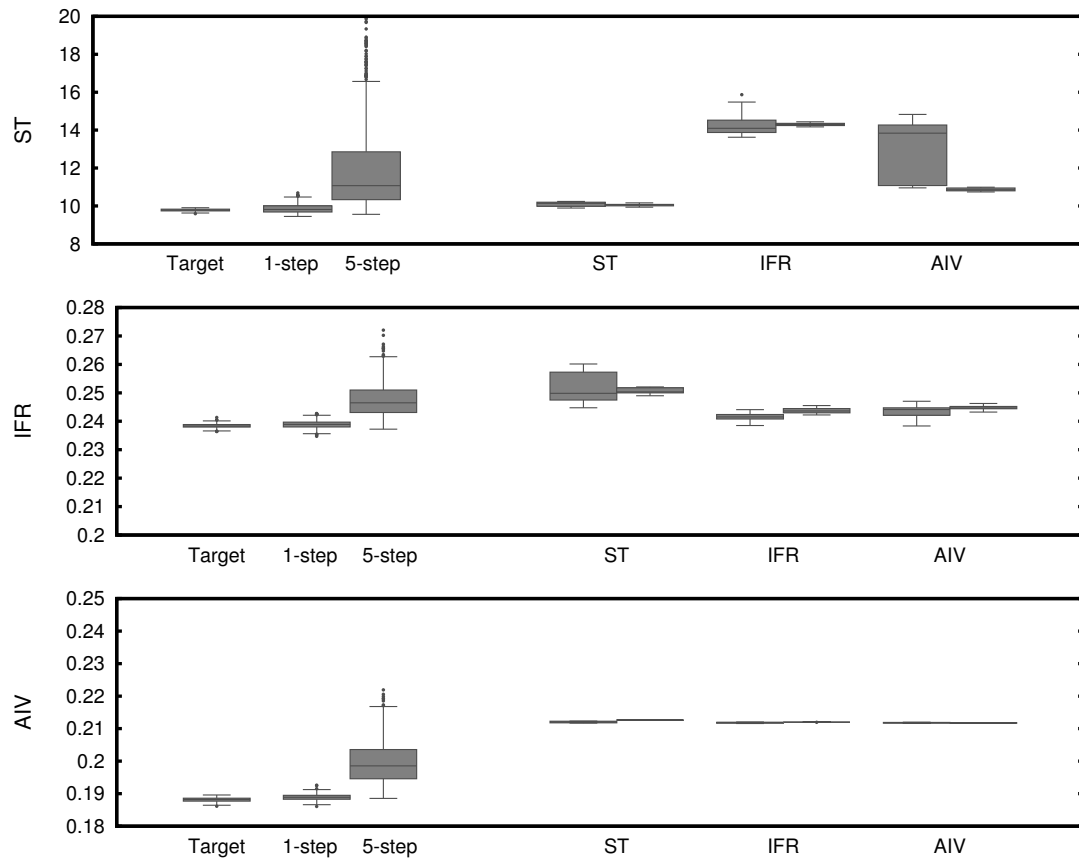


Figure 5.13: Cross comparison of best genomes generated using GAs with 100 repetitions, measured against the target, 1-step and 5-step parameter perturbation distributions. The box plots show the best genomes evaluated ten times for each cost function.

5.4 Discussion

5.4.1 Matching a BNN to a Known Target Network: Performance of GA and Cost Functions

We tested the ability of GAs to constrain models of BNNs using surrogate data from a known target network under simulation. Three cost functions were investigated, based on spike timing, firing rate (IFR) or intracellular recordings (AIV). Performance of the GA with the three different cost functions was evaluated in two ways. First, using a cross comparison of cost function scores, whereby best genomes obtained from the GA using one cost function were evaluated using each of the three cost functions. Second, using relative parameter errors between the best genomes and the target genomes. Our analyses showed that all three cost functions gave a similar overall level of performance

in matching to the target network, although there were some important qualifications, which will be discussed below. The two different methods of evaluation, by cost function and by relative parameter error, gave different pictures of GA performance.

Best genomes were able to attain scores close to those obtained for the target network. This is best demonstrated in Figure 5.10, which shows the cross comparison of cost function scores for all types of best genomes examined in this study. GAs run with the ST cost function were able to consistently achieve convergence of best genome scores to very near the target score. The deviation was less than that due to a 1 unit step cost function. For GAs run with the IFR or AIV cost function, convergence to target scores was good, but not as consistent as the ST cost function. For both types of best genome, scores were best relative to target when evaluated using the IFR cost function. When evaluated with 25 stimulus repetitions, the scores were equivalent to a 1-unit step perturbation, but when evaluated with 100 stimulus repetition the scores were equivalent to a 5-unit step perturbation. Both IFR- and AIV-trained best genomes scored significantly worse when evaluated with the ST cost function, with scores falling in the upper tail of the distribution obtained with 5 unit step perturbations of the target genome. The performance of IFR- and AIV-trained best genomes, when evaluated with the AIV cost function, was similar to that of the ST-trained best genome, namely that AIV scores were limited to the upper half of the distribution obtained with 5 unit step parameter perturbations of the target genome.

In summary, the cross comparison analysis of cost functions showed good matching between best genome and target genome scores. ST-trained best genomes were the most successful at mimicking the spike timing behaviour of the target network, while IFR and AIV-trained genomes were best at mimicking the mean firing rate behaviour of the target network. However, the ST-trained genome showed the best ability to generalise in order to mimic network behaviour as characterised by all three cost function types. Experimentally, spike timing information is easier to record *in vivo* than intracellular voltage.

In contrast to the positive findings of the cross comparison of cost function scores, the relative parameter error was highly variable, ranging from very good (as little as 0%) to very poor (over 1000%), depending on the specific parameter. Most parameters

had a relative error of between 10% and 1000%, with the distribution being roughly uniform over this range on a logarithmic scale. This was true for best genomes obtained using all three cost functions. Overall therefore, while some parameters were well constrained, many had large relative errors and were poorly constrained.

These two pictures of GA performance can be reconciled by recognising that one BNN can mimic the behaviour of another by using a close match between only a fraction of the parameter values in the model. Many parameters may only affect network behaviour weakly and may thus have minor effects on cost function scores. Given the relatively good performance of the GA in terms of cost function scores, it appears that many of the parameters undergoing optimisation fall into this category.

Does the poor constraint of some parameters indicate a deficiency in the choice of cost functions? The strength with which parameters affect cost function scores may depend on the choice of cost function. It can also depend on the choice of stimulus. In our model, all three cost functions gave a similar magnitude of relative parameter error for any given parameter. The large relative errors observed for some parameters are therefore more likely to be due to either the choice of stimulus, or the fact that the network model behaviour is generally insensitive to these parameters within the ranges investigated.

5.4.2 Benefits of Reducing Noise

Noise enters the GA optimisation process by stochastic AN inputs, both in the data to be fitted and in the model simulations. We considered whether this noise reduces the ability of the GA to find a network model that fits the data well. Noise was reduced by increasing the functions, from 25 to 100 (for both target and candidate networks). As expected, this reduced noise, as demonstrated by the reduced scores for all numbers of repetitions used to obtain data for evaluating the three cost functions. However, this did not improve the ability of the best genome network to fit the data as demonstrated by the cross comparison of cost function scores. The best genomes trained with either 25 or 100 AN repetitions performed equally well when evaluated with the same cost function and the same number of repetitions.

Taken together, these findings indicate that noise was not a significant impediment

to obtaining good model fits to data in this study. Twenty five repetitions appeared to be sufficient to render unimportant the negative effects of noise. This eases the burden on both experimental data models. Caution is required, however, in applying these numbers of repetitions in absolute terms in other settings. For any data collection and computational simulation time, in constraining these type of given data sets with N repetitions, it may be helpful to apply the methodology used here to evaluate whether more repetitions would lead to improved model fits. This study provides strong evidence for applying the GA using two values of repetition numbers (e.g. N and $N \times 100$) and undertaking a cross-comparison of the kind performed here to judge whether any improvement in fit can be achieved by increasing the number of repetitions. If an improvement does occur, this indicates that there may be a benefit in increasing the number of repetitions beyond N .

5.4.3 Comparison with Other Studies

Using GAs or evolutionary methods to constrain parameters in artificial neural networks is not novel; however, the application of GAs on realistic microcircuits is increasingly gaining the interest of neuroscientists (Keren et al. 2005). The parameter search space for BNNs is infinitely large and non-differentiable and makes GAs a promising method. Substitution of the GA with another optimisation method could easily be performed. Gradient-descent methods are easily trapped in local minima and have difficulty with noisy models due to sensitivity to initial conditions. Other evolutionary or stochastic optimisation methods have been shown to be effective in large parameter spaces within a noisy fitness environment. Hybrid techniques may be advantageous, considering network structure and synaptic weights may not be well suited to the same optimisation method (Angeline et al. 1994; Sohn and Dagli 2004).

Using experimental data from populations of neurons adds more complexity to the problem of constraining BNNs. Optimising spiking neural networks to an exact solution relies on analytically differentiable neural models and synapses (Brette 2006; Brette and Guigón 2003), and other analytical methods have been reviewed (Brette 2007; Eggert and van Hemmen 2001). Alternative methods to infer connectivity and weights on a generic spiking model using extracellular spiking data have had some success

(Makarov et al. 2005), but the underlying properties of neuron types and the size of populations are restrictive. Small BNNs enable the manipulation of cell-based as well as network-based parameters (Taylor and Enoka 2004).

Reduction of parameters to cell types or connections between cell types, rather than individual cell or individual synapse, is a necessity with larger BNN models. A further dilemma of data reduction is in the cost function. Whether spike-timing information or intracellular voltages are the best way of reducing BNN output for optimisation has not yet been resolved. Spike-based methods are preferred (Victor 2005) and many post-hoc methods can be used in the fitness function (Schaffer et al. 2009; Victor et al. 2007). It is likely that a combination of spike timing, AIV or internal state information has advantages over individual methods (Keren et al. 2005, 2009; Rossant et al. 2010; Vanier and Bower 1999).

Intracellular voltage data has been used in constraining the membrane conductances of multi-compartmental single-neuron models (Keren et al. 2005; Le Masson 2000). These methods are not always effective in single simulations unless combined with other cost functions. Intracellular voltage data has been shown to be very effective in optimising membrane parameters (Keren et al. 2005; Van Geit et al. 2008) but would not be suitable for a BNN as inter-spike intervals (Keren et al. 2005). Phase-plane analysis due to variation in the synaptic input and the loss of temporal information. It is not currently possible to obtain simultaneous IV recordings from more than two neurons let alone a whole nucleus, but limited AIV data could be used in conjunction with other cost functions to constrain BNN models.

5.4.4 Other Considerations for Constraining BNNs

In this chapter, limiting the number of parameters used to define the connectivity of a BNN was critical to establish a practical method of optimisation. Simplifying the synaptic strength between two cell types to uniform weight and number significantly reduced the number of parameters required for optimisation, but uniformity is unlikely for the real network weights. A Gaussian weight distribution is common among network models and would only add one parameter per connection (i.e. standard deviation with the existing uniform mean parameter). Optimising conduction and synaptic

delay was not included in this chapter, but could add to further realism in BNN optimisation.

A further dilemma with increasing size of the model or experimental data is the information loss in data reduction. Data reduction is the decomposition of high dimensional data down to a single value within the cost function. Whether this reduction is performed before or after the difference or error comparison function between the reference and the test data set is an important issue. Data reduction preceding the comparison function generally includes a feature-based function across populations of neurons; for example, Taylor and Enoka (2004) calculated the synchronisation index of cell types. This method is fast and reduces noise, but the information carried by individual cells is lost. The cost functions in this chapter performed data reduction after the error comparisons at the individual neuron level.

A final issue that should be considered for modelling and optimising BNN models is computational efficiency. In this chapter, the CN stellate network consisted of 240 HH-like cells simulated in NEURON and took approximately 90 seconds to run a 80 msec stimulus on a 1.8 GHz CPU (32-bit Itanium, SGI Altix)². Evaluations of the AIV and IFR cost functions were a minor fraction of the total computational time, being less than 3 seconds per network. The ST cost function was at a considerable disadvantage because its evaluation took approximately 90 seconds. Further investigation is needed to improve the method for calculating the dynamic programming spike time distance. A small cluster of 9 PCs simulated a GA routine in approximately three days. On the 64-CPU SGI Altix, the amount of time required to run the GA for 201 generations of 100 genomes took approximately 8 hours (a maximum of 40 CPUs were used at any point). These computational loads are feasible in modern systems and will enhance the development of more realistic BNN models.

5.5 Conclusion

The development of methods for constraining new BNN models is an important step for generating microcircuits and larger networks. The study reported in this chapter

²Note that the ANF instantaneous rate for each frequency channel was already calculated and retrieved from file at the beginning of each simulation.

has shown that the GA is an adequate method for parameter optimisation and that the ST and AIV cost functions are comparably good methods for constraining BNNs. Further development is needed to enhance the robustness of the cost function methods to input noise, especially for sensitivity and robustness of inhibitory connections in the CN stellate microcircuit.

This page intentionally left blank.

Chapter 6

Discussion and Conclusion

6.1 Introduction

This thesis investigated neural modelling techniques in order to generate new insights into neural processing mechanisms in the stellate microcircuit of the cochlear nucleus (CN). It focused specifically on rate-place and temporal processing enhancement in the microcircuit regulating the output of T stellate (TS) cells. It achieved this through the development the cochlear nucleus stellate microcircuit (CNSM) model and deploying methods to set parameters, based on experimental data. Computer modelling enhances our knowledge of complex neural interactions in TS cells and provides further understanding of inputs to higher centres. By developing a biophysically-realistic neural network (BNN) with a high degree of realism at the individual cell level, this thesis has contributed to our understanding of the influence of synaptic organisation on physiological behaviour in the stellate microcircuit.

This thesis argued that the BNN models of the CN or models of individual cells in the CNSM model have not been sufficiently considerate of the most current physiological data. To address these deficiencies, the thesis designed, optimised and tested a new model of the stellate microcircuit. It demonstrated through rigorous sequential optimisation that the cell models and connectivity parameters in the CNSM model were created to replicate known cell type behaviour in response to simple stimuli. The temporal responses of the optimised CNSM model's neurons to amplitude modulation (AM) tones were also investigated.

Additionally, the thesis applied simultaneous optimisation methods to all network parameters in the CNSM model using genetic algorithms (GAs) and the sensitivity of

parameters given the noise in neural inputs. It developed cost functions to condense the neural outputs of the whole network into a single value. These cost functions investigated different analysis modalities including intracellular responses, spike times and time-varying average firing rate as separate alternatives for optimising BNN parameters.

This chapter concludes the thesis by drawing together the results of the design and optimisation of the CNSM model. It describes the usefulness of the model as well as the optimisation methods used throughout the thesis. It reflects on the implications of the research for the design and optimisation of BNNs. Finally, it describes the limitations of the research and makes recommendations for future work arising out of the thesis.

6.2 Overview of Research Findings

Chapter 1 identified a range of deficiencies in previous approaches to modelling and optimisation in the CN. In particular, previous modelling studies of TS cells and their microcircuit were limited by their outdated input auditory nerve (AN) models, errors in network connectivity and lack of documentation of parameter optimisation methods. Additionally, previous network-based approaches used insufficiently complex neural models that pre-dated the kinetic current models of Rothman and Manis (2003c). These deficiencies limit our insight into neural processing in the CN, and call for more refined model development and optimisation approaches.

Chapter 2 presented the general methods used to create and optimise the CNSM model. The methods were used to improve the design and development of the CNSM model as a NEURON package, cnstellate. This model integrated extensive studies of AN models, physiological experimentation data at the synapse and cell levels and, more broadly, evidence of connectivity across the nuclei into a more realistic model.

Chapter 3 developed output responses for each neuron in the CNSM model through a detailed, evidence-driven, sequential optimisation using simple stimuli. The Golgi (GLG) cell model was developed using a novel filter-based neural model, due to the limited intracellular and extracellular data. Its parameters were optimised to rate-level response data drawn from the leading study of granule cell domain (GCD)

units (Ghoshal and Kim 1996a). GLG cells are critical to controlling the activity of granule cells in the GCD, D stellate (DS) and TS cells with increasing sound intensity through tonic, GABAergic inhibition.

The DS cell model's intrinsic and extrinsic parameters were optimised using responses to tones, noise and click pairs. DS cells are known to be wide band, onset, glycinergic inhibitors of the stellate microcircuit. Their intracellular behaviour is characteristic of a coincidence detector and was modelled using the type I-II Rothman and Manis (RM) neural model (Rothman and Manis 2003c). The leak conductance of the model and parameters controlling synaptic connections were optimised to mimic the physiological responses of DS cells to tones and noise (Arnott et al. 2004). Further optimisation was required to modify the GABAergic subtype A (GABA_A) synapse on DS cells to best model the response recovery to click pairs (Backoff et al. 1997).

The Tuberculoventral (TV) cell model's synaptic inputs were optimised using rate level curves of tones and noise to fit the typical type II dorsal cochlear nucleus (DCN) unit behaviour (Spirou et al. 1999). A further optimisation of the offset parameter in DS cell to TV cell connectivity using notch noise did not confirm the asymmetry suggested by Reiss and Young (2005); however, the model demonstrated that LSR inputs contribute to asymmetry in the response of type II units to notch noise.

In Chapter 3, the network parameters of TS cells were fit into three chopper subtypes using spike-based and intracellular voltage responses to tones based on experimental data in rat TS neurons (Paolini et al. 2005). Inter-spike intervals used in the coefficient of variation (CV) comparison were accurately fit in each of the chopper subtypes. The regularity of spikes in the first 10 msec window was critical to ensuring consistency between the TS cell models (each with CV below 0.2) and reproducing important onset features of TS cells (Needham and Paolini 2006; Paolini et al. 2004, 2005). In this analysis, limitations in the comparison of the neural models with the experimental data affected the outcomes in the average intracellular voltage (AIV) measures. The post-stimulus hyperpolarisation offset was consistently greater in the TS neural models compared to the *in vivo* experimental data. Dependency on the resting membrane potential (RMP) in the model and experimental units was accounted for in the AIV measures, but it is likely that the differences between each chopper model and

test unit RMP influenced subthreshold dynamics in active currents, such as I_h and I_{KA} . Opportunities to improve the TS neural model were identified, particularly appending dendritic filtering components.

The study of AM tone responses in the CNSM model in Chapter 4 investigated the rate and temporal responses of cells in the stellate microcircuit. In the AN, temporal information is encoded through finely-timed spikes that phase-lock to the envelope of the stimulus. This poses problems for hearing in loud, noisy and reverberant environments, and also in neural transfer. The stellate microcircuit is the first step in transforming timing-based temporal information to a more stable rate-based code in the inferior colliculus (IC). The rate and temporal responses of each cell in the CNSM model were investigated after the presentation of AM tones of varying sound intensity and envelope modulation frequency.

The non-linear response of the AN model to increasing AM sound intensity showed the limiting effect of the auditory nerve fibres (ANFs) on characteristic frequency (CF), which is exacerbated by saturation at the inner hair cell (IHC)-AN synapse. Encoding of temporal information in modulation transfer functions (MTFs) of high spontaneous rate (HSR) ANFs was found to be strongest in the lateral frequency sidebands of the fibres' response area. Low spontaneous rate (LSR) ANFs had moderate to high temporal encoding of AM tones throughout their response area. In the absence of experimental evidence of GLG cells' response to AM tones, the novel GLG cell model within the CNSM model proposed that GLG cells diminish timing information contained in their ANF inputs. This approach derives from the hypothesis that GLG cells are purely rate-level encoders and contribute to automatic gain mechanisms in the microcircuit (Ferragamo et al. 1998a). The DS cell model's response to AM tones matched the extensive experimental evidence of DS cells (Frisina et al. 1990a; Joris et al. 2004; Rhode and Greenberg 1994a). Phase-locking in DS cells is greatly enhanced, relative to ANFs, due to their receipt of large numbers of ANF inputs and fast intrinsic membrane mechanisms. Experimental evidence of TV cells' response to AM tones is inconclusive. The integration of predominantly LSR inputs and strong inhibition from DS cells meant that the TV cell model's AM tone responses were equivalent to a half-wave rectification and low-pass filter transformation.

The temporal responses of the TS cell models to AM tones were indicative of the success of the CNSM model, given their favourable comparison with experimental data (Frisina 2001; Frisina et al. 1990a,b, 1993; Joris et al. 2004; Rhode and Greenberg 1994a). The TS cell models generally showed enhanced tMTF responses relative to ANFs. The MTF transformation seen in each of the TS cell models of low-pass to band-pass MTF responses is important for appropriate BMF selectivity in higher auditory centres (Joris et al. 2004). In the fundamental frequency (f_0) analysis, the transient chopper (ChT) models were more robust in their temporal output in response to high SPL AM tones than the sustained chopper (ChS) model. The lateral side-bands of the TS cell subtypes reflected the complex spectro-temporal processing in the CNSM model.

Chapter 5 reported on the use of GAs and three novel cost functions to simultaneously optimise BNN parameters. For this analysis, a simplified CNSM model was used as the exemplar BNN model and real experimental data was substituted for a known BNN target network. The results showed the limited benefits of stimulus repetitions for overcoming noise in the stimulus, synaptic inputs and smoothing of neural outputs. The spike timing cost function, using dynamic programming to compare multi-neuronal spike trains, performed better than the intracellular responses or time-varying rate cost functions.

6.3 Synthesis and Contributions

6.3.1 The CNSM Model Advances BNN Models of the Stellate Microcircuit

The CNSM model comprises a phenomenologically-realistic AN input model that allows arbitrary auditory stimuli to be used in simulations, especially temporally complex sounds such as AM tones and speech (Zilany and Bruce 2007; Zilany and Carney 2010; Zilany et al. 2009). The ANF model used in this thesis was modified to avoid the addition of fractional Gaussian noise in the AN synapse to ensure deterministic spontaneous rates in the HSR and LSR ANF models. The neural and synaptic models in the CNSM model are deterministic and the introduction of noise comes from the stimulus input and the spike generators of the ANF and GLG cell models.

This thesis contributes to the understanding of neural processing performed within

the stellate microcircuit of the CN. It utilises a framework of established input, neural and synapse models along with connectivity reflecting substantial experimental evidence, to create a BNN model of the microcircuit across the whole nuclei. Its methodology demonstrates the steps required to fit a large number of parameters to achieve necessary neural outputs in an ordered and sequential manner, using a variety of experimental data.

6.3.2 Optimisation Methods Must be Shared to Facilitate Model Reproducibility

As Chapter 1 showed, there is inconsistent documentation of optimisation methods in the literature on BNN models. The lack of such documentation creates important challenges for the development of research in the field. First, it inhibits comprehensive evaluation of the quality of the research. Second, it makes replication of existing research difficult.

Replication and reproducibility are critical to the development of computational models of the brain. The compact tables in Chapters 3 and 4 contain the information required for model replication, as suggested by Nordlie et al. (2009). Reproducibility of simulations is best supported by making the model software and analysis scripts publicly available and open-source. It is intended that the code developed in this thesis will ultimately be made available online. Through the use of these approaches, the thesis contributes to the reproducibility of the techniques used in modelling the CNSM.

6.4 Limitation of the Research

The specific limitations of the studies in this thesis were canvassed in the relevant chapters. The limitations of the CNSM model, described and developed in Chapter 3, relate to the specificity of the neural models' morphology and the exclusion of synaptic connections without solid empirical foundations. The most important limitation is the exclusion of some cells and synaptic connections that have known interactions with neurons in the microcircuit from the CNSM model. Key examples of these are the local DCN cells connecting with TV cells (Spirou et al. 1999; Young and Davis 2002), commis-

sural inhibition from DS neurons of the contralateral CN (Needham and Paolini 2003, 2006, 2007), GABAergic collaterals of the periolivary region (Backoff et al. 1999; Caspary et al. 1994; Evans and Zhao 1993b, 1998; Palombi and Caspary 1992), cholinergic medial olivocochlear (MOC) collaterals interacting with neurons in the ventral cochlear nucleus (VCN) (Mulders et al. 2003), and hypothetical recurrent connections between TS cells (Ferragamo et al. 1998b). The inclusion of these interactions was beyond the scope of this thesis, and could be addressed in further research in the field.

6.5 Recommendations for Future Work

Despite the contribution of the thesis, fundamental questions about the behaviour of TS cells remain in need of exploration (Oertel et al. 2011). Do intrinsic membrane mechanism or network and synaptic mechanisms play a greater role in the behaviour of TS cells? How are the different categories of ANFs (LSR and HSR) processed by the stellate microcircuit? What are the effects of synaptic connections and how do these impact upon the temporal and spectral representation across the population of TS cells? Can the optimised CNSM model reproduce responses to complex stimuli, particularly vowel encoding in sustained and transient chopper units? While answering these questions was beyond the scope of this thesis, the model and optimisation methods established by the thesis provide valuable tools for use in those inquiries.

Given the use of open-source software and reproducible reporting methods, the CNSM model and the optimisation methods can be used in future research. A promising next step in the use of the CNSM model would be to investigate the blocking of synaptic connections within the microcircuit with direct experimental examples using pharmacological blockers of GABA and glycine, especially to AM tones (Backoff et al. 1999; Caspary et al. 1994; Evans and Zhao 1993b, 1998; Palombi and Caspary 1992). Another would be to build on the investigation in Chapter 4 through further comparison with experimental data of the output responses in the current CNSM model to complex stimuli (such as harmonic complexes (Pressnitzer et al. 1999; Recio 2001), vowels (May 2003), vowels in noise (May and Sachs 1998; May et al. 1998), consonant-vowel tokens (Clarey et al. 2004), and simultaneous double vowels (Keilson et al. 1997)). The CNSM

model could be further exploited through the investigation and optimisation of new synaptic connections within the microcircuit, including TV to DS, TS to TV, and recurrent TS to TS cell connections, and their effects in the processing of simple tones and noise and AM tones. The inclusion of feedback connection would require a full network optimisation method, necessitating further development of the GA method used Chapter 5.

Additionally, enhanced understanding of the complex neural processing done by the CNSM model has the potential to contribute to the refinement of hearing-impairment devices. Further insight into the processing of sound in noisy environments within the network could aid in developing new sound processing strategies for the cochlear implant and hearing aids.

Simultaneous optimisation of BNN models also requires further exploration. In particular, attention is required to improve the final best parameter outcome using modification of GAs or hybrid algorithms. Multi-unit recording of populations of neurons opens new doors for understanding microcircuits, and introduces additional problems for modelling. There is a need to develop cost function methods that are capable of using a limited number of neural outputs, and to enhance their robustness to various sources of noise. The methods used in this thesis make a useful contribution to these avenues of inquiry.

6.6 Concluding Remarks

In computational neuroscience, the development of biophysically-realistic neural network models is a promising means by which we can understand highly complex neural processing. The accuracy of this understanding relies on the quality of design and optimisation methods, and experimental data used. This thesis presented a novel biophysically-realistic neural network model of the stellate microcircuit of the cochlear nucleus, which was optimised using detailed experimental evidence-based sequential methods. In addition it investigated whole-network simultaneous optimisation using genetic algorithms. The thesis demonstrates the utility of this approach for biophysically-realistic neural network models and enhancing our understanding of

neural processing in the cochlear nucleus.

This page intentionally left blank.

Appendix A

Appendix: Rothman and Manis neural model

A.1 Activation and Deactivation Current Equations

The activation and de-activation variable equations were reproduced from Rothman and Manis (2003c). The core of the Hodgkin-Huxley (HH)-like current equations are the activation and de-activation variables. The time- and voltage-dependent current variables follow a first-order differential equation in time:

$$\frac{dx}{dt} = (x_\infty - x) / \tau_x, \quad (\text{A.1})$$

where τ_x is the time constant of x and x_∞ is the steady-state value of x (i.e. the value of x when $t \gg \tau_x$).

The voltage dependence of the activation and de-activation variables $a, b, c, w, z, n, p, m, h$, and r are shown in the following equations.

Fast transient K⁺ current

$$I_{\text{KA}}(t, V) = \bar{g}_{\text{KA}} a^4 b c (V - E_{\text{K}}) \quad (\text{A.2})$$

$$a_\infty(V) = [1 + \exp(-(V + 31)/6)]^{-1/4} \quad (\text{A.3})$$

$$b_\infty(V) = [1 + \exp((V + 66)/7)]^{-1/2} \quad (\text{A.4})$$

$$c_\infty(V) = b_\infty \quad (\text{A.5})$$

$$\tau_a(V) = 100[7 \exp((V + 60)/14) + 29 \exp(-(V + 60)/24)]^{-1} + 0.1 \quad (\text{A.6})$$

$$\tau_b(V) = 1000[14 \exp((V + 60)/27) + 29 \exp(-(V + 60)/24)]^{-1} + 1 \quad (\text{A.7})$$

$$\tau_c(V) = 90[1 + \exp(-(V + 66)/17)]^{-1} + 10 \quad (\text{A.8})$$

Low-threshold K⁺ current

$$I_{\text{KLT}}(t, V) = \bar{g}_{\text{KLT}} w^4 z(V - E_{\text{K}}) \quad (\text{A.9})$$

$$w_{\infty}(V) = [1 + \exp(-(V + 48)/6)]^{-1/4} \quad (\text{A.10})$$

$$z_{\infty}(V) = 0.5[1 + \exp((V + 71)/10)]^{-1} + 0.5 \quad (\text{A.11})$$

$$\tau_w(V) = 100[6 \exp((V + 60)/6) + 16 \exp(-(V + 60)/45)]^{-1} + 1.5 \quad (\text{A.12})$$

$$\tau_z(V) = 1000[\exp((V + 60)/20) + \exp(-(V + 60)/8)]^{-1} + 50 \quad (\text{A.13})$$

High-threshold K⁺ current

$$I_{\text{KHT}}(t, V) = \bar{g}_{\text{KHT}}[\phi n^2 + (1 - \phi)p](V - E_{\text{K}}) \quad (\phi = 0.85) \quad (\text{A.14})$$

$$n_{\infty}(V) = [1 + \exp(-(V + 15)/5)]^{-1/2} \quad (\text{A.15})$$

$$p_{\infty}(V) = [1 + \exp(-(V + 23)/6)]^{-1} \quad (\text{A.16})$$

$$\tau_n(V) = 100[11 \exp((V + 60)/24) + 21 \exp(-(V + 60)/23)]^{-1} + 0.7 \quad (\text{A.17})$$

$$\tau_p(V) = 100[4 \exp((V + 60)/32) + 5 \exp(-(V + 60)/22)]^{-1} + 5 \quad (\text{A.18})$$

Fast Na⁺ current

$$I_{\text{Na}}(t, V) = \bar{g}_{\text{Na}} m^3 h(V - E_{\text{Na}}) \quad (\text{A.19})$$

$$m_{\infty}(V) = [1 + \exp(-(V + 38)/7)]^{-1} \quad (\text{A.20})$$

$$h_{\infty}(V) = [1 + \exp((V + 65)/6)]^{-1} \quad (\text{A.21})$$

$$\tau_m(V) = 10[5 \exp((V + 60)/18) + 36 \exp(-(V + 60)/25)]^{-1} + 0.04 \quad (\text{A.22})$$

$$\tau_h(V) = 100[7 \exp((V + 60)/11) + 10 \exp(-(V + 60)/25)]^{-1} + 0.6 \quad (\text{A.23})$$

Hyperpolarisation-activated, mixed-cation current

$$I_h(t, V) = \bar{g}_h r(V - E_h) \quad (\text{A.24})$$

$$r_\infty(V) = [1 + \exp((V + 76)/7)]^{-1} \quad (\text{A.25})$$

$$\tau_r(V) = 10^5 [237 \exp((V + 60)/12) + 17 \exp(-(V + 60)/14)]^{-1} + 25 \quad (\text{A.26})$$

Leak current

$$\bar{g}_{\text{leak}} = \bar{g}_{\text{leak}}(V - E_{\text{leak}}) \quad (\text{A.27})$$

This page intentionally left blank.

Bibliography

This page intentionally left blank.

Bibliography

- J. C. Adams. Cytology of periolivary cells and the organization of their projections in the cat. *J Comp Neurol*, 215(3):275–89, 1983.
- J. C. Adams. Projections from octopus cells of the posteroventral cochlear nucleus to the ventral nucleus of the lateral lemniscus. *Auditory Neurosci*, 3:335–50, 1997.
- L. Alibardi. Ultrastructural and immunocytochemical characterization of neurons in the rat ventral cochlear nucleus projecting to the inferior colliculus. *Ann Anat*, 180(5):415–26, 1998.
- L. Alibardi. Characterization of tuberculo-ventral neurons in the dorsal cochlear nucleus of the guinea pig. *J Submicr Cytol Pathol*, 31(2):295–300, 1999.
- L. Alibardi. Cytology, synaptology and immunocytochemistry of commissural neurons and their putative axonal terminals in the dorsal cochlear nucleus of the rat. *Ann Anat*, 182(3):207–20, 2000a.
- L. Alibardi. Identification of tuberculo-ventral neurons in the polymorphic layer of the rat dorsal cochlear nucleus. *Eur J Morphol*, 38(3):153–66, 2000b.
- L. Alibardi. Ultrastructural distribution of glycinergic and GABAergic neurons and axon terminals in the rat dorsal cochlear nucleus, with emphasis on granule cell areas. *J Anat*, 203(1):31–56, 2003a.
- L. Alibardi. Ultrastructural immunocytochemistry for glycine in neurons of the dorsal cochlear nucleus of the guinea pig. *J Submicr Cytol Pathol*, 35(4):373–87, 2003b.
- L. Alibardi. Review: Cytological characteristics of commissural and tuberculo-ventral

- neurons in the rat dorsal cochlear nucleus. *Hearing Research The Cochlear Nucleus - A tribute to Aage Møller*, 216–217:73–80, 2006.
- R. A. Altschuler, J. M. Juiz, S. E. Shore, S. C. Bledsoe, R. H. Helfert, and R. J. Wenthold. Inhibitory amino acid synapses and pathways in the ventral cochlear nucleus. In M. A. Merchan, J. M. Juiz, D. A. Godfrey, and E. Mugnaini, editors, *The Mammalian Cochlear Nuclei: Organisation and Function*, volume 239 of *NATO ASI Series. Series A, Life Sciences*, pages 411–20. Plenum Press, New York, 1993.
- S. Amari. Topographic organization of nerve fields. *Bull Math Biol*, 42:339–64, 1980.
- M. J. Anderson and E. D. Young. Isoflurane/n₂O anesthesia suppresses narrowband but not wideband inhibition in dorsal cochlear nucleus. *Hear Res*, 188(1-2):29–41, 2004.
- P. Angeline, G. M. Saunders, and J. P. Pollack. An evolutionary algorithm that constructs recurrent neural networks. *IEEE T. Neural. Netw.*, 5(1):54–65, 1994.
- J. E. Arle. *Neural modeling of the cochlear nucleus*. 9232990, The University of Connecticut, 1992.
- J. E. Arle and D. O. Kim. A modelling study of single neurons and neural circuits of the ventral and dorsal cochlear nucleus. In F. Eeckman, editor, *Analysis and Modelling Neural Systems*. Kluwer, Boston, 1990.
- J. E. Arle and D. O. Kim. Neural modeling of intrinsic and spike-discharge properties of cochlear nucleus neurons. *Biol Cybern*, 64(4):273–83, 1991a.
- J. E. Arle and D. O. Kim. Simulations of cochlear nucleus neural circuitry: Excitatory inhibitory response-area Type-I - Type-IV. *J Acoust Soc Am*, 90(6):3106–21, 1991b.
- A. R. Arnesen and K. K. Osen. The cochlear nerve in the cat: topography, cochleotomy, and fiber spectrum. *J Comp Neurol*, 178(4):661–78, 1978.
- R. H. Arnott, M. N. Wallace, T. M. Shackleton, and A. R. Palmer. Onset neurones in the anteroventral cochlear nucleus project to the dorsal cochlear nucleus. *J Assoc Res Otolaryngol*, 5(2):153–70, 2004. doi: 10.1007/s10162-003-4036-8.

- D. Aronov. Fast algorithm for the metric-space analysis of simultaneous responses of multiple single neurons. *J Neurosci Methods*, 124(2):175–79, 2003.
- G. B. Awatramani, Rostislav Turecek, and Laurence O. Trussell. Inhibitory control at a synaptic relay. *J Neurosci*, 24:2643–2647, 2004. doi: 10.1523/JNEUROSCI.5144-03.2004.
- G. B. Awatramani, R. Turecek, and L. O. Trussell. Staggered Development of GABAergic and Glycinergic Transmission in the MNTB. *J Neurophysiol*, 93(2):819–28, 2005.
- A. L. Babalian, A. V. Jacomme, J. R. Doucet, D. K. Ryugo, and E. M. Rouiller. Commisural glycinergic inhibition of bushy and stellate cells in the anteroventral cochlear nucleus. *Neuroreport*, 13(4):555–8, 2002.
- A. L. Babalian, D. K. Ryugo, and E. M. Rouiller. Discharge properties of identified cochlear nucleus neurons and auditory nerve fibers in response to repetitive electrical stimulation of the auditory nerve. *Exp Brain Res*, 153(4):452–60, 2003.
- P. M. Backoff, P. S. Palombi, and D. M. Caspary. Glycinergic and GABAergic inputs affect short-term suppression in the cochlear nucleus. *Hear Res*, 110(1-2):155–63, 1997.
- P. M. Backoff, P. Shadduck Palombi, and D. M. Caspary. Gamma-aminobutyric acidergic and glycinergic inputs shape coding of amplitude modulation in the chinchilla cochlear nucleus. *Hear Res*, 134(1-2):77–88, 1999.
- A. Bahmer and G. Langner. Oscillating neurons in the cochlear nucleus: I. Experimental basis of a simulation paradigm. *Biol Cybern*, 95(4):371–9, 2006a.
- A. Bahmer and G. Langner. Oscillating neurons in the cochlear nucleus: II. Simulation results. *Biol Cybern*, 95(4):381–92, 2006b.
- R. Bal, G. Baydas, and M. Naziroglu. Electrophysiological properties of ventral cochlear nucleus neurons of the dog. *Hear Res*, 256(0378-5955):93–103, 2009. doi: 10.1016/j.heares.2009.07.004.
- M. I. Banks and M. B. Sachs. Regularity analysis in a compartmental model of chopper units in the anteroventral cochlear nucleus. *J Neurophysiol*, 65(3):606–29, 1991.

- O. Belluzzi, O. Sacchi, and E. Wanke. A fast transient outward current in the rat sympathetic neurone studied under voltage-clamp conditions. *J Physiol*, 358:91–108, 1985.
- T. E. Benson and M. C. Brown. Postsynaptic targets of type II auditory nerve fibers in the cochlear nucleus. *J Assoc Res Otolaryngol*, 5(2):111–25, 2004.
- P. Berens. Circstat: A matlab toolbox for circular statistics. *Journal of Statistical Software*, 31(10), 2009.
- C. C. Blackburn and M. B. Sachs. Classification of unit types in the anteroventral cochlear nucleus: PST histograms and regularity analysis. *J Neurophysiol*, 62(6):1303–29, 1989.
- C. C. Blackburn and M. B. Sachs. The representations of the steady-state vowel sound /e/ in the discharge patterns of cat anteroventral cochlear nucleus neurons. *J Neurophysiol*, 63(5):1191–212, 1990.
- J. J. Blum and M. C. Reed. Effects of wide band inhibitors in the dorsal cochlear nucleus. II. Model calculations of the responses to complex sounds. *J Acoust Soc Am*, 103(4):2000–9, 1998.
- J. J. Blum and M. C. Reed. Model calculations of time dependent responses to binaural stimuli in the dorsal nucleus of the lateral lemniscus. *Hear Res*, 149(1-2):77–90, 2000.
- J. J. Blum, M. C. Reed, and J. M. Davies. A Computational Model for Signal-Processing by the Dorsal Cochlear Nucleus II. Responses to Broad-Band and Notch Noise. *J Acoust Soc Am*, 98(1):181–91, 1995.
- T. R. Bourk. *Electrical response of neural units in the anteroventral cochlear nucleus of the cat*. Doctoral dissertation, MIT, 1976.
- J. R. Brawer, D. K. Morest, and E. C. Kane. The neuronal architecture of the cochlear nucleus of the cat. *J Comp Neurol*, 155:251–300, 1974.
- A. S. Bregman. *Auditory Scene Analysis: The Perceptual Organization of Sound*. MIT Press, Cambridge, MA, 1990.

- R. Brent. A new algorithm for minimizing a function of several variables without calculating derivatives. In *Algorithms for Minimization without Derivatives*, pages 200–248. Prentice Hall, Englewood Cliffs, NJ, 1976.
- R. Brette. Exact simulation of integrate-and-fire models with synaptic conductances. *Neural Comput*, 18(8):2004–27, 2006.
- R. Brette. Exact simulation of integrate-and-fire models with exponential currents. *Neural Comput*, 19(10):2604–2609, 2007. ISSN 0899-7667.
- R. Brette and E. Guigón. Reliability of Spike Timing Is a General Property of Spiking Model Neurons. *Neural Comput*, 15(2):279–308, 2003.
- Romain Brette, Michelle Rudolph, Ted Carnevale, Michael Hines, David Beeman, James Bower, Markus Diesmann, Abigail Morrison, Philip Goodman, Frederick Harris, Milind Zirpe, Thomas Natschläger, Dejan Pecevski, Bard Ermentrout, Mikael Djurfeldt, Anders Lansner, Olivier Rochel, Thierry Vieville, Eilif Müller, Andrew Davison, Sami El Boustani, and Alain Destexhe. Simulation of networks of spiking neurons: A review of tools and strategies. *J Comput Neurosci*, 23:349–398, 2007. ISSN 0929-5313. doi: 10.1007/s10827-007-0038-6. 10.1007/s10827-007-0038-6.
- E. N. Brown, R. E. Kass, and P. P. Mitra. Multiple neural spike train data analysis: state-of-the-art and future challenges. *Nat. Neurosci.*, 7(5):456–61, 2004.
- M. C. Brown. Anatomical and physiological studies of type I and type II spiral ganglion neurons. In M. A. Merchan, J. M. Juiz, D. A. Godfrey, and E. Mugnaini, editors, *The Mammalian Cochlear Nuclei: Organisation and Function*, volume 239 of *NATO ASI Series. Series A, Life Sciences*, pages 43–54. Plenum Press, New York, 1993.
- I. C. Bruce, M. B. Sachs, and E. D. Young. An auditory-periphery model of the effects of acoustic trauma on auditory nerve responses. *J Acoust Soc Am*, 113(1):369–88, 2003.
- M. Burck and J. L. van Hemmen. Modeling the cochlear nucleus: A site for monaural echo suppression? *J Acoust Soc Am*, 122(4):2226–35, 2007.
- P. Bush and T. Sejnowski. Inhibition synchronizes sparsely connected cortical neurons

- within and between columns in realistic network models. *J Comput Neurosci*, 3(2):91–110, 1996.
- Y. Cai, J. McGee, and E. J. Walsh. Contributions of ion conductances to the onset responses of octopus cells in the ventral cochlear nucleus: simulation results. *J Neurophysiol*, 83(1):301–14, 2000.
- M. L. Campos, C. de Cabo, W. Wisden, J. M. Juiz, and D. Merlo. Expression of GABA(A) receptor subunits in rat brainstem auditory pathways: cochlear nuclei, superior olive complex and nucleus of the lateral lemniscus. *Neurosci*, 102(3):625–38, 2001.
- N. Cant and K. Gaston. Pathways connecting the right and left cochlear nuclei. *J Comp Neurol*, 212:313–26, 1982.
- N. B. Cant. The fine structure of two types of stellate cells in the anterior division of the anteroventral cochlear nucleus of the cat. *Neurosci*, 6(12):2643–55, 1981.
- N. B. Cant. Identification of cell types in the anteroventral cochlear nucleus that project to the inferior colliculus. *Neurosci Lett*, 32(3):241–46, 1982.
- N. B. Cant. The cochlear nucleus: neuronal types and their synaptic organization. In D. B. Webster, A. N. Popper, and R. R. Fay, editors, *The Mammalian Auditory Pathway: Neuroanatomy*, pages 66–116. Springer-Verlag, New York, 1992.
- N. B. Cant. The synaptic organization of the ventral cochlear nucleus of the cat: the peripheral cap of small cells. In M. A. Merchan, J. M. Juiz, D. A. Godfrey, and E. Mugnaini, editors, *The Mammalian Cochlear Nuclei: Organisation and Function*, volume 239 of *NATO ASI Series. Series A, Life Sciences*, pages 91–105. Plenum Press, New York, 1993.
- N. B. Cant and C. G. Benson. Parallel auditory pathways: projection patterns of the different neuronal populations in the dorsal and ventral cochlear nuclei. *Brain Res Bull*, 60(5-6):457–74, 2003.
- N. B. Cant and C. G. Benson. Organization of the inferior colliculus of the gerbil (*Meriones unguiculatus*): differences in distribution of projections from the cochlear nuclei and the superior olive complex. *J Comp Neurol*, 495(5):511–28, 2006.

- X. J. Cao and D. Oertel. Auditory nerve fibers excite targets through synapses that vary in convergence, strength, and short-term plasticity. *J Neurophysiol*, 104(5):2308–20, Nov 2010. doi: 10.1152/jn.00451.2010.
- P. A. Cariani and B. Delgutte. Neural correlates of the pitch of complex tones. I. Pitch and pitch salience. *J Neurophysiol*, 76(3):1698–716, 1996.
- Robert P Carlyon and Shihab Shamma. An account of monaural phase sensitivity. *J Acoust Soc Am*, 114(1):333–348, Jul 2003.
- N. T. Carnevale and M. L. Hines. *The NEURON Book*. Cambridge University Press, Cambridge, UK, 2006.
- L. H. Carney. A model for the responses of low-frequency auditory-nerve fibers in cat. *J Acoust Soc Am*, 93(1):401–17, 1993.
- L. H. Carney and T. C. Yin. Temporal coding of resonances by low-frequency auditory nerve fibers: single-fiber responses and a population model. *J Neurophysiol*, 60(5):1653–1677, 1988.
- D. M. Caspary and P. S. Palombi. GABA inputs control discharge rate within the excitatory response area of chinchilla inferior colliculus neurons. *Assoc Res Otolaryngol Abstr*, 109, 1993.
- D. M. Caspary, D. C. Havey, and C. L. Faingold. Effects of microiontophoretically applied glycine and GABA on neuronal response patterns in the cochlear nuclei. *Brain Res*, 172(1):179–85, 1979.
- D. M. Caspary, P. S. Palombi, P. M. Backoff, R. H. Helfert, and P. G. Finlayson. GABA and glycine inputs control discharge rate within the excitatory response area of primary-like and phase-locked AVCN neurons. In M. A. Merchan, J. M. Juiz, D. A. Godfrey, and E. Mugnaini, editors, *The Mammalian Cochlear Nuclei: Organisation and Function*, volume 239 of *NATO ASI Series. Series A, Life Sciences*, pages 239–52. Plenum Press, New York, 1993.
- D. M. Caspary, P. M. Backoff, P. G. Finlayson, and P. S. Palombi. Inhibitory inputs

- modulate discharge rate within frequency receptive fields of anteroventral cochlear nucleus neurons. *J Neurophysiol*, 72(5):2124–33, 1994.
- D. M. Caspary, R. H. Helfert, and P. S. Palombi. The role of GABA in shaping frequency response properties in the chinchilla inferior colliculus. In J. Syka, editor, *Acoustic Signal Processing in the Central Auditory System*, pages 227–38. Plenum press, New york, 1997.
- D. M. Caspary, P. S. Palombi, and L. F. Hughes. GABAergic inputs shape responses to amplitude modulated stimuli in the inferior colliculus. *Hear Res*, 168(1-2):163–73, 2002.
- E. J. Chichilnisky. A simple white noise analysis of neuronal light responses. *Network-Comput Neural*, 12(2):199–213, 2001.
- J. C. Clarey, A. G. Paolini, D. B. Grayden, A. N. Burkitt, and G. M. Clark. Ventral cochlear nucleus coding of voice onset time in naturally spoken syllables. *Hear Res*, 190(1-2):37–59, 2004.
- B. M. Clopton, J. A. Winfield, and F. J. Flammino. Tonotopic organization: review and analysis. *Brain Res*, 76(1):1–20, 1974.
- P. F. Costa. The kinetic parameters of sodium currents in maturing acutely isolated rat hippocampal ca1 neurons. *Brain Res Dev Brain Res*, 91:29–40, 1996.
- R. Dahlhaus, M. Eichler, and J. Sandkuhler. Identification of synaptic connections in neural ensembles by graphical models. *J Neurosci Meth*, 77(1):93–107, 1997.
- W. R. D’Angelo, S. J. Sterbing, E.-M. Ostapoff, and S. Kuwada. Effects of Amplitude Modulation on the Coding of Interaural Time Differences of Low-Frequency Sounds in the Inferior Colliculus. II. Neural Mechanisms. *J Neurophysiol*, 90(5):2827–36, 2003.
- K. A. Davis and H. F. Voigt. Neural modeling of the DCN: cross-correlation analysis using short-duration tone-burst stimuli. In *Bioengineering Conference, 1991 , Proceedings the 1991 IEEE Seventeenth Annual Northeast*, pages 211–12, 1991.

- K. A. Davis and H. F. Voigt. Neural modeling of the dorsal cochlear nucleus: cross-correlation analysis of short-duration tone-burst responses. *Biol Cybern*, 71(6):511–21, 1994.
- K. A. Davis and H. F. Voigt. Computer simulation of shared input among projection neurons in the dorsal cochlear nucleus. *Biol Cybern*, 74(5):413–25, 1996.
- K. A. Davis and H. F. Voigt. Evidence of stimulus-dependent correlated activity in the dorsal cochlear nucleus of decerebrate gerbils. *J Neurophysiol*, 78(1):229–47, 1997.
- K. A. Davis and E. D. Young. Pharmacological evidence of inhibitory and disinhibitory neuronal circuits in dorsal cochlear nucleus. *J Neurophysiol*, 83(2):926–40, 2000.
- S. Dehmel, C. Kopp-Scheinpflug, G. J. Dorrscheidt, and R. Rubsam. Electrophysiological characterization of the superior paraolivary nucleus in the Mongolian gerbil. *Hear Res*, 172(1-2):18–36, 2002.
- B. Delgutte and N. Y. S. Kiang. Speech coding in the Auditory Nerve: I. Vowel-like sounds. *J Acoust Soc Am*, 75:866–78, 1984a.
- B. Delgutte and N. Y. S. Kiang. Speech coding in the Auditory Nerve: II. Processing schemes for vowel-like sounds. *J Acoust Soc Am*, 75:879–86, 1984b.
- B. Delgutte and N. Y. S. Kiang. Speech coding in the Auditory Nerve: III. Voiceless fricative consonants. *J Acoust Soc Am*, 75:887–96, 1984c.
- B. Delgutte and N. Y. S. Kiang. Speech coding in the Auditory Nerve: IV. Sounds with Consonant-like Dynamic Characteristics. *J Acoust Soc Am*, 75:897–907, 1984d.
- E. V. Denardo. *Dynamic Programming*. Prentice-Hall, Englewood Cliffs, NJ, 1982.
- D. A. Depireux and S. A. Shamma. Neuronal correlates of pitch in the inferior colliculus. *J Acoust Soc Am*, 100(4):2787, 1996.
- J. Ding and H. F. Voigt. Intracellular response properties of units in the dorsal cochlear nucleus of unanesthetized decerebrate gerbil. *J Neurophysiol*, 77(5):2549–72, 1997.
- J. R. Doucet and D. K. Ryugo. Projections from the ventral cochlear nucleus to the dorsal cochlear nucleus in rats. *J Comp Neurol*, 385(2):245–64, 1997.

- J. R. Doucet and D. K. Ryugo. Structural and functional classes of multipolar cells in the ventral cochlear nucleus. *Anat Rec Part A*, 288(4):331–44, 2006.
- J. R. Doucet, A. T. Ross, M. B. Gillespie, and D. K. Ryugo. Glycine immunoreactivity of multipolar neurons in the ventral cochlear nucleus which project to the dorsal cochlear nucleus. *J Comp Neurol*, 408(4):515–31, 1999.
- Antonio Eblen-Zajjur, Rafael Salas, and Horacio Vanegas. Fractal analysis of spinal nociceptive neuronal responses to receptive field stimulation and to heterotopic noxious stimulation in the rat. *Neuroscience Research Communications*, 25(1):51–60, 1999. ISSN 1520-6769. doi: 10.1002/(SICI)1520-6769(199907/08)25:1<51::AID-NRC6>3.0.CO;2-J.
- J. Eggert and J. L. van Hemmen. Modeling neuronal assemblies: theory and implementation. *Neural Comput*, 13(9):1923–74, 2001.
- M. Eichler, R. Dahlhaus, and J. Sandkuhler. Partial correlation analysis for the identification of synaptic connections. *Biol Cybern*, 89(4):289–302, 2003.
- J. L. Eriksson and A. Robert. The representation of pure tones and noise in a model of cochlear nucleus neurons. *J Acoust Soc Am*, 106(4 Pt 1):1865–79, 1999.
- E. F. Evans. Auditory Processing of Complex Sounds: An Overview. *Philos T Roy Soc B*, 336(1278):295–306, 1992.
- E. F. Evans and P. G. Nelson. The response of single neurons in the cochlear nucleus of the cat as a function of their location and anaesthetic state. *Exp Brain Res*, 17:402–27, 1973.
- E. F. Evans and W. Zhao. Neuropharmacological and neurophysiological dissection of inhibition in the mammalian dorsal cochlear nucleus. In M. A. Merchan, J. M. Juiz, D. A. Godfrey, and E. Mugnaini, editors, *The Mammalian Cochlear Nuclei: Organisation and Function*, volume 239 of *NATO ASI Series. Series A, Life Sciences*, pages 253–66. Plenum Press, New York, 1993a.
- E. F. Evans and W. Zhao. Varieties of inhibition in the processing and control of processing in the mammalian cochlear nucleus. *Prog Brain Res*, 97:117–26, 1993b.

- E. F. Evans and W. Zhao. Periodicity Coding of the fundamental frequency of harmonic complexes: Physiological and Pharmacological Study of Onset units in the ventral cochlear nucleus. In A. R. Palmer, A. Rees, A. Q. Summerfield, and R. Meddis, editors, *Psychophysical and Physiological Advances in Hearing*, pages 186–92. Whurr Publ., London, 1998.
- R. R. Fay and A. N. Popper, editors. *Comparative hearing: Mammals*, volume 4 of *Springer Handbook Auditory Res.* Springer, New York, 1994.
- D. M. Fekete. *The Central Projections Of Auditory Nerve Fibers In Cats (Hearing, Neuron)*. 8419336, Harvard University, 1984.
- M. L. Feldman. *The Projection Of The Cochlear Nerve Onto The Ventrail Cochlear Nucleus Of the Rat: A Golgi Study*. 6918792, Boston University Graduate School, 1969.
- J. J. Feng, S. Kuwada, E. M. Ostapoff, R. Batra, and D. K. Morest. A physiological and structural study of neuron types in the cochlear nucleus. I. Intracellular responses to acoustic stimulation and Current injection. *J Comp Neurol*, 346(1):1–18, 1994. ISSN 1096-9861. doi: 10.1002/cne.903460102.
- M. J. Ferragamo, N. L. Golding, S. M. Gardner, and D. Oertel. Golgi cells in the superficial granule cell domain overlying the ventral cochlear nucleus: morphology and electrophysiology in slices. *J Comp Neurol*, 400(4):519–28, 1998a.
- M. J. Ferragamo, N. L. Golding, and D. Oertel. Synaptic inputs to stellate cells in the ventral cochlear nucleus. *J Neurophysiol*, 79(1):51–63, 1998b.
- N. I. Fisher. *Statistical analysis of circular data*. Cambridge University Press, 1996.
- D. C. Fitzpatrick, S. Kuwada, D. O. Kim, K. Parham, and R. Batra. Responses of neurons to click-pairs as simulated echoes: Auditory nerve to auditory cortex. *J Acoust Soc Am*, 106(6):3460–72, 1999.
- D. R. Friedland, T. Pongstaporn, J. R. Doucet, and D. K. Ryugo. Ultrastructural examination of the somatic innervation of ventrotubercular cells in the rat. *J Comp Neurol*, 459(1):77–89, 2003.

- D. R. Frisina. *Enhancement of Responses to Amplitude Modulation in the Gerbil Cochlear Nucleus: Single-Unit Recordings Using an Improved Surgical Approach.* 8410710, Syracuse University, 1983.
- R. D. Frisina. Enhancement of responses to amplitude modulation in the gerbil cochlear nucleus: Single-unit recordings using an improved surgical approach. *J Acoust Soc Am*, 76(6):1865, 1984.
- R. D. Frisina. Subcortical neural coding mechanisms for auditory temporal processing. *Hear Res*, 158(1-2):1–27, 2001.
- R. D. Frisina, R. L. Smith, and S. C. Chamberlain. Differential encoding of rapid changes in sound amplitude by second-order auditory neurons. *Exp Brain Res*, 60(2):417–22, 1985.
- R. D. Frisina, R. L. Smith, and S. C. Chamberlain. Encoding of amplitude modulation in the gerbil cochlear nucleus: I. a hierarchy of enhancement. *Hear Res*, 44(2-3):99–122, Mar 1990a.
- R. D. Frisina, R. L. Smith, and S. C. Chamberlain. Encoding of amplitude modulation in the gerbil cochlear nucleus: II. possible neural mechanisms. *Hear Res*, 44(2-3):123–41, Mar 1990b.
- R. D. Frisina, J. P. Walton, and K. J. Karcich. Cochlear nucleus neural mechanisms preserve complex- sound feature encoding in the presence of background noise. *J Acoust Soc Am*, 93(4):2410, 1993.
- R. D. Frisina, J. P. Walton, and K. J. Karcich. Dorsal cochlear nucleus single neurons can enhance temporal processing capabilities in background noise. *Exp Brain Res*, 102(1):160–4, 1994.
- R. D. Frisina, K. J. Karcich, T. C. Tracy, D. M. Sullivan, J. P. Walton, and J Colombo. Preservation of amplitude modulation coding in the presence of background noise by chinchilla auditory-nerve fibers. *J Acoust Soc Am*, 99(1):475–90, Jan 1996.
- K. Fujino and D. Oertel. Cholinergic modulation of stellate cells in the mammalian ventral cochlear nucleus. *J Neurosci*, 21(18):7372–83, 2001.

- S. M. Gardner. *AMPA receptors and their targeting in the cochlear nuclei.* 9996893, The University of Wisconsin - Madison, 2000.
- S. M. Gardner, L. O. Trussell, and D. Oertel. Time course and permeation of synaptic AMPA receptors in cochlear nuclear neurons correlate with input. *J Neurosci*, 19(20): 8721–9, 1999.
- A. Geist, A. Beguelin, J. Dongarra, W. Jiang, R. Manchek, and V. Sunderam. *PVM: Parallel Virtual Machine A Users' Guide and Tutorial for Networked Parallel Computing.* MIT Press, 1994.
- S. Ghoshal. *Single-unit physiology of the cat anteroventral cochlear nucleus: A comparison of the marginal shell and the central core.* 9821906, The University of Connecticut, 1997.
- S. Ghoshal and D. O. Kim. Marginal shell of the anteroventral cochlear nucleus: acoustically weakly-driven and not-driven units in the unanesthetized decerebrate cat. *Acta Otolaryngol*, 116(2):280–3, 1996a.
- S. Ghoshal and D. O. Kim. Marginal shell of the anteroventral cochlear nucleus: intensity coding in single units of the unanesthetized, decerebrate cat. *Neurosci Lett*, 205: 71–74, 1996b.
- S. Ghoshal and D. O. Kim. Marginal shell of the anteroventral cochlear nucleus: single-unit response properties in the unanesthetized decerebrate cat. *J Neurophysiol*, 77(4): 2083–97, 1997.
- S. Ghoshal, D. O. Kim, and R. B. Northrop. Amplitude-modulated tone encoding behavior of cochlear nucleus neurons: Modeling study. *Hear Res*, 58(2):153–65, 1992.
- D. E. Goldberg. *Genetic Algorithms in Search, Optimisation and Machine Learning.* Addison Wesley, 1989.
- J. M. Goldberg and P. B. Brown. Response of binaural neurons of dog superior olfactory complex to dichotic tonal stimuli: some physiological mechanisms of sound localization. *J Neurophysiol*, 22:613–636, 1969.

- N. L. Golding, M. J. Ferragamo, and D. Oertel. Role of intrinsic conductances underlying responses to transients in octopus cells of the cochlear nucleus. *J Neurosci*, 19(8):2897–905, 1999.
- D. Greenwood. A cochlear frequency-position function for several species - 29 years later. *J Acoust Soc Am*, 87(6):2592–605, 1990.
- S. Grillner, H. Markram, E. De Schutter, G. Silberberg, and F. E. N. Le Beau. Microcircuits in action - from CPGs to neocortex. *Trends Neurosci*, 28(10):525–33, 2005.
- A. Grinvald and R. Hildesheim. VSDI: A New Era In Functional Imaging Of Cortical Dynamics. *Nat. Rev. Neurosci.*, 5(11):874–85, 2004.
- K. E. Hancock, K. A. Davis, and H. F. Voigt. Modeling inhibition of type II units in the dorsal cochlear nucleus. *Biol Cybern*, 76(6):419–28, 1997.
- K. E. Hancock, K. A. Davis, and H. F. Voigt. Computer simulations of dorsal cochlear nucleus neural circuitry. In *Engineering in Medicine and Biology Society, 2001 Proceedings the 23rd Annual Int Conference the IEEE*, volume 1, pages 666–69 vol1, 2001.
- T. P. Harty and P. B. Manis. Glycine-evoked currents in acutely dissociated neurons of the guinea pig ventral cochlear nucleus. *J Neurophysiol*, 75(6):2300–11, 1996.
- T. P. Harty and P. B. Manis. Kinetic analysis of glycine receptor currents in ventral cochlear nucleus. *J Neurophysiol*, 79(4):1891–901, 1998.
- R. S. Heffner, G. Koay, and H. E. Heffner. Audiograms of five species of rodents: implications for the evolution of hearing and the perception of pitch. *Hear Res*, 157 (1-2):138–52, 2001.
- Peter Heil, Heinrich Neubauer, Dexter R. F. Irvine, and Mel Brown. Spontaneous activity of auditory-nerve fibers: Insights into stochastic processes at ribbon synapses. *The Journal of Neuroscience*, 27(31):8457–8474, 2007. doi: 10.1523/JNEUROSCI.1512-07.2007.
- M. G. Heinz, X. Zhang, I. C. Bruce, and L. H. Carney. Auditory nerve model for predicting performance limits of normal and impaired listeners. *Acoustics Res Letters Online*, 2(3):91–96, 2001.

- R. H. Helfert, J. M. Bonneau, R. J. Wenthold, and R. A. Altschuler. GABA and glycine immunoreactivity in the guinea pig superior olivary complex. *Brain Res*, 501(2):269–86, 1989.
- M. J. Hewitt, R. Meddis, and T. M. Shackleton. A computer model of a cochlear-nucleus stellate cell: responses to amplitude-modulated and pure-tone stimuli. *J Acoust Soc Am*, 91(4 Pt 1):2096–109, 1992.
- M. L. Hines and N. T. Carnevale. Expanding NEURON's repertoire of mechanisms with NMODL. *Neural Comput*, 12:995–1007, 2000.
- M. L. Hines, T. Morse, M. Migliore, N. T. Carnevale, and G. M. Shepherd. ModelDb: A Database to Support Computational Neuroscience. *J Comput Neurosci*, 17(1):7–11, 2004.
- A. L. Hodgkin and A. F. Huxley. Propagation of electrical signals along giant nerve fibers. *Proc R Soc Lond B Biol Sci*, 140(899):177–83, 1952a.
- A. L. Hodgkin and A. F. Huxley. A quantitative description of membrane Current and its application to conduction and excitation in nerve. *J Physiol*, 117(4):500–44, 1952b.
- J. Holland. *Adaptation in natural and artificial systems*. University of Michigan Press, Ann Arbor, MI, 1975.
- L. B. Hurd, K. A. Hutson, and D. K. Morest. Cochlear nerve projections to the small cell shell of the cochlear nucleus: the neuroanatomy of extremely thin sensory axons. *Synapse*, 33(2):83–117, 1999.
- J. S. Isaacson and B. Walmsley. Counting quanta: direct measurements of transmitter release at a central synapse. *Neuron*, 15(4):875–84, 1995.
- B. S. Jackson. *Consequences Of Long-Range Temporal Dependence In Neural Spiking Activity For Theories Of Processing And Coding*. Phd, Syracuse University, 2003.
- B. S. Jackson. Including Long-Range Dependence in Integrate-and-Fire Models of the High Interspike-Interval Variability of Cortical Neurons. *Neural Comput*, 16(10):2125–95, 2004.

- B. S. Jackson and L. H. Carney. The spontaneous-rate histogram of the auditory nerve can be explained by only two or three spontaneous rates and long-range dependence. *J Assoc Res Otolaryngol*, 6(2):148–59, 2005.
- S. R. Jammalamadaka. *Topics in circular statistics*. World Scientific, 2001.
- D. Jiang, A. R. Palmer, and I. M. Winter. Frequency extent of two-tone facilitation in onset units in the ventral cochlear nucleus. *J Neurophysiol*, 75(1):380–95, 1996.
- P. X. Joris. Response classes in the dorsal cochlear nucleus and its output tract in the chloralose-anesthetized cat. *J Neurosci*, 18(10):3955–66, 1998.
- P. X. Joris and P. H. Smith. Temporal and binaural properties in dorsal cochlear nucleus and its output tract. *J Neurosci*, 18(23):10157–70, 1998.
- P. X. Joris and P. H. Smith. The volley theory and the spherical cell puzzle. *J Neurosci*, 154:65–76, 2008. doi: 10.1016/j.neuroscience.2008.03.002.
- P. X. Joris and T. C. T. Yin. Response to amplitude-modulated tones in the auditory nerve of the cat. *J Acoust Soc Am*, 91(1):215–32, 1992.
- P. X. Joris, C. E. Schreiner, and A. Rees. Neural Processing of Amplitude-Modulated Sounds. *Physiol Rev*, 84(2):541–77, 2004.
- E. M. Josephson and D. Morest. A quantitative profile of the synapses on the stellate cell body and axon in the cochlear nucleus of the chinchilla. *J Neurocytol*, 27(11):841–64, 1998.
- J. M. Juiz, R. H. Helfert, J. M. Bonneau, R. J. Wenthold, and R. A. Altschuler. Three classes of inhibitory amino acid terminals in the cochlear nucleus of the guinea pig. *J Comp Neurol*, 373(1):11–26, 1996.
- A. Kadner, R. J. Kulesza, and A. S. Berrebi. Neurons in the medial nucleus of the trapezoid body and superior paraolivary nucleus of the rat may play a role in sound duration coding. *J Neurophysiol*, 95(3):1499–508, 2006.
- Y. Kajikawa and T. A. Hackett. Entropy analysis of neuronal spike train synchrony. *J Neurosci Methods*, 149(1):90–93, 2005.

- S. Kalluri and B. Delgutte. Mathematical models of cochlear nucleus onset neurons: I. Point neuron with many weak synaptic inputs. *J Comput Neurosci*, 14(1):71–90, 2003.
- M. Kaminski, M. Ding, W. A. Truccolo, and B. S. L. Evaluating causal relations in neural systems: Granger causality, directed transfer function and statistical assessment of significance. *Biol Cybern*, 85(2):145–57, 2001.
- P. O. Kanold and P. B. Manis. A physiologically based model of discharge pattern regulation by transient K⁺ currents in cochlear nucleus pyramidal cells. *J Neurophysiol*, 85(2):523–38, 2001.
- P. O. Kanold and P. B. Manis. Encoding the timing of inhibitory inputs. *J Neurophysiol*, 93(5):2887–97, 2005.
- S. E. Keilson, V. M. Richards, B. T. Wyman, and E. D. Young. The representation of concurrent vowels in the cat anesthetized ventral cochlear nucleus: evidence for a periodicity-tagged spectral representation. *J Acoust Soc Am*, 102(2 Pt 1):1056–71, 1997.
- N. Keren, N. Peled, and A. Korngreen. Constraining compartmental models using multiple voltage recordings and genetic algorithms. *J Neurophysiol*, 94(6):3730–42, Dec 2005. doi: 10.1152/jn.00408.2005.
- N. Keren, D. Bar-Yehuda, and A. Korngreen. Experimentally guided modelling of dendritic excitability in rat neocortical pyramidal neurones. *J Physiol*, 587(Pt 7):1413–37, Apr 2009. doi: 10.1113/jphysiol.2008.167130.
- D. O. Kim, W. S. Rhode, and S. Greenberg. Responses of cochlear nucleus neurons to speech signals: Neural encoding of pitch, intensity and other parameters. In B. C. J. Moore and R. D. Patterson, editors, *Auditory Frequency Selectivity*, pages 281–88. Plenum Press, New York, 1986.
- D. O. Kim, J. G. Sirianni, and S. O. Chang. Responses of DCN-PVCN neurons and auditory nerve fibers in unanesthetized decerebrate cats to AM and pure tones: Analysis with autocorrelation/power-spectrum. *Hear Res*, 45(1-2):95–113, 1990.
- C. Koch and I. Segev. *Methods in Neuronal Modeling : from Ions to Networks*. MIT Press, Cambridge, Mass, 2nd edition, 1998.

- T. Kohonen. *Self-organizing maps*. Springer, Berlin, 2001.
- T. Kohonen. Self-organizing neural projections. *Neural Networks*, 19(6-7):723–33, 2006.
- J. Kolston, K. K. Osen, C. M. Hackney, O. P. Ottersen, and J. Storm-Mathisen. An atlas of glycine- and GABA-like immunoreactivity and colocalization in the cochlear nuclear complex of the guinea pig. *Anat Embryol*, 186(5):443–65, 1992.
- A. Korzeniewska, M. Manczak, M. Kaminski, K. J. Blinowska, and S. Kasicki. Determination of information flow direction among brain structures by a modified directed transfer function (dDTF) method. *J Neurosci Methods*, 125(1-2):195–207, 2003.
- L. Kostal, P. Lansky, and J.-P. Rospars. Neuronal coding and spiking randomness. *Eur J Neurosci*, 26(10):2693–701, 2007.
- J. R. Koza and J. P. Rice. Genetic programming of both the weights and architecture a neural network. In *Int Joint Conference on Neural networks, IJCNN-91*, pages 8–12, Seattle, WA, 1991. IEEE Computer Society.
- B. S. Krishna and M. N. Semple. Auditory Temporal Processing: Responses to Sinusoidally Amplitude-Modulated Tones in the Inferior Colliculus. *J Neurophysiol*, 84(1):255–73, 2000.
- R. J. Jr. Kulesza, A. Kadner, and A. S. Berrebi. Distinct Roles for Glycine and GABA in Shaping the Response Properties of Neurons in the Superior Paraolivary Nucleus of the Rat. *J Neurophysiol*, 97(2):1610–20, 2007.
- E. A. Lachica, R. Rubsam, L. Zirpel, and E. W. Rubel. Glutamatergic inhibition of voltage-operated calcium channels in the avian cochlear nucleus. *J Neurosci*, 15(3 Pt 1):1724–34, 1995.
- Y. C. Lai, R. L. Winslow, and M. B. Sachs. The Functional-Role of Excitatory and Inhibitory Interactions in Chopper Cells of the Anteroventral Cochlear Nucleus. *Neural Comput*, 6(6):1127–1140, 1994a. ISSN 0899-7667. doi: 10.1162/neco.1994.6.6.1127.
- Y. C. Lai, R. L. Winslow, and M. B. Sachs. A model of selective processing of auditory-nerve inputs by stellate cells of the antero-ventral cochlear nucleus. *J Comput Neurosci*, 1(3):167–94, 1994b.

- G. Langner, M. Albert, and T. Briede. Temporal and spatial coding of periodicity information in the inferior colliculus of awake chinchilla (*Chinchilla laniger*). *Hear Res*, 168(1-2):110–30, 2002.
- G Le Masson. [neuronal and synaptic properties: fundamentals of network plasticity]. *Rev Neurol (Paris)*, 156(2):127–36, Feb 2000.
- P. A. Leake, R. L. Snyder, and G. Hradek. Topographic organisation of inner hair cell synapses and cochlear spiral ganglion projections to the ventral cochlear nucleus. In M. A. Merchan, J. M. Juiz, D. A. Godfrey, and E. Mugnaini, editors, *The Mammalian Cochlear Nuclei: Organisation and Function*, volume 239 of *NATO ASI Series. Series A, Life Sciences*, pages 55–64. Plenum Press, New York, 1993.
- R. N. Leao, S. Oleskevich, H. Sun, M. Bautista, R. E. W. Fyffe, and B. Walmsley. Differences in Glycinergic mIPSCs in the Auditory Brain Stem of Normal and Congenitally Deaf Neonatal Mice. *J Neurophysiol*, 91(2):1006–12, 2004.
- M. C. Liberman. Auditory Nerve response of cats raised in low-noise chamber. *J Acoust Soc Am*, 63:442–55, 1978.
- M. C. Liberman. The cochlear frequency map for the cat: labelling auditory nerve fibres of known characteristic frequency. *J Acoust Soc Am*, 72:1441–49, 1982.
- M. C. Liberman. Central Projection of Auditory Nerve Fibres of Differing Spontaneous Rate, I: Anteroventral Cochlear Nucleus. *J Comp Neurol*, 313:240–58, 1991.
- M. C. Liberman. Central projections of auditory nerve fibers of differing spontaneous rate, ii: Posteroventral and dorsal cochlear nuclei. *J Comp Neurol*, 327(1):17–36, 1993. ISSN 0021-9967.
- R. Lim, F. J. Alvarez, and B. Walmsley. GABA mediates presynaptic inhibition at glycinergic synapses in a rat auditory brainstem nucleus. *J Physiol*, 525 Pt 2:447–59, 2000.
- R. Lim, S. Oleskevich, A. P. Few, R. N. Leao, and B. Walmsley. Glycinergic mIPSCs in mouse and rat brainstem auditory nuclei: modulation by ruthenium red and the role of calcium stores. *J Physiol*, 546(Pt 3):691–9, 2003.

- Oleg Lomakin and Kevin A. Davis. On the role of the wideband inhibitor in the dorsal cochlear nucleus: A computational modulating study. *J Assoc Res Otolaryngol*, 9:506–20, 2008. doi: 10.1007/s10162-008-0133-z.
- E. A. Lopez-Poveda. Spectral processing by the peripheral auditory system: Facts and models. In M. S. Malmierca, D. R. F. Irvine, R. A. Harris, and P. Jenner, editors, *Auditory Spectral Processing*, volume 70 of *International review of neurobiology*. Elsevier Academic Press, London, UK, 2005.
- R. Lorente de Nó. Anatomy of the eighth nerve. III. General plan of the structure of the cochlear nuclei. *Laryngoscope*, 43:327–50, 1933.
- R. Lorente de Nó. *The Primary Acoustic Nuclei*. Raven Press, New York, 1981.
- W. W. Lytton and T. J. Sejnowski. Simulations of cortical pyramidal neurons synchronized by inhibitory interneurons. *J Neurophysiol*, 66(3):1059–79, 1991.
- R. J. MacGregor. *Theoretical mechanics of biological neural networks*. Academic, San Diego, 1993.
- S. Mahendrasingam, C. A. Wallam, and C. M. Hackney. An immunogold investigation of the relationship between the amino acids GABA and glycine and their transporters in terminals in the guinea-pig anteroventral cochlear nucleus. *Brain Res*, 887(2):477–81, 2000.
- S. Mahendrasingam, C. A. Wallam, A. Polwart, and C. M. Hackney. An immunogold investigation of the distribution of GABA and glycine in nerve terminals on the somata of spherical bushy cells in the anteroventral cochlear nucleus of guinea pig. *Eur J Neurosci*, 19(4):993–1004, 2004.
- V. A. Makarov, F. Panetsos, and O. d. Feo. A method for determining neural connectivity and inferring the underlying network dynamics using extracellular spike recordings. *J Neurosci Meth*, 144(2):265–79, 2005.
- C. Malsberg. Self-organization of orientation sensitive cells in the striate cortex. *Kybernetik*, 14:85–100, 1973.

- P. Manis. Membrane properties and discharge characteristics of guinea pig dorsal cochlear nucleus neurons studied in vitro. *J Neurosci*, 10(7):2338–51, 1990.
- P. B. Manis and S. O. Marx. Outward Currents in Isolated Ventral Cochlear Nucleus Neurons. *J Neurosci*, 11(9):2865–80, 1991.
- P. B. Manis, S. C. Molitor, and H. Wu. Subthreshold oscillations generated by TTX-sensitive sodium currents in dorsal cochlear nucleus pyramidal cells. *Exp Brain Res*, 153(4):443–51, 2003.
- Y. Manor, J. Rinzel, I. Segev, and Y. Yarom. Low-amplitude oscillations in the inferior olive: a model based on electrical coupling of neurons with heterogeneous channel densities. *J Neurophysiol*, 77(5):2736–52, 1997.
- K. V. Mardia and P. E. Jupp. *Directional Statistics*. Wiley, New York, 1999.
- B. J. May. Physiological and psychophysical assessments of the dynamic range of vowel representations in the auditory periphery. *Speech Commun*, 41(1):49–57, 2003.
- B. J. May and M. B. Sachs. Effects of stimulus level and background noise on vowel representations in the auditory brain stem of cats. *J Acoust Soc Am*, 103(5):2976, 1998.
- B. J. May, G. S. Prell, and M. B. Sachs. Vowel representations in the ventral cochlear nucleus of the cat: effects of level, background noise, and behavioral state. *J Neurophysiol*, 79(4):1755–67, 1998.
- R. Meddis. Auditory-nerve first-spike latency and auditory absolute threshold: A computer model. *J Acoust Soc Am*, 119(1):406–17, 2006.
- R. Meddis and M. Hewitt. Computer Modeling of the cochlear nucleus. In M. A. Merchan, J. M. Juiz, D. A. Godfrey, and E. Mugnaini, editors, *The Mammalian Cochlear Nuclei: Organisation and Function*, volume 239 of *NATO ASI Series. Series A, Life Sciences*. Plenum Press, New York, 1993.
- R. Meddis, M. J. Hewitt, and T. M. Shackleton. Implementation details of a computational model of the inner hair cell/auditory nerve synapse. *J Acoust Soc Am*, 87: 1813–18, 1990.

- R. Meddis, L. P. O'Mard, and E. A. Lopez-Poveda. A computational algorithm for computing nonlinear auditory frequency selectivity. *J Acoust Soc Am*, 109:2852–2861, 2001.
- N. E. Meltzer and D. K. Ryugo. Projections from auditory cortex to cochlear nucleus: A comparative analysis of rat and mouse. *Anat Rec Part A*, 288(4):397–408, 2006.
- M. Migliore, W. Cannia, X. Lytton, H. Markram, and M. Hines. Parallel network simulations with neuron. *J. Comput. Neurosci.*, 21:110–119, 2006.
- R. E. Millman, G. G. R. Green, C. Lorenzi, and A. Rees. Effect of a noise modulation masker on the detection of second-order amplitude modulation. *Hear Res*, 178(1-2):1–11, 2003.
- M. Mitchell. *An Introduction to Genetic Algorithms*. MIT Press, 1996.
- A. R. Møller. Dynamic properties of primary auditory nerve fibres compared with cells in the cochlear nucleus. *Acta Physiol Scand*, 98:157–67, 1976.
- J. K. Moore and K. K. Osen. The cochlear nuclei in man. *American J Anatomy*, 154(3):393–418, 1979.
- E. Mugnaini. GABA neurons in the superficial layers of the rat dorsal cochlear nucleus: light and electron microscopic immunocytochemistry. *J Comp Neurol*, 235:61–81, 1985.
- E. Mugnaini, K. K. Osen, A. L. Dahl, V. L. Friedrich, and G. Korte. Fine structure of granule cells and related interneurons (termed Golgi cells) in the cochlear nuclear complex of cat, rat and mouse. *J Neurocytol*, 9(4):537–70, 1980.
- W. H. Mulders, A. G. Paolini, K. Needham, and D Robertson. Olivocochlear collaterals evoke excitatory effects in onset neurones of the rat cochlear nucleus. *Hear Res*, 176 (1-2):113–21, Feb 2003.
- S. Munirathinam, E. M. Ostapoff, J. Gross, G. S. Kempe, J. A. Dutton, and D. K. Morest. Organization of inhibitory feed-forward synapses from the dorsal to the ventral cochlear nucleus in the cat: a quantitative analysis of endings by vesicle morphology. *Hear Res*, 198(1-2):99–115, 2004.

- M. Mller. Frequency representation in the rat cochlea. *Hear Res*, 51(2):247–54, 1991.
- K. Needham and A. G. Paolini. Fast inhibition underlies the transmission of auditory information between cochlear nuclei. *J Neurosci*, 23(15):6357–61, Jul 2003.
- K. Needham and A. G. Paolini. Neural timing, inhibition and the nature of stellate cell interaction in the ventral cochlear nucleus. *Hear Res*, 216–217:31–42, 2006. doi: 10.1016/j.heares.2006.01.016.
- K. Needham and A. G. Paolini. The commissural pathway and cochlear nucleus bushy neurons: an in vivo intracellular investigation. *Brain Res*, 1134(1):113–21, Feb 2007. doi: 10.1016/j.brainres.2006.11.058.
- I. Nelken and E. D. Young. Linear and nonlinear spectral integration in type IV neurons of the dorsal cochlear nucleus. I. Regions of linear interaction. *J Neurophysiol*, 78(2): 790–9, 1997.
- V. Neuert, J. L. Verhey, and I. M. Winter. Responses of dorsal cochlear nucleus neurons to signals in the presence of modulated maskers. *J Neurosci*, 24(25):5789–97, 2004.
- Eilen Nordlie, Marc-Oliver Gewaltig, and Hans Ekkehard Plesser. Towards reproducible descriptions of neuronal network models. *PLoS Comput Biol*, 5(8):e1000456, 08 2009. doi: 10.1371/journal.pcbi.1000456.
- D. Oertel. Synaptic responses and electrical properties of cells in brain slices of the mouse anteroventral cochlear nucleus. *J Neurosci*, 3(10):2043–53, 1983.
- D. Oertel. Encoding of timing in the brain stem auditory nuclei of vertebrates. *Neuron*, 19(5):959–62, 1997.
- D. Oertel and R. E. Wickesberg. Glycinergic inhibition in the cochlear nuclei: evidence for tuberculoventral neurons being glycinergic. In M. A. Merchan, J. M. Juiz, D. A. Godfrey, and E. Mugnaini, editors, *The Mammalian Cochlear Nuclei: Organisation and Function*, volume 239 of *NATO ASI Series. Series A, Life Sciences*, pages 411–20. Plenum Press, New York, 1993.
- D. Oertel and S. Wu. Morphology and physiology of cells in slice preparations of the dorsal cochlear nucleus of mice. *J Comp Neurol*, 283(2):228–47, 1989.

- D. Oertel, S. H. Wu, and J. A. Hirsch. Electrical characteristics of cells and neuronal circuitry in the cochlear nuclei studied with intracellular recording from brain slices. In G. M. Edelman, W. E. Gall, and W. M. Cowan, editors, *Auditory Function*, pages 313–36. John Wiley and Sons, New York, 1988.
- D. Oertel, S. H. Wu, M. W. Garb, and C. Dizack. Morphology and physiology of cells in slice preparations of the posteroventral cochlear nucleus of mice. *J Comp Neurol*, 295(1):136–54, 1990.
- D. Oertel, R. Bal, S. M. Gardner, P. H. Smith, and P. X. Joris. Detection of synchrony in the activity of auditory nerve fibers by octopus cells of the mammalian cochlear nucleus. *Proc Natl Acad Sci U S A*, 97(22):11773–9, 2000.
- Donata Oertel, Samantha Wright, Xiao-Jie Cao, Michael Ferragamo, and Ramazan Bal. The multiple functions of t stellate/multipolar/chopper cells in the ventral cochlear nucleus. *Hearing Research*, 276:61–69, Nov 2011. ISSN 0378-5955. doi: 10.1016/j.heares.2010.10.018.
- M. Ohlrogge, J. R. Doucet, and D. K. Ryugo. Projections of the pontine nuclei to the cochlear nucleus in rats. *J Comp Neurol*, 436(3):290–303, 2001.
- M. Okatan, M. A. Wilson, and E. N. Brown. Analyzing Functional Connectivity Using a Network Likelihood Model of Ensemble Neural Spiking Activity. *Neural Comput*, 17(9):1927–61, 2005.
- K. K. Osen. Cytoarchitecture of the cochlear nuclei in the cat. *J Comp Neurol*, 136(4):453–84, 1969.
- E. M. Ostapoff, D. K. Morest, and S. J. Potashner. Uptake and retrograde transport of [³H]GABA from the cochlear nucleus to the superior olive in the guinea pig. *J Chem Neuroanat*, 3(4):285–95, 1990.
- E. M. Ostapoff, J. J. Feng, and D. K. Morest. A physiological and structural study of neuron types in the cochlear nucleus. II. Neuron types and their structural correlation with response properties. *J Comp Neurol*, 346(1):19–42, 1994.

- E. M. Ostapoff, C. G. Benson, and R. L. Saint Marie. GABA- and glycine-immunoreactive projections from the superior olivary complex to the cochlear nucleus in guinea pig. *J Comp Neurol*, 381(4):500–12, 1997.
- E. M. Ostapoff, D. K. Morest, and K. Parham. Spatial organization of the reciprocal connections between the cat dorsal and anteroventral cochlear nuclei. *Hear Res*, 130 (1-2):75–93, 1999.
- A. R. Palmer and S. Shamma. Physiological Representations of Speech. In S. Greenberg, W. A. Ainsworth, A. N. Popper, and R. R. Fay, editors, *Speech processing in the auditory system*, volume 18 of *Springer Handbook of Auditory Research*. Springer, New York, 2003.
- A. R. Palmer, D. Jiang, and D. H. Marshall. Responses of ventral cochlear nucleus onset and chopper units as a function of signal bandwidth. *J Neurophysiol*, 75(2):780–94, 1996.
- A. R. Palmer, M. N. Wallace, R. H. Arnott, and T. M. Shackleton. Morphology of physiologically characterised ventral cochlear nucleus stellate cells. *Exp Brain Res*, 153(4): 418–26, 2003.
- P. S. Palombi and D. M. Caspary. GABA_A receptor antagonist bicuculline alters response properties of posteroventral cochlear nucleus neurons. *J Neurophysiol*, 67(3): 738–46, 1992.
- L. Paninski, J. W. Pillow, and E. P. Simoncelli. Maximum Likelihood Estimation of a Stochastic Integrate-and-Fire Neural Encoding Model. *Neural Comput*, 16(12):2533–61, 2004.
- A. G. Paolini and G. M. Clark. Intracellular responses of the rat anteroventral cochlear nucleus to intracochlear electrical stimulation. *Brain Res Bull*, 46(4):317–27, 1998.
- A. G. Paolini and G. M. Clark. Intracellular responses of onset chopper neurons in the ventral cochlear nucleus to tones: evidence for dual-component processing. *J Neurophysiol*, 81(5):2347–59, 1999.
- A. G. Paolini, G. M. Clark, and A. N. Burkitt. Intracellular responses of the rat cochlear nucleus to sound and its role in temporal coding. *Neuroreport*, 8(15):3415–21, 1997.

- A. G. Paolini, J. C. Clarey, K. Needham, and G. M. Clark. Fast inhibition alters first spike timing in auditory brainstem neurons. *J Neurophysiol*, 92(4):2615–21, Oct 2004. doi: 10.1152/jn.00327.2004.
- A. G. Paolini, J. C. Clarey, K. Needham, and G. M. Clark. Balanced inhibition and excitation underlies spike firing regularity in ventral cochlear nucleus chopper neurons. *Eur J Neurosci*, 21(5):1236–48, Mar 2005. doi: 10.1111/j.1460-9568.2005.03958.x.
- K. Parham, H. B. Zhao, Y. Ye, and D. O. Kim. Responses of anteroventral cochlear nucleus neurons of the unanesthetized decerebrate cat to click pairs as simulated echoes. *Hear Res*, 125(1-2):131–46, 1998.
- R. R. Pfeiffer. *Electro-physiological response characteristics of single units in the cochlear nucleus of the cat*. Phd, Massachusetts Institute of Technology, 1963.
- R. R. Pfeiffer. Anteroventral cochlear nucleus: Waveforms of extracellularly recorded spike potentials. *Science*, 134:667–68, 1966a.
- R. R. Pfeiffer. Classification of response patterns of spike discharges for units in the cochlear nucleus: tone-burst stimulation. *Exp Brain Res*, 1:220–35, 1966b.
- K. Piechotta, F. Weth, R. J. Harvey, and E. Friauf. Localization of rat glycine receptor alpha1 and alpha2 subunit transcripts in the developing auditory brainstem. *J Comp Neurol*, 438(3):336–52, 2001.
- J. W. Pillow, L. Paninski, V. J. Uzzell, E. P. Simoncelli, and E. J. Chichilnisky. Prediction and decoding of retinal ganglion cell responses with a probabilistic spiking model. *J Neurosci*, 25(47):11003–13, 2005.
- D. Pressnitzer, R. D. Patterson, and K. Krumbholz. The lower limit of melodic pitch with filtered harmonic complexes. *J Acoust Soc Am*, 105(2):1152, 1999.
- D. Pressnitzer, R. Meddis, R. Delahaye, and I. M. Winter. Physiological correlates of comodulation masking release in the mammalian ventral cochlear nucleus. *J Neurosci*, 21(16):6377–86, 2001.

- J. Qiu, J. Wang, and J. Shi. [collateral projections of gamma-aminobutyric acid positive neurons from the lateral superior nucleus to the cochlea and cochlear nucleus in guinea pigs]. *Zhonghua Er Bi Yan Hou Ke Za Zhi*, 30(5):279–81, 1995.
- A. Recio. Representation of harmonic complex stimuli in the ventral cochlear nucleus of the chinchilla. *J Acoust Soc Am*, 110(4):2024–33, 2001.
- A. Recio and W. S. Rhode. Basilar membrane responses to broadband stimuli. *J Acoust Soc Am*, 108(5):2281–98, 2000a.
- A. Recio and W. S. Rhode. Representation of vowel stimuli in the ventral cochlear nucleus of the chinchilla. *Hear Res*, 146(1-2):167–84, 2000b.
- E. E. Redd, H. B. Cahill, T. Pongstaporn, and D. K. Ryugo. The effects of congenital deafness on auditory nerve synapses: Type I and type II multipolar cells in the anteroventral cochlear nucleus of cats. *J Assoc Res Otolaryngol*, 3(4):403–417, Dec 2002. doi: 10.1007/s101620020043.
- M. C. Reed and J. J. Blum. A computational model for signal processing by the dorsal cochlear nucleus. I. Responses to pure tones. *J Acoust Soc Am*, 97(1):425–38, 1995.
- M. C. Reed and J. J. Blum. Model calculations of the effects of wide-band inhibitors in the dorsal cochlear nucleus. *J Acoust Soc Am*, 102(4):2238–44, 1997.
- L. A. Reiss and E. D. Young. Spectral edge sensitivity in neural circuits of the dorsal cochlear nucleus. *J Neurosci*, 25(14):3680–91, 2005.
- W. S. Rhode. Temporal coding of 200% amplitude modulated signals in the ventral cochlear nucleus of cat. *Hear Res*, 77(1-2):43–68, 1994.
- W. S. Rhode. Interspike intervals as a correlate of periodicity pitch in cat cochlear nucleus. *J Acoust Soc Am*, 97(4):2414–29, 1995.
- W. S. Rhode. Neural encoding of single-formant stimuli in the ventral cochlear nucleus of the chinchilla. *Hear Res*, 117(1-2):39–56, 1998.
- W. S. Rhode. Vertical cell responses to sound in cat dorsal cochlear nucleus. *J Neurophysiol*, 82(2):1019–32, 1999.

- W. S. Rhode and S. Greenberg. Encoding of amplitude modulation in the cochlear nucleus of the cat. *J Neurophysiol*, 71(5):1797–825, 1994a.
- W. S. Rhode and S. Greenberg. Lateral suppression and inhibition in the cochlear nucleus of the cat. *J Neurophysiol*, 71(2):493–514, 1994b.
- W. S. Rhode and R. E. Kettner. Physiological study of neurons in the dorsal and posteroverentral cochlear nucleus of the unanesthetized cat. *J Neurophysiol*, 57(2):414–42, 1987.
- W. S. Rhode and P. H. Smith. Encoding timing and intensity in the ventral cochlear nucleus of the cat. *J Neurophysiol*, 56(2):261–86, 1986.
- W. S. Rhode, D. Oertel, and P. H. Smith. Physiological response properties of cells labeled intracellularly with horseradish peroxidase in cat ventral cochlear nucleus. *J Comp Neurol*, 213(4):448–63, 1983a.
- W. S. Rhode, P. H. Smith, and D. Oertel. Physiological response properties of cells labeled intracellularly with horseradish peroxidase in cat dorsal cochlear nucleus. *J Comp Neurol*, 213(4):426–47, 1983b.
- J. J. Rice, E. D. Young, and G. A. Spirou. Auditory-nerve encoding of pinna-based spectral cues: Rate representation of high-frequency stimuli. *J Acoust Soc Am*, 97(3):1764–76, 1995.
- A. R. Robert and J. L. Eriksson. A composite model of the auditory periphery for simulating response to complex sounds. *J Acoust Soc Am*, 106:1852–64, 1999.
- A. R. Rodrigues and D. Oertel. Hyperpolarization-activated currents regulate excitability in stellate cells of the mammalian ventral cochlear nucleus. *J Neurophysiol*, 95(1):76–87, 2006.
- J. E. Rose, R. Galambos, and J. R. Hughes. Microelectrode Studies of the Cochlear Nuclei of the Cat. *Bulletin of the Johns Hopkins Hospital*, 104(5):211–51, 1959.
- C. Rossant, D. F. M. Goodman, J. Platkiewicz, and R. Brette. Automatic fitting of spiking neuron models to electrophysiological recordings. *Front. Neuroinform.*, 4(2):1–10, 2010. doi: 10.3389/neuro.11.002.2010.

- J. S. Rothman and P. B. Manis. Differential expression of three distinct potassium currents in the ventral cochlear nucleus. *J Neurophysiol*, 89(6):3070–82, 2003a.
- J. S. Rothman and P. B. Manis. Kinetic analyses of three distinct potassium conductances in ventral cochlear nucleus neurons. *J Neurophysiol*, 89(6):3083–96, 2003b.
- J. S. Rothman and P. B. Manis. The roles potassium currents play in regulating the electrical activity of ventral cochlear nucleus neurons. *J Neurophysiol*, 89(6):3097–113, 2003c.
- M. E. Rubio. Differential distribution of synaptic endings containing glutamate, glycine, and GABA in the rat dorsal cochlear nucleus (vol 477, pg 253, 2004). *J Comp Neurol*, 485(3):266–66, 2005.
- M. E. Rubio. Redistribution of synaptic AMPA receptors at glutamatergic synapses in the dorsal cochlear nucleus as an early response to cochlear ablation in rats. *Hear Res*, 216–217:154–67, 2006.
- M. E. Rubio and J. M. Juiz. Differential distribution of synaptic endings containing glutamate, glycine, and GABA in the rat dorsal cochlear nucleus. *J Comp Neurol*, 477 (3):253–72, 2004.
- David E. Rumelhart, Geoffrey E. Hinton, and Ronald J. Williams. Learning representations by back-propagating errors. *Nature*, 323(6088):533–536, Oct 1986. doi: 10.1038/323533a0.
- D. Ryugo, D. Wrigth, and T. Pongstaporn. Ultrastructural analysis of synaptic endings of auditory nerve fibres in cats: correlations with spontaneous discharge rate. In M. A. Merchan, J. M. Juiz, D. A. Godfrey, and E. Mugnaini, editors, *The Mammalian Cochlear Nuclei: Organisation and Function*, volume 239 of *NATO ASI Series. Series A, Life Sciences*, pages 65–73. Plenum Press, New York, 1993.
- D. K. Ryugo. The auditory nerve: Peripheral innervation, cell body morphology and central projections. In D. B. Webster, A. N. Popper, and R. R. Fay, editors, *The Mammalian Auditory Pathway: Neuroanatomy*, pages 23–65. Springer-Verlag, New York, 1992.

- D. K. Ryugo. Projections of low spontaneous rate, high threshold auditory nerve fibers to the small cell cap of the cochlear nucleus in cats. *Neuroscience*, 154(1):114–126, Jun 2008. doi: 10.1016/j.neuroscience.2007.10.052.
- D. K. Ryugo and T. N. Parks. Primary innervation of the avian and mammalian cochlear nucleus. *Brain Res Bull*, 60(5-6):435–56, 2003.
- D. K. Ryugo, C. A. Haenggeli, and J. R. Doucet. Multimodal inputs to the granule cell domain of the cochlear nucleus. *Exp Brain Res*, 153(4):477–85, 2003.
- M. B. Sachs and E. D. Young. Patterns of auditory-nerve fiber responses to steady-state vowels. *J Acoust Soc Am*, 63(S1):S76, 1978.
- M. B. Sachs and E. D. Young. Effects of nonlinearities on speech encoding in the auditory nerve. *J Acoust Soc Am*, 65(S1):S102, 1979.
- M. B. Sachs and E. D. Young. Effects of nonlinearities on speech encoding in the auditory nerve. *J Acoust Soc Am*, 68(3):858–75, 1980.
- M. B. Sachs, R. L. Winslow, and B. H. A. Sokolowski. A computational model for rate-level functions from cat auditory-nerve fibers. *Hear Res*, 41(1):61–69, 1989.
- R. L. Saint Marie, D. K. Morest, and C. J. Brandon. The form and distribution of GABAergic synapses on the principal cell types of the ventral cochlear nucleus of the cat. *Hear Res*, 42(1):97–112, 1989.
- R. L. Saint Marie, C. G. Benson, E.-M. Ostapoff, and D. K. Morest. Glycine immunoreactive projections from the dorsal to the anteroventral cochlear nucleus. *Hear Res*, 51(1):11–28, 1991.
- K. Sameshima and L. A. Baccala. Using partial directed coherence to describe neuronal ensemble interactions. *J Neurosci Methods*, 94(1):93–103, 1999.
- J. David Schaffer, Heike Sichtig, and Craig Laramee. A series of failed and partially successful fitness functions for evolving spiking neural networks. In *Proceedings of the 11th Annual Conference Companion on Genetic and Evolutionary Computation Conference: Late Breaking Papers*, GECCO '09, pages 2661–2664, New York, NY, USA, 2009. ACM. ISBN 978-1-60558-505-5. doi: 10.1145/1570256.1570378.

- R A Schmiedt. Spontaneous rates, thresholds and tuning of auditory-nerve fibers in the gerbil: comparisons to cat data. *Hearing Research*, 42(1):23–35, 1989.
- B. R. Schofield. Superior paraolivary nucleus in the pigmented guinea pig: separate classes of neurons project to the inferior colliculus and the cochlear nucleus. *J Comp Neurol*, 312(1):68–76, 1991.
- B. R. Schofield. Projections from the cochlear nucleus to the superior paraolivary nucleus in guinea pigs. *J Comp Neurol*, 360(1):135–49, 1995.
- B. R. Schofield. Ascending and descending projections from the superior olfactory complex in guinea pigs: different cells project to the cochlear nucleus and the inferior colliculus. *J Comp Neurol*, 453(3):217–25, 2002.
- B. R. Schofield and N. B. Cant. Origins and targets of commissural connections between the cochlear nuclei in guinea pigs. *J Comp Neurol*, 375(1):128–46, 1996.
- I. Segev, , R. E. Burke, and M. Hines. Compartmental Models of Complex Neurons. In C. Koch and I. Segev, editors, *Methods in neuronal modeling : from ions to networks*, pages 63–96. MIT Press, Massachusetts, 2nd edition, 1998.
- S. Shamma. Spatial and temporal processing in central auditory networks. In C. Koch and I. Segev, editors, *Methods in Neuronal Modeling: From Ions to Networks*, pages 411–60. MIT Press, Cambridge, MA, 1998.
- S. A. Shamma. Speech processing in the auditory system. ii: Lateral inhibition and the central processing of speech evoked activity in the auditory nerve. *J Acoust Soc Am*, 78(5):1622–1632, Nov 1985.
- R. V. Shannon, F.-G. Zeng, V. Kamath, J. Wygonski, and M. Ekelid. Speech Recognition with Primarily Temporal Cues. *Science*, 270(5234):303–04, 1995.
- W. P. Shofner and E. D. Young. Excitatory/inhibitory response types in the cochlear nucleus: relationships to discharge patterns and responses to electrical stimulation of the auditory nerve. *J Neurophysiol*, 54(4):917–39, 1985.
- S. E. Shore, D. A. Godfrey, R. H. Helfert, R. A. Altschuler, and S. C. Bledsoe. Connections between the cochlear nuclei in guinea pig. *Hear Res*, 62(1):16–26, 1992.

- Heike Sichtig, J. David Schaffer, and Craig B. Laramee. Snnns -: a suite of tools to explore spiking neural networks. In *Proceedings of the 2008 GECCO conference companion on Genetic and evolutionary computation*, GECCO '08, pages 1787–1790, New York, NY, USA, 2008. ACM. ISBN 978-1-60558-131-6. doi: 10.1145/1388969.1388971.
- A. M. Simmons, A. N. Popper, and R. R. Fay, editors. *Acoustic communication*, volume 16 of *Springer handbook auditory Res*. Springer, New York, 2002.
- P. Smith, P. Joris, M. Banks, and T. C. T. Yin. Responses of cochlear nucleus cells and projections of their axons. In M. A. Merchan, J. M. Juiz, D. A. Godfrey, and E. Mugnaini, editors, *The Mammalian Cochlear Nuclei: Organisation and Function*, volume 239 of *NATO ASI Series. Series A, Life Sciences*, pages 349–60. Plenum Press, New York, 1993.
- P. H. Smith, A. Massie, and P. X. Joris. Acoustic stria: anatomy of physiologically characterized cells and their axonal projection patterns. *J Comp Neurol*, 482(4):349–71, 2005.
- Philip H. Smith and William S. Rhode. Structural and functional properties distinguish two types of multipolar cells in the ventral cochlear nucleus. *The Journal of Comparative Neurology*, 282(4):595–616, 1989. ISSN 1096-9861. doi: 10.1002/cne.902820410.
- Sunghwan Sohn and Cihan H. Dagli. Ensemble of evolving neural networks in classification. *Neural Process. Lett.*, 19:191–203, June 2004. ISSN 1370-4621. doi: 10.1023/B:NEPL.0000035600.72270.f3.
- K. M. Spangler, N. B. Cant, C. K. Henkel, G. R. Farley, and W. B. Warr. Descending projections from the superior olivary complex to the cochlear nucleus of the cat. *J Comp Neurol*, 259(3):452–65, 1987.
- G. A. Spirou and E. D. Young. Organization of Dorsal Cochlear Nucleus Type-Iv Unit Response Maps and Their Relationship to Activation by Band-Limited Noise. *J Neurophysiol*, 66(5):1750–68, 1991.
- G. A. Spirou, K. A. Davis, I. Nelken, and E. D. Young. Spectral integration by type II interneurons in dorsal cochlear nucleus. *J Neurophysiol*, 82(2):648–63, 1999.

- H. Spoendlin. The innervation of the cochlear receptor. In A. R. Møller, editor, *Basic Mechanisms in Hearing*, pages 185–230. Academic Press, New York, 1973.
- Christian J. Sumner, Enrique A. Lopez-Poveda, Lowel P. O'Mard, and Ray Meddis. A revised model of the inner-hair cell and auditory-nerve complex. *The Journal of the Acoustical Society of America*, 111(5):2178–2188, 2002. doi: 10.1121/1.1453451.
- G. Svirskis and J. Rinzel. Influence of subthreshold nonlinearities on signal-to-noise ratio and timing precision for small signals in neurons: minimal model analysis. *Network-Comput Neural*, 14(1):137–50, 2003.
- T. Takahama and S. Sakai. Constrained optimization by applying the /spl alpha/ constrained method to the nonlinear simplex method with mutations. *Evol Comput*, 9(5):437–51, 2005.
- Q. Tan and L. Carney. An auditory-nerve model with an instantaneous frequency glide and its application to modeling psychophysical results. *J Acoust Soc Am*, 109(5):2374, 2001.
- Q. Tan and L. H. Carney. A phenomenological model for the responses of auditory-nerve fibers. II. Nonlinear tuning with a frequency glide. *J Acoust Soc Am*, 114:2007–20, 2003.
- A. M. Taylor and R. M. Enoka. Optimization of input patterns and neuronal properties to evoke motor neuron synchronization. *J Comput Neurosci*, 16(2):139–57, 2004.
- F. E. Theunissen, K. Sen, and A. J. Doupe. Spectral-temporal Receptive Fields of Non-linear Auditory Neurons Obtained Using Natural Sounds. *J Neurosci*, 20(6):2315–31, 2000.
- L. P. Tolbert and D. K. Morest. The neuronal architecture of the anteroventral cochlear nucleus of the cat in the region of the cochlear nerve root: Golgi and Nissl methods. *Neurosci*, 7(12):3013–25, 1982a.
- L. P. Tolbert and D. K. Morest. The neuronal architecture of the anteroventral cochlear nucleus of the cat in the region of the cochlear nerve root: Electron microscopy. *Neurosci*, 7(12):3053–67, 1982b.

- W. Van Geit, P. Achard, and E. De Schutter. Neurofitter: a parameter tuning package for a wide range of electrophysiological neuron models. *Frontiers in Neuroinformatics*, 1:1, 2007. doi: 10.3389/neuro.11/001.2007.
- W. Van Geit, E. De Schutter, and P Achard. Automated neuron model optimization techniques: a review. *Biol Cybern*, 99(4-5):241 – 251, 2008. ISSN 1432-0770.
- C. A. van Vreeswijk, L. F. Abbott, and G. B. Ermentrout. Inhibition, not excitation, synchronizes coupled neurons. *J Comp Neurosci*, pages 303–313, 1995.
- M. C. Vanier and J. M. Bower. A Comparative Survey of Automated Parameter-Search Methods for Compartmental Neural Models. *J Comput Neurosci*, 7:149–71, 1999.
- J. D. Victor. Spike train metrics. *Current Opinion in Neurobiology Neuronal and glial cell biology / New technologies*, 15(5):585–92, 2005.
- J. D. Victor, D. H. Goldberg, and D. Gardner. Dynamic programming algorithms for comparing multineuronal spike trains via cost-based metrics and alignments. *J Neurosci Methods*, 161(2):351–60, 2007.
- N. F. Viemeister. Temporal modulation transfer functions based upon modulation thresholds. *J Acoust Soc Am*, 66:1364–80, 1979.
- H F Voigt and E D Young. Evidence of inhibitory interactions between neurons in dorsal cochlear nucleus. *Journal of Neurophysiology*, 44(1):76–96, 1980. URL <http://jn.physiology.org/content/44/1/76.short>.
- H. F. Voigt and E. D. Young. Cross correlation analysis of inhibitory interationsin the dorsal cochlear nuclei. *J Neurophysiol*, 64:1590–610, 1990.
- M. Wall. GALIB: A C++ library of genetic algorithm components, 2006. URL <http://lancet.mit.edu/ga>.
- J. Wang, N. L. Powers, Hofstetter P., P. Trautwein, D. Ding, and R. Salvi. Effects of selective inner hair cell loss on auditory nerve fiber threshold, tuning and spontaneous and driven discharge rate. *Hear Res*, 107:67–82, 1997.

- X. Wang and M. B. Sachs. Neural encoding of single-formant stimuli in the cat. I. Responses of auditory nerve fibers. *J Neurophysiol*, 70(3):1054–75, 1993.
- X. Wang and M. B. Sachs. Neural encoding of single-formant stimuli in the cat. II. Responses of anteroventral cochlear nucleus units. *J Neurophysiol*, 71(1):59–78, 1994.
- X. Wang and M. B. Sachs. Transformation of temporal discharge patterns in a ventral cochlear nucleus stellate cell model: implications for physiological mechanisms. *J Neurophysiol*, 73(4):1600–16, 1995.
- Xiaoqin Wang. Analyticity theorems for parameter-dependent currents. *Mathematica Scandinavica*, 69(2):179–198, 1991.
- R. J. Wenthold. Evidence for a glycinergic pathway connecting the two cochlear nuclei: an immunocytochemical and retrograde transport study. *Brain Res*, 415:183–87, 1987.
- L. A. Westerman and R. L. Smith. A diffusion model of the transient response of the cochlear inner hair cell synapse. *J Acoust Soc Am*, 83:2266–2276, 1988.
- J. A. White, E. D. Young, and P. B. Manis. Application of new electrotonic modeling methods: Results from Type I cells in guinea pig ventral cochlear nucleus. *Soc Neurosci Abst*, 16:870, 1990.
- J. A. White, E. D. Young, and P. B. Manis. The electrotonic structure of regular-spiking neurons in the ventral cochlear nucleus may determine their response properties. *J Neurophysiol*, 71(5):1774–86, 1994.
- D. L. Whitley. Genetic Algorithms and Neural Networks. In G. Winter, J. Periaux, M. Galan, and P. Cuesta, editors, *Genetic Algorithms in Engineering and Computer Science*, pages 203–16. John Wiley and Sons, Ltd., Chichester, 1995.
- R. Wickesberg and D. Oertel. Tonotopic projection from the dorsal to the anteroventral cochlear nucleus of mice. *J Comp Neurol*, 268(3):389–99, 1988.
- R. Wickesberg and D. Oertel. Delayed, frequency-specific inhibition in the cochlear nuclei of mice: a mechanism for monaural echo suppression. *J Neurosci*, 10(6):1762–68, 1990.

- R. Wickesberg and D. Oertel. Intrinsic connections in the cochlear nucleus complex studied in vitro and in vivo. In M. A. Merchan, J. M. Juiz, D. A. Godfrey, and E. Mugnaini, editors, *The Mammalian Cochlear Nuclei: Organisation and Function*, volume 239 of *NATO ASI Series. Series A, Life Sciences*. Plenum Press, New York, 1993.
- R. Wickesberg, D. Whitlon, and D. Oertel. Tuberculoventral neurons project to the multipolar cell area but not to the octopus cell area of the posteroventral cochlear nucleus. *J Comp Neurol*, 313(3):457–68, 1991.
- L. Wiegrefe and R. Meddis. The representation of periodic sounds in simulated sustained chopper units of the ventral cochlear nucleus. *J Acoust Soc Am*, 115(3):1207–18, 2004.
- R. L. Winslow, P. E. Barta, and M. B. Sachs. Rate coding in the auditory nerve. In W. A. Yost and C. S. Watson, editors, *Auditory Processing Complex Sounds*, pages 212–24. Lawrence Erbaum, NJ, 1987.
- I. M. Winter and A. R. Palmer. Level dependence of cochlear nucleus onset unit responses and facilitation by second tones or broadband noise. *J Neurophysiol*, 73(1):141–59, 1995.
- I. M. Winter, A. R. Palmer, and R. Meddis. The response of guinea pig auditory-nerve fibers with high spontaneous discharge rates to increments in intensity. *Brain Res*, 618(1):167–70, 1993.
- S. H. Wu and D. Oertel. Intracellular injection with horseradish peroxidase of physiologically characterized stellate and bushy cells in slices of mouse anteroventral cochlear nucleus. *J Neurosci*, 4(6):1577–88, 1984.
- Y. J. Xu, L. H. Zhou, and Z. J. Xiao. [response properties of cochlear nucleus neurons: a digital model-based study.]. *Nan Fang Yi Ke Da Xue Xue Bao*, 31(1):77–81, Jan 2011.
- S. Yamada, K. Matsumoto, M. Nakashima, and S. Shiono. Information theoretic analysis of action potential trains II. Analysis of correlation among n neurons to deduce connection structure. *J Neurosci Meth*, 66(1):35–45, 1996.

- L. Yang, P. Monsivais, and E. W. Rubel. The Superior Olivary Nucleus and Its Influence on Nucleus Laminaris: A Source of Inhibitory Feedback for Coincidence Detection in the Avian Auditory Brainstem. *J Neurosci*, 19(6):2313–25, 1999.
- S.-M. Yang, T. Doi, M. Asako, A. Matsumoto-Ono, T. Kaneko, and T. Yamashita. Multiple-site optical recording of mouse brainstem evoked by vestibulocochlear nerve stimulation. *Brain Res*, 877(1):95–100, 2000.
- X. Yao. Evolving artificial neural networks. *Proceedings of the IEEE*, 87(9):1423–47, 1999.
- E. D. Young. Identification of response properties of ascending axons from the dorsal cochlear nucleus. *Brain Res*, 200:23–38, 1980.
- E. D. Young. Response characteristics of neurons in the cochlear nuclei. In C. I. Berlin, editor, *Hearing Science*, pages 423–59. College Hill Press, San Diego, CA, 1984.
- E. D. Young and W. E. Brownell. Responses to tones and noise of single cells in the dorsal cochlear nucleus of the unanaesthetised cat. *J Neurophysiol*, 39:282–300, 1976.
- E. D. Young and K. A. Davis. Circuitry and Function of the Dorsal Cochlear Nucleus. In D. Oertel, A. N. Popper, and R. R. Fay, editors, *Integrative Functions in the mammalian Auditory Pathway*, volume 15 of *Springer Handbook of Auditory Research*, pages 160–206. Springer, New York, 2002.
- E. D. Young and D. Oertel. Cochlear Nucleus. In G. M. Shepherd, editor, *The synaptic organization the brain*. Oxford University Press, New York, 4th edition, 2004.
- E. D. Young and M. B. Sachs. Representation of Steady-state Vowels in the Temporal Aspects of the Discharge Patterns of Populations of Auditory-nerve Fibers. *J Acoust Soc Am*, 66:1381 – 403, 1979.
- E. D. Young and H. F. Voigt. The internal organization of the dorsal cochlear nucleus. In J. Syka and L. Aitkin, editors, *Neuronal Mechanisms in Hearing*, pages 127–33. Plenum Press, New York, 1981.
- E. D. Young and H. F. Voigt. Response properties of type II and type III units in dorsal cochlear nucleus. *Hear Res*, 6(2):153–69, 1982.

- E. D. Young, J. M. Robert, and W. P. Shofner. Regularity and latency of units in ventral cochlear nucleus: implications for unit classification and generation of response properties. *J Neurophysiol*, 60(1):1–29, 1988.
- E. D. Young, G. A. Spirou, J. J. Rice, and H. F. Voigt. Neural Organization and Responses to Complex Stimuli in the Dorsal Cochlear Nucleus. *Philos T Roy Soc B*, 336(No. 1278, Processing of Complex Sounds by the Auditory System):407–13, 1992.
- E. D. Young, I. Nelken, and G. A. Spirou. Nonlinearity of spectra processing in the dorsal cochlear nucleus (DCN). *J Acoust Soc Am*, 93(4):2294, 1993.
- J. H. Zar. *Biostatistical Analysis*. Prentice Hall, 1999.
- H. Zhang and J. B. Kelly. Glutamatergic and GABAergic Regulation of Neural Responses in Inferior Colliculus to Amplitude-Modulated Sounds. *J Neurophysiol*, 90(1):477–90, 2003.
- S. Zhang and D. Oertel. Tuberculoventral cells of the dorsal cochlear nucleus of mice: intracellular recordings in slices. *J Neurophysiol*, 69(5):1409–21, 1993.
- X. Zhang and L. H. Carney. A coincidence-detection model for level discrimination of tones in roving-level noise. *J Acoust Soc Am*, 109(5):2375, 2001.
- X. Zhang, M. G. Heinz, I. C. Bruce, and L. H. Carney. A phenomenological model for the responses of auditory-nerve fibers: I. Nonlinear tuning with compression and suppression. *J Acoust Soc Am*, 109(2):648–70, 2001.
- H. B. Zhao and Z. A. Liang. Temporal encoding and transmitting of amplitude and frequency modulations in dorsal cochlear nucleus. *Hear Res*, 106(1-2):83–94, 1997.
- M. S. A. Zilany and I. C. Bruce. Modeling auditory-nerve responses for high sound pressure levels in the normal and impaired auditory periphery. *J Acoust Soc Am*, 120(3):1446–66, 2006.
- M. S. A. Zilany and I. C. Bruce. Representation of the vowel /epsilon/ in normal and impaired auditory nerve fibers: Model predictions of responses in cats. *J Acoust Soc Am*, 122(1):402–17, 2007.

Muhammad S. A. Zilany and Laurel H. Carney. Power-law dynamics in an auditory-nerve model can account for neural adaptation to sound-level statistics. *J Neurosci*, 30:10380–10390, 2010.

Muhammad S. A. Zilany, Ian C. Bruce, Paul C. Nelson, and Laurel H. Carney. A phenomenological model of the synapse between the inner hair cell and auditory nerve: Long-term adaptation with power-law dynamics. *J Acoust Soc Am*, 126(5):2390–2412, 2009. doi: 10.1121/1.3238250.

E. Zwicker and H. Fastl. *Psychoacoustics : facts and models*. Springer, Berlin ; New York, 2nd edition, 1999.